

DISSERTATION

# Reliability Issues in High-Voltage Semiconductor Devices

ausgeführt zum Zwecke der Erlangung des akademischen Grades  
eines Doktors der technischen Wissenschaften

eingereicht an der Technischen Universität Wien  
Fakultät für Elektrotechnik und Informationstechnik  
von

OLIVER TRIEBL



Wien, im Oktober 2012

---



# Abstract

Semiconductor devices are used in many different application areas and play an important role in the modern world. Advances in technology, customer demands, and cost pressure lead to higher integration densities and to smart power structures, which incorporate high- and low-voltage devices on the same chip. Because of the down-scaling and the rising complexity of devices, it becomes an increasingly challenging task to obtain the required reliability demands. Therefore, technology computer-aided design (TCAD) tools are used to simulate semiconductor devices.

While the term high-voltage is often used for a wide range of devices, this thesis is focused on field-effect transistors with operating voltages ranging from 5 to 60 V. The most important devices among this class type as well as relevant design techniques are presented. Since reliability in these high-voltage field-effect transistors is a major concern for the semiconductor industry, the physical processes behind the degradation occurring in semiconductor bulk, oxide, and their interfaces are discussed in this work. However, probably the most important degradation processes in high-voltage devices are those related to the hot-carrier phenomena impact-ionization and hot-carrier degradation. These two topics are addressed in detail from a modeling and simulation perspective. In particular, simulations based on the drift-diffusion (DD) framework are used and the possibilities and limitations of modeling hot-carrier induced phenomena herein are discussed.

Impact-ionization generation is the first hot-carrier process presented in this thesis, starting with a summary on the different modeling approaches. The importance of impact-ionization generation for the reliability of high-voltage smart power devices is demonstrated in a case-study. In this study the snap-back behavior of a parasitic bipolar structure is investigated and structure optimizations are discussed. The second process driven by high energetic carriers is hot-carrier degradation. A physics-based modeling approach relying on the carrier energy distribution function which is derived from Boltzmann's transport equation is presented. The long simulation times required to calculate the distribution function make this approach not very flexible for industrial use. Therefore, variations of this model based on the DD framework have been investigated and show to deliver good results for relevant devices.

Simulations of high-voltage devices often lead to numerical difficulties, especially if impact-ionization generation has to be considered. In the DD framework the modeling of impact-ionization requires an accurate discretization of vector quantities such as the current densities and the driving force, which is numerically very challenging. Different vector discretization schemes are presented and their influence on the convergence behavior and accuracy is analyzed.



# Kurzfassung

Halbleiterbauelemente spielen in den verschiedensten Anwendungsbereichen eine bedeutende Rolle. Technologische Fortschritte, Anforderungen von Kunden und nicht zuletzt der Kostendruck führen zu immer höheren Packungsdichten. Weiters werden häufig *High-Voltage* Bauelemente mit hoch integrierten digitalen Schaltkreisen auf einem Siliziumchip zu sogenannten *Smart-Power* Bauelementen vereint. Um die Anforderungen bei der stetig steigenden Komplexität der Bauelemente erfüllen zu können, ist der Einsatz von Simulationssoftware erforderlich. Dabei handelt es sich um so genannte *Technology Computer-Aided Design* (TCAD) Tools.

Aus der Reihe von verfügbaren *High-Voltage* Bauelementen konzentriert sich diese Arbeit auf Feldeffekttransistoren mit Betriebsspannungen zwischen 5 und 60 V. Die wichtigsten Transistortypen sowie Designtechniken werden vorgestellt. Eine hohe Zuverlässigkeit dieser Bauteile ist für die Halbleiterindustrie von essenzieller Bedeutung, weswegen in dieser Arbeit die für die Degradation relevanten physikalischen Prozesse erörtert werden. In *High-Voltage* Bauelementen zählen Mechanismen in Verbindung mit heißen Ladungsträgern zu den wichtigsten Verursachern von Zuverlässigkeitsproblemen. Daher widmet sich diese Arbeit den beiden Prozessen Stoßionisation und *Hot-Carrier* Degradation und untersucht die Prozesse vor allem aus dem Blickwinkel der Modellierung und Simulation. Hierbei wird im speziellen mit dem Drift-Diffusionsmodell gearbeitet und dabei werden die Möglichkeiten sowie Grenzen dieses Modells aufgezeigt.

Der erste durch heiße Ladungsträger verursachte Prozess, der in dieser Dissertation behandelt wird, ist die Stoßionisation. Die Relevanz für die Zuverlässigkeit im Bereich der *Smart-Power* Bauelemente wird anhand einer Simulationsstudie über das *Snap-Back* Verhalten aufgezeigt und mögliche Optimierungen werden diskutiert. Beim zweiten in dieser Arbeit behandelten Prozess, der *Hot-Carrier* Degradation, wird im Besonderen auf einen neuen, auf die Verteilungsfunktion der Ladungsträger basierenden Ansatz eingegangen. Da die vollständige Berechnung der Verteilungsfunktion aus der Boltzmannschen Transportgleichung sehr zeitintensiv ist, erscheint der Nutzen dieses Modells für die Industrie derzeit noch gering. Als Alternative dazu werden in dieser Arbeit Ansätze, die auf dem Drift-Diffusionsmodell basieren, untersucht, welche für die maßgeblichen Bauelemente gute Ergebnisse liefern.

Bei der Simulation von *High-Voltage* Bauelementen kommt es oft zu numerischen Problemen, im Besonderen bei der Berücksichtigung der Stoßionisation. Für eine akkurate Modellierung dieses Prozesses im Drift-Diffusionsmodell ist eine passende Diskretisierung von Vektorgößen von essenzieller Bedeutung. In dieser Arbeit wird daher der Einfluss verschiedener Verfahren für die Vektordiskretisierung auf das Konvergenzverhalten und die erzielte Genauigkeit untersucht.



# Acknowledgment

Writing and finishing this thesis wouldn't have been possible with the support of my colleagues at the Institute of Microelectronics. The most important person for my work is definitely my advisor Prof. Tibor Grasser, who didn't get tired of motivating me to continue and especially to finally finish writing my thesis. Special thanks also go to Prof. Martin Gröschl, who agreed on a very short notice to be the second reviewer. I also want to thank Prof. Hans Kosina, Prof. Erasmus Langer, and Prof. Siegfried Selberherr, in whose projects I could participate in times when funding was short. In the daily organizational work Ewald Haslinger, Manfred Katterbauer, and Renate Winkler were always at hand to help and to give advice.

I also want to thank the companies *Infineon Villach*, *ams*, and *Sony Japan* for giving their share of the financial support. For the job opportunity and financial support beside the university I want to acknowledge Markus Karner and Christian Kernstock, the founders of *Global TCAD Solutions*.

Writing this thesis was a long process and luckily there were many colleagues who were there for help and discussions. Also chats during coffee breaks and the many private activities were important for the good collaboration. I have the best memories of my early days at the institute among my room mates Gerhard Karlowatz, Victor Sverdlov, and Wilfried Wessner. Also my other colleagues, especially Johann Cervenka, Robert Entner, Stefan Holzer, Philipp Schwaha, Enzo Ungersböck, and Martin Wagner were responsible for this very good atmosphere. These people helped me to get to know how things are working at the institute and how to get along in this new environment. I will not forget the common activities, including a marathon run, a trip to India joining the wedding of our colleague Siddhartha Dhar, going for a hike in France, and the common motorcycle trips. I am really happy to still be in contact with most of these colleagues.

Among the people who joined the institute later than I did, I want to specially thank Martin Vasicek, Wolfgang Gös, and Stanislav Tyaginov. Together with Johann, they were in charge of proofreading this thesis. Stanislav was always there to check my texts and to give scientific advice, sometimes even during long night shifts. An office which I will definitely remember was occupied by Philipp Hehenberger, Franz Schanovsky, and Paul-Jürgen Wagner. In this office every single word could trigger one of the most intellectual and philosophical discussions. More people I want to thank for the good collaborations are Oskar Baumgartner (viva Las Vegas), Markus Bina (thanks for the good work done in MINIMOS-NT), Neophytos Neophytou (sorry for

the idea of going downhill skiing), Zlatan Stanojevic, Ivan Starkov (thanks for the simulation results I could borrow), and Thomas Windbacher. And thanks to all the colleagues I didn't mention here but who are also responsible for the in general good time I had at the Institute of Microelectronics.

Finally, I want to thank my family. My parents Erika and Wilhelm didn't stop motivating me and I wouldn't have joined the institute without my father's convincing words. My wife Martina always tried to cheer me up and supported me, also in times of my biggest frustrations. Also a big "thank you", for the patience with me during the last months, in which I was at home just for sleeping, because there was no time left between studies and work.



# Contents

|   |             |
|---|-------------|
| <b>Abstract</b>   | <b>i</b>    |
| <b>Kurzfassung</b>  | <b>iii</b>  |
| <b>Acknowledgment</b>   | <b>v</b>    |
| <b>Contents</b>   | <b>vii</b>  |
| <b>List of Abbreviations and Acronyms</b>                         | <b>xiii</b> |
| <b>1 Introduction</b>   | <b>1</b>    |
| <b>2 High-Voltage and Power Devices</b>                           | <b>3</b>    |
| 2.1 High-Voltage Device Types . . . . .                           | 3           |
| 2.1.1 Metal Oxide Semiconductor Field-Effect Transistor . . . . . | 3           |
| 2.1.2 Insulated Gate Bipolar Transistor . . . . .                 | 5           |
| 2.2 Device Design Techniques . . . . .                            | 6           |
| 2.2.1 Vertical and Lateral Devices . . . . .                      | 6           |
| 2.2.2 Reduced Surface Field Technique . . . . .                   | 8           |
| 2.3 Smart Power Devices . . . . .                                 | 10          |
| 2.3.1 Isolation . . . . .   | 11          |
| 2.3.2 Industrial Examples . . . . .                               | 12          |

|          |   |           |
|----------|---|-----------|
| <b>3</b> | <b>Reliability in Semiconductor Devices</b>                               | <b>15</b> |
| 3.1      | Reliability in General . . . . .  | 15        |
| 3.1.1    | History of Reliability . . . . .  | 16        |
| 3.1.2    | Keywords and Definitions . . . . .  | 17        |
| 3.1.3    | The Bathtub Curve . . . . .   | 17        |
| 3.1.4    | Reliability Calculations and Statistics . . . . .                         | 19        |
| 3.1.5    | Reliability and Yield . . . . .   | 23        |
| 3.2      | Failure and Degradation Mechanisms . . . . .                              | 25        |
| 3.2.1    | Mass Transport . . . . .  | 25        |
| 3.2.2    | Oxide- and Interface-Related Failure and Degradation Mechanisms . . . . . | 26        |
| 3.2.3    | Bulk Semiconductor Related Reliability Issues . . . . .                   | 30        |
| 3.2.4    | Overvoltage and Electrostatic Discharge . . . . .                         | 30        |
| 3.2.5    | Environmental Impacts . . . . .   | 32        |
| <b>4</b> | <b>Device Simulation and Parameter Modeling</b>                           | <b>33</b> |
| 4.1      | Semiconductor Equations . . . . .   | 33        |
| 4.1.1    | Poisson's and Continuity Equation . . . . .                               | 33        |
| 4.1.2    | Carrier Transport Equations . . . . .                                     | 35        |
| 4.1.3    | The Drift-Diffusion Model . . . . .                                       | 36        |
| 4.1.4    | Higher-Order Transport Models . . . . .                                   | 36        |
| 4.2      | Parameter Modeling . . . . .  | 38        |
| 4.2.1    | Mobility . . . . .  | 38        |
| 4.2.2    | Carrier Generation and Recombination . . . . .                            | 42        |
| 4.2.3    | Thermal Modeling . . . . .  | 44        |
| 4.2.4    | Additional Physical Effects . . . . .                                     | 45        |
| 4.3      | Carrier Energy Distribution Function . . . . .                            | 46        |
| 4.3.1    | Carrier Temperature Estimation in the Drift-Diffusion Model . . . . .     | 46        |

|          |   |           |
|----------|---|-----------|
| 4.3.2    | Distribution Function Approximations . . . . .              | 50        |
| 4.4      | Summary . . . . .   | 54        |
| <b>5</b> | <b>Impact-Ionization Generation</b>                         | <b>55</b> |
| 5.1      | Basics of Impact-Ionization . . . . .                       | 55        |
| 5.1.1    | Ionization Rate . . . . .                                   | 56        |
| 5.1.2    | Ionization Integral . . . . .                               | 57        |
| 5.2      | Modeling Approaches . . . . .                               | 59        |
| 5.2.1    | Local Electric Field Based Modeling . . . . .               | 60        |
| 5.2.2    | Non-Local Extensions to Local Field Models . . . . .        | 62        |
| 5.2.3    | Lucky Electron Model . . . . .                              | 63        |
| 5.2.4    | Carrier Temperature Based Modeling . . . . .                | 63        |
| 5.2.5    | Distribution Function Based Modeling . . . . .              | 64        |
| 5.2.6    | Energy Driven Paradigm . . . . .                            | 65        |
| 5.3      | Case Study: Simulation of Breakdown and Snap-Back . . . . . | 67        |
| 5.3.1    | Specifications . . . . .                                    | 67        |
| 5.3.2    | The Snap-Back Curve . . . . .                               | 68        |
| 5.3.3    | Structure Variations . . . . .                              | 72        |
| 5.3.4    | Simulation Difficulties . . . . .                           | 73        |
| 5.3.5    | Discussion . . . . .  | 74        |
| <b>6</b> | <b>Hot-Carrier Reliability Modeling</b>                     | <b>75</b> |
| 6.1      | Characteristics of Hot-Carrier Degradation . . . . .        | 75        |
| 6.1.1    | Multiple-Particle Process . . . . .                         | 76        |
| 6.1.2    | Giant Isotope Effect . . . . .                              | 77        |
| 6.2      | Review of Modeling Approaches . . . . .                     | 78        |
| 6.2.1    | Lucky Electron Approach . . . . .                           | 79        |

|          |  |            |
|----------|--|------------|
| 6.2.2    | Hess Model . . . . .   | 79         |
| 6.2.3    | Energy Driven Approach by Rauch and La Rosa . . . . .          | 82         |
| 6.2.4    | Bravaix Model . . . . .  | 83         |
| 6.3      | Distribution Function Based Modeling . . . . .                 | 85         |
| 6.3.1    | Model Implementation . . . . .                                 | 88         |
| 6.3.2    | Model Evaluation . . . . .                                     | 89         |
| 6.3.3    | Model Discussion . . . . .                                     | 91         |
| 6.3.4    | Modifications . . . . .  | 94         |
| 6.4      | Acceleration Integral Estimation in Drift-Diffusion . . . . .  | 95         |
| 6.4.1    | Distribution Function Based Estimation . . . . .               | 96         |
| 6.4.2    | Carrier Temperature Based Evaluation . . . . .                 | 98         |
| 6.4.3    | Results and Discussion . . . . .                               | 101        |
| <b>7</b> | <b>Numerical Considerations</b>                                | <b>103</b> |
| 7.1      | Meshing . . . . .  | 103        |
| 7.2      | Box Discretization . . . . .                                   | 106        |
| 7.2.1    | Derivation . . . . .   | 107        |
| 7.2.2    | Discretization of Edges . . . . .                              | 108        |
| 7.2.3    | Discretization of the Right Hand Side . . . . .                | 109        |
| 7.2.4    | Limitations of the Box Discretization Method . . . . .         | 111        |
| 7.3      | Vectors in Discretized Systems . . . . .                       | 112        |
| 7.3.1    | Discretization Approach by Laux . . . . .                      | 112        |
| 7.3.2    | Box Discretized Vector Quantities . . . . .                    | 114        |
| 7.3.3    | Comparison of the Discretization Schemes . . . . .             | 118        |
| 7.4      | Numerical Challenges Related to High-Voltage Devices . . . . . | 120        |
| 7.5      | Summary . . . . .  | 121        |

|          |   |            |
|----------|---|------------|
| <b>8</b> | <b>Conclusions and Outlook</b>                      | <b>123</b> |
| <b>A</b> | <b>Derivation of the Impact-Ionization Integral</b> | <b>125</b> |
|          | <b>Bibliography</b>                                 | <b>127</b> |
|          | <b>Own Publications</b>                             | <b>149</b> |
|          | <b>Curriculum Vitae</b>                             | <b>151</b> |



# List of Abbreviations and Acronyms

|        |     |   |
|--------|-----|---|
| BCD    | ... | Bipolar, CMOS, and DMOS                                     |
| BJT    | ... | Bipolar junction transistor                                 |
| BTE    | ... | Boltzmann transport equation                                |
| CMOS   | ... | Complementary MOS   |
| DD     | ... | Drift-diffusion   |
| DMOS   | ... | Double-diffused MOS   |
| EPI    | ... | Epitaxial (layer)   |
| ESD    | ... | Electrostatic discharge                                     |
| GTO    | ... | Gate turn off   |
| HBM    | ... | Human body model  |
| HCD    | ... | Hot-carrier degradation                                     |
| HD     | ... | Hydro dynamic   |
| IEEE   | ... | The Institute of Electrical and Electronics Engineering     |
| IGBT   | ... | Insulated gate bipolar transistor                           |
| LDD    | ... | Lightly doped drain extension                               |
| LDMOS  | ... | Lateral double-diffused MOSFET                              |
| MC     | ... | Monte Carlo   |
| MOS    | ... | Metal-oxide-semiconductor, often used as synonym for MOSFET |
| MOSFET | ... | MOS field-effect transistor                                 |
| MP     | ... | Multiple-particle (in context of HCD)                       |
| MTTF   | ... | Mean time to failure  |
| NBTI   | ... | Negative bias temperature instability                       |
| RESURF | ... | Reduced surface field                                       |
| RF     | ... | Radio frequency   |
| SOI    | ... | Silicon on insulator  |
| SILC   | ... | Stress-induced leakage current                              |
| SIMS   | ... | Secondary ion mass spectrometry                             |
| SP     | ... | Single-particle (in context of HCD)                         |
| SRH    | ... | Shockley-Read-Hall  |
| TCAD   | ... | Technology computer-aided design                            |
| TDDB   | ... | Time dependent dielectric breakdown                         |
| TLP    | ... | Transmission line pulse                                     |





# Chapter 1

## Introduction

In the modern world, electronic components based on semiconductor devices have become a very important part of an uncountable number of applications. The performance gain and the miniaturization of semiconductor devices continuously open up new possibilities. Of comparable importance for the entire development is the decreasing costs per device. The main factor for cost reduction is the dramatic increase of the device density on a silicon waver [1, 2]. Therefore, a considerable amount of industrial and academical research is being performed to enable the continued shrinking of the devices.

Another important method for the cost reduction of electronic components is to combine different functional groups in a single integrated semiconductor die. This technique is applied, for example, in smart power devices which incorporate power and high-voltage devices with additional functions, such as power control, sensing and protection, and interfacing. To accomplish this, different technologies have to be combined. A majority of the smart power applications integrates low-voltage CMOS logic with high-voltage and/or power device technologies [3–6].

When talking about high-voltage devices, one has to clarify more specifically the voltage range, because the terminus “high-voltage” strongly depends on the application field. In power engineering and in the area of transmission and distribution, for example, voltages above 1,000 V are considered as high-voltages [7]. In long-distance electric power transmission lines this lower limit is as high as 100 kV. At the other end of the voltage range, especially in smart power devices in which CMOS logic is integrated, one considers voltages starting from 5 V as high voltages [5]. In the automotive industry, for example, the high-voltage part of smart power devices is dominated by the 14 V vehicle power supply. Contributing to the disturbances on the supply and signal lines encountered in automotive environments, these devices are often rated in the range of 50–100 V [8–10]. In this thesis the term high-voltage refers to the range from 5 to 60 V. In **Chapter 2** various device architectures, which are used in this voltage range, are presented. Due to the wide usage in industry, the focus is put on the double-diffused metal-oxide-semiconductor field-effect transistor (DMOSFET) and its variants in lateral and vertical orientation. Also several device design approaches such as field shaping and isolation techniques are shortly described.

## CHAPTER 1. INTRODUCTION

Modern semiconductor devices have to fulfill many requirements in terms of performance, reliability, and costs. Certain reliability goals must be met, which depend on the field of application and other considerations, for example, safety, security, and liability issues. An overview on reliability in general followed by some specific reliability concerns found in semiconductor devices is given in **Chapter 3**. However, the down-scaling and the increasing complexity of devices and integrated circuits make it very challenging to reach all specified design goals. Therefore, more and more often device simulation tools are employed in development, research, and optimization. These tools, commonly referred to as technology computer aided design (TCAD) tools, aim to reproduce the physical mechanisms and hope to predict the device behavior [11–14]. The most important formulas and physical models which are needed for device simulation within the drift-diffusion model are described in **Chapter 4**. This chapter also discusses the possibilities and limitations of this model to describe hot-carrier phenomena, which are of crucial importance for high-voltage device reliability. Strictly speaking, a physics-based modeling approach of these effects requires an exact solution of the Boltzmann transport equation. In this context the Monte Carlo method [15,16] proved to be one of the most popular approaches. In fact, this method gives accurate results and allows to easily incorporate various physical models. Unfortunately, the computational cost required for this method are very high, which make them not too appealing for industrial use. On the other hand, the drift-diffusion model is numerically stable and can be solved efficiently [11,14]. The modeling approaches presented in this thesis aim to deliver good results in reasonable simulation times and, therefore, are based on the drift-diffusion model.

The two hot-carrier related reliability effects discussed in this thesis are the impact-ionization generation and hot-carrier degradation. **Chapter 5** is devoted to the physical phenomenon of impact-ionization and presents different modeling strategies and aspects. The importance of impact-ionization for the reliability of smart power devices is demonstrated in a case study. In **Chapter 6** hot-carrier degradation in MOS devices is discussed. After a review of currently used modeling techniques, a distribution function based model is presented, which is currently under development [17,18]. This model is based on results obtained within the Monte Carlo simulations and is therefore computationally very demanding. To overcome this disadvantage, possible approximations using the drift-diffusion scheme are presented and discussed.

The simulation of semiconductor devices in TCAD tools requires the solution of a system of non-linear differential equations. To solve this system, a spatial discretization scheme has to be used to transform the equations into a system of difference equations. In the context of device simulation, the box integration method proved to be very reliable. Iterative solution techniques are required to obtain a solution for this numerical problem. Simulations in high-voltage devices turned out to be numerically challenging, especially in combination with impact-ionization. Hence, investigations on various vector discretization schemes were done, which are presented in **Chapter 7**.

## Chapter 2

# High-Voltage and Power Devices

High-voltage semiconductor devices exist for many different applications. The devices can be fabricated as single packaged discrete device or embedded in smart power structures. This chapter gives a short introduction on a selection of device types and presents basic device design techniques.

### 2.1 High-Voltage Device Types

The huge voltage range to be covered by semiconductor devices already suggests that it is not possible to satisfy all requirements with a single device type. In fact, a wide range of different devices is used. Today, for switching applications it is commonplace to use the two major device types MOSFET (Metal Oxide Semiconductor FET) and IGBT (Insulated-Gate Bipolar Transistor) [19]. The latter one is especially used for voltages above 300 V. Currently IGBT modules are available for blocking voltages of up to 6.5 kV [20, 21] and with a maximum total current of up to a few thousand ampere [22]. For the sake of completeness, both devices will be briefly described, despite this work being focused on MOSFET devices in automotive applications where IGBT devices are rarely used.

#### 2.1.1 Metal Oxide Semiconductor Field-Effect Transistor

The principle of field effect transistors (FET) is to control a current in a solid semiconductor by an electric field. This concept was first proposed by Lilienfeld [23] in two patents [24, 25] granted in 1930 and 1933. The functionality was confirmed in 1948, but due to interface and surface problems and due to the invention and success of the bipolar junction transistor (BJT) the field effect transistor was not further pursued. The introduction of thermally-grown silicon dioxides in 1959 [26] paved the way for MOSFET devices. Compared to the BJT, the advantages of MOS devices are the simpler processing and the better scalability along with

## CHAPTER 2. HIGH-VOLTAGE AND POWER DEVICES

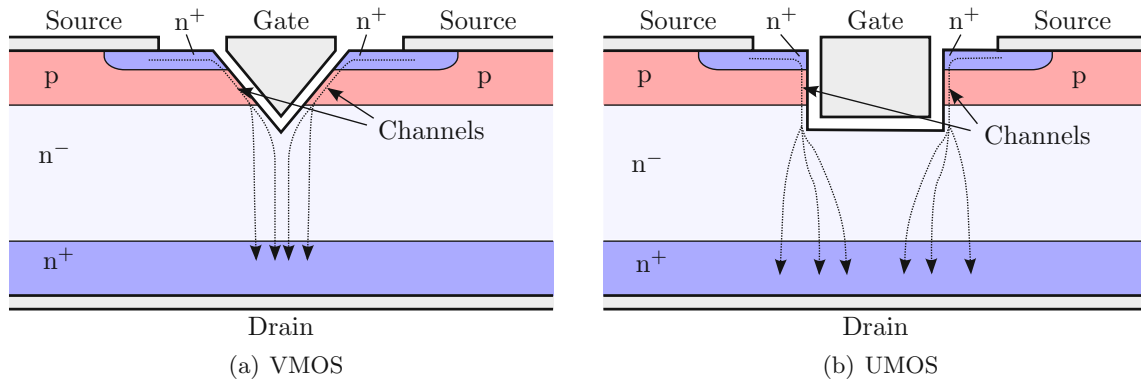


**Figure 2.1:** MOS devices with V-shaped (a) and U-shaped (b) gate structures used for power MOSFET devices.

reduced power consumption [27]. However, the real breakthrough came with the increasing demands on integrated circuits and the CMOS (Complementary MOS) fabrication methods [27].

In the power and high-voltage domain the BJT was widely used until the 1980's [28]. The major drawback of the BJT in this regime is the low current gain which required complex and expensive control circuits to generate the base current. These circuits required additional power and the increased heat dissipation was a big issue. Also the introduction of mobile devices increased the demand for higher effectiveness. The attempt of increasing the current gain in BJTs leads to lower breakdown voltages and is therefore also no universal solution. On the other hand, field effect transistors are voltage controlled and no static control current is required. This helped to overcome the control circuit problems. An additional advantage of MOSFET devices is that there is no second breakdown. Higher temperatures lead to a decrease of the carrier mobility, and consequently, the drain current is reduced. This results in a reduced power loss and heat generation. Therefore, in contrast to BJTs, MOSFET devices can be simply connected in parallel [29], which is the basis for the design of power MOSFET structures.

These power MOSFET devices consist of numerous single MOSFET structures connected in parallel on chip level. At first, the structures were built with a V-shaped gate etched into the silicon giving the device the name VMOS (see Fig. 2.1(a)). In this fabrication method it was problematic to produce stable threshold voltages. Another problem were the high electric fields near the bottom peak of the oxide which degraded the breakdown voltage. An evolution of the VMOS is the UMOS (see Fig. 2.1(b)) where the gate is etched in a U-shape, resulting in a channel current flow vertical to the chip surface. This structure avoided the peak electric field that appeared at the bottom of the V-shaped structure. The UMOS is fabricated using trench etching which was originally introduced for the fabrication of highly integrated dynamic memory cells.

A different fabrication method for the channel structure is used in the double-diffused MOSFET or simply DMOS (see Fig. 2.2). Here, the channel area is built by lateral diffusion of the n- and p-dopants, both masked by the gate. The channel length is determined by the diffusivity

## 2.1. HIGH-VOLTAGE DEVICE TYPES

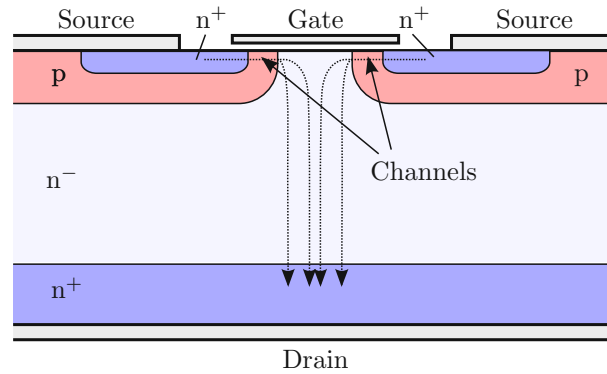


**Figure 2.2:** DMOS device with its lateral channel which is fabricated by lateral diffusion.

of the dopants and by the diffusion process temperature and time. Lithographic limitations do not influence the minimum channel length, since it can be adjusted by changing temperature and time of the diffusion process. Since the gate can be used as mask for the channel diffusion this process is self aligning and a high precision can be obtained.

### 2.1.2 Insulated Gate Bipolar Transistor

The insulated gate bipolar transistor (IGBT) [30] combines the high input impedance of a MOS transistor and the high current densities which are possible due to the bipolar current transport. A very low sheet resistance can be achieved which leads to a low voltage drop and therefore reduces the thermal power generated in the device. In Fig. 2.3 two different forms of IGBT structures are shown. The first structures proposed were fabricated using the double-diffusion techniques as it is used for DMOSFET. The other structure introduces the trench gate of the UMOS to the IGBT and helps to further decrease the on-state voltage drop. The main advantage of the IGBT compared to the thyristor and the gate turn off transistor (GTO) is the capacitive gate control. For low frequencies, this results in a nearly power-less voltage control. Therefore, complex driving circuits which are especially required to turn off a GTO can be avoided.

Comparing the IGBT and the MOSFET in high-voltage applications shows that lower specific sheet resistances in the on-state can be achieved using the IGBT. However, the switching behavior of the bipolar device is much slower compared to MOSFET devices. This is caused by the high density of minority carriers in the drift region coming from the collector while the transistor is switched on. The time needed to switch of the IGBT is therefore mainly determined by the recombination process and therefore the carrier lifetime. The main application field of IGBT devices is for a voltage range above 300 V [19]. Since this work focuses on smart power devices in automotive environments the operating voltages are mostly far below 100 V. IGBT structures therefore have only little importance for this work.

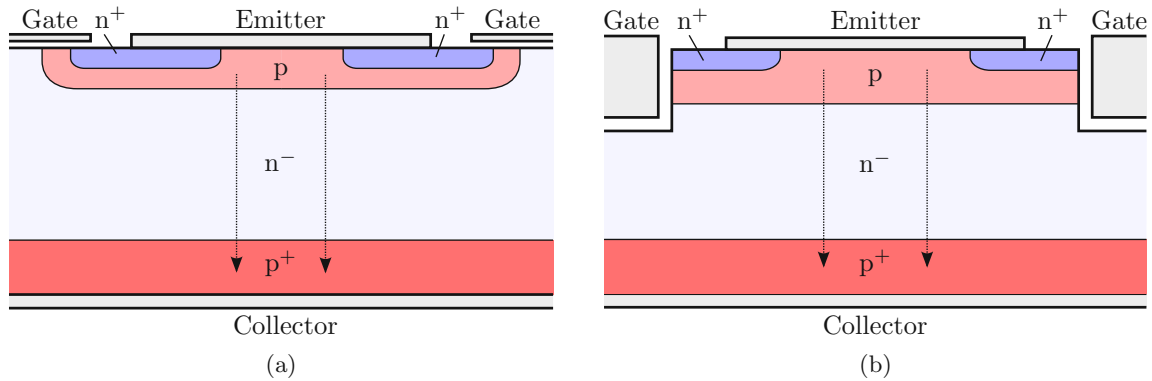


**Figure 2.3:** IGBT device based on the DMOS-technology (a) and on U-shaped trench gates (b). Both structures can be used for high current applications.

## 2.2 Device Design Techniques

Various design techniques are available to optimize the device behavior and to integrate high-voltage devices in integrated circuits. In the following considerations the two important properties blocking voltage and on-current are of special interest. Closely related is the on-resistance which also determines the power losses in the device. To achieve a cost efficient design the required chip surface is one of the most important constraints which has to be minimized. Other important goals not considered here are, for example, the turn on and off delays which lead to the maximum switching frequency.

### 2.2.1 Vertical and Lateral Devices

In the previous section, the basics of the two device types MOSFET and IGBT for high-voltage and high power applications were explained. In the corresponding figures, the devices were shown in vertical orientation which is typically used for discrete power devices. Here, the main current flow is oriented vertically, meaning perpendicular to the semiconductor surface. The drain/collector contacts are placed at the bottom of the devices. The elementary transistor cells can be placed side by side on the chip and can be simply connected in parallel. This is a common method to achieve a high current component and is especially used for discrete high current power devices.

Especially in smart power devices, the processing and packaging often requires that all contacts must be situated on the top side of the die. There are techniques that allow the use of vertical structures in planar environments. The vertical current is commonly collected by a highly doped buried layer. These collected carriers are transported to the top surface using sinker structures. This concept typically looks similar to the structure shown in Fig. 2.4. To keep the resistivity low, the buried layer and sinker structures have to be highly doped. These types of devices are also called horizontal devices [6].

## 2.2. DEVICE DESIGN TECHNIQUES

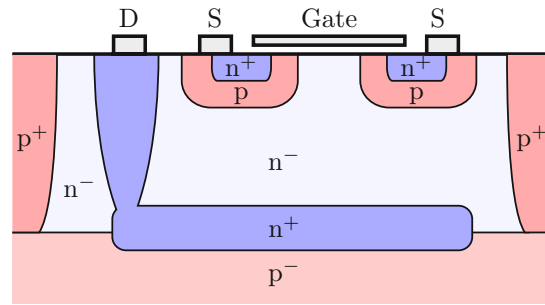


**Figure 2.4:** Vertical DMOS structure with its drain contact on top of the device. The transport of the carriers to the surface is accomplished by a highly n-doped buried layer and sinker structure.

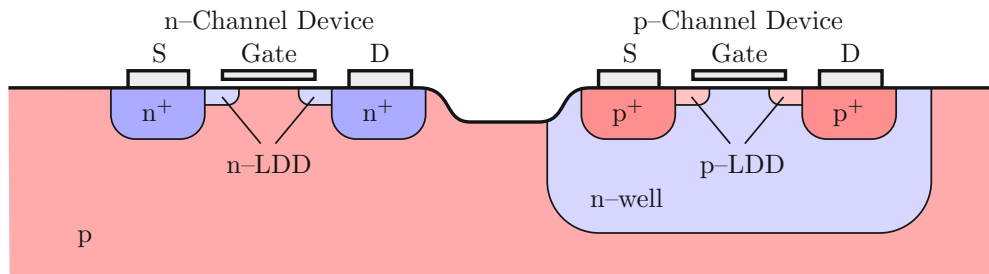


**Figure 2.5:** Typical CMOS structure with lightly doped drain and source extensions (LDD) on a p-type substrate or on a p-type epitaxial grown layer.

In contrast to the vertical devices, the dominant current flow of lateral devices is in horizontal direction, that is, in parallel to the semiconductor surface [31]. For low-voltage and low-power transistors like in CMOS environments, this is the typical design method for MOSFET devices (see Fig. 2.5). For devices having higher blocking voltages, long drift regions are required, which are necessary to keep the electric field moderate in blocking state. The typically used MOS transistor in lateral high-voltage designs is the LDMOS (Lateral Double-diffused MOSFET) [32]. The basic scheme of an LDMOS transistors is shown in Fig. 2.6. However, in the shown version of the device, high voltages in the junction area between channel and drift zone will lead to low breakdown voltages (see Fig. 2.7(b)). The field in the junction can be reduced by incorporating a very low doping in the drift region [32]. Since this increases the resistance other solutions are required. A better method to decrease the peak of the electric field is the RESURF technique which is discussed in the next section [33].

Comparing the vertical and the lateral design in terms of integrability into the CMOS processes, as it is required in smart power devices, clearly favors the LDMOS [34]. Here, the voltage rating for each individual transistor is achieved by changing implantation conditions and by adjusting the device layout. It is also simpler to implement field shaping techniques in lateral than in vertical design. Hence, lateral devices are traditionally better optimized for high-voltage applications, while vertical devices are mainly used for high-current applications [35]. Opti-



## CHAPTER 2. HIGH-VOLTAGE AND POWER DEVICES

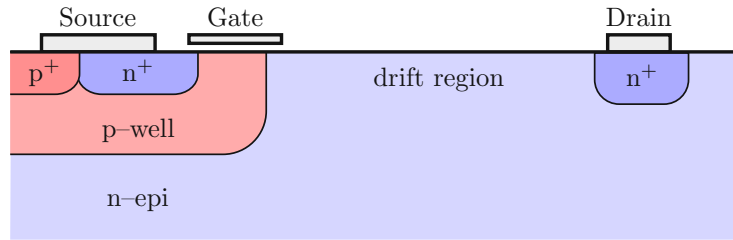


**Figure 2.6:** Basic lateral high voltage double diffused MOS transistor (LDMOS). The electric field is consumed by the relatively low doped drift region.

mizations also make the chip surface of lateral LDMOS devices smaller compared to vertical implementations [36].

On the other hand, the fabrication of buried layers and sinkers which redirect the current to the silicon surface considerably increase the complexity of the standard CMOS process for vertical devices [34]. Additionally, drain contacts are often tied together in vertical design. This complicates the monolithic integration of n- and p-channel devices, because independent buried layers are required. However, an important advantage of the vertical DMOS is the increased electrical safe operating area, which is of special importance for electrostatic discharge (ESD) [34, 37].

### 2.2.2 Reduced Surface Field Technique

To resist high blocking voltages, the simplest approach is to make long and lowly doped drift regions. Both parameters, length and low doping, lead to large on-resistance ( $R_{DS,on}$ ) and therefore to higher drop voltages, and higher power loss. Another aspect of long, lateral drift regions is the additionally required chip area which increases costs. A trade off between blocking voltage and on-resistance has to be found. For a given breakdown voltage the optimal drift length and doping can be determined [38, 39].

The peak electric field is typically concentrated near the pn-junction close to the surface which is illustrated by a diode in Fig. 2.7(a). With the RESURF (REduced SURface Field) concept introduced by Appels and Vaes this maximum field can be reduced [33, 40]. This is accomplished by changing the design such that the space charge region in the blocking state extends over the whole drift zone. The resulting charge distribution leads to a continuous potential drop along the whole drift zone and not only across the junctions. Therefore the same terminal voltages cause lower electric fields in the device. This effect is illustrated in Fig. 2.7(b) by a diode structure, too. RESURF is used in modern LDMOS devices. In n-channel LDMOS devices commonly a p-doped layer is introduced below the drift region and the thickness of the drift region is chosen that in blocking mode the space charge region extends up to the silicon surface, just like in the diode structure. Fig. 2.8 shows an implementation using a p-type epitaxial layer. For a given maximum blocking voltage the length of the drift region can therefore be reduced. This minimizes both critical parameters, the on-resistance and the chip surface.



## 2.2. DEVICE DESIGN TECHNIQUES

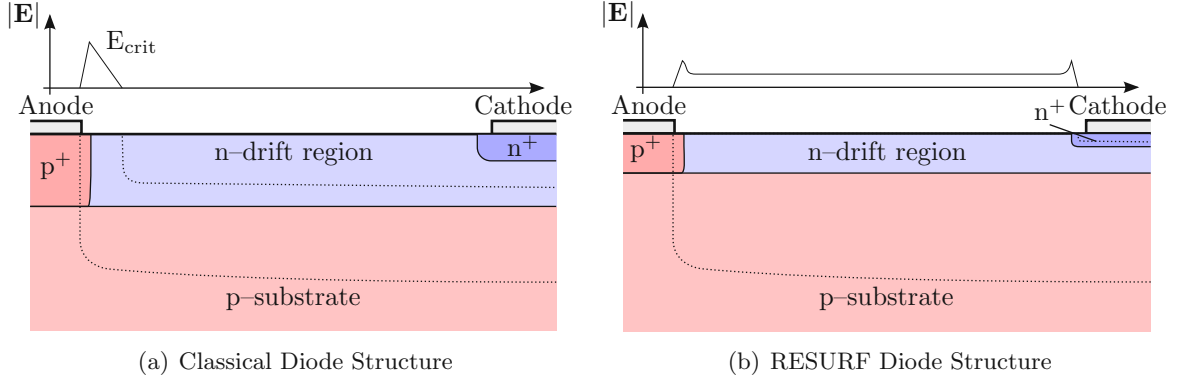


**Figure 2.7:** The blocking voltage drop in the classical diode structure (a) is only in the space charge region around the pn-junction as indicated by the dotted line. The electric field along the surface of the device is schematically shown. The thinner drift-zone which is used in the RESURF structure (b) causes the space charge region to extend up to the silicon surface in the blocking state. The voltage drop is therefore distributed along the drift zone which leads to a reduced peak field.

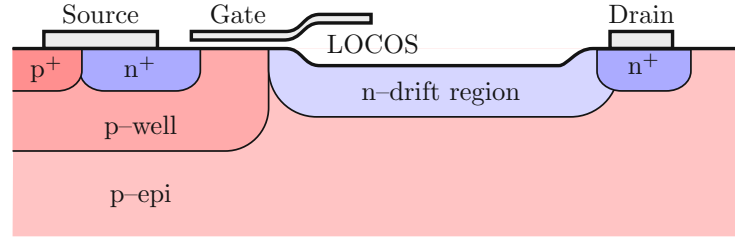


**Figure 2.8:** High-voltage LDMOS transistor using the RESURF (reduced surface field) technique and a field plate deposited on top of the LOCOS (LOCAl Oxidation of Silicon). Both methods reduce the peak electric field near the surface.

Since the peak fields are avoided by using the RESURF technique, the doping of the drift region can be increased and the drift zone can be shortened. Both variations reduce the on-resistance of the MOSFET. Therefore the drop voltage and the power dissipation are considerably lower. The RESURF concept is nowadays widely used in high-voltage LDMOSFET structures [41–43].

An extension of the RESURF concept is the Super Junction structure which basically consists of layers or stripes of alternating n- and p-doped areas (see Fig. 2.9) [44]. With reverse bias, the space charge region extends throughout the whole drift area and removes all free carriers. Electric field peaks are avoided which allows high blocking voltages. Also a high doping can be chosen for the stripes, which results in a very low on-resistance. Production of such Super Junction structures is quite complex and was realized, for example, in the vertical COOLMOS<sup>TM</sup> [45] structure by *Infineon Technologies*.

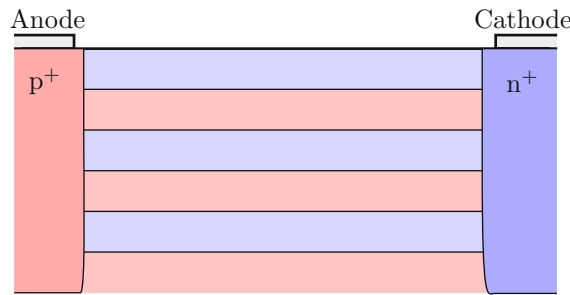


**Figure 2.9:** The basic structure of a Super Junction diode. In the blocking state the space charge region extends over the whole stacked p- and n-type layers. This allows high doping levels which give a low on-resistance with high blocking capability.

### 2.3 Smart Power Devices

In smart power devices, discrete power semiconductors are merged with additional functional units to increase the usability of the device. The idea is to fabricate one component that integrates control and diagnostic circuits with power devices. In smart power technologies, this is implemented on a single semiconductor die which is typically accomplished using BCD (Bipolar, CMOS, DMOS), also called BiC-DMOS, technology [46–48]. With this integration the complexity of external circuits can be reduced, resulting in cost benefits especially for standard high volume components.

In many application fields the advances of smart power devices help to make products cheaper, smaller, and more reliable. Simple transistors are exchanged by smart switching devices or even complete amplifiers. The integrated control and analysis functionality may also allow a direct connection to microprocessors. The higher level of integration reduces the number of components required to design circuits which reduces design and fabrication costs and increases the reliability. Integrated features like load, supply voltage, and temperature monitoring are easily accessible to product designers. It is also possible to fabricate complete microcomputer environments including memory and serial interfaces together with high-voltage and power devices. A wide variety of system on a chip (SoC) solutions can be realized [5].

There are two major approaches for designing smart power devices. One approach is to build the low-voltage part on top of a power device technology [49]. This approach is especially used for high current applications based on vertical device structures (see Fig. 2.10). The other approach is based on a CMOS VLSI (Very Large Scale Integration) process. Here, the CMOS process is extended to allow for the integration of lateral high-voltage and current devices (see Fig. 2.11) [5,51]. Due to high investments made into the field of VLSI by the computer industry, this approach benefits from highly advanced fabrication and design methods. Circuits for smart power devices usually do not require the most advanced VLSI technology node, so the designs can be based on mature, well established process technologies.

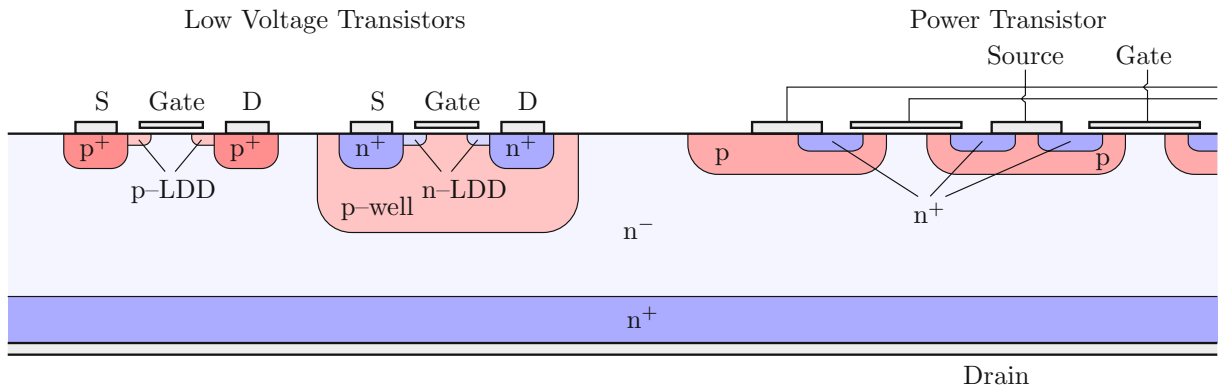


**Figure 2.10:** Smart power device based on a vertical DMOS device fabricated on an n-epi on  $n^+$  substrate (simplified from [50]).

### 2.3.1 Isolation

Isolation between different devices in integrated circuits plays a key role in integrated device design. A special challenge in smart power devices is the protection of the low-voltage circuits from high voltages. There are basically three different isolation methods in use [6]:

- Self isolation
- Junction isolation
- Dielectric isolation

The self isolation technique can be applied when single devices inherently form reverse-biased junctions. CMOS structures (refer Fig. 2.5) are a good example which allow to apply this self isolation technique. Processing of this isolation type is very simple since no special steps have to be introduced. A disadvantage of this technique is the high number of parasitic devices generated due to the missing isolation. Also the flexibility of the circuit is reduced since it has to be assured that the pn-junctions between the devices need to be permanently reverse-biased.

In the junction isolation technique, additional doped areas are introduced between devices to ensure proper isolation. For p-type substrates with n-type epitaxial layers, for example, diffused p-doped regions from the surface down to the substrate are used [6]. An example is shown in Fig. 2.11. This technique is still cost efficient and is often used since it gives higher flexibility than the self isolation technique.

From the isolation point of view, the best option is the dielectric isolation. Here, a silicon dioxide layer separates the devices leading to much lower ohmic and capacitive coupling compared to junction isolation techniques. There are no parasitic devices between the transistors, since there are no additional pn-junctions. Fig. 2.12 shows a typical fabrication method that uses SOI (Silicon On Insulator). Comparing Fig. 2.11 and 2.12 shows that the isolation structures in SOI require less space and a more compact implementation is possible [49]. Another benefit

## CHAPTER 2. HIGH-VOLTAGE AND POWER DEVICES

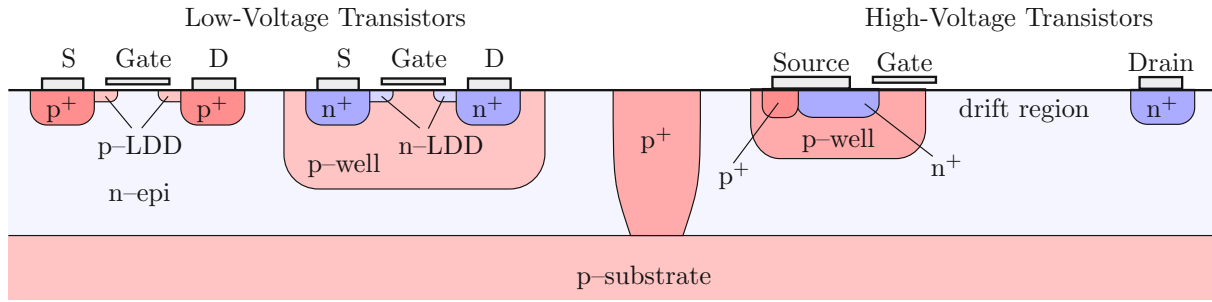


**Figure 2.11:** Horizontal smart power device based on CMOS technology using junction isolation (simplified version from [49]).

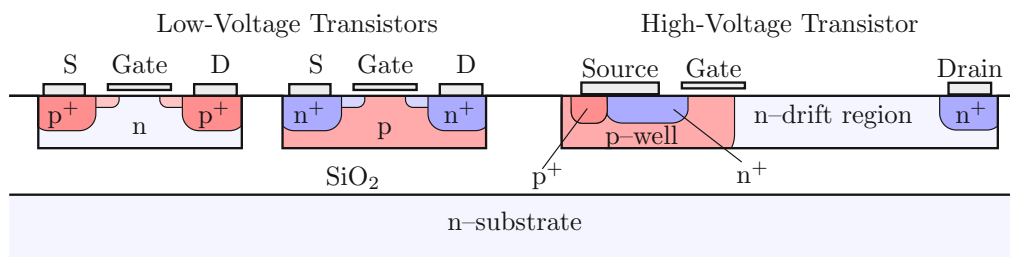


**Figure 2.12:** Horizontal smart power device manufactured using SOI technology. The single devices are separated using dielectric isolation which allows a more compact design (simplified version from [49]).

of the dielectric isolation is that devices next to each other can be operated using arbitrary potentials and it is not required to take care of blocking voltages for the isolating pn-junctions. This makes, for example, the implementation of bridge circuits for stepper motors much easier. However, there are two major disadvantages of the SOI technique. First, the costs of the SOI wafers are still higher compared to standard wafers [52]. However, the reduction of the required surface often compensates these additional costs [53]. The second problem is the low thermal conductivity of the isolating oxide structures [54, 55]. In bulk technology the heat generated in the devices is transported into the bulk of the device very efficiently which is not possible in SOI devices.

### 2.3.2 Industrial Examples

Monolithic integration of devices with different power and voltage levels allows to fabricate products for many different applications. A random exemplary selection of devices from industry is given in the following to show some products that are available on the market:

As a first example, the PROFET<sup>TM</sup><sup>1</sup> high side switch series is probably the most typical smart power device in this selection. Here, a MOSFET transistor is enhanced by diagnostic functionality including overload protection, over- and under-voltage shutdown and auto-restart, current

<sup>1</sup>Automotive device series from *Infineon Technologies*

## 2.3. SMART POWER DEVICES

limitation, short circuit protection, thermal shutdown, and many more features. The main application area for this device series is the automotive industry. The breakdown voltage range lies between 28 and 60 V. Device failure or load irregularities can therefore be detected. Hence, the on-board electronic system gets feedback on failure events, which helps to diagnose or solve the fault.

Two other examples, which are usually not explicitly considered as smart power devices, but nevertheless make extensive use of integration of different technologies. Both are highly integrated applications for single chip solutions, one for mobile phones and the other for mobile audio players. The example of the mobile phone system is from *NXP Semiconductors*. It includes all required GSM/GPRS applications which are “[.] the analog and digital basebands, RF transceiver, power management, battery interface and charging electric circuit, and audio in a single monolithic CMOS IC[.]”<sup>2</sup>. The other example is for mobile entertainment equipments, like digital music players from *ams*. It is a system on a chip solution “[.]for high performance and ultra low power audio products with minimum count of external components[.]”<sup>3</sup>. This component integrates all functionalities required to build a mobile player, including main processor, audio amplifier, display controller, internal memory, external memory interface, battery controller, high-speed serial interface, and many more features.

These examples highlight the high usability that can be achieved by integrating different technologies on the same semiconductor die. The overall system also benefits from the increased reliability using highly integrated chips. One aspect for this is the reduced number of external connections between the single components which makes the printed circuit board smaller and its fabrication more simple. The electric circuit for the specific functionality is shifted into the semiconductor chip which allows an optimized, well tuned design. Additionally electrostatic discharge (ESD) and other hazard impacts can only occur at external terminals, the chip internal connections are not affected.

---

<sup>2</sup>Product description of the PNX4901 from *NXP Semiconductors*.

<sup>3</sup>Product description of the AS3531 from *ams*.



## Chapter 3

# Reliability in Semiconductor Devices

This chapter gives an introduction to semiconductor device reliability, starting with general aspects. The second half of this chapter introduces some of the most important failure and degradation mechanisms relevant in semiconductor devices.

### 3.1 Reliability in General

Electronic products introduced to the market have to fulfill specific quality criteria. There are definitely major differences in the customer's expectations depending on the product type and application field. It appears commonly acceptable if a cheap give-away gadget fails after one year. On the other hand, malfunctioning of an airbag system in a ten year old car is a serious, safety relevant failure. This shows that the customers expectations on the reliability depend on the product. Especially high expectations are associated with safety and security components.

The IEEE defines reliability as the ability of an item to perform a required function under stated conditions for a stated period of time [7]. In this context, an item can be any system or product, e.g. a mobile phone, an integrated power amplifier, or an airbag system. For the discussion on reliability a specification that defines good and failed devices is required. Specifications have to include tolerances, therefore, a changing device parameter does not automatically imply a failure. They also have to include the allowed operating conditions, including circuitry and environmental impacts. Note that the IEEE definition also includes the factor time, highlighting its importance when talking about reliable or unreliable components. However, not only the operating time but also the storage time for devices on stock has to be considered. This is on one hand important for components which are not permanently used and wearout therefore cannot be monitored, and, on the other hand, for articles that are kept on stock for long periods. This is especially the case for spare parts.

## CHAPTER 3. RELIABILITY IN SEMICONDUCTOR DEVICES

### 3.1.1 History of Reliability

Beginning from the early stages of the industrialization of electricity, reliability was and still is a major concern. It is also often a show-stopper for the introduction of new technologies. Looking back in history, it required nearly 70 years until the reliability of the incandescent light bulb was high enough to make electrical lighting commercially interesting. Engineers had put much effort into finding materials used for the filament as well as for the gas surrounding it. Further technological advances finally offered high-performance vacuum pumps. This made the fabrication of the evacuated bulbs possible, which finally became even more successful. This example shows that reliability is important for new products and that the two key issues for the development of reliable products are materials and technology.

One of the first systematic approaches for investigating system reliability and reliability prediction was initiated by military institutions. The topic became important due to the high failure rates of electronic equipment during World War II. The common approach to keep systems in operation was to stock up spare parts. However, this logistically challenging and very cost intensive. Hence, the demand emerged to increase and to quantitatively specify the reliability. In 1952 the U.S. Defense Department founded together with electronics industry the Advisory Group on Reliability of Electronic Equipment (AGREE) whose charter was to identify actions that could be taken to provide more reliable electronic equipment [56]. Soon after, the reliability community split into supporters of two general approaches [57]. On one side there is a community supporting the physics-of-failure models which could be described as bottom-up approaches [58]. On the other side, there are the proponents of empirical models which are solely based on *historical* data. In this context, historical data means collected information from comparable systems previously designed, manufactured, and already used. Only for those system is historical data like wearout and lifetime available. This empirical approach originates from the desire to determine the prospective reliability of systems from the beginning of the design phase long before specific parts have been selected. This strategy can be considered as top-down approach. One of the oldest and for a long time widely accepted document giving guidelines on reliability estimations using empirical based models is the MIL-HDBK-217 [59] entitled “Reliability Prediction of Electronic Equipment”. The first release was issued in 1962 by the US Department of Defense. Even if this document was widely used, many authors criticized the proposed failure-rate prediction. The obvious problem of a design guideline that is based on historical data is the delay between the introduction of new materials and technologies and the availability of collected field data. This prevented the use of benefits of new developments for a long time [60]. Furthermore, engineers emphasized the important missing links between stress history, environmental impacts, and actual cause of failure.

In contrast to empirical methods, physics-of-failure approaches have the goal to identify the root failure mechanism based on physical principles [61]. This approach helps to localize the problem and to improve components efficiently. Criticism of this approach concerns the increased complexity using physics-based modeling and the incapability of this low-level approach to capture a complex system as a whole. For a long time proponents of empirical and physics-of-failure approaches were arguing with each other, which method is better and should be used. Morris *et al.* [62] concluded that both methods have their according application field and should be



used in conjunction. However, the reliability investigations in this work only consider physical impacts on the device and therefore only contribute to the physics-of-failure approach.

#### 3.1.2 Keywords and Definitions

Systems are often required to be available and working for a certain amount of time during their lifetime. Manufacturers or service operators have to guarantee their customers that a given device or infrastructure operates at least for a specific time per month/year. This implies that the system can be repaired and maintainability is given. Failed systems can therefore be restored to working condition by repairing or changing parts. However, for a single semiconductor device, maintainability is not given, since failures cannot be repaired. Hence, in reliability engineering the term survivability is used for systems that cannot be repaired. This is also used when a repair is not an option. This is true for cheap products, e.g. inkjet printing cartridges, or for products where once set in operation, repair is impossible, for example, due to inaccessibility.

Considering a specific physical failure, one has to distinguish between failure mode and failure mechanism or failure cause. A symptom observed in a failed or degraded device is called failure mode. This can be, for example, an increased current or an open circuit. A failure mode can be caused by different physical failures, so-called failure mechanisms. The same failure mechanism does not necessarily lead to the same failure mode. An oxide breakdown, for example, can lead to a short or to an open circuit. The open circuit can also be caused by some other failure mechanism, for example by electromigration.

#### 3.1.3 The Bathtub Curve

The statistical temporal distribution of failures can be visualized using the hazard curve. This curve shows the device's failure rate, also known as hazard rate, over the operating time. The widely accepted typical shape of the hazard curve is the bathtub curve shown in Fig. 3.1. This curve is originally derived from the life expectations of humans. In this theory, the lifetime of a system is split into three major parts. In the first part a high failure rate can be observed, called the infant mortality. This is reasoned to be due to major weaknesses in materials, production defects, faulty design, omitted inspections, and mishandling [63]. These failures are also considered as extrinsic failures [64] and it is suggested that all systems with gross defects fail during the early operation time. This leads to the next period, the system's useful time. Here, a low failure rate can be observed. This part is often modeled using a constant failure rate. Therefore, the probability of a system to fail is randomly distributed. Even though this assumption is heavily debated, many reliability calculations are based on such a constant rate. At the end of the lifetime, the wearout period follows due to fatigue of materials. An intelligent product design makes sure that wearout occurs after some time greater than the planned lifetime of the product [64].

One of the strong opponents of the bathtub curve is Wong [65–67] who suggested that the hazard rate follows a roller-coaster curve as shown in Fig. 3.2. He initiated the idea, that the constant

## CHAPTER 3. RELIABILITY IN SEMICONDUCTOR DEVICES

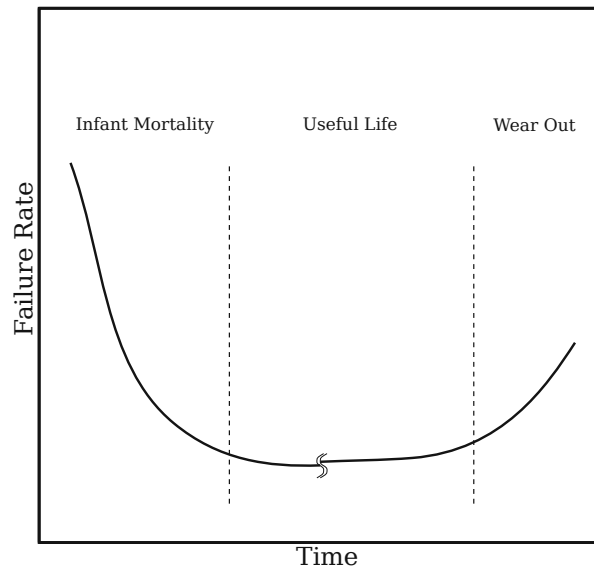


**Figure 3.1:** Bathtub hazard function showing a high failure rate during infancy, a low, nearly constant rate during the useful life, and a raising failure rate due to wearout at the end of the lifetime.

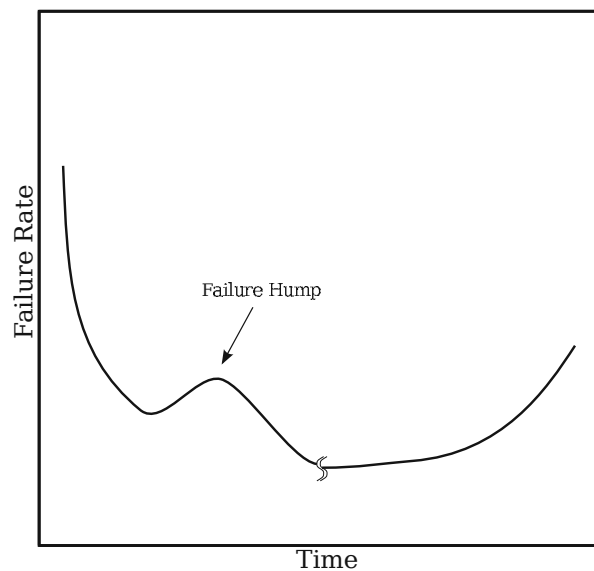


**Figure 3.2:** The roller-coaster hazard curve proposed by Wong [66] with a failure hump following the infant mortality phase.

failure rate throughout the useful life is not caused by randomly distributed errors. Instead, weaknesses in sub-items of the whole electronic system cause one or more humps. He assumes, that these are extrinsic failures already present but not found after fabrication. Wong stated that the constant failure rate has been defended for so long because it is based on tainted field data. On the other hand, the failure rate in the useful lifetime can be attributed partly to environmental impacts which are not intrinsic to the device. The occurrence of those external events, like an electrostatic discharge event, are furthermore random and, therefore, lead to a nearly flat phase in the hazard curve. If these external events are included in the total reliability of the electronic system, the bathtub curve becomes valid again.

#### 3.1.4 Reliability Calculations and Statistics

Traditional reliability calculations are based on statistical data collected using failure records. For  $n$  statistically identical and independent items the time between putting the device into service and occurrence of a failure can be collected. This can be used to determine the empirical expectation value for the mean failure-free time  $\tau$  as

$$\hat{E}[\tau] = \frac{t_1 + t_2 + \dots + t_n}{n}. \quad (3.1)$$

For  $n \rightarrow \infty$ ,  $\hat{E}[\tau]$  converges to the expectation value  $E[\tau]$  which is the mean time-to-failure (MTTF). The time dependent failure density  $f(t)$  is described using probability density functions. The number of devices that fail until a certain time is described using the cumulative distribution function  $F(t)$ ,

$$F(t) = \int_0^t f(t') dt'. \quad (3.2)$$

The relative number of items that have not failed until  $t$  can be expressed using the survival or reliability function

$$R(t) = 1 - F(t). \quad (3.3)$$

Often the hazard rate  $\lambda$  is used to describe failure behavior of items. It defines at a given time the ratio between items that have failed and items that are still operating. It is formulated as

$$\lambda(t) = -\frac{dR(t)}{dt} \frac{1}{R(t)} = \frac{f(t)}{1 - F(t)}. \quad (3.4)$$

With a given failure rate, the reliability function can be derived from (3.4)

$$R(t) = \exp \left( - \int_0^t \lambda(t') dt' \right), \quad (3.5)$$

and the MTTF can be expressed as

$$\text{MTTF} = \int_0^\infty t f(t) dt. \quad (3.6)$$

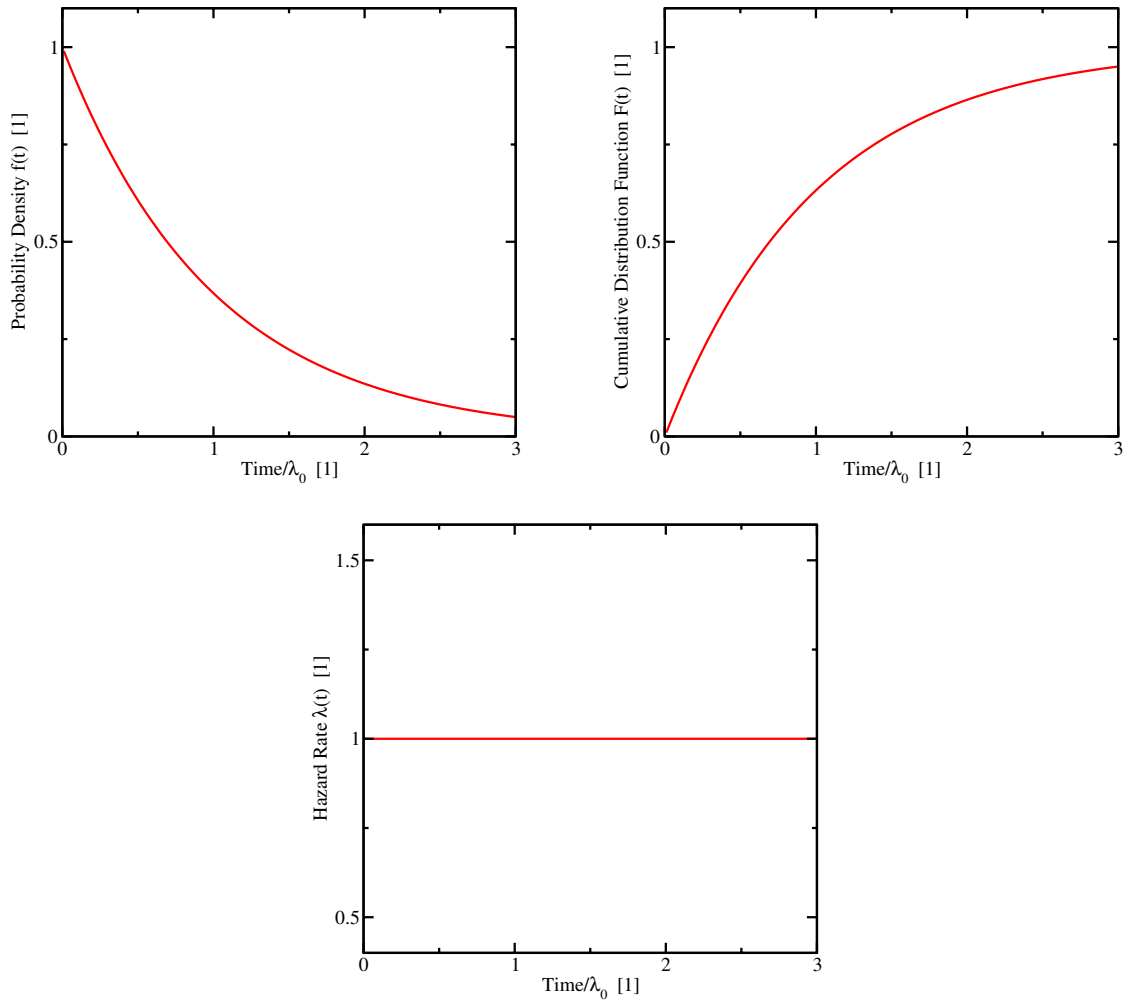


**Figure 3.3:** The exponential distribution: probability density function  $f(t)$  (3.7), cumulative distribution function  $F(t)$  (3.8) and constant hazard rate  $\lambda$ .

Different failure distributions  $f(t)$  have been used to describe the failure events for devices and systems. A convenient modeling approach is to apply a constant failure rate. This is also assumed for the useful time phase in the bathtub curve. The guidelines in MIL-HDBK-217, too, are based on this approach. Using  $\lambda(t) = \lambda_0$  yields an exponential distribution. The probability density function results in

$$f(t) = \lambda_0 \exp(-\lambda_0 t), \quad (3.7)$$

the cumulative distribution function in

$$F(t) = 1 - \exp(-\lambda_0 t), \quad (3.8)$$

and the mean time-to-failure evaluates to  $\text{MTTF} = 1/\lambda_0$ . The shapes of those functions are depicted in Fig. 3.3.

### 3.1. RELIABILITY IN GENERAL

The probability that a failure event occurs is equal for any point in time, no matter how old the device is. This means that a device that as an age  $t$  is as good as a new item [68]. This characteristic is called memoryless and makes calculations possible without knowledge of the past operating time. In the first reliability models, it was assumed that the failure rate is constant over the device lifetime. However, this seems not to be the case, as already explained in the context of the bathtub curve. It is suspected that the constant failure rate was assumed due to systematic errors and misinterpretation of results during data acquisition [63]. For example, due to continuous repair work performed on the test system, in fact data of time-in-between-failures, which has a constant failure rate, was mixed with data of time-to-failure measurements.

For the description of more realistic failure rates numerous other distribution functions have been used. Two prominent examples are the Weibull and the lognormal distribution. The latter one is derived from the normal distribution by taking natural logarithms of all data points. The probability density function is given by

$$f(t) = \frac{1}{\sigma t \sqrt{2\pi}} \exp \left[ -\frac{1}{2\sigma^2} \left( \ln \left( \frac{t}{\mu} \right) \right)^2 \right], \quad (3.9)$$

with its cumulative distribution function resulting in

$$F(t) = \Phi \left( \frac{1}{\sigma} \ln \left( \frac{t}{\mu} \right) \right), \quad (3.10)$$

$$\Phi(z) = \frac{1}{2} \left( 1 + \operatorname{erf} \left( \frac{z}{\sqrt{2}} \right) \right). \quad (3.11)$$

The parameter  $\mu$  represents the median time of the distribution until which 50% of the population has failed and  $\sigma$  influences its shape, as can be seen in Fig. 3.4. An application example for the lognormal distribution is the long term reliability prediction for light bulbs [69], see Fig. 3.4. Using a superposition of lognormal distributions and varying values of  $\sigma$  gives the possibility to represent the early failure and the wearout behavior of a bathtub shaped hazard rate [63].

The Weibull distribution, shown in Fig. 3.5 can be used to model monotonous falling or rising hazard curves. The density function for the Weibull distribution reads

$$f(t) = \frac{\beta t^{\beta-1}}{\alpha^\beta} \exp \left( -\left( \frac{t}{\alpha} \right)^\beta \right), \quad (3.12)$$

and the corresponding distribution function is

$$F(t) = 1 - \exp \left( -\left( \frac{t}{\alpha} \right)^\beta \right). \quad (3.13)$$

$\alpha$  scales the function in time and  $\beta$  determines the shape of the function. By varying  $\beta$ , the Weibull distribution can model the shape of all phases of the bathtub curve [68]. The early failure, the steady state, and the wearout regimes. With  $\beta = 1$  the Weibull distribution simplifies to the exponential distribution. With  $\beta = 2$  a linearly increasing failure rate can be observed, called the Rayleigh distribution, which is used, for example, to model moisture-induced corrosion

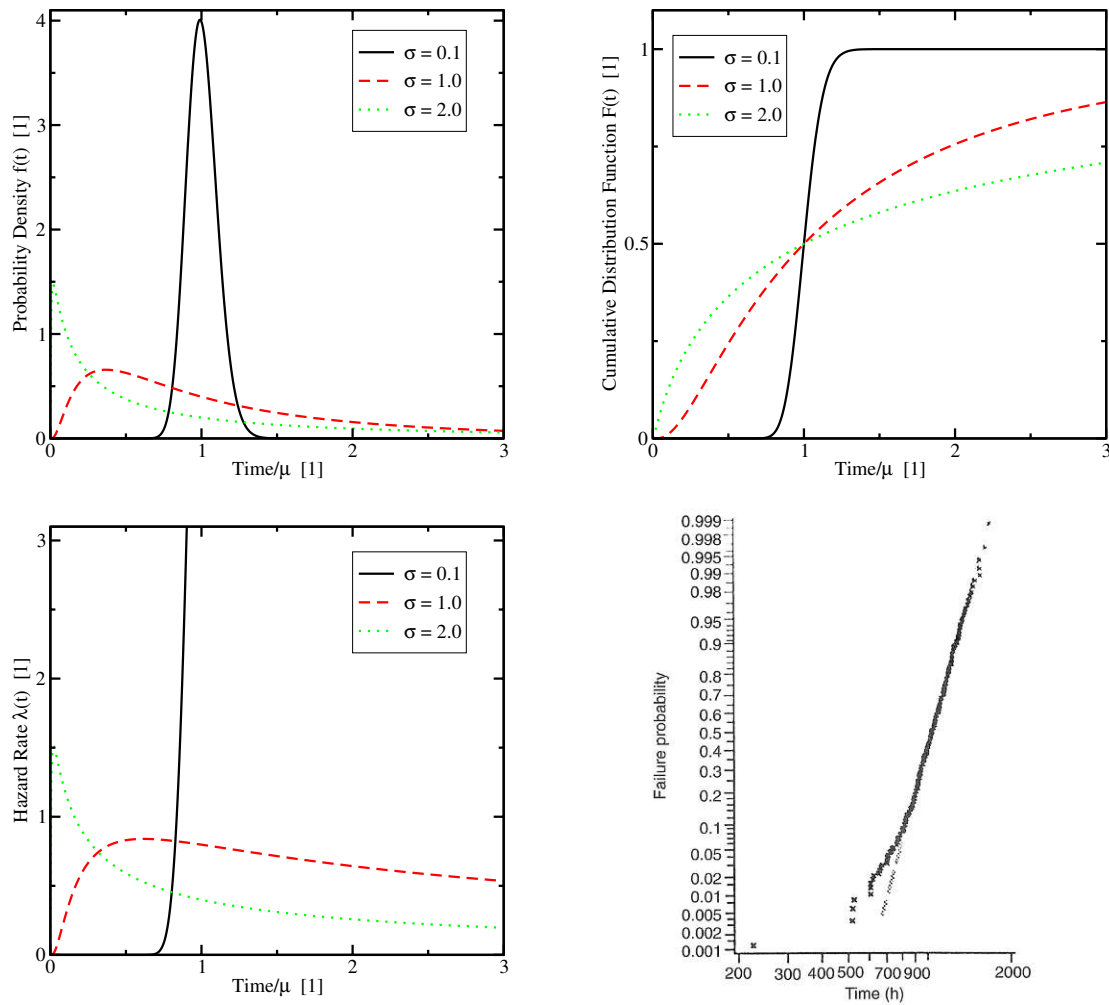


**Figure 3.4:** The lognormal distribution: probability density function (3.9), cumulative distribution function (3.10), and hazard rate; shown for different values of  $\sigma$ . The lower right figure shows failure times for light bulbs plotted in terms of the lognormal distribution (Figure taken from [63]).

failures in microelectronic packages [71]. The Weibull distribution can be derived from the weakest-link theory, which considers the case where the integrity of a system is broken whenever a single flow exceeds a critical size, just like in a chain. It is also used, for example, for reliability prediction for dielectric breakdown [72] or optical fiber fracture [73].

Statistical reliability considerations help to quantify the expected lifetime of electronic components and systems. Distribution functions are used to describe the expected failure rate of a certain population but it is not possible to make a prediction for a certain device. There is only a weak link between this statistical modeling approach and the underlying physics. Very often, this link is missing at all. To improve the reliability and to make more physics-based predictions,

### 3.1. RELIABILITY IN GENERAL

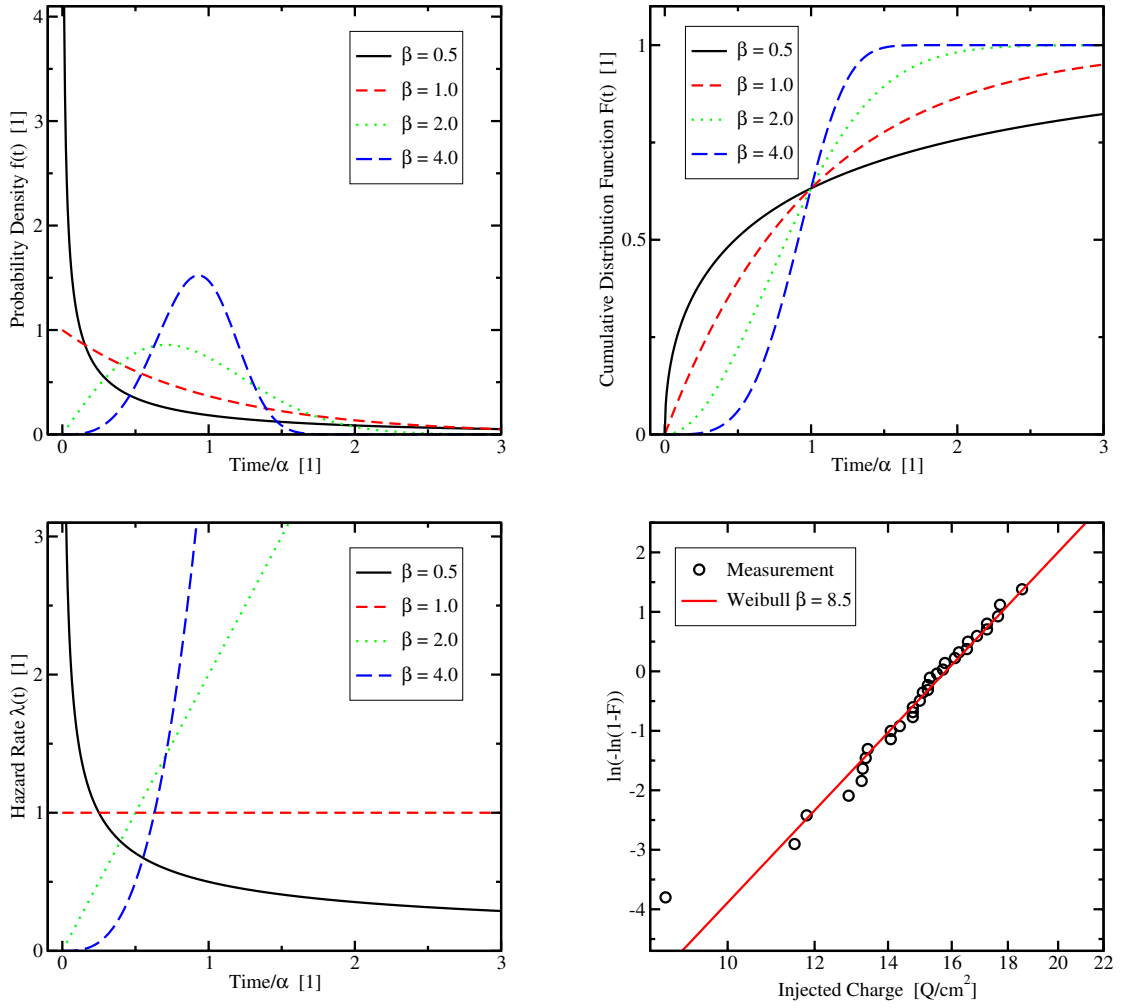


**Figure 3.5:** The Weibull distribution: probability density function (3.12), cumulative distribution function (3.13), and hazard rate function; shown for different values of  $\beta$ . The special cases of exponential ( $\beta = 1$ ) and Rayleigh ( $\beta = 2$ ) distribution are shown. The lower right figure shows a fit using the Weibull distribution for experimental data of oxide breakdown (Data taken from [70]).

it is required to take a closer look at the failure mechanisms and the underlying physics. Using this insight also helps to improve the reliability as well as reliability predictions.

#### 3.1.5 Reliability and Yield

To run a semiconductor production line economically, one of the most important key figures is to reach high yield. Yield describes the number of useful devices at the end of the production line in relation to the number of potentially useful devices at the beginning of processing [74].

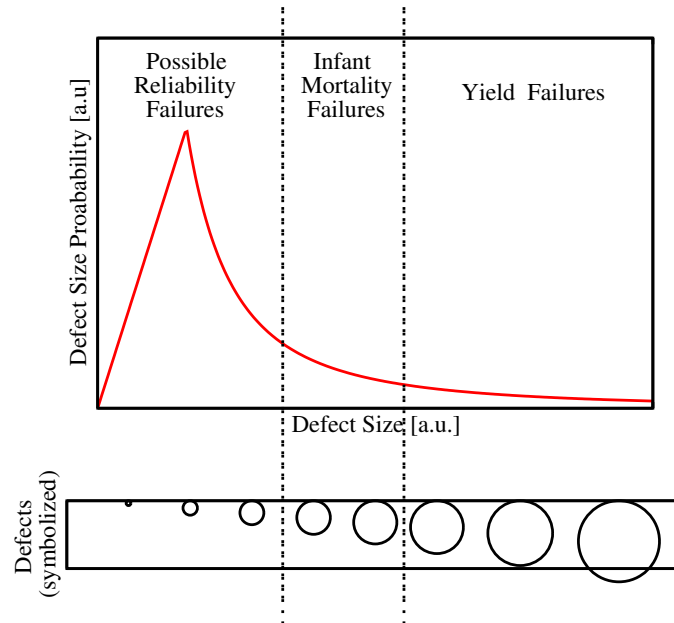


**Figure 3.6:** Typical defect size distribution in semiconductor production lines. At the bottom a comparison of defects with a structure in feature size is symbolized. (Idea of graph taken from [75])

Therefore, all defects which can be detected after manufacturing are called yield defects. Hence, yield can also be described as the probability that a device has no yield defects [75].

Defects introduced during production which are not detected, can lead to device failures. This failure type can be classified as extrinsic failure. This gives a relation between reliability and yield. Huston *et al.* [64] have shown this correlation by considering the size of defects introduced during processing. In his work, the defect size on interconnects was investigated, but the model was also applied for gate oxide yield [75, 76], where defects are considered as a local effective oxide thinning [77].

In these considerations, large defects resulting in non-working devices are detected in the production line or during device tests. These defects are therefore called yield defects and the devices are rejected [64]. The smallest failures might have negligible effects or might lead to random reliability failures during the lifetime of the device. In between are intermediate sized defects which might be detected during fabrication but might also remain undiscovered. Hence, these defects especially tend to cause infant mortality. Usually burn-in tests are used to prevent that those devices are delivered to customers. Note, that the distinction between large and small defects depend on the defect type and is obviously different for the two oxides and interconnects

A defect size distribution, as schematically shown in Fig. 3.6, allows to estimate correlations between reliability and yield. Various investigations on this relation have confirmed this by using field data from different fabrication lines and different processes [64, 78]. Devices coming from batches which reached high yield show a lower infant failure rate. This can be explained by



## 3.2. FAILURE AND DEGRADATION MECHANISMS

the overall lower failure rate which also reduces the number of reliability failures appearing in the form of extrinsic failures. Since ongoing productions are monitored and optimized, mature processes commonly have higher yield. At the same time, the reliability is also increased.

### 3.2 Failure and Degradation Mechanisms

Many different failure mechanisms exist in semiconductor devices. For virtually all of them the root cause can be traced back to a relocation or displacement of material or charge. Atoms, ions, electrons, or holes are shifted from their designated to a harmful position. An isolated single movement usually does not cause a device failure. However, in highly down-scaled semiconductor devices, also single defect can lead to device failure. A major problem is the accumulation or depletion around an initially single defect, which consequently leads to further degradation of the device until parameters shift out of their specification or a severe failure occurs.

#### 3.2.1 Mass Transport

A representative failure mechanism based on transport of material is electromigration. In modern microelectronic devices, interconnect wires are required to carry high current densities. The positively charged metal ions in the interconnects are exposed to two counteracting forces. Due to the positive charge, ions experience a force towards the cathode. On the other hand, the mean velocity of the electrons is oriented towards the anode. A part of their moment is transmitted on to the atoms which also causes a force on the ions. This second force dominates at high current flow conditions which results in an effective force on ions oriented in the same direction as the electron flow. This effect is called electron wind [79]. The major part of the mass transport in interconnects follows grain boundaries and interfaces. This transport produces areas that suffer from material depletion and areas that suffer from material accumulation. The former ones are called voids and can grow until the interconnect is cut. Hence, the resistivity suddenly increases leading to a drop of the current. In areas of material accumulation, the additional atoms form hillocks. Most reliability considerations for electromigration have been done statistically. Commonly, the time until a massive resistivity increase appears. A frequently used estimation for the mean time-to-failure is expressed as [80]

$$\text{MTTF} = AJ^{-n} \exp \frac{\mathcal{E}_e}{k_B T}. \quad (3.14)$$

Here,  $\mathcal{E}_e$  is the activation energy of the electromigration mechanism (estimated between 0.5 and 0.9 eV),  $k_B$  is the Boltzmann constant,  $T$  the temperature,  $J$  the (electron) current density with the fitting parameter  $n$  and  $A$ . Electromigration reliability predictions are based on acceleration tests at elevated temperatures and high currents. The fitted parameters have to be transferred from test structures operated under high-stress conditions onto actual devices operated at use-conditions. However, it would be better to follow a physics-of-failure approach by considering models based on the atomistic processes and by taking the detailed structure including grain

## CHAPTER 3. RELIABILITY IN SEMICONDUCTOR DEVICES

boundaries and interfaces into account. This could give more profound estimations and would help to locate the weakest-link along interconnects.

Another example of a reliability issue due to atomistic transport in semiconductor devices is related to hydrogen transport. In device fabrication hydrogen is especially important for the passivation of dangling bonds at silicon/silicon-dioxide (Si/SiO<sub>2</sub>) and polysilicon/silicon-dioxide interfaces. Under stress conditions the hydrogen atoms can break free, leaving back traps. This hydrogen release and possibly also the transport, is an important failure mechanism in negative bias temperature instability (NBTI) and hot-carrier degradation. The former will be briefly described in the next section. The hot-carrier degradation and related modeling approaches for hydrogen dissociation are discussed in Chapter 6.

### 3.2.2 Oxide- and Interface-Related Failure and Degradation Mechanisms

Semiconductor oxides in electronic devices serve as isolation structures, as gate dielectrics, and as protection against environmental harms. Especially the native oxide of silicon, silicon dioxide, forms a stable and reliable interface on top of silicon surfaces. SiO<sub>2</sub> is an insulator with a very high bandgap of about 9 eV [32] and with high resistivity, high breakdown voltage, and an adequate permittivity [81]. It can be grown easily and in a well-controlled manner with a low defect density. Considering this excellent behavior in the fabrication process, the wide usage of silicon and its oxide becomes evident. Green *et al.* [81] stated, that SiO<sub>2</sub> is with the exception of its lower dielectric constant an ideal dielectric material.

Due to the importance of SiO<sub>2</sub> and the Si/SiO<sub>2</sub> interface, it is obvious that its reliability is of crucial significance and a considerable amount of research has been related to that topic. Like all insulators, SiO<sub>2</sub> loses its insulating property at certain electric fields, where a breakdown occurs. The maximum electric field a dielectric material can be used without severe damage is called dielectric strength. The breakdown can occur because of intrinsic or extrinsic phenomena, whereas the first ones are due to weaknesses of the material itself and the latter ones are due to defects at the surface or in the bulk of the oxide. Because of the extremely down-scaled semiconductor devices, oxides have to resist enormous electric fields. The operation conditions get close to the dielectric strength which increases the risk of wearout and its consequences on device behavior.

#### Oxide Leakage Current and Oxide Breakdown

During operation various mechanisms can lead to the creation and activation of oxide or interface defects acting as traps. As a consequence, the device degrades and parameters can drift out of their specification. Especially MOSFET devices are affected by oxide degradation. This wearout process during device operation can increase the gate leakage current which is called stress-induced leakage current (SILC) [82]. The ongoing degradation can further lead to breakdown, which is believed to be caused by a critical density of defects [83]. This time-dependent dielectric breakdown (TDDB) is a very important reliability issue [84]. It is still under discussion which

### 3.2. FAILURE AND DEGRADATION MECHANISMS

physical processes are responsible for oxide deterioration, leading to SILC and TDDB, and in a further consequence how they are interrelated. The defects for the two processes are often assumed to be the same [85], however, there are also opinions against this connection, which claim that different processes and different defects are relevant for the two degradation mechanisms [86].

The monitoring of oxide degradation is based on measurements of different phenomena. The interface trap creation is commonly assessed using capacity over voltage and charge pumping experiments [87]. Measurement techniques like constant-current stress (CCS) and constant-voltage stress (CVS) are used to analyze the SILC and TDDB degradation. Changes of the voltage during CCS or the current during CVS suggest that charge trapping in the oxide leads to changes in the tunnel current density [88]. Another widely discussed observation is the substrate hole current. It is measured in n-channel MOS devices with source and drain grounded and a positive voltage applied to the gate. The hole current which is some orders of magnitude below the electron current seems to be correlated to the oxide deterioration [89]. Measurements show that breakdown is observed after a certain hole fluence through the oxide is reached. One explanation for this is the Anode Hole Injection (AHI) [90]. Here, electrons tunnel from the cathode into the anode and transfer their excess energy to holes. These holes gain high energy and can be injected back into the oxide. With a given probability they can cause the observed bulk hole current. In this AHI model, these injected holes create the oxide damage. Estimations of the time to breakdown ( $t_{BD}$ ) using the AHI model lead to a relation where the logarithm of  $t_{BD}$  depends linearly on the reciprocal oxide field and is therefore called the ' $1/E$ '-model [91]. Early empirical models, however, suggested a linear dependence of the logarithm of  $t_{BD}$  on the electric field. These models are therefore called the ' $E$ '-model. Several physical explanations have been suggested for this phenomenon, however, none of them correlates the degradation with the electron tunnel current [91]. One of the oldest ' $E$ '-models, the thermochemical model [92], for example, gives a physical explanation based on Si-Si bond breaking in  $\text{SiO}_2$ . Interestingly, both, the ' $E$ '- and the ' $1/E$ '-model allow to fit TDDB data rather well over limited field ranges used in acceleration tests [92]. Obviously, the extrapolations to low electric fields give very different lifetime projections. A wide range of measurements and especially long-term measurements close to normal operating fields of approximately 5 MV/cm are required to clearly distinguish between the models [92]. However, for low electric fields  $t_{BD}$  increases drastically which makes measurements nearly impossible.

Breakdown mechanisms due to the accumulation of oxide defects are often explained using the percolation model [70]. Generated electron traps are believed to form a breakdown path from the anode to the cathode. In this model, the traps are represented using spheres, which are randomly placed in the oxide volume (see Fig. 3.7). If two spheres overlap, conduction is possible between them. An oxide is broken if a single breakdown path is generated [93]. In oxides thicker than approximately 5 nm the heat generated by the localized current immediately propagates and results in thermal damage. This leads to a highly conductive short across the oxide, which is called hard breakdown [81]. However, in thinner oxides a non-destructive or soft breakdown is observed [94]. Here, a more resistive current path is created. Therefore, no thermally induced lateral extension of the percolation path is triggered [81]. Both, hard and soft breakdown can be described using the percolation model [95]. Good agreement is found by comparing this model with measurements. By partitioning the oxide capacity into a

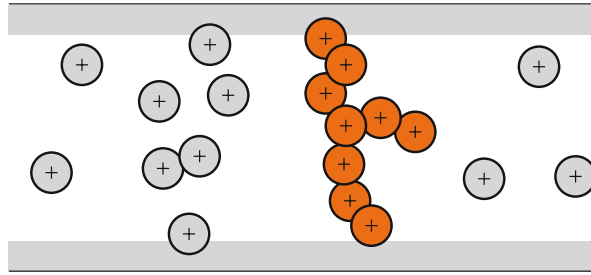


**Figure 3.7:** Breakdown in an oxide as explained by the percolation model. Generated traps are symbolized using spheres and are randomly distributed in the oxide. Overlapping spheres symbolize a path for current flow. A breakdown path between the boundaries is shown in the figure (orange).

row of small independent capacitances, one can empirically assume that the failure of a single component leads to the failure of the whole oxide. Therefore, the breakdown mechanism can be explained by the weakest-link theory, which can be fit using the Weibull distribution [70,95] (see Fig. 3.5).

### Negative Bias Temperature Instability

A recently and heavily discussed reliability topic is the negative bias temperature instability (NBTI). It can be observed by applying negative voltages to the gate of a MOSFET with all other contacts connected to ground. Since negative gate voltages are more common in p-MOSFETs, p-type transistors are more susceptible than the n-types. The degradation leads to a shift of the threshold voltage, a change in the subthreshold slope, and a reduction of the mobility. Its underlying mechanism becomes stronger at elevated temperatures and high voltages. In contrast to the other degradation mechanisms discussed so far, a relaxation can be observed as soon as NBTI stress ends. However, a part of the damage remains permanent or at least relaxes only very slowly [96].

NBTI has already been known for forty years and has long been explained and modeled by the reaction-diffusion (RD) theory [97]. In this model, the de-passivation of  $P_b$  centers is assumed as the main degradation mechanism NBTI.  $P_b$  centers are dangling bonds at the Si/SiO<sub>2</sub> interface. During the production of the devices, hydrogen is used to passivate these bonds and to make them electrically inactive. During stress, this hydrogen is released causing the device degradation. In the RD model, the de-passivated hydrogen is assumed to diffuse away from the interface through the oxide leaving back dangling bonds at the interface. The degradation is therefore diffusion dominated. In the relaxation phase hydrogen near the interface can passivate the interface again. Hence, the diffusion process of hydrogen plays an important role in the RD model. Various NBTI stress measurements have been fitted successfully with this method. However, modeling of the relaxation phase shows considerable deviations between measurements and simulations. The model predicts a retarded relaxation which is not found in measurement data. Subsequently the tendency changes insofar that the prediction relaxes too fast. During

### 3.2. FAILURE AND DEGRADATION MECHANISMS

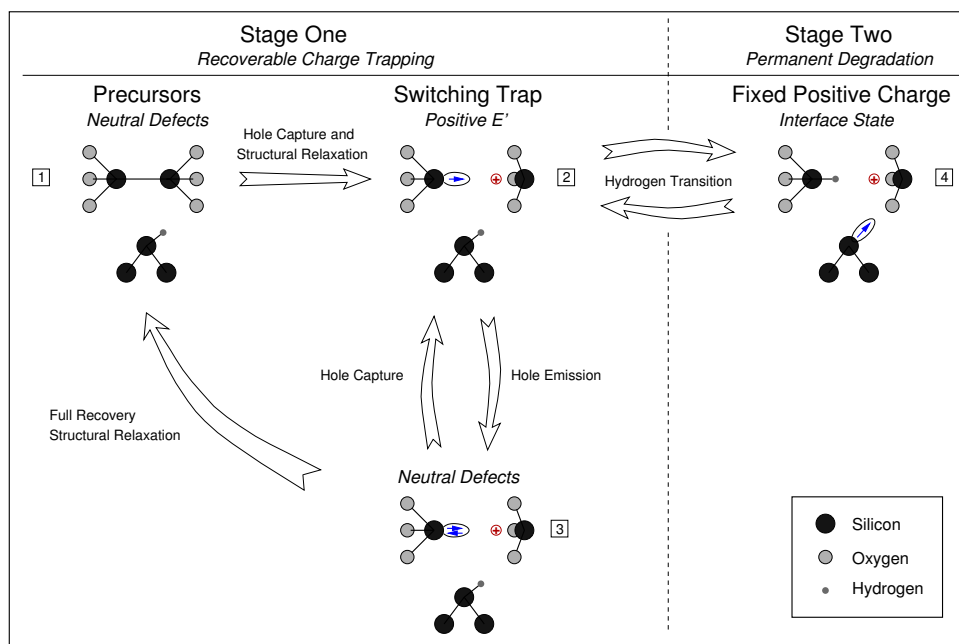


**Figure 3.8:** Sketch of the four configurations considered in the two-stage model. The possible transitions between the states 1–4 are indicated by the arrows. (Figure taken from [101])

NBTI stress the forward and the backward reactions contribute to the degradation. Considering that the relaxation alone is evidently not described correctly, the correctness of the RD model is questionable. Hence, extensions to the RD approach have been suggested, that assumed a dispersive hydrogen transport in the oxide [98,99]. But this and other variations do not seem to fit satisfyingly. Additionally, many published approaches seem to be based on tainted measurement data and it shows that it is very important to consider the measurement techniques used to quantify the degradation of device parameters [100]. This is caused by the fact that measurements are commonly performed by gate voltage sweeps and subsequent current measurements to estimate the threshold voltage. This requires an interruption of the stress cycle and relaxation immediately takes place. Since the time constants for relaxation are very small, measurement results can change significantly with the measurement delay.

Recently an advanced physically based NBTI modeling approach has been proposed by Grassler *et al.* [101]. In this work, the degradation is described using two stages. The key ingredient in this model is the near-interfacial oxygen vacancy in the amorphous SiO<sub>2</sub> gate dielectric. Holes from the silicon are captured by this defect, breaking up the Si-Si bond (state 1) which creates a positively charged  $E'$  center (see the transition from state 1 to 2 in Fig. 3.8). On hole emission, i.e. on electron capture, the defect is neutralized (state 3) but does not relax immediately to its initial configuration. Now, the neutral  $E'$  center can recapture a hole returning to the charged state 2 or the structure relaxes back to its precursor configuration. The hole capture and emission between state 2 and 3 can be very efficient. Therefore, such a kind of defect is called switching trap. The states 1, 2, and 3 represent the first stage in this two-stage model.

## CHAPTER 3. RELIABILITY IN SEMICONDUCTOR DEVICES

The second stage of the degradation process is initiated by the dangling bond of the positively charged Si atom of the  $E'$  center. It attracts a hydrogen atom, which comes originally from the passivated interface, where it leaves back a positive interface charge. Repassivation of those dangling bonds requires free hydrogen atoms. For a full recovery, the defect has to pass through state 2 and 3. Hence, the full relaxation is slow, especially from stage 2. At least a part of those traps seems to remain permanent. The possible transitions between the four states of this model are illustrated in Fig. 3.8. The simulation results using this model in comparison with measurement data of devices with different technologies and geometries deliver very promising results [101, 102]. Also the fast and the slow/permanent degradation observed in measurements are described very well using this two-stage model [101, 102].

### Hot-Carrier Reliability

Another reliability concern comes from hot-carriers in the channel. Due to the high electric fields along the channel in MOS transistors, carriers gain a considerable amount of energy. This is especially true at the drain end of the channel. These carriers can break silicon-hydrogen bonds at the interface which generates interface traps. Hence, charges can get trapped and consequently change the device parameters. This degradation mechanism is essential for the operation of high-voltage devices and is discussed in detail in Chapter 6.

### 3.2.3 Bulk Semiconductor Related Reliability Issues

High energetic carriers are not only responsible for interface reliability. Another hot-carrier process, impact-ionization is also of special interest for reliability engineering. It is especially pronounced at the drain end of the channel region in MOSFET devices. The cascaded impact-ionization carrier generation increases the carrier concentrations, the current densities, and finally leads to avalanche breakdown. Devices have to be designed carefully to avoid breakdown under all operating conditions within the specifications [103, 104]. In some applications the breakdown conditions initiated by, for example, electrostatic discharge or power supply peaks, cannot be fully prevented. The breakdown can lead to latch-up, snap-back, or immediate device failure with all consequential reliability issues. The topic of modeling and simulation of impact-ionization is an important part of this thesis, addressed in Chapter 5.

### 3.2.4 Overvoltage and Electrostatic Discharge

MOSFET transistors and especially CMOS (Complementary MOS) integrated circuits inherently suffer under the high susceptibility of the gate oxides to electrostatic discharge (ESD). In integrated circuits ESD stress leads to gate oxide or thermal junction breakdown [105–107]. The risk of ESD shocks is not only present before and during assembly, but also prior to the packaging and bonding of the die. On the semiconductor wafer, for example, etching, testing, and dicing can also introduce ESD [106, 108]. The risk of damage obviously increases with the



### 3.2. FAILURE AND DEGRADATION MECHANISMS

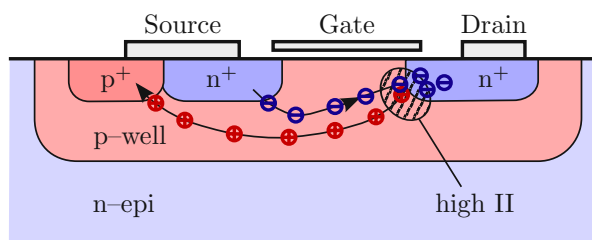


**Figure 3.9:** Schematic carrier flow in a gate-grounded NMOS (ggNMOS).

ongoing shrinking of the gate oxide. Since ESD events cannot be fully avoided during the product life-cycle, the most practical approach is the integration of protection circuits against ESD threats directly in the microelectronic structures [8].

Most work in reliability research concerning ESD is related to the optimization of existing protection structures and to the development of new structures [109, 110]. The procedure of transferring ESD protection devices from one technology node to the next one is not straightforward. Thereby changes in the dimensions, the introduction of buried oxides, and different EPI (epitaxy layer) thicknesses introduce new uncertainties. Various structures are used as protection circuits. The first protection structures in the beginning of CMOS technology, required serial resistors. Hence, the overall performance of the integrated circuit was reduced. However, optimal designed ESD devices are electrically invisible during functional operation, but become active quickly, if needed, to keep the voltage low and to dissipate high currents. To accomplish this, new devices were introduced, one of them is the silicon controlled rectifier (SCR) based on *npnp*-structures [111]. This type of device is hard to calibrate and small process variations can lead to significant changes in the turn-on voltage. Nowadays, a very common structure is the gate-grounded NMOS transistor (ggNMOS), which makes use of the parasitic bipolar transistor [111]. To minimize the fabrication costs, the same technology as for the integrated circuit itself is used. The ggNMOS is actually built like a common MOSFET, only the dimensions have to be adapted (see Fig. 3.9). Source and gate are grounded and the drain is connected to the external input pin that needs to be clamped down to a low voltage. On ESD events, the rising voltage generates an increased reverse current leading to impact-ionization near the drain region. Eventually, the drain junction breaks down yielding a high carrier generation rate. Electrons are driven towards the drain and holes are driven to the *p+* area (actually the bulk contact). This hole current flow under the *n+* source area increases the electrostatic potential in the bulk so that the source-bulk junction gets forward biased and electrons are injected into the bulk. The increased electron current leads to a positive feedback and to a further increased impact-ionization generation. Hence, the resistance between source and drain drops. In the *I/V* characteristics this gives a negative differential resistance (see Fig. 3.10). The lower the voltage drops, the lower is the dissipated heat during ESD.

Structures like the ggNMOS are used to protect integrated circuits efficiently against ESD events. Especially measures to prevent damage due to electrostatic discharge events caused by people touching the device are carefully implemented. This stress event is also well modeled by the human body model (HBM).

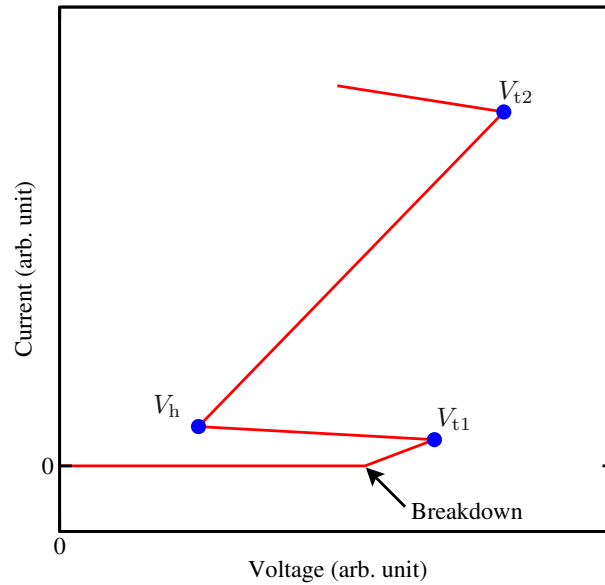


**Figure 3.10:** Typical quasi-static snap-back characteristic of a ggNMOS ESD protection device. In normal operation, only the junction leakage current flows. On breakdown of the drain junction, the current increases and after reaching the threshold voltage  $V_{t1}$  the parasitic bipolar configuration induces the negative differential resistance leading to snap-back. The device design must guarantee, that the holding voltage  $V_h$  is lower than the breakdown voltage of the protected devices. A further increase of voltage and current continues to increase the generated heat which finally leads to thermal breakdown at  $V_{t2}$ .

### 3.2.5 Environmental Impacts

One of the most often considered environmental influences is the temperature [112–114]. High temperatures in silicon devices lead to changes of the device parameters and to accelerated device degradation [115–117]. It has to be ensured that cooling is properly designed for all environmental temperatures that can be expected [118]. Since most degradation mechanisms are thermally activated, elevated temperatures during usage decrease the lifetime of the device. A proper buffer in the design is needed to ensure design goals.

Other environmental impacts include radiation-induced degradation which can lead to displacement or ionization effects [63]. Also mechanical, physical, as well as chemical influences may penetrate the protection layers of integrated circuits and eventually degrade the device or open up paths to the semiconductor surface [63]. By such a path, foreign atoms, or simply moisture, can react with the metalization [71]. Therefore, a proper coating and packaging is very important for protection against environmental impacts [119].



## Chapter 4

# Device Simulation and Parameter Modeling

This chapter explains the concept of device simulation, especially in the context of the drift-diffusion transport model. Additionally to the semiconductor equations, a summary on modeling of the important parameters mobility and generation/recombination is given. Particularly with regard to the hot-carrier modeling in high-voltage devices, concepts for the estimation of the energy distribution function in the drift-diffusion model are presented.

Most of the simulations in this chapter are calculated using sample devices which are based on high-voltage devices made by *ams* [9]. They are n-channel lateral DMOSFETs with a gate oxide thickness of 7 nm, fabricated in a 0.35  $\mu\text{m}$  CMOS-based technology. The gate length is 0.5  $\mu\text{m}$ , the width is 40  $\mu\text{m}$ , and the specified application voltage is 50 V. The doping profile and the geometry are depicted in Fig. 4.1. The simulation domain extends in a depth of 15  $\mu\text{m}$ , while the figures depict only the upper half of the device. The drift-diffusion and hydrodynamic simulations in this work were performed using the device simulation tool MINIMOS-NT [120] and the GTS FRAMEWORK from *Global TCAD Solutions* [121].

### 4.1 Semiconductor Equations

#### 4.1.1 Poisson's and Continuity Equation

In macroscopic semiconductor device modeling, Poisson's equation and the continuity equations play a fundamental role. Poisson's equation, one of the basic equations in electrostatics, is derived from the Maxwell's equation  $\nabla \cdot \mathbf{D} = \rho$  and the material relation  $\mathbf{D} = \hat{\epsilon}\mathbf{E}$ .  $\mathbf{D}$  stands for the electric displacement field,  $\mathbf{E}$  for the electric field,  $\rho$  is the charge density, and  $\hat{\epsilon}$  is

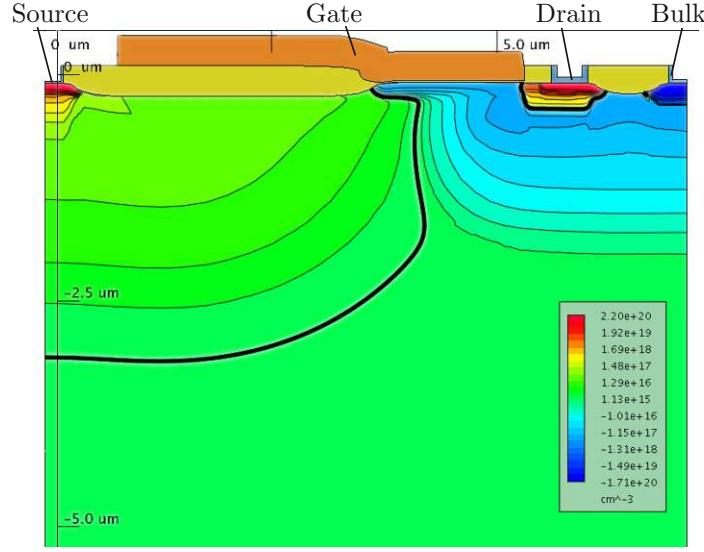


**Figure 4.1:** Structure of the sample n-channel LDMOSFET used for simulation examples. The transitions between n- and p-doped regions are marked with bold black lines and the value of the net doping concentration is shown. The simulated structure of the device continues to 15  $\mu\text{m}$ , while only the upper part is presented.

the permittivity tensor. Using the electrostatic potential  $\psi$  with  $\mathbf{E} = -\nabla\psi$  leads to Poisson's equation

$$\nabla \cdot (\hat{\epsilon} \nabla \psi) = -\rho. \quad (4.1)$$

Even for high frequencies, where the wavelengths are typically much smaller than the device dimension, the quasi stationary approximation used to justify Poisson's equation is still valid. Also the permittivity tensor  $\hat{\epsilon}$  is considered time invariant in this derivation. In isotropic materials like silicon the permittivity can be additionally approximated by the scalar value  $\epsilon$ . Furthermore the permittivity is often considered to be constant within a material segment.

In semiconductors the charge density is commonly split into fixed charges which are in particular ionized acceptors  $N_A^-$  and donors  $N_D^+$  and into free charges which are electrons  $n$  and holes  $p$ . Including the acceptors, donors, electrons, and holes into (4.1), Poisson's equation can be written as

$$\nabla^2 \psi = \frac{q}{\epsilon} (n - p + N_A^- - N_D^+). \quad (4.2)$$

The right hand side of (4.2) becomes zero in ideal oxides, and Poisson's equation reduces to the Laplace equation. However, the existence of oxide charges  $N_{\text{ox}}$  has to be considered, which yields

$$\nabla^2 \psi = -\frac{q}{\epsilon} N_{\text{ox}}. \quad (4.3)$$

Additionally, at interfaces and surfaces, the interface trap concentration  $N_{\text{it}}$  has to be considered.

## 4.1. SEMICONDUCTOR EQUATIONS

The continuity equation, can be also derived from Maxwell's equations and reads

$$\nabla \cdot \mathbf{J} + \frac{\partial \rho}{\partial t} = 0. \quad (4.4)$$

The current density  $\mathbf{J}$  is split into  $\mathbf{J}_n$  and  $\mathbf{J}_p$ , for the contribution of electrons and holes, respectively. The electron and hole concentrations are written as  $n$  and  $p$ , respectively, and  $q$  is used to represent the elementary charge. By introducing the recombination rate  $R$ , two separate continuity equations can be formulated as

$$\nabla \cdot \mathbf{J}_n - q \frac{\partial n}{\partial t} = +qR, \quad (4.5)$$

for electrons and

$$\nabla \cdot \mathbf{J}_p + q \frac{\partial p}{\partial t} = -qR, \quad (4.6)$$

for holes. The separation into two equations allows independent transport modeling of the carrier types. The rate  $R$  represents the net rate, which is zero in thermal equilibrium, following that generation and recombination are balanced. Generation and recombination rates of electrons and holes are expressed using physically or empirically based recombination models [11], which will be presented in Section 4.2. The equations (4.5) and (4.6) can alternatively be derived from Boltzmann's transport equation using the method of moments [15].

### 4.1.2 Carrier Transport Equations

A semiclassical description of carrier transport is given by Boltzmann's transport equation (BTE) which describes the evolution of the distribution function in the six-dimensional phase space  $(x, y, z, p_x, p_y, p_z)$ . Unfortunately, analytical solutions exist only for very simple configurations. One popular approach for solving the BTE in arbitrary structures is the Monte Carlo method [122] which gives highly accurate results. However, due to the statistical nature of the Monte Carlo method solutions are computationally very expensive. Due to the good agreement with experiments [123] results are often used as reference for the evaluation of simpler models. Alternatively, the spherical harmonics expansion (SHE) method as a deterministic numerical solution method of the BTE was presented already in the 1960s [124]. However, it has just been recently, that an efficiently use on real devices has been realized [125].

Device simulations on an engineering level require simpler transport equations which can be solved for complex structures within reasonable time. One method to perform this simplification is to consider only moments of the distribution function [126]. Depending on the number of moments considered in the model, different transport equations can be derived. The use of the first two moments, leads to the well known drift-diffusion model, a widely used approach for modeling carrier transport.

### 4.1.3 The Drift-Diffusion Model

Beside the derivation of the drift-diffusion by the method of moments [11], it is also possible using basic principles of irreversible thermodynamics [127]. The resulting electron and hole current relations contain at least two components caused by carrier drift and carrier diffusion. Additionally, the gradient of the lattice temperature ( $\nabla T_L$ ) acts as a driving force on the free carriers leading to [128]

$$\mathbf{J}_n = qn\mu_n\mathbf{E} + qD_n\nabla n + qnD_n^T\nabla T_L, \quad (4.7)$$

and

$$\mathbf{J}_p = qp\mu_p\mathbf{E} - qD_p\nabla p - qpD_p^T\nabla T_L. \quad (4.8)$$

$\mu_n$  and  $\mu_p$  represent the carrier electron and hole mobility,  $D_n^T$  and  $D_p^T$  the thermal diffusion coefficients, and  $D_n$  and  $D_p$  the diffusivity, respectively. The diffusivities are commonly expressed via the mobility invoking the Einstein relation

$$D_\nu = \mu_\nu \frac{k_B T_L}{q}. \quad (4.9)$$

The index  $\nu$  stands for  $n$  and  $p$ , respectively, while  $k_B$  is the Boltzmann constant. The Einstein relation is strictly valid only in equilibrium [16].

The equations (4.7) and (4.8) together with (4.5), (4.6), and (4.2) form the drift-diffusion model which was first presented by Van Roosbroeck in the year 1950 [129]. Rigorous derivations from the BTE show that many simplifications are required to obtain the drift-diffusion equations as will be shown. Simplifications include, for example, the assumption of a single parabolic band structure and the cold Maxwellian carrier distribution function. This assumes the carrier temperature equal to the lattice temperature. Nevertheless, due to its simplicity and its excellent numerical properties, the drift-diffusion equations have become the workhorse for most TCAD applications.

### 4.1.4 Higher-Order Transport Models

To obtain a better approximation of the BTE, higher-order transport models can be derived using more than just the first two moments [130]. The most prominent models beside the drift-diffusion model are the energy-transport/hydrodynamic models which use three or four moments. These models are based on the work of Stratton [131] and Bløtekjær [132]. A detailed review is given in [15]. In addition to the quantities used in the drift-diffusion model, the energy flux and the carrier temperatures are introduced as independent variables. Also new balance and flux equations are required, which introduce additional transport parameters. The carrier energy distribution function is here modeled using the heated Maxwellian distribution. Modeling of carrier mobility and impact-ionization benefit from more accurate models based on the carrier temperatures rather than the electric field. This advantage is caused by the non-local behavior of the average energy with respect to the electric field and becomes especially relevant for small device structures. This context is explained in Fig. 4.2(a). More detailed

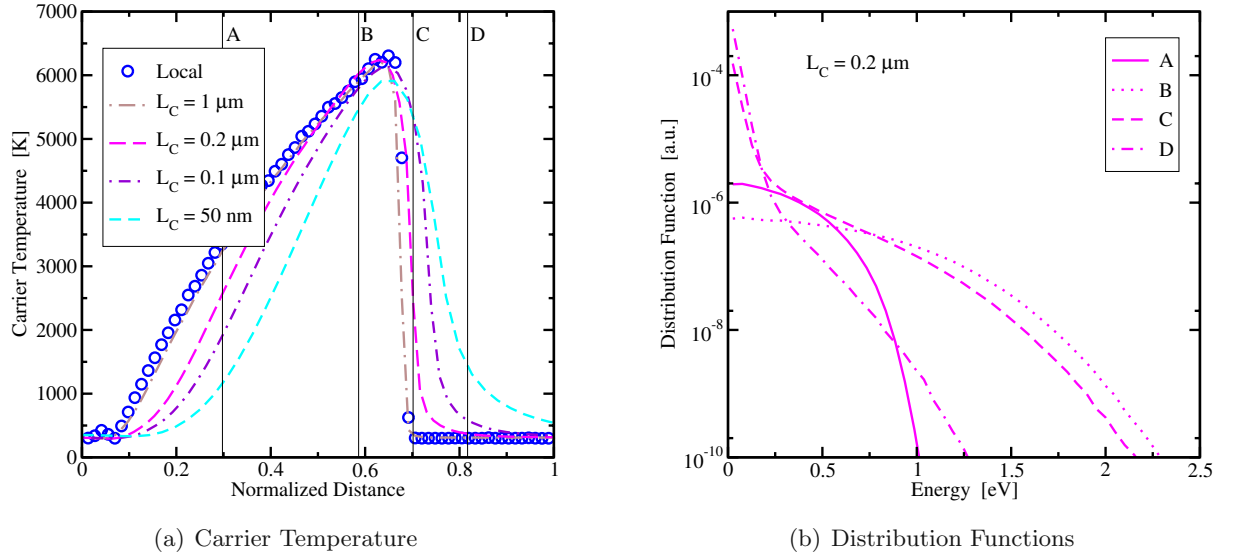


**Figure 4.2:** Electron temperature along the channel of comparable  $n^+ \text{-} n \text{-} n^+$  structures with varying channel lengths  $L_C$  (a). The spatial coordinates have been normalized to get an overlapping electric field. Therefore, the local electric field approach yields the same results for all device lengths. However, it can be seen that the local electric field approach is sufficient for larger structures only, but gives poor results for small structures. The distribution functions (b) are shown for  $L_C = 0.2 \mu\text{m}$  at the positions A to D marked in (a). Note that the average energies at the points A and C are the same, whereas the distribution function looks completely different. Also note the high-energy tail at point D where the carrier temperature is already close to the lattice temperature. (Data taken from [133])

examinations in the far sub-micron area show that describing the energy distribution function using only the carrier concentration and the carrier temperature is still not sufficient for specific problems which depend on high energy tails (see Fig. 4.2(b)). Hot carrier modeling in small structures, for example, which is based on accurate modeling of the high-energy part of the distribution function would require more complex models. Also the reliability modeling benefits of the detailed knowledge of the distribution function (more on this is highlighted in Chapter 6). One method for improving the approximation of the distribution function is the six moments method [134]. It introduces the kurtosis, which is the deviation of the distribution function from the heated Maxwellian.

It is evident that higher-order transport models give a closer solution of the BTE and therefore lead to a better agreement between simulation results and measurements of real devices. This effect is especially relevant for small structures, where non-local effects gain importance (see Fig. 4.2). Simulation results with drift-diffusion in deep sub-micrometer structures therefore seem to be very questionable [135].

The high-voltage devices considered in this work are relatively large. Hence, a rather high number of mesh points is required for a proper discretization. In combination with more elaborative transport equations, this leads to a higher computational time. Additionally, the convergence properties degrade significantly for higher moments models [136]. However, the relatively large dimensions of the high-voltage devices justify the use of the drift-diffusion model in this work.

In case advanced transport models have to be solved in complex devices, it is also possible to combine different transport equations in one simulation. To accomplish this, the semiconductor domain must be partitioned into separate segments. One segment must contain the critical areas, e.g. the channel area. Hence, the higher-order transport equations are solved for this segment, and the drift-diffusion model is used for the remaining ones. Here, it is essential to define proper boundary conditions between the segments [137].

### 4.2 Parameter Modeling

The semiconductor equations discussed above show the basic relations between carrier distribution and the electrostatic potential. Two parameters, the mobility and the recombination rate were introduced, which require appropriate modeling. The physical phenomena which are crucial for modeling of these parameters will be discussed in the following.

#### 4.2.1 Mobility

The derivation of the mobility originates from carrier relaxation times. The mobility is influenced by the lattice and its thermal vibrations, impurity atoms, surfaces and interfaces, interface charges and traps, the carriers themselves, the energy of the carriers, and other effects like lattice defects. Mobility models are used to make an estimation considering these effects and make simulations in continuous systems possible. Since exact derivations are too complex or just do not exist, empirical approaches are often used. Some of the commonly used approaches will be presented here.

A common method for modeling the mobility is the hierarchically encapsulation of the physical mechanisms. In this approach, the most fundamental mechanism is considered to be the lattice scattering dependence ( $\mu^L$ ) followed by the ionized impurity dependence ( $\mu^I$ ). Especially in MOS devices, a surface correction ( $\mu^S$ ) is of special importance. These three contributions classify the low-field mobility models. Modeling of high-field effects is introduced with a field dependence model ( $\mu^F$ ). These contributions can be combined like in the MINIMOS mobility model [138], for example, which looks like

$$\mu^{\text{LISF}} = \mu^F(\mu^S(\mu^I(\mu^L))). \quad (4.10)$$

The individual mechanisms are assumed to be independent of each other. All values resulting from mobility calculations are obviously different for electrons and holes. In contrast to the encapsulation approach (4.10) for the mobility calculation used in the MINIMOS model, the Lombardi model [139] combines three carrier mobility components using Matthiessen's rule. The

components are derived from surface acoustic phonon scattering, from bulk carrier mobility, and from surface-roughness scattering. A similar expression has been used by Agostinelli [140] for holes, additionally accounting for interface charge and screened Coulomb scattering:

$$\frac{1}{\mu_{\nu}^{\text{LIS}}} = \frac{1}{\mu_{\nu}^{\text{ph}}} + \frac{1}{\mu_{\nu}^{\text{sr}}} + \frac{1}{\mu_{\nu}^{\text{c}}} \quad (4.11)$$

Here, the phonon scattering component  $\mu_{\nu}^{\text{ph}}$  combines scattering with bulk phonons, surface phonons, and fixed interface charges.  $\mu_{\nu}^{\text{sr}}$  includes the dependence of the surface-roughness scattering on the electric field orthogonal to the interface and  $\mu_{\nu}^{\text{c}}$  models the screened Coulomb scattering. Other mobility models based on Matthiessen's rule have been developed, for example, by Darwish [141] or Neinhüs [142].

Effects like negative bias temperature instability [143] or hot carrier degradation (see Chapter 6) generate interface traps leading to interface charges. Modeling of their influence on the mobility is of special interest in reliability modeling [144]. A mobility reduction due to oxide charges in inversion layers has been proposed by Sun *et al.* [145] as

$$\mu_{\text{max}} = \frac{\mu_0(N_A)}{1 + \alpha Q_{\text{IF}}}, \quad (4.12)$$

where  $Q_{\text{IF}}$  is the surface oxide charge density (or treated as the interface charge density),  $\mu_0(N_A)$  is the impurity dependent mobility, and  $\alpha$  is modeled as a parameter which depends weakly on the impurity. This mobility reduction model was extended by Wong *et al.* [146] to consider the influence of the trapped charges and of the interface states independently with separate coefficients. In the hot-carrier degradation simulations performed in this work, the model of Sun was applied in the following extended form as

$$\mu_{\text{max}} = \frac{\mu_{\text{LIS}}}{1 + \alpha Q_{\text{IF}} \exp\left(-\frac{d}{d_{\text{ref}}}\right)}. \quad (4.13)$$

The influence of the interface charge is here weighted with the negative exponent of the reciprocal interface distance  $d$  to include the distance dependent influence of the charges with  $d_{\text{ref}}$  as a model parameter.

The carrier mobility also depends on the carrier energy distribution. However, in the drift-diffusion model the electric field is usually employed. Simulation tools commonly differ between low- and high-field mobility and let the user select the models independently. The high-field mobility modeling approaches are often accomplished using the model presented by Caughey and Thomas [147]. A slightly different version, suggested by Jaggi [148, 149], is used in the MINIMOS mobility model,

$$\mu_{\nu}^{\text{LISF}} = \frac{2\mu_{\nu}^{\text{LIS}}}{1 + \left(1 + \left(\frac{2\mu_{\nu}^{\text{LIS}}|\mathbf{F}_{\nu}|}{v_{\nu}^{\text{sat}}}\right)^{\beta_{\nu}}\right)^{1/\beta_{\nu}}}. \quad (4.14)$$

$\mathbf{F}_{\nu}$  describes the driving force, which is the gradient of the quasi-Fermi level and proved to give better results than just the electric field,  $v_{\nu}^{\text{sat}}$  is the saturation velocity, and the value of the



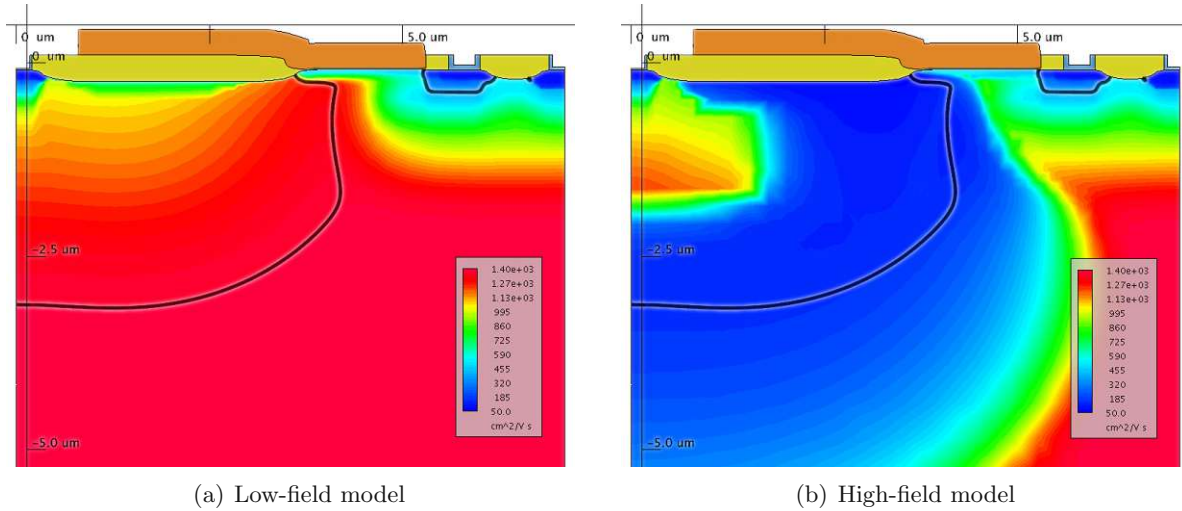


**Figure 4.3:** The electron mobility distribution without (a) and with (b) the contribution of a high-field dependent mobility model.

coefficient  $\beta_v$  is 1 for holes and 2 for electrons. The impact of this field dependence is visible in the mobility distribution of the sample device shown in Fig. 4.3.

To illustrate the impact of mobility models a comparison of simulation results with constant mobility, a low-field mobility model, and a high-field mobility model are shown in Fig. 4.4. Comparing the constant mobility and the low-field mobility model, one can see that the shape changes only slightly, but the total current is reduced significantly for the low-field mobility model (note the multiplication factors in the legend). This is caused by the reduction of the mobility, especially near the surface, which can be clearly seen in Fig. 4.3(a). The transconductance is only slightly influenced, whereas for the high-field mobility model, a strong reduction can be observed. Hence, for the 3.0 V curve, it can be seen clearly that the current initially increases steeply with the drain voltage, but immediately flattens, since the mobility reduction becomes effective. The effective mobility distribution at  $V_{DS} = 50$  V can be seen in Fig. 4.3(b).

Carrier mobility modeling has been investigated since the beginning of semiconductor engineering, and there are still new models published [150]. However, all approaches in the drift-diffusion model which incorporate the influence of carriers that are not in thermal equilibrium basically rely on the electric field. Changes in the electric field therefore directly change the calculated mobility (see Fig. 4.5), whereas the distribution function and therefore the carrier temperature do not change immediately. Mobility models in higher-order transport models can use more information from the distribution function. In energy-transport, for example, the carrier temperature can be used as a parameter. As a consequence effects like the velocity overshoot can be described.



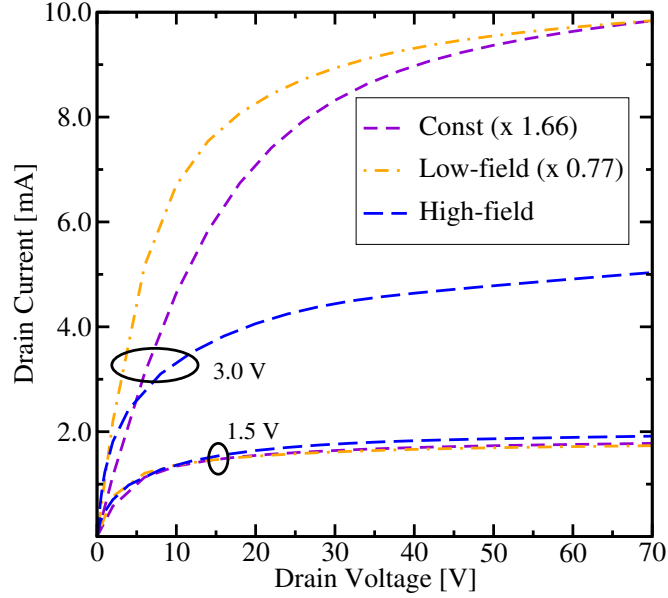


**Figure 4.4:** Output characteristics of the sample device for different gate voltages using a constant mobility, a low-field mobility, and a high-field mobility model (4.14). For visualization the curves were scaled along the current axis so that the output for the gate voltage of 1.5 V overlaps.

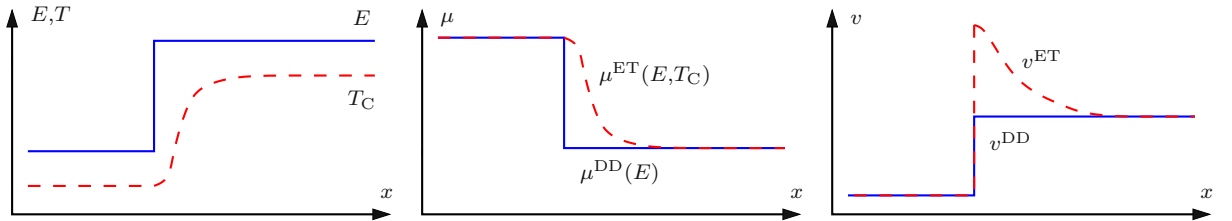


**Figure 4.5:** Carriers traversing an abruptly changing electric field do not immediately change the carrier temperature, instead a delayed increase can be observed (left). High-field mobility models for drift-diffusion are based on the electric field and therefore react instantly to changes of the field while models based on the carrier temperature capture that delay (center). As a consequence the velocity overshoot ( $v = \mu E$ ) cannot be described in the drift-diffusion model (right). (Figure taken from [151].)

### 4.2.2 Carrier Generation and Recombination

The recombination rate  $R$  was formally introduced in the drift-diffusion equations (4.5) and (4.6) by splitting the continuity equation into two individual parts for electrons and holes. From a physical point of view this term includes the generation and the recombination of electron-hole pairs. In thermal equilibrium carrier generation and recombination are balanced and the carrier concentrations are given by their equilibrium values  $n_0$  and  $p_0$  ( $n_0 p_0 = n_i^2$ ). The net recombination rate therefore vanishes. An excess number of carriers leads to an increased recombination, a low carrier concentration leads to an increased generation. The generation and recombination processes contributing to the total effective net generation rate are based on different physical effects which are modeled independently of each other. The separately evaluated models add up to the total net recombination rate. The resulting rate is used to complete the continuity equations (4.5) and (4.6).

One important generation/recombination process is the well-known Shockley-Read-Hall (SRH) mechanism [152, 153] which describes a two-step phonon transition. One trap level which is energetically located within the band-gap is utilized. Four partial processes can be separated: the capture and the emission of both, electrons and holes, on the trap level. Balance equations can be formulated for the trap occupancy function. In the stationary case the rates for electrons and holes are equal. The trap occupancy function can then be eliminated and the SRH generation rate results in

$$R^{\text{SRH}} = \frac{np - n_i^2}{\tau_p(n + n_1) + \tau_n(p + p_1)}. \quad (4.15)$$

$n_1$  and  $p_1$  are auxiliary concentrations depending on the energy level of the traps and  $\tau_n$  and  $\tau_p$  are carrier lifetimes for electrons and holes, respectively.

In MOS devices SRH generation especially influences the bulk current. In n-channel devices, for example, holes generated at the pn-junction are attracted by the low bulk potential leading to the bulk current. The influence can be easily observed in device simulation since models can be switched on or off allowing to deactivate SRH. Fig. 4.6(a) shows the hole current flow and the SRH generation rate in the sample device and in Fig. 4.6(b) the current components on the bulk contact are compared with and without SRH enabled.

The SRH model is not restricted to the description of capture and emission of carriers in the bulk, it can also be extended to determine the occupancy of interface traps [154]. Like most interface related mechanisms this is especially relevant for MOS devices. Simulations of charge pumping (CP) measurements [155], which are used to determine interface trap distributions, require appropriate modeling of trapping and de-trapping effects of carriers in interface traps. In a CP-simulation the measurement procedure is replicated, by performing a transient simulation for each gate pulse level (Fig. 4.7(a)). In contrast to the stationary SRH formulation shown in (4.15), time dependent simulations require to capture the transient behavior of the occupancy function [156]. The final charge pumping curve can be constructed by extracting the mean bulk current of the simulations for every single gate pulse (Fig. 4.7(b)).

## 4.2. PARAMETER MODELING

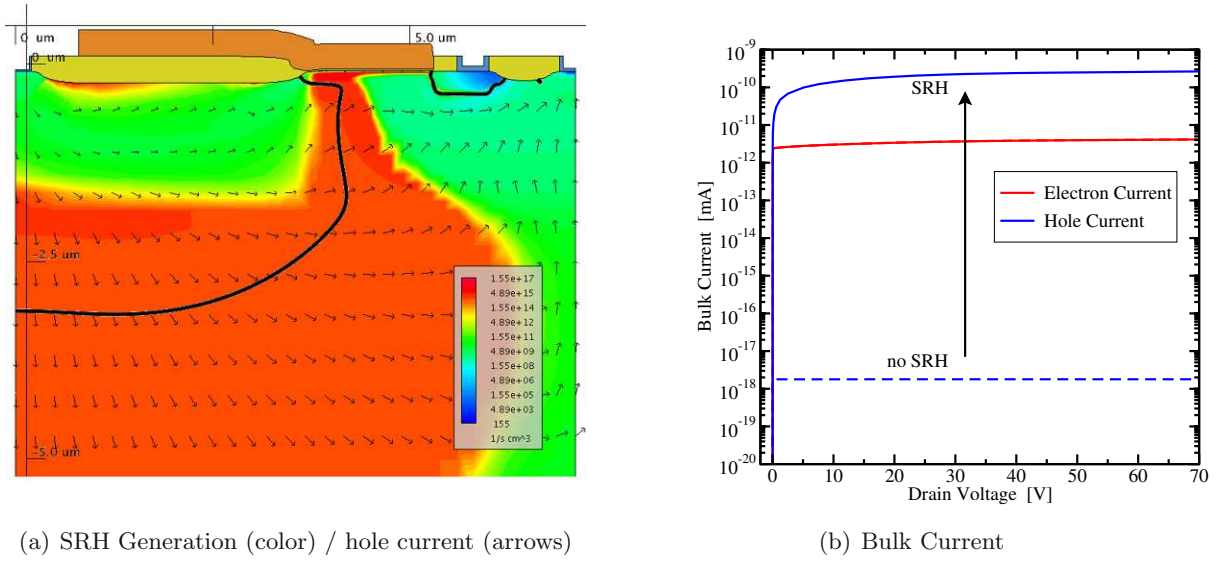


**Figure 4.6:** The SRH generation rate (a) in the sample device with a drain voltage of 50 V and a gate voltage of 2 V, the arrows show the hole current flow. Note that the bulk contact is in the upper right corner. A comparison of the bulk current (b) with and without the SRH model activated. While the electron current stays the same, the hole current increases due to the SRH generated holes in the space charge region.

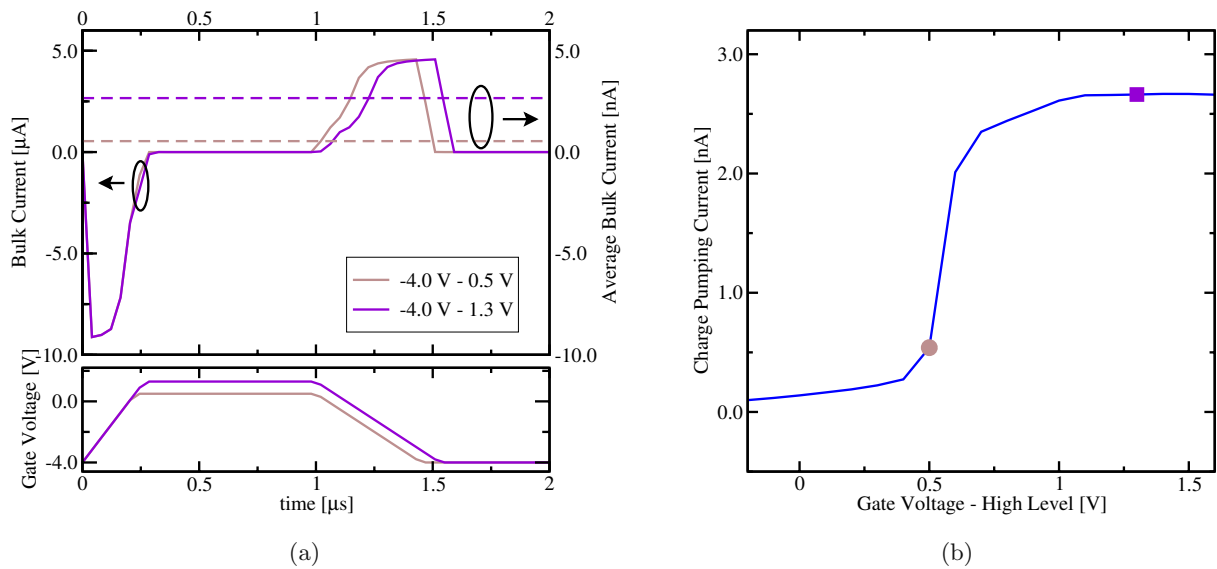


**Figure 4.7:** Charge pumping simulations: In (a) the bulk current during two different gate voltage pulses is shown. The average currents are the charge pumping currents which are transferred to the charge pumping curve in (b).

## CHAPTER 4. DEVICE SIMULATION AND PARAMETER MODELING

In addition to the two-particle SRH mechanism there are other important generation mechanisms to mention: the Auger and the impact-ionization process, both of which are three-particle processes. The impact-ionization process, a very important mechanism when considering hot-carrier processes, is discussed in detail in Chapter 5. The Auger generation is a pure generation process. The energy required for carrier generation is delivered by a third higher-energetic electron or hole. In the Auger process, additionally the excess energy which is available after a recombination process is transferred to a third particle electron or hole. Modeling of this process can be achieved by defining rates for each partial process. In the stationary case the rate evaluates to [11]

$$R^{\text{AUG}} = (nC_n^{\text{AUG}} + pC_p^{\text{AUG}})(np - n_i^2). \quad (4.16)$$

The coefficients  $C_n^{\text{AUG}}$  and  $C_p^{\text{AUG}}$  have a weak dependence on the temperature [157, 158]. However, the coefficients are often assumed to be constant.

There are various other generation and recombination mechanisms which have not been mentioned here. Among them are, just to mention a few, the direct recombination which is crucial for direct bandgap semiconductors, the direct [159] and trap assisted [160] band-to-band tunneling in high field regions, and optical generation [11].

### 4.2.3 Thermal Modeling

Many physical properties of semiconductor devices strongly depend on the lattice temperature. Especially in high-voltage and power devices, the self-heating of the device is of special importance and the temperature distribution within a device is needed to estimate the device behavior at operating conditions. Regions of special interest are associated to high-current densities. In MOSFETs, these regions are commonly at the drain end of the channel, in the drain extensions and drift zones, and at corners [161].

For the definition of a reference temperature and for the dissipation of the generated heat, the simulation domain must be connected to one or more external reference temperatures or heat sinks. This connection is modeled in terms of thermal contacts, which have assigned fixed temperatures and are connected to the simulation domain via thermal resistances. It is also important to consider that the heat flow in a semiconductor device extends to areas that are electrically less important. Hence, the simulation domain usually has to be extended in comparison to iso-thermal simulations [162]. At the simulation domain boundaries representing symmetries in the device, Dirichlet conditions are used. For a proper modeling of corner effects, a three-dimensional simulation has to be used [163, 164].

The lattice temperature distribution  $T_L$  is modeled using the heat conduction equation [127]

$$c_{\text{tot}} \frac{\partial T_L}{\partial t} = \nabla \cdot (\kappa_{\text{tot}} \nabla T_L) + H, \quad (4.17)$$

where  $c_{\text{tot}}$  is the total heat capacity and  $\kappa_{\text{tot}}$  the total thermal conductivity. Both parameters include contributions from the lattice, the electron, and the hole subsystem. The temperature

## 4.2. PARAMETER MODELING

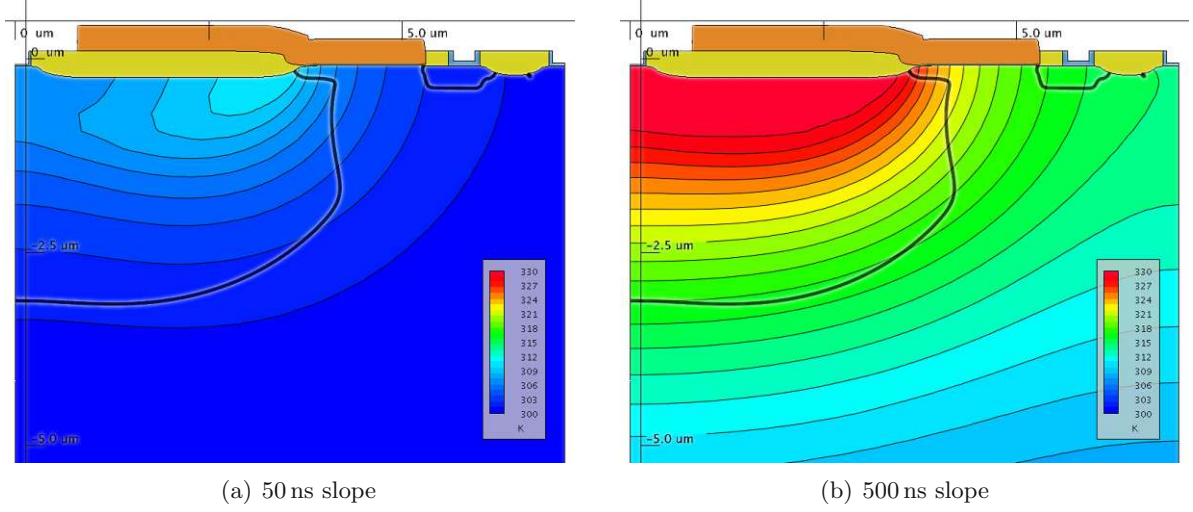


**Figure 4.8:** Temperature distribution in the sample device with the gate biased to 2 V at the end of a linearly increase of the drain voltage from 0 to 50 V in 50 ns (a) and 500 ns (b).

differences in the lattice lead to an additional driving force on the carriers which is already considered in the last terms in the current equations (4.7) and (4.8).

Different approaches of modeling the heat generation rate  $H$  have been proposed. The most simple approach considers only the Joule heat  $\mathbf{J} \cdot \mathbf{E}$  [165]. A more accurate model according to Adler [166] describes the generated heat using

$$H = \mathbf{J}_n \cdot \nabla \frac{E_c}{q} + \mathbf{J}_p \cdot \nabla \frac{E_v}{q} + R(E_c - E_v). \quad (4.18)$$

Here, the energy dissipation due to recombination is considered. A more rigorous treatment to thermal generation is given by Wachutka [127].

Transient simulations including thermal modeling were performed using the sample device. The lower bulk contact is linked with a thermal resistance to the ambient temperature of 300 K. In this simulation, the drain voltage is raised linearly from 0 V to 50 V using two different slopes. The temperature distributions at the end of the two voltage ramps are depicted in Fig. 4.8. At the end of the 50 ns slope a rapid increase of the temperature near the birds beak can be observed.

### 4.2.4 Additional Physical Effects

In addition to the physical mechanisms addressed so far, there are many other relevant modeling issues for semiconductor devices. For most of them, well established approaches are available in TCAD device simulation environments. The simulation tools typically incorporate models

for the bandgap energy and for bandgap narrowing [167]. At low temperatures, incomplete ionization becomes important [168]. Also, semiconductor-metal contacts require appropriate treatment. The most common contact models are the well-known ohmic contact model, where charge neutrality and equilibrium are assumed at the electrodes [11], and the Schottky contact model [32].

Especially in highly down-scaled MOS devices, tunneling and quantum effects have to be considered. For direct tunneling typically the Tsu-Esaki [169] or the Fowler-Nordheim [170] models are used. Herrmann and Schenk [171] proposed models for trap assisted tunneling, which has also been extended to multi-trap assisted tunneling models [172], especially interesting for highly degraded devices.

The inclusion of quantum confinement effects becomes especially important in modern devices [173] like silicon-on-insulator (SOI) structures, double-gate or FinFET devices. One modeling proposal is the modified local density approach [174] which is used in the model of Hänsch [175]. Here, a local correction of the effective density of states near the gate oxide is used to contribute to the quantum effects. An empirical correction approach has been presented by Van Dort *et al.* [176] which models the quantum confinement by increasing the band-gap near the interface.

### 4.3 Carrier Energy Distribution Function

The carrier energy distribution function gives important information on the state of carriers in semiconductor devices. The detailed knowledge of the distribution allows an accurate estimation of the carrier mobility, the impact-ionization rates, and of other carrier energy dependent issues. As already pointed out earlier in this chapter, the carrier distribution function is described by the semi-classical BTE [15, 123].

The average carrier energy, commonly expressed through the carrier temperature, is available in energy-transport/hydrodynamic transport models [131, 132]. The carrier temperature is solved as an independent quantity, where the heated Maxwellian distribution function is used for the formulation of the closure relation.

#### 4.3.1 Carrier Temperature Estimation in the Drift-Diffusion Model

In the drift-diffusion framework the distribution function is assumed to be a cold Maxwellian distribution and the carriers are per definition in thermal equilibrium, meaning that the carrier temperature ( $T_\nu$ ) equals the lattice temperature ( $T_L$ ). There is no information on the distribution function available. However, to estimate the carrier temperature  $T_\nu$ , the local energy balance equation in the stationary, homogenous case in bulk is often used. With  $\nu = n$  for electrons and  $\nu = p$  for holes, the estimation reads [15, 177]

$$T_\nu = T_L + \frac{2}{3} \frac{q}{k_B} \tau_{\mathcal{E},\nu} \mu_\nu \mathbf{E}^2. \quad (4.19)$$

### 4.3. CARRIER ENERGY DISTRIBUTION FUNCTION

$\tau_{\mathcal{E},\nu}$  represents the energy relaxation time for the carrier type  $\nu$ . In the derivation of (4.19) it was assumed that the carrier transport is field dominated and the velocity  $\mathbf{v}_\nu$  was modeled considering only the drift component

$$\mathbf{v}_\nu = s_\nu \mu_\nu \mathbf{E}. \quad (4.20)$$

$s_\nu$  is  $-1$  for electrons and  $+1$  for holes and the mobility can be estimated using a high-field mobility model as described in Section 4.2.1. The energy relaxation time is often assumed to be constant, with typical values  $\tau_{\mathcal{E},n} = 0.35$  ps [177] and  $\tau_{\mathcal{E},p} = 0.4$  ps [178]. However, in this work the energy relaxation time has also been used as a fitting parameter. Putting all this together (4.19) can be used to estimate the mean carrier temperature in the drift-diffusion model. A comparison of those calculations with data from homogenous Monte Carlo simulations is shown in the figures on the following page. For fields of up to 600 kV/cm, good results are obtained.

It is possible to perform further simplifications on (4.19): For moderate fields, the mobility can be assumed as constant, which leads to  $T_\nu \propto E^2$ . For increasing fields the carrier velocity approaches the saturation velocity  $v_\nu^{\text{sat}}$  and the mobility can be estimated as

$$\mu_\nu = \frac{v_\nu^{\text{sat}}}{E}. \quad (4.21)$$

Using this relation, the carrier temperature for high fields gives [177]

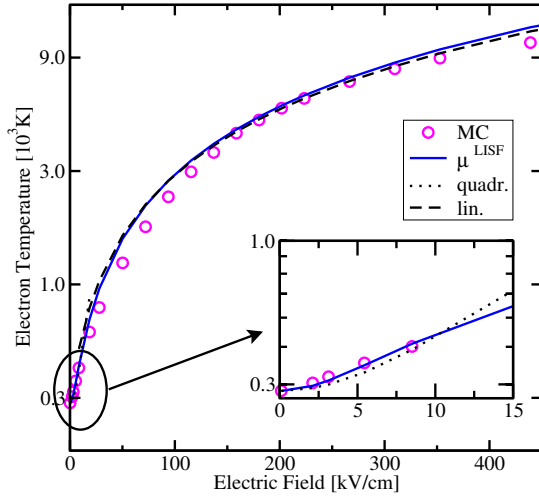
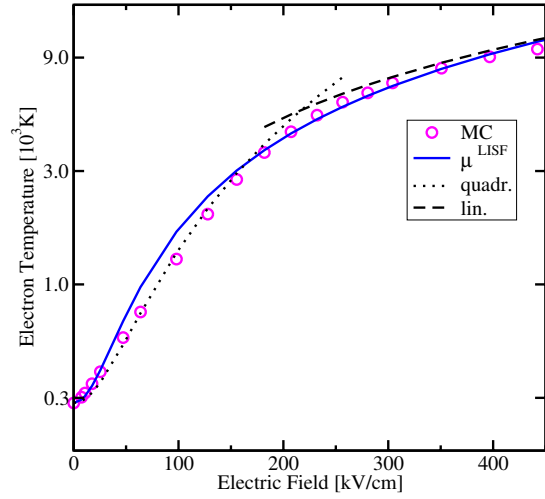
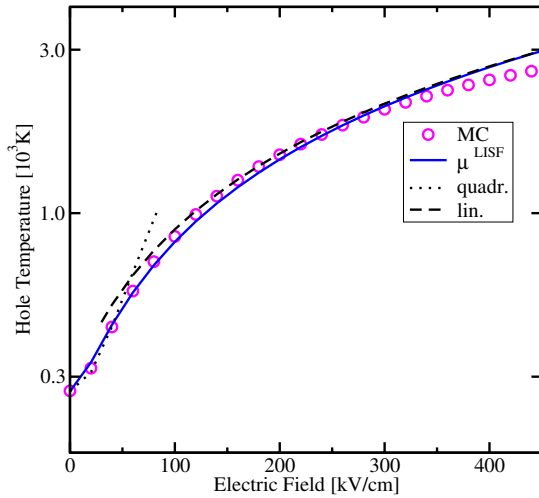
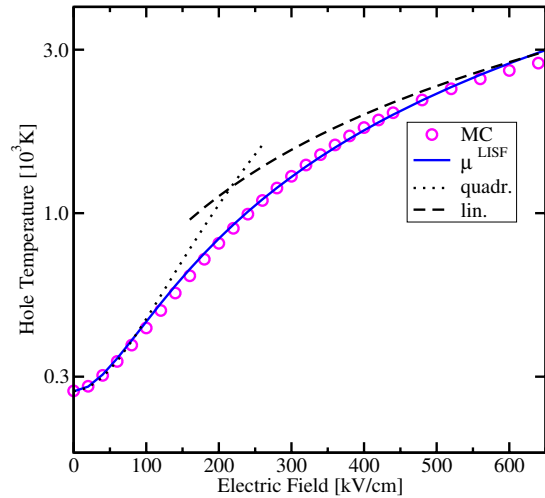
$$T_\nu = T_L + \frac{2}{3} \frac{q}{k_B} \tau_{\mathcal{E},\nu} v_\nu^{\text{sat}} E \quad (4.22)$$

meaning that for high fields, the proportionality between the carrier temperature and the electric field becomes approximately linear. This estimation has also been introduced in Fig. 4.9. It can be seen, that the carrier temperature estimation using the two equations (4.19) and (4.22) with constant mobility, constant energy relaxation time, and constant saturation velocity give reasonable results for electric fields of up to  $> 400$  kV/cm. For even higher fields the energy relaxation decreases due to optical phonon scattering which has to be considered for reasonable results.

In two- or three-dimensional simulations, one has to consider that the perpendicular component of the electric field on the current flow has no impact on the carrier energy. The electric field in (4.19) is therefore often replaced by the electric field projected in the direction of the current density,  $\mathbf{E} \rightarrow \mathbf{E} \cdot \mathbf{J}/J$ . In Fig. 4.10 this method is applied on a simple planar MOS transistor and compared to results from a hydrodynamic simulation. A more detailed comparison with Monte Carlo data along the channel of an  $0.5 \mu\text{m}$  n-MOS device is shown in Fig. 4.11.

In Fig. 4.9 one can see, that the carrier temperature already doubles at electric fields which are in the order of 10 kV/cm. Considering that fields in devices can reach up to 1 MV/cm, it is clear that the deviation from the assumption of equal carrier and lattice temperature has to be taken into account for hot-carrier reliability considerations as will be discussed in Chapter 6.

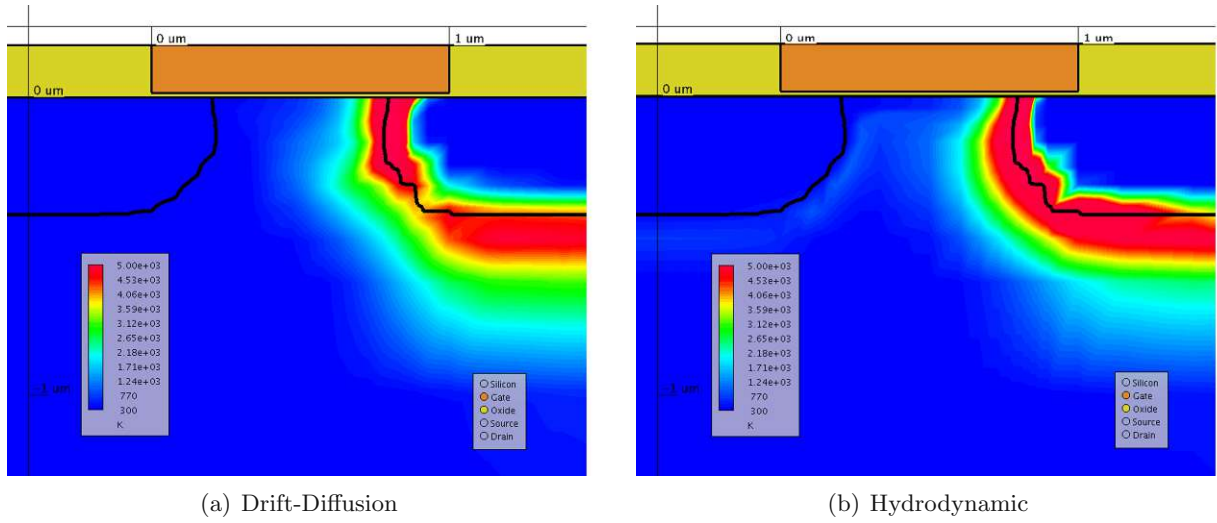



 (a) Electron Temperature,  $N_D = 10^{16}$ 

 (b) Electron Temperature,  $N_D = 10^{20}$ 

 (c) Hole Temperature,  $N_A = 10^{16}$ 

 (d) Hole Temperature,  $N_A = 10^{20}$ 

**Figure 4.9:** Carrier temperature dependence on the electric field for different doping concentrations. The temperature is modeled using the approximation (4.19) including the  $\mu^{\text{LISF}}$ -mobility model from (4.14). The quadratic and linear approximations using constant mobility are also shown. Monte Carlo data is used as the reference.



### 4.3. CARRIER ENERGY DISTRIBUTION FUNCTION



**Figure 4.10:** The electron temperature distribution in a planar n-MOS transistor with a channel length of  $1\ \mu\text{m}$ . The Drain is set to  $4\text{ V}$ , the Gate to  $1.2\text{ V}$ , the Source and Bulk contacts are grounded. Since the device is rather large the non-local effects are not very pronounced and a reasonable result can be obtained using the drift-diffusion simulation, although the differences are evident.

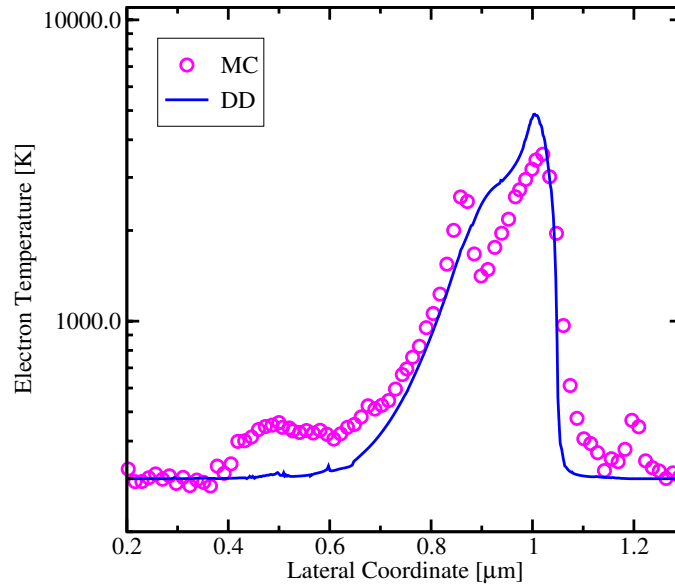


**Figure 4.11:** Monte Carlo and drift-diffusion simulation results of the electron temperature along the channel of an n-MOS transistor (see Fig. 6.5 on page 90) at a gate voltage of  $V_{GS} = 2.0\text{ V}$  and a drain voltage of  $V_{DS} = 6.25\text{ V}$ .

## Non-Local Estimations

Sofar only the local electric field was used to model the carrier temperature. However, carriers do not gain or loose the energy as fast as the electric field changes. This non-local behavior is especially relevant for rapidly changing electric fields (see Fig. 4.5 on page 41). The electric field is the only quantity in drift-diffusion simulations that can be used to estimate the carrier temperature. Approaches have been suggested to estimate this non-local behavior using the electric field. In the approach by Slotboom *et al.* [179], the temperature along a one-dimensional path is derived from a simplified, stationary one-dimensional energy balance equation, which reads

$$T_\nu(x) = T_L + \frac{2}{5} \frac{q}{k_B} \int_0^x E(u) \exp\left(\frac{u-x}{\lambda_e}\right) du. \quad (4.23)$$

The energy relaxation length  $\lambda_e$  is given by  $\lambda_e = \frac{5}{3} v \tau_e$  and is assumed to be constant. Experimental estimates of  $\lambda_e$  are given in [179]. To solve this estimation in a two-dimensional device, drift-diffusion simulation results are used to extract current paths through the device and integration has to be performed along those paths. Even though good results have been found, a self consistent implementation for two- or three-dimensional device simulation has not been reported.

### 4.3.2 Distribution Function Approximations

The real distribution function in a MOS transistor in a down-scaled technology node under operation conditions varies strongly along the channel and commonly differs from the Maxwellian shape. Targeting on hot-carrier reliability considerations, especially the high-energy tail which describes the hot-carrier population is of major importance. This section examines only the electron distributions and the approximations are based on the electron temperature, although the shape of the distribution function can vary strongly for the same temperatures (compare Fig. 4.2 on page 37). It is also important to consider that a change in the hot-electron population of an order of a magnitude usually hardly changes the mean temperature of the total electron population but strongly influences hot-carrier effects like the impact-ionization rate (see Chapter 6). The hot-electron tail is not captured at all in the cold Maxwellian distribution,

$$f(\mathcal{E}) = A \exp\left(-\frac{\mathcal{E}}{k_B T_L}\right), \quad (4.24)$$

and commonly dramatically overestimated in the heated Maxwellian distribution

$$f(\mathcal{E}) = A \exp\left(-\frac{\mathcal{E}}{k_B T_n}\right), \quad (4.25)$$

as can be seen in the figures on the next page.

### 4.3. CARRIER ENERGY DISTRIBUTION FUNCTION

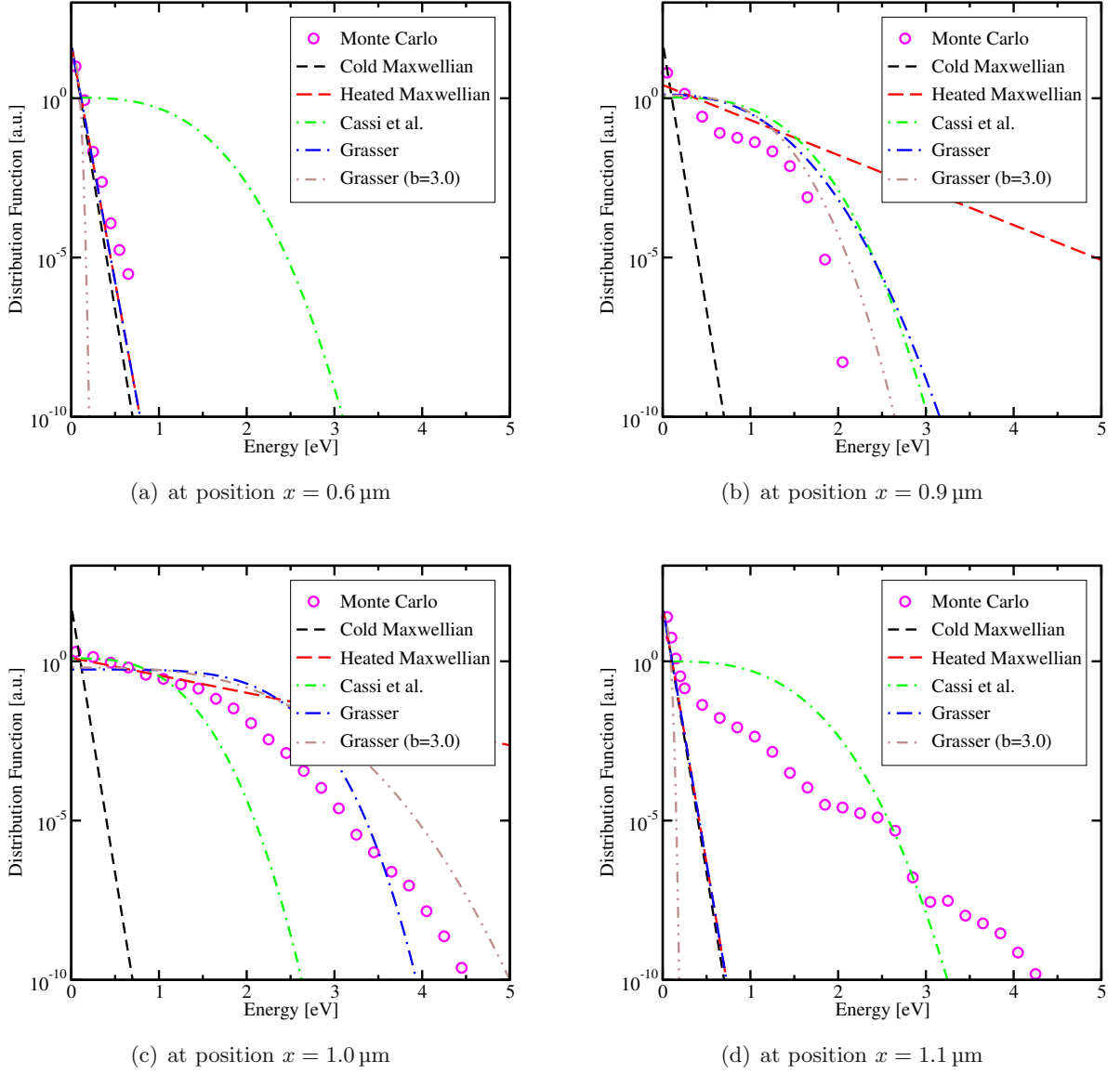


**Figure 4.12:** Normalized approximations of the electron distribution functions are compared to Monte Carlo results. The calculation was performed at different positions at the interface using the n-MOS device from Fig. 6.5 on page 90. The electron temperatures correspond to the values in Fig. 4.11.

## CHAPTER 4. DEVICE SIMULATION AND PARAMETER MODELING

A better approach to represent the high energy part of the distribution function was proposed by Cassi and Ricò as [180]

$$f(\mathcal{E}) = A \exp \left( -\chi \frac{\mathcal{E}^3}{T_n^{1.5}} \right), \quad (4.26)$$

with  $A$  and  $\chi$  being constant parameters. This distribution gives especially for high fields, where drift dominates over diffusion, a much better agreement to Monte Carlo results than the cold or heated Maxwellian distributions. However, the inflexible shape of the function totally fails in regions of thermodynamic equilibrium as shown in Fig. 4.12(a). This method was further extended by Concannon *et al.* [181] to explicitly represent the high energy tail:

$$f(\mathcal{E}) = A \left[ \exp \left( -\frac{\chi_a \mathcal{E}^3}{T_n^{1.5}} \right) + C_0 \exp \left( -\frac{\chi_b \mathcal{E}^3}{T_n^{1.5}} \right) \right]. \quad (4.27)$$

$A$ ,  $C_0$ ,  $\chi_a$ , and  $\chi_b$  are constant fit values. This approach was used in particular to model impact-ionization and it was reported that simulated terminal currents in MOSFET devices showed good agreements with measurement data.

Another approach was given by Grasser *et al.* [182] who proposed to use the electron distribution function

$$f(\mathcal{E}) = A \exp \left[ -\left( \frac{\mathcal{E}}{\mathcal{E}_{\text{ref}}} \right)^b \right]. \quad (4.28)$$

$\mathcal{E}_{\text{ref}}$  and  $b$  depend on the local electron temperature and the kurtosis. Using an estimation for the kurtosis and assuming a parabolic band structure,  $\mathcal{E}_{\text{ref}}$  can be evaluated as

$$\mathcal{E}_{\text{ref}} = k_B T_n \frac{3}{2} \frac{\Gamma \left( \frac{3}{2b} \right)}{\Gamma \left( \frac{5}{2b} \right)}, \quad (4.29)$$

where the Gamma function is

$$\Gamma(x) = \int_0^{\infty} \exp(-\alpha) \alpha^{x-1} d\alpha. \quad (4.30)$$

The parameter  $b$  can be expressed using the polynomial approximation [183]

$$b(T_n) = 1 + b_0 \left( 1 - \frac{T_L}{T_n} \right)^{b_1} + b_2 \left( 1 - \frac{T_L}{T_n} \right)^{b_3}, \quad (4.31)$$

using the constants  $b_0 = 38.82$ ,  $b_1 = 101.11$ ,  $b_2 = 3.40$ , and  $b_3 = 12.93$ . In Fig. 4.12 this approach is shown beside the other approximations presented here.

A special variation of the last representation has been used in the attempt to simulate hot-carrier degradation in the drift-diffusion framework as described in Section 6.4.1 on page 96. Here the exponent  $b$  in (4.28) has been empirically set to 3.0 and  $\mathcal{E}_{\text{ref}}$  has still been evaluated using (4.29).

### 4.3. CARRIER ENERGY DISTRIBUTION FUNCTION

As described in the referred section, this approximation delivers in the given sample the best agreement to the Monte Carlo results.

Comparing the different approximations, one has to distinguish the specific conditions along the MOS channel area. At the position  $0.6\text{ }\mu\text{m}$  (Fig. 4.12(a)) the carriers have not been accelerated yet and are in thermodynamic equilibrium. As can be seen in Fig. 4.11, the electron temperature of the drift-diffusion solution matches the lattice temperature at  $T_n = T_L = 300\text{K}$ . Only the distribution function model by Cassi cannot reproduce the result due to the fixed parameters in (4.26). At  $0.9\text{ }\mu\text{m}$  (Fig. 4.12(b)) and  $1.0\text{ }\mu\text{m}$  (Fig. 4.12(c)) it is obvious, that the cold Maxwellian distribution does not reproduce the electron distribution at all and the heated Maxwellian distribution only approximates the Monte Carlo results at low energies. Any conclusion on high energy processes would clearly lead to overestimations. The approaches by Cassi and Grassser at least catch the trend of the Monte Carlo results. In this example, the Grassser approach also captures the trend of the growing high energy tail at  $1.0\text{ }\mu\text{m}$ . This is true for a constant and a calculated  $b$  value. Finally, at the position  $1.1\text{ }\mu\text{m}$  (Fig. 4.12(d)) the shortcoming of the drift-diffusion equations becomes very clear. The field and therefore the electron temperature has already dropped, but there exists a high energy population of carriers, which still can strongly influence high energy processes. The distribution by Cassi does not catch this tendency, the other distributions match the cold Maxwellian. This last condition, which is already in the highly doped drain area of this transistor, cannot be described at all using the drift-diffusion framework.

#### Advanced Modeling

All estimates of the distribution function which are solely based on the electric field and/or the mean carrier temperature, can only lead to good results in special applications. One approach to overcome this is to handle two different carrier populations, one for hot and one for cold carriers [184]. For this, transport equations have to be solved for both populations and rate equations for carrier interchange between both populations.

The probably best macroscopic approach to capture the high-energy tail correctly all over the device is to apply higher order moment transport equations with at least six moments [134] of the BTE. In the six moments model additionally to the mean carrier temperatures  $T_\nu$  the kurtosis  $\beta_\nu$  is available which quantifies the deviation of the distribution function from the Maxwellian shape. Grassser *et al.* [134] made the following proposal, similar to the one from Sonoda *et al.* [185],

$$f(\mathcal{E}) = A \left\{ \exp \left[ - \left( \frac{\mathcal{E}}{k_B T_{\text{ref}}} \right)^b \right] + c \exp \left[ - \frac{\mathcal{E}}{k_B T_2} \right] \right\}, \quad (4.32)$$

describing the hot and cold populations independently. The parameters  $A$ ,  $T_{\text{ref}}$ ,  $b$ ,  $c$  and  $T_2$  can be calculated so that the even moments of the distribution function fit the six moments model [186]. An example on the good results are shown in Fig. 4.13 [187].

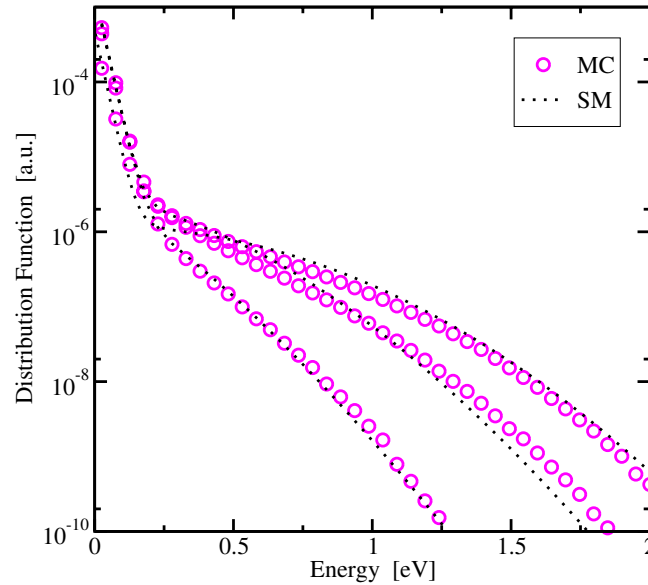


**Figure 4.13:** The Monte Carlo calculated electron distribution function at different positions in an n-MOS transistor with a channel length of 200 nm is compared to the analytical estimation from (4.32) (results taken from [187]). The distinct derivation from the Maxwellian distribution can be clearly seen.

## 4.4 Summary

Numerical device simulation using TCAD software with focus on the drift-diffusion framework has been presented in this chapter. The collection of models show that good simulation results can be obtained for characteristic lengths above 200 nm. Beside the commonly used parameter models for mobility and for generation/recombination, electron temperature and distribution function estimations have been discussed, which is of crucial importance for hot-carrier modeling.

## Chapter 5

# Impact-Ionization Generation

This chapter discusses impact-ionization generation and its influence on the device behavior. Modeling techniques for the impact-ionization rate are presented, which are based on the local field, the local energy, and the carrier energy distribution function. The chapter ends with a case study on the snap-back behavior in a smart power device.

### 5.1 Basics of Impact-Ionization

Impact-ionization is a three-particle generation process. Carriers that gain high energies while traveling through high field regions undergo scattering events with bonded electrons in the valence band. The excess energy is transferred to this electron which is lifted into the conduction band creating a new electron-hole pair. This secondary electron-hole pair can also have a rather high energy. In this case the avalanche effect is triggered and the carrier density increases heavily. This effect is sketched for pure electron induced generation in Fig. 5.1.

The device behavior is heavily affected by impact-ionization. In MOS devices, the peak of generation is commonly observed in the channel near the drain area. The minority carriers contribute to the drain current, while the majority carriers are attracted and collected by the bulk electrode. A common measure for the occurrence of impact-ionization in MOS devices is, therefore, the bulk current. For reverse-biased pn-junctions, for example, the avalanche breakdown usually defines the maximum blocking voltage. To overcome this, doping profiles are specially graded to decrease the maximum fields for a given voltage. Unfortunately, this often has a detrimental impact on the forward behavior. Therefore, application specific trade offs between forward and reverse behaviors have to be found (see also Section 2.2.2). Moreover, also forward biased pn-junctions suffer due to impact-ionization. The additionally generated carriers increase the forward currents in transistors. In the worst-case, gate- (or base-control) can be lost. Increasing currents lead to massively growing heat generation and can finally lead to device failure. Especially bipolar transistors are vulnerable due to the positive temperature coefficient. Another effect which has to be considered in the device design are majority carrier

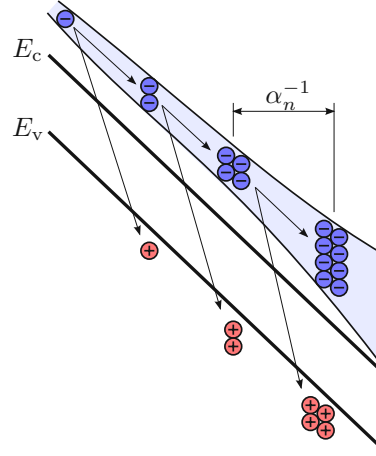


**Figure 5.1:** Symbolized process of a pure electron induced impact-ionization avalanche generation. After an electron is accelerated along an average distance  $\alpha_n^{-1}$  it undergoes a collision and the excess energy produces a new electron-hole pair. Consecutive collisions can trigger an avalanche.

current flows initiated by strong generation which can trigger parasitic devices, thereby leading to unexpected device behavior. Since impact-ionization has such a strong influence on the device behavior, it is compulsory to include proper models into device simulation tools.

### 5.1.1 Ionization Rate

In the drift-diffusion model, the impact-ionization rate is usually expressed using the impact-ionization coefficients  $\alpha_n$  and  $\alpha_p$ . These two coefficients describe the number of electron-hole pairs generated per unit distance traveled [32] by a solitary carrier between two collisions. Considering only electrons generated by electrons, one can write

$$\alpha_n = \frac{1}{n} \frac{dn}{d(tv_n)} = \frac{1}{nv_n} \frac{dn}{dt}. \quad (5.1)$$

Here  $v_n$  is the electron velocity and  $dn/d(tv_n)$  therefore describes the generated carriers per distance.  $n$  is the electron concentration and  $dn/dt$  the electron generation rate. Accounting also for the generated holes and for the holes that contribute to the impact-ionization multiplication, the generation rate can be written as

$$G^{\text{II}} = \frac{dn}{dt} = \frac{dp}{dt} = \alpha_n nv_n + \alpha_p pv_p \quad (5.2)$$

$$= \alpha_n \frac{J_n}{q} + \alpha_p \frac{J_p}{q}. \quad (5.3)$$

The coefficients  $\alpha_n$  and  $\alpha_p$  in bulk silicon, as shown in Fig. 5.2, are strongly field dependent. A typical model is



## 5.1. BASICS OF IMPACT-IONIZATION

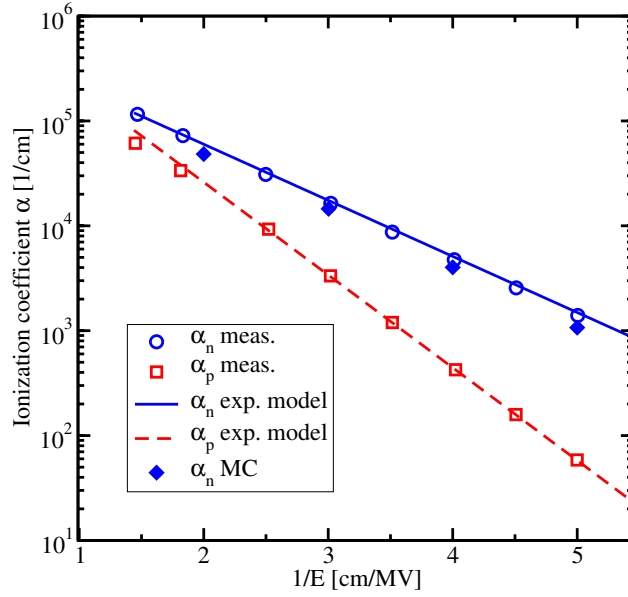


**Figure 5.2:** Comparison of measurement data with the exponential modeling approach (5.4) and with Monte Carlo simulation results [188] of the impact-ionization coefficients over the reciprocal electric field for electrons ( $\alpha_n$ ) and holes ( $\alpha_p$ ) in bulk silicon. The measurements are originally from [189] and were taken from [190].

$$\alpha_\nu \propto \exp\left(-\frac{E_\nu^{\text{crit}}}{E}\right). \quad (5.4)$$

A discussion on modeling of the impact-ionization coefficients in device simulation tools will be given in Section 5.2.

### 5.1.2 Ionization Integral

To describe the impact-ionization caused avalanche breakdown, for example, in reverse-biased junctions, a macroscopic formalism called *ionization integral* is introduced. This quantity is based on the impact-ionization coefficients. It considers carriers which enter the depletion region and are then accelerated by the electric field. The carriers gain enough energy to generate new electron-hole pairs by impact-ionization. If these newly generated carriers have high enough energy they can launch a secondary branch of impact-ionization. Therefore, the entire process can be cascaded, leading to avalanche carrier multiplication. This results in high currents and eventually leads to breakdown.

For a one-dimensional consideration, a depletion region with width  $W$  is assumed. An initial hole current density at the position of  $x = 0$ ,  $J_p(0) = J_{p0}$ , is considered to trigger the avalanche. The density  $J_p(x)$  steadily increases throughout the depletion region due to the holes generated by impact-ionization as shown in Fig. 5.3(a). The simultaneously generated electrons are accel-

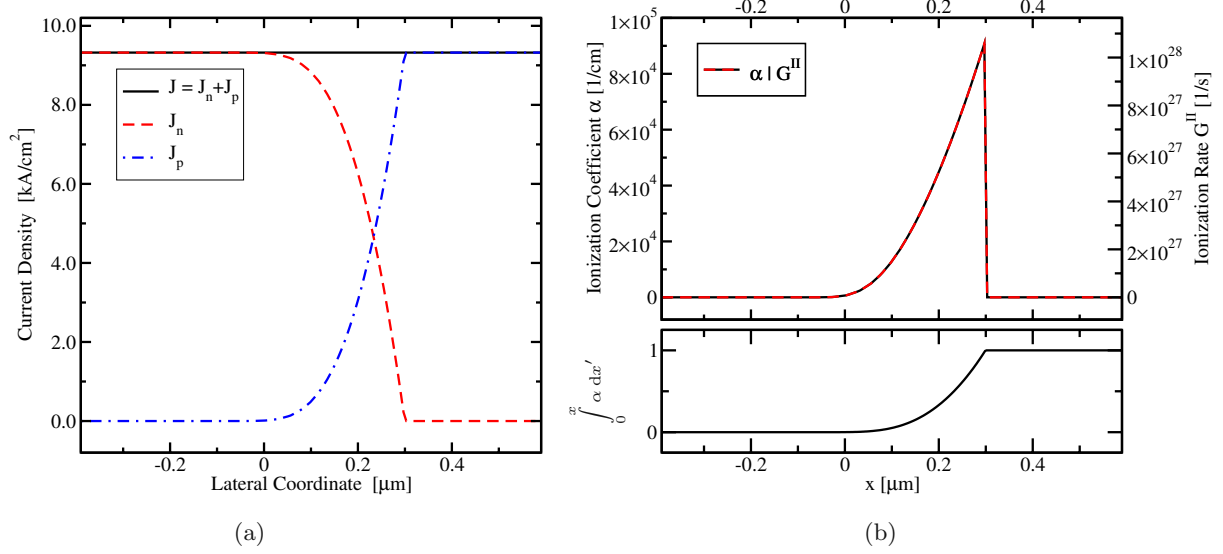


**Figure 5.3:** Electron and hole current densities (a) and ionization coefficient, rate, and ionization integral (b) in a one dimensional simulation of a reverse-biased diode operated at breakdown. The abrupt pn-junction at the position  $x = 0.3 \mu\text{m}$  is n-doped ( $10^{19} \text{ cm}^{-3}$ ) in the right and p-doped ( $10^{17} \text{ cm}^{-3}$ ) in the left side. The ionization coefficients are set equal ( $\alpha = \alpha_n = \alpha_p$ ). Equal coefficients and constant total current lead to the overlapping shape of the ionization coefficient  $\alpha$  and ionization rate  $G^{II}$ . The ionization integral (5.12) at the bottom of (b) equals 1 at the end of the depletion zone.

erated in the opposite direction resulting in an electron current density  $J_n$ . In steady-state, the total current density  $J$ , defined as

$$J = J_n + J_p, \quad (5.5)$$

must be constant along the device. At the end of the depletion region, i.e. at  $x = W$ , the hole current reaches its maximum which is described by applying the multiplication factor  $M_p$  as

$$J_p(W) = J_{p0} M_p = J. \quad (5.6)$$

Using (5.3) and  $v = dx/dt$  the change of the  $J_p$  passing through the depletion region is evaluated as

$$dJ_p = J_p \alpha_p dx + J_n \alpha_n dx. \quad (5.7)$$

Together with (5.5) one reformulates to

$$\frac{dJ_p}{dx} - (\alpha_p - \alpha_n) J_p = \alpha_n J. \quad (5.8)$$

## 5.2. MODELING APPROACHES

Applying the stated boundary conditions, this differential equation can be solved, as shown in Appendix A, to yield

$$J_p(x) = J \exp \left( \int_0^x (\alpha_p - \alpha_n) dx \right) \left[ \int_0^x \alpha_n \exp \left( - \int_0^x (\alpha_p - \alpha_n) dx' \right) dx + \frac{1}{M_p} \right]. \quad (5.9)$$

At the position  $x = W$ , the hole current density becomes  $J_p(W) = J$  and (5.9) evaluates to (see Appendix A)

$$1 - \frac{1}{M_p} = \int_0^W \alpha_p \exp \left( - \int_0^x (\alpha_p - \alpha_n) dx' \right) dx. \quad (5.10)$$

The avalanche breakdown sets in if the multiplication factor  $M_p$  approaches infinity. The relation between depletion region width and the ionization coefficients at breakdown therefore reads

$$1 = \int_0^W \alpha_p \exp \left( - \int_0^x (\alpha_p - \alpha_n) dx' \right) dx. \quad (5.11)$$

The derivation for an initial electron current instead of an initial hole current leads to an equivalent result [32] and it therefore does not make a difference which carrier type triggers the avalanche breakdown. In the case shown in Fig. 5.3(b) the ionization coefficients  $\alpha_n$  and  $\alpha_p$  have been set equal to  $\alpha = \alpha_n = \alpha_p$  and the ionization integral now reads

$$1 = \int_0^W \alpha dx. \quad (5.12)$$

Using the ionization integral the correlation between the width ( $W$ ) of the depletion region and the ionization coefficients  $\alpha_n$  and  $\alpha_p$  can be derived at least for simplified structures and coefficient models. The current density is not required for modeling of the breakdown condition. Hence, for evaluation of the breakdown voltage one may solve the simplified Poisson equation by assuming constant quasi-Fermi levels in the depletion region.

Obtaining the numerical solution using this approach saves a lot of computational power. However, due to severe simplifications required to compute this integral, this method is not relevant for real devices. An important application field of the ionization integral is the measurement of the ionization rate. The latter quantity is not achievable in direct measurements, and thus the ionization integral can be used to conclude on the ionization rate using breakdown conditions.

## 5.2 Modeling Approaches

Only carriers with high energies contribute to the avalanche process. Like all high-energy mechanisms, impact-ionization is a non-local process (compare Section 4.3.1). This leads to problems

## CHAPTER 5. IMPACT-IONIZATION GENERATION

in classical drift-diffusion simulation environments, because only local quantities are available, while no exact information on the distribution function can be obtained. Also hydrodynamic simulations deliver only the mean energy. Thus, the information on high-energy tails of the carrier distribution function is not available (see Section 4.3.2). As a result, drift-diffusion and/or hydrodynamic schemes require modeling approaches which are only based on local quantities.

### 5.2.1 Local Electric Field Based Modeling

In drift-diffusion simulations, the only local quantity that allows conclusions on the carrier temperature and therefore on the impact-ionization rate is the electric field. Many authors who investigated the ionization coefficients, both, experimentally and theoretically, suggested an exponential relation to the electric field  $E$  as [11]

$$\alpha_\nu = \alpha_\nu^\infty \exp \left[ - \left( \frac{E_\nu^{\text{crit}}}{E} \right)^{\beta_\nu} \right], \quad (5.13)$$

where the index  $\nu$  stands for electrons  $n$  and holes  $p$ .  $\alpha_\nu^\infty$  and  $E_\nu^{\text{crit}}$  are the high-field value of the ionization rate and the reference field, respectively. Although these quantities have certain physical meanings, commonly they are used as fitting parameters. This equation originates from the classic paper by Chynoweth [191], where the power  $\beta_\nu$  was assumed to be 1. In different modeling and experimental works, however, values of this exponent are found between 1 (Chynoweth [191] or Shockley [192]) and 2 (Wolff [193]). An important extension of this model was made including the electric field  $\mathbf{E}$  in the direction of the carrier flow, i.e. the current density  $\mathbf{J}$ . Therefore, the absolute value of the electric field  $E$  is often replaced by  $E = E_{\parallel} = \mathbf{E} \cdot \mathbf{J}_\nu / J_\nu$  [120, 194].

An early approach deriving the value of the parameter  $\beta_\nu$  from the BTE was performed by Baraff [195]. He showed that the different values 1 and 2 used for  $\beta_\nu$  are the limiting cases for relatively low and high fields. However, there is no closed solution of his approach, but approximations have been presented in various publications, for example, by Crowell *et al.* [196],

$$\alpha_\nu = \frac{1}{\lambda_\nu} \exp [C_0(r) + C_1(r)x(E) + C_2(r)x(E)^2]. \quad (5.14)$$

In this formalism,  $r$  is the ratio between the average energy loss per collision  $\mathcal{E}_r$  and the ionization energy  $\mathcal{E}_i$ ,  $r = \mathcal{E}_r / \mathcal{E}_i$ , and  $x$  incorporates the mean free path  $\lambda$  between collisions with high energetic phonons and is defined as  $x(E) = \mathcal{E}_i / q\lambda E$ . The coefficients  $C_i(r)$  are fitted to second order polynomial functions. This approximation fits the theoretical data from Baraff over a wide range of voltages. An improved approximation has been given by Sutherland [197] using additionally a third order term of  $x$  in (5.14) and for the coefficients  $C_i(r)$ .

Another local-field model was presented by Lackner [198], who derived an expression which leads to an extension of Chynoweth's law ,

$$\alpha_\nu = \frac{a_\nu}{z} \exp \left( - \frac{b_\nu}{E} \right), \quad (5.15)$$

## 5.2. MODELING APPROACHES

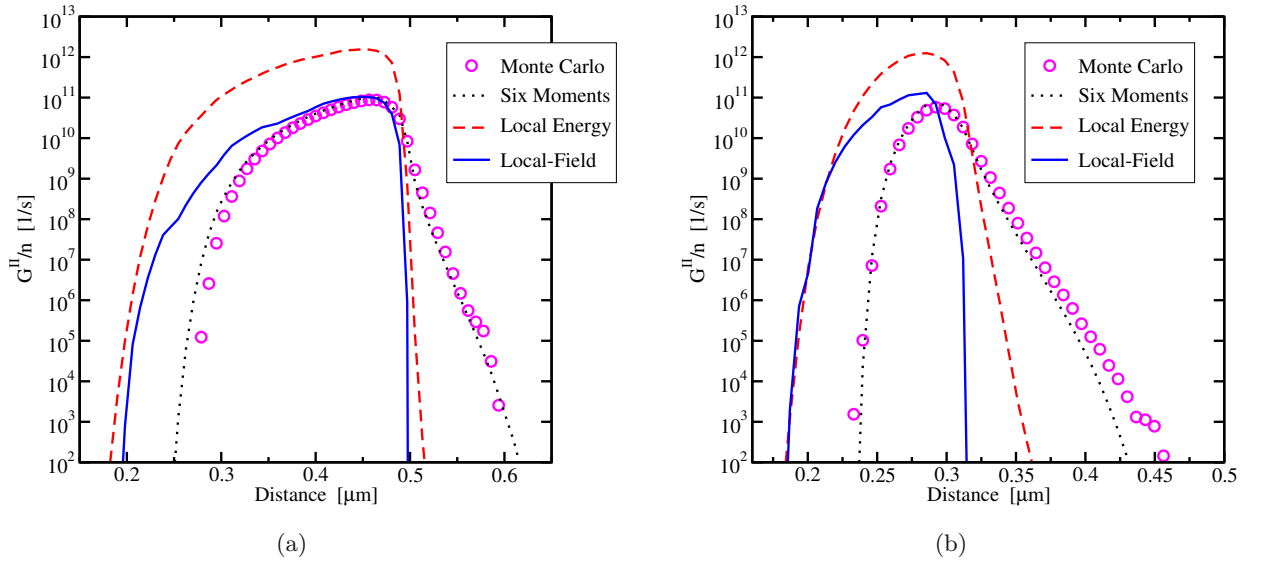


**Figure 5.4:** Impact-ionization rates in two comparable  $n^+$ - $n$ - $n^+$  structures with a channel length of 200 nm (a) and 50 nm (b) (data from [186]). The local-field approach is calculated using Chynoweth’s law (5.13) and the local energy approach using (5.19). The lateral shift of both approximations in comparison to the Monte Carlo can be seen. The smaller device, the more severe this gets. Also the typical overestimation using the local energy can be observed. The six moments method can reproduce the Monte Carlo data very well.

including the field correction term

$$z = 1 + \frac{b_n}{E} \exp\left(-\frac{b_n}{E}\right) + \frac{b_p}{E} \exp\left(-\frac{b_p}{E}\right). \quad (5.16)$$

The parameters  $a_\nu$  and  $b_\nu$  are described using the mean free carrier paths and the critical threshold energy which are not solely fitting parameters.

Slotboom *et al.* [199] have observed lower impact ionization rates for currents near the surface. As a consequence, models describing the transition between surface and bulk impact ionization have been developed [200]. However, Monte Carlo simulations have shown that there are no or only minor differences between surface and bulk impact ionization rates [201]. This means that there is no physical evidence of different rates near the surface and that those models are based on artifacts resulting from the approximate ionization rates based on the electric field.

In many applications, local-field based models deliver good results. However, from the physical point of view, impact-ionization is not field dependent. This is especially important in areas of rapidly changing electric fields and in small devices. This weakness can be observed in Fig. 5.4 for a 200 nm and a 50 nm structure. This figure compares generation rates calculated using different transport schemes. In this example, the electrons are accelerated from left to right. As soon as the electric field is risen, the local-field model predicts the carrier generation rate. However,

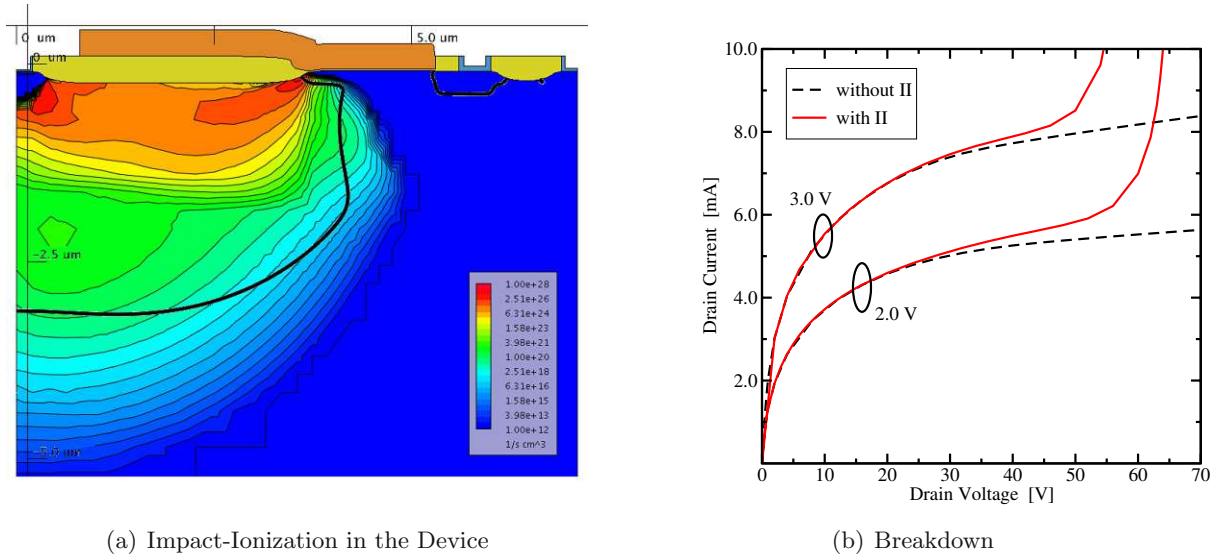


**Figure 5.5:** Distribution of the impact-ionization generation rate in the sample device with a drain voltage of 40 V and a gate voltage of 2 V (a). Influence of impact-ionization on the output characteristic using the LDMOS transistor from Chapter 4 (b).

physically more correct are the Monte Carlo reference simulations. They demonstrate that the carrier energy can follow changes in the electric field with a certain delay. At characteristic lengths shown in that figure, the validity of the local-field approach becomes questionable.

As long as device expansions are well above 200 nm, the advantages of local-field models are the good integrability in drift-diffusion schemes which are the workhorse in device simulation tools. Most TCAD simulators therefore commonly include one or more of the local electric field models. A typical application where drift-diffusion models deliver good results are high-voltage LDMOS transistors. Fig. 5.5 shows some results based on (5.13) and also clearly shows the importance of this physical effect. A more comprehensive example incorporating breakdown and snap-back simulations is presented in Section 5.3.

## 5.2.2 Non-Local Extensions to Local Field Models

Local modeling approaches do not provide information about where carriers come from and if they have already gained high energy. But since electrons and holes have to be accelerated to gain at least the threshold energy before impact-ionization can occur, this information is relevant. The area where there is a high electric field but impact-ionization has not started yet is often called dark-space [202]. This dark-space has to be considered also in experimental extractions of the ionization coefficients. Measuring of the coefficients cannot be performed directly. Therefore, they are commonly extracted out of the multiplication factor using the ionization integral (5.10). While considering the dark-space, the boundaries of the ionization integral are shifted so that only regions where impact-ionization takes place are included. With

## 5.2. MODELING APPROACHES

this approximation Okuto and Crowell [202] could explain anomalous energies which were found previously for the parameters  $E_r$ ,  $E_i$ , and  $\lambda$  in (5.14). They have obtained more realistic energies employing a pseudo-local approximation which is also valid for high fields. In their work, a model using apparent and *real* ionization coefficients was developed. This technique delivered reasonable results for the given one-dimensional examples.

An interesting approach which includes local changes of the electric field is the method presented by Slotboom *et al.* [179] (compare (4.23)). The required post-processing which is necessary after a conventional drift-diffusion simulation, makes this method elaborative to implement, especially if self-consistent solutions are required.

### 5.2.3 Lucky Electron Model

The lucky electron concept [192, 203] introduces a threshold energy level  $\mathcal{E}_{II}$ . The carriers need to surmount this potential barrier in order to trigger impact-ionization. Hu *et al.* [203] describes that this energy can be reached if a carrier travels a sufficiently long distance without collisions. In this work by Hu, a compact model is formulated, which relates the substrate current  $I_{\text{Sub}}$  as a consequence of impact-ionization with the drain current  $I_D$  and the maximum electric field  $E_{\text{max}}$  in the device. The drain current acts as a source function (the supply of carriers) and the peak field is used together with the (hot-carrier) mean free path  $\lambda$  to describe the ionization probability. This leads to

$$I_{\text{Sub}} = C_1 I_D \exp \left( -\frac{\mathcal{E}_{II}}{q E_{\text{max}} \lambda} \right), \quad (5.17)$$

where the derivation is based on the ionization rate similar to the definition in (5.13) [204].

A method to utilize the lucky electron model in device simulation and to introduce the non-locality has been proposed by Meinerzhagen [205]. In this work, the electric field line is followed starting from a point  $P$  until the electrostatic potential difference of  $V_B = \mathcal{E}_{II}/q$  has been reached at a point  $P_n$ . The length along the field line between  $P$  and  $P_n$  is  $d$ . The generation rate in the point  $P$  yields

$$G^{II}(P) = \alpha^\infty n(P_n) v^{\text{sat}} \exp \left( -\frac{d}{\lambda} \right), \quad (5.18)$$

where  $n(P_n)$ ,  $v^{\text{sat}}$ , and  $\alpha^\infty$  are the electron concentration in point  $P_n$ , the saturation velocity, and measured value from [189] to calibrate the results.

### 5.2.4 Carrier Temperature Based Modeling

Another approach for modeling impact-ionization employs the carrier temperature, i.e. the local mean carrier energy, as the key parameter. The formalism for the rate calculation is very similar to the local-field model. For the transformation of the commonly used local field based models, the electric field can be replaced by the homogenous stationary energy balance equation, compare (4.19), to form  $E = E(T_\nu, T_L)$  [206]. Thus, Chynoweth's law can be transformed from (5.13)



## CHAPTER 5. IMPACT-IONIZATION GENERATION

to a carrier temperature dependent model. An often used estimation combining all coefficients reads [207]

$$\alpha_\nu = \alpha_\nu^\infty \exp\left(-\frac{\mathcal{E}_\nu^{\text{crit}}}{k_B T_\nu}\right). \quad (5.19)$$

The values  $\alpha_\nu^\infty$  and  $\mathcal{E}_\nu^{\text{crit}}$  are the high carrier temperature value of the ionization rate and the reference energy, respectively. Although these quantities have certain physical meanings, commonly they are used as fitting parameters.

It seems natural to use the carrier energy in place of the electric field to model the impact-ionization rate and it is commonly used in the energy-transport or hydrodynamic simulation frameworks. Hence, it is possible to approximately consider non-local issues like the dark-space phenomenon. However, the carrier temperature alone cannot reflect the existence and strength of high-energy tails, i.e. the amount of high energetic carriers available. Completely different shapes of the distribution function can lead to the same average energy [15]. Additionally, high-energy tails can also exist if the average energies are low (compare Fig. 4.2 and 4.12). Therefore, the carrier temperature is commonly overestimated in small devices, which also leads to an overestimation of the impact-ionization rate [186, 208]. These effects, which are especially relevant for aggressively down-scaled devices, can only be considered by incorporating the full distribution function.

### 5.2.5 Distribution Function Based Modeling

Instead of using the electric field, the carrier temperature, hot-carrier sub-populations, or some non-local approximations, the most rigorous modeling approach is to directly incorporate the carrier distribution function  $f(\mathcal{E})$ . This allows one to calculate the total generation rate using [187]

$$G^{\text{II}} = \int_{\mathcal{E}_{\text{th}}}^{\infty} P_{\text{II}}(\mathcal{E}) f(\mathcal{E}) g(\mathcal{E}) d\mathcal{E}. \quad (5.20)$$

Here, the threshold energy is described using the symbol  $\mathcal{E}_{\text{th}}$ ,  $g(\mathcal{E})$  is the density of states, and  $P_{\text{II}}(\mathcal{E})$  the ionization probability. This probability is often represented by the Keldysh [209] approach

$$P_{\text{II}}(\mathcal{E}) = P_0 \left( \frac{\mathcal{E} - \mathcal{E}_{\text{th}}}{\mathcal{E}_{\text{th}}} \right)^2, \quad (5.21)$$

or the approach presented by Kamakura [210]

$$P_{\text{II}}(\mathcal{E}) = P_0 (\mathcal{E} - \mathcal{E}_{\text{th}})^p, \quad p = 4.6, \quad \mathcal{E}_{\text{th}} = 1.1 \text{ eV}. \quad (5.22)$$

The integration boundaries in (5.20) show that only carriers above a certain energy threshold  $\mathcal{E}_{\text{th}}$  influence the generation rate and highlight that high energies are of vital importance. Approximations of the distribution function based on splitting hot and cold carrier fractions (as shown in (4.32) for the six moments model [134]) provide results in good agreement with the more precise but also very time-consuming full-band Monte Carlo method (see Fig. 5.4).



## 5.2.6 Energy Driven Paradigm

In the work of Rauch and La Rosa [211,212], a compact modeling approach for the total substrate current is presented. Although this compact model cannot be used for TCAD, it highlights the importance of the shape of the distribution function. Here, the substrate current of an n-MOSFET is formulated as

$$\frac{I_{\text{Sub}}}{I_D} \propto F(I_S) \int_{\mathcal{E}_C}^{\infty} P_{\text{II}}(\mathcal{E}) f_c(\mathcal{E}) d\mathcal{E}, \quad (5.23)$$

where  $f_c(\mathcal{E})$  is the carrier energy distribution function and  $P_{\text{II}}$  stands for the impact-ionization cross section [211]. The function of the source current  $F(I_S)$  enters either linearly as  $F(I_S) = I_S$  or quadratically as  $F(I_S) = I_S^2$ , depending on the importance of electron-electron scattering [213,214]. The authors suggest that there are commonly one or more dominant energies ( $qV_{\text{eff}}^i$ ) at which the integrand of (5.23) peaks and one can approximate the integral as

$$\int P_{\text{II}}(\mathcal{E}) f_c(\mathcal{E}) d\mathcal{E} \approx \sum_i P_{\text{II}}(qV_{\text{eff}}^i) f_c(qV_{\text{eff}}^i). \quad (5.24)$$

The dominant energies can be extracted by comparing the slopes of  $P_{\text{II}}(\mathcal{E})$  and  $f_c(\mathcal{E})$  in logarithmic scale. The knee energies correspond to the maximum of the integrand in (5.23). This corresponds to the position where the multipliers have the same steepness but one is decaying (the distribution function) while the other one is increasing (the probability). Mathematically, this gives

$$\frac{d \ln f_C}{d\mathcal{E}} = -\frac{d \ln P_{\text{II}}}{d\mathcal{E}}, \quad (5.25)$$

and commonly coincides with knee points of  $f(\mathcal{E})$  or  $P_{\text{II}}(\mathcal{E})$ . For  $P_{\text{II}}$  the Kamakura relation (5.22) is assumed, with  $\mathcal{E}_{\text{th}}$  being the band-gap energy  $\mathcal{E}_g$ . In long channel devices  $f_C(\mathcal{E})$  can be described using the heated Maxwellian distribution function as  $f_C(\mathcal{E}) \propto \exp(-\mathcal{E}/q\lambda E_{\text{max}})$ .  $f_C$  has no knee and the slope is controlled by the maximum electric field ( $-1/q\lambda E_{\text{max}}$ ). As shown in Fig. 5.6(a) the maximum of the integrand depends on the slope of the carrier energy distribution and results according to (5.25) in

$$qV_{\text{eff}} = \mathcal{E}_g + p q \lambda E_{\text{max}}. \quad (5.26)$$

Due to the dependence of  $qV_{\text{eff}}$  on the maximum electric field, Rauch *et al.* call this relation the field driven approximation. By inserting this result in (5.23) one obtains

$$\frac{I_{\text{Sub}}}{I_D} \propto G(E_{\text{max}}) \exp\left(-\frac{\mathcal{E}_g}{q\lambda E_{\text{max}}}\right), \quad (5.27)$$

where  $G(E_{\text{max}})$  summarizes the remaining components which are not evaluated explicitly. This result corresponds to the lucky electron model (5.17).

In down-scaled devices the carrier energy distribution exhibits a knee near the maximum energy available from the steep potential drop along the pinch off region which is approximated as

## CHAPTER 5. IMPACT-IONIZATION GENERATION

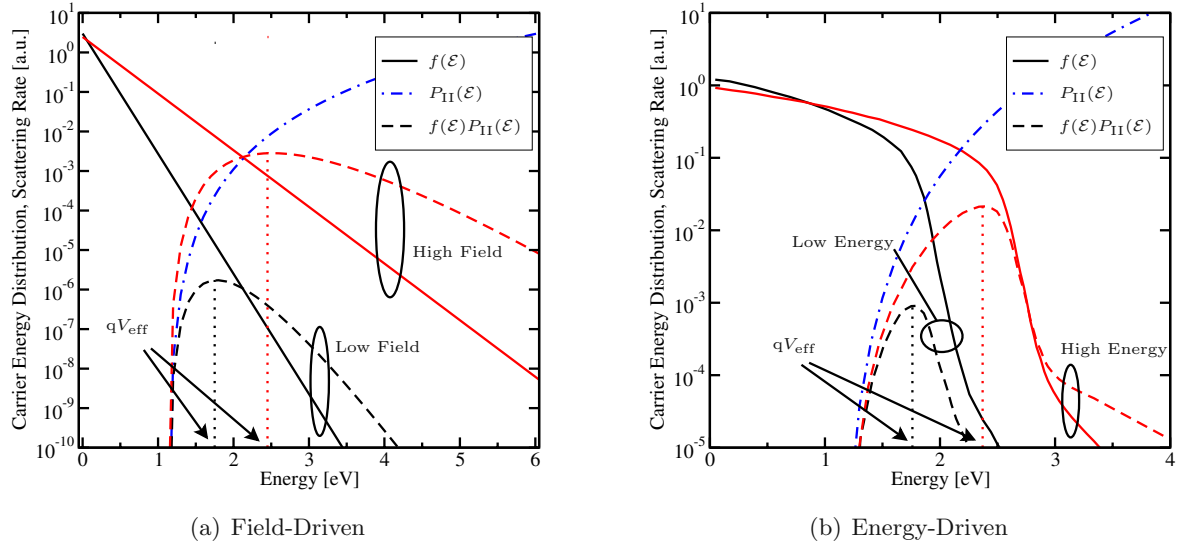


**Figure 5.6:** Schematic representation of the field (a) and energy driven (b) paradigms by Rauch and La Rosa. In the field driven paradigm a heated Maxwellian distribution is assumed with the carrier energy defined by  $q\lambda E_{\max}$ . The maximum of the integrand is therefore found at the energy  $qV_{\text{eff}}$  and can be evaluated using  $E_{\max}$  as given in (5.24). In the energy driven paradigm  $V_{\text{eff}}$  is controlled by the knee of the energy distribution function estimated according to (5.28).

$V_{\text{DS}} - V_{\text{D,sat}}$  [211]. Due to the constantly rising scattering rate and the abrupt decrease of the carrier distribution function near the knee point the maximum of the integrand in (5.23) at  $qV_{\text{eff}}^i$  coincides with the knee near (see Fig. 5.6(b))

$$V_{\text{eff}} \approx V_{\text{DD}} - V_{\text{D,sat}}. \quad (5.28)$$

In this case the dominant energy is determined by the knee of the distribution function, which by itself depends on the bias conditions and therefore on the available energy [215]. Further influences of voltage changes seem not to shift this peak level. Hence, the final rate is proposed to be

$$\frac{I_{\text{Sub}}}{I_{\text{D}}} \propto BP_{\text{II}}(q\lambda V_{\text{eff}}), \quad (5.29)$$

where  $B$  includes that part of (5.23) which is not explicitly evaluated.

This particular idea of this compact model is to combine the two regimes in one model. It hereby highlights the necessity of new modeling paradigms when proceeding to small, down-scaled devices. The validity of both regimes has been shown in [211].

## 5.3 Case Study: Simulation of Breakdown and Snap-Back

In this case study a smart power test structure from *Infineon Technologies* is analyzed. This structure is used for switching purposes in automotive applications. It shows that electronic equipment has to cope with very harsh conditions in these environments [113, 216]. Hence, semiconductor devices have to withstand ambient temperatures of as low as  $-40^{\circ}\text{C}$ . On the other hand, in the drivers interior temperatures can raise to up to  $+85^{\circ}\text{C}$ , under the hood up to  $+125^{\circ}\text{C}$ , and for the devices mounted on the engine temperatures can reach  $+150^{\circ}\text{C}$  [113, 216]. Not only the temperature, but also electrical harsh conditions are typical for vehicles. The power supply, the grounding, and voltage levels on signal lines experience high disturbances. These high energetic interfering signals can lead to voltage pulses increasing the nominal supply voltage up to 5 times [216]. Electronic devices in automotive environments have therefore be rated of up to 70 V, although the power lane is nominally 14 V.

### 5.3.1 Specifications

The structure that is analyzed in this study is basically a vertical smart DMOS with an architecture similar to the one shown in Fig. 2.10. The device demonstrated random failures during operation. It was suspected that voltage peaks lead to breakdown and further to the snap-back state (compare Section 3.2.4). Therefore, the responsible parasitic n-p-n bipolar structure was measured using the TLP (transmission line pulse) method [217]. A snap-back characteristic with a holding voltage of approximately 10 V was observed. This holding voltage lies below the supply bias of 14 V. Therefore, the device remains in snap-back state and the resulting high current does not decay. Eventually, this leads to the destruction of the device due to overheating.

The idea is to investigate the influence of the doping profile on the holding voltage using device simulation. To accomplish this, the first necessary step is to reproduce the experimental snap-back characteristics. Especially the holding voltage has to show good agreement. As the next step, a structure which is similar to the first one should be analyzed and optimized. Unfortunately, no measurement data are provided for this second device.

Simplified versions of the devices are used for the simulations. They basically consist of an n-doped EPI layer on top of an  $n^{+}$  backside doping. An implanted p-well extends across the whole simulation domain. Finally an  $n^{+}$  implant and a contact are placed in the right upper corner. The device is sketched in Fig. 5.7. The first structure is generated using one-dimensional measured SIMS-profiles of the different dopants incorporated into the device. The profiles represent vertical cuts through different regions. For the second structure, some of the SIMS-profiles were exchanged by those obtained from process simulation. Also the vertical extension was increased. All doping profiles and contacts which are not relevant for the simulation have been omitted. Additionally, the structures are assumed to be symmetric. Both basically act as a vertical parasitic n-p-n bipolar transistor. The emitter contact is on the top surface and the collector contact is at the backside. The p-well acts as the base region. It is not connected and therefore remains floating.

## CHAPTER 5. IMPACT-IONIZATION GENERATION

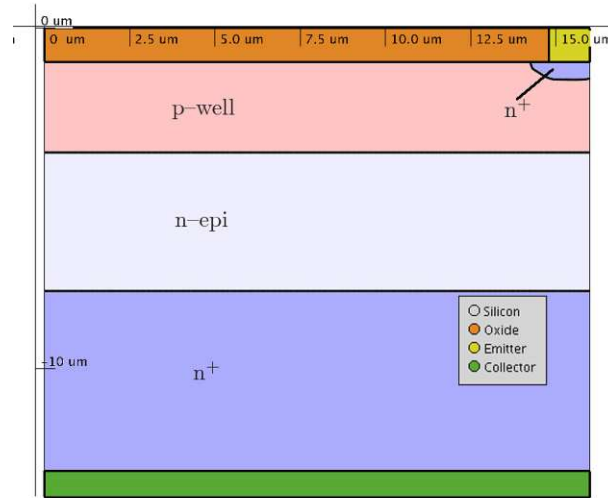


**Figure 5.7:** Sketch of the simplified smart power device with  $n^+$  backside, n-EPI, p-well and  $n^+$  emitter contact. The collector is at the bottom of the device.

To model the characteristics of these structures, the device simulator MINIMOS-NT is used. The large dimensions of the device suggest to employ the drift-diffusion framework. The probably most important physical mechanism responsible for the breakdown and snap-back effect is the impact-ionization generation. For proper modeling of the impact-ionization rates, the extended Chynoweth relation is used as presented in (5.13).

### 5.3.2 The Snap-Back Curve

First the snap-back simulation is performed using a voltage boundary condition. The collector voltage is increased starting from 0 V up to the breakdown voltage. From there on, a current boundary condition is used. This method gives the possibility to trace the whole snap-back curve. Fig. 5.8 demonstrates the simulation results against the measurement data. For a better orientation along the snap-back curve, the points I–IV have been marked in Fig. 5.8(b). The distributed values of the II rate and the electron density at those positions are shown in Fig. 5.9 and Fig. 5.10, respectively.

Until the device breakdown (point I), only the small cut-off current can be observed. The electric field in the device peaks at the base–collector junction and increases with the collector voltage. Due to the increasing field the impact-ionization generation becomes more pronounced. Eventually, the avalanche breakdown occurs at the point I.

Continuing to the point II, the further increase of current is related to an intensified impact-ionization generation. The rapidly growing concentration of carriers generated in the gate region makes it possible to carry higher currents at lower collector voltages. This explains the negative differential resistivity in this area. Additionally, the electrostatic potential in the base region

### 5.3. CASE STUDY: SIMULATION OF BREAKDOWN AND SNAP-BACK

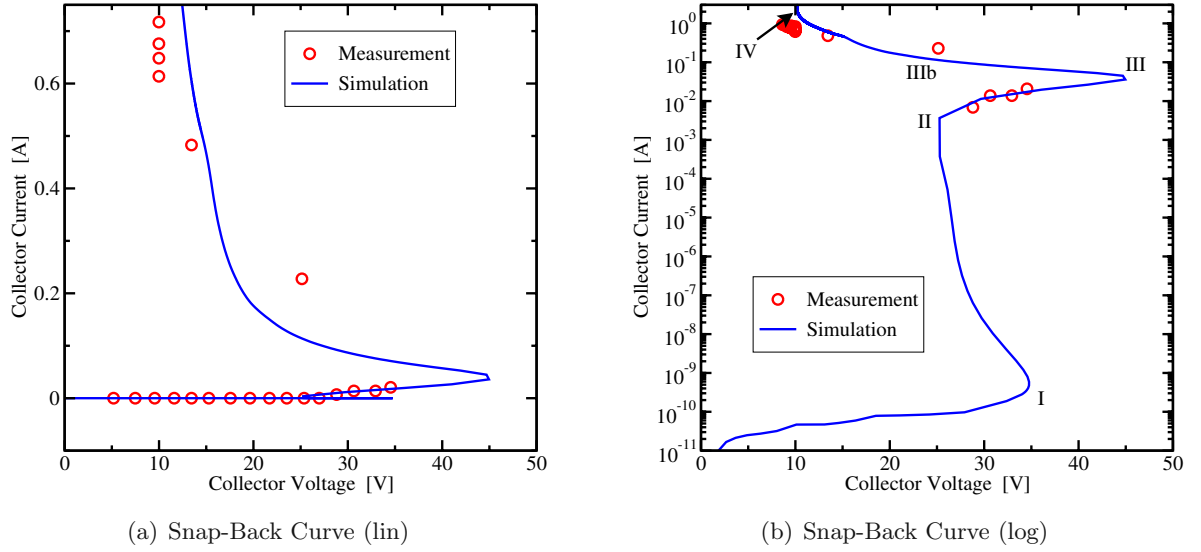


**Figure 5.8:** The snap-back characteristics of the test structure using linear (a) and logarithmic (b) scale. In the right plot, the markers I–IV which are used in the text are shown.

increases. This leads to a forward bias across the base emitter region and turns on the n-p-n transistor. Therefore, additional electrons are injected into the base region [109, 218].

Between the points II and III, the concentration of electrons in the base region begins to exceed the acceptor concentration. Consequently, the mobile charge density becomes higher than the fixed charge density [109, 218] and the metallurgical junctions are therefore not valid anymore. Hence, the effective base–collector junction is pushed towards the n-n<sup>+</sup> junction between the EPI layer and the backside doping. This effect is called “base push-out” or “Kirk effect” [32] and evolves around the snap-back voltage at the point III. Together with the base push-out, also the peak electric field and the impact-ionization are moved deeper into the silicon.

Finally, the peak electric field reaches the backside of the structure. The higher doping concentration in this region yields a higher impact-ionization generation. Additionally, the current path through the device becomes broader. This finally leads to the voltage drop down to the holding voltage in point IV. Here, the generated carriers flood the whole device. At this state, no stationary operation would be possible. The high current densities lead to a rapid temperature increase and the device would be destroyed very quickly. However, with TLP measurements, these operating points can still be observed. Although no self-heating is employed in this simulation, the calculated holding voltage agrees well with the measurement data.

## CHAPTER 5. IMPACT-IONIZATION GENERATION

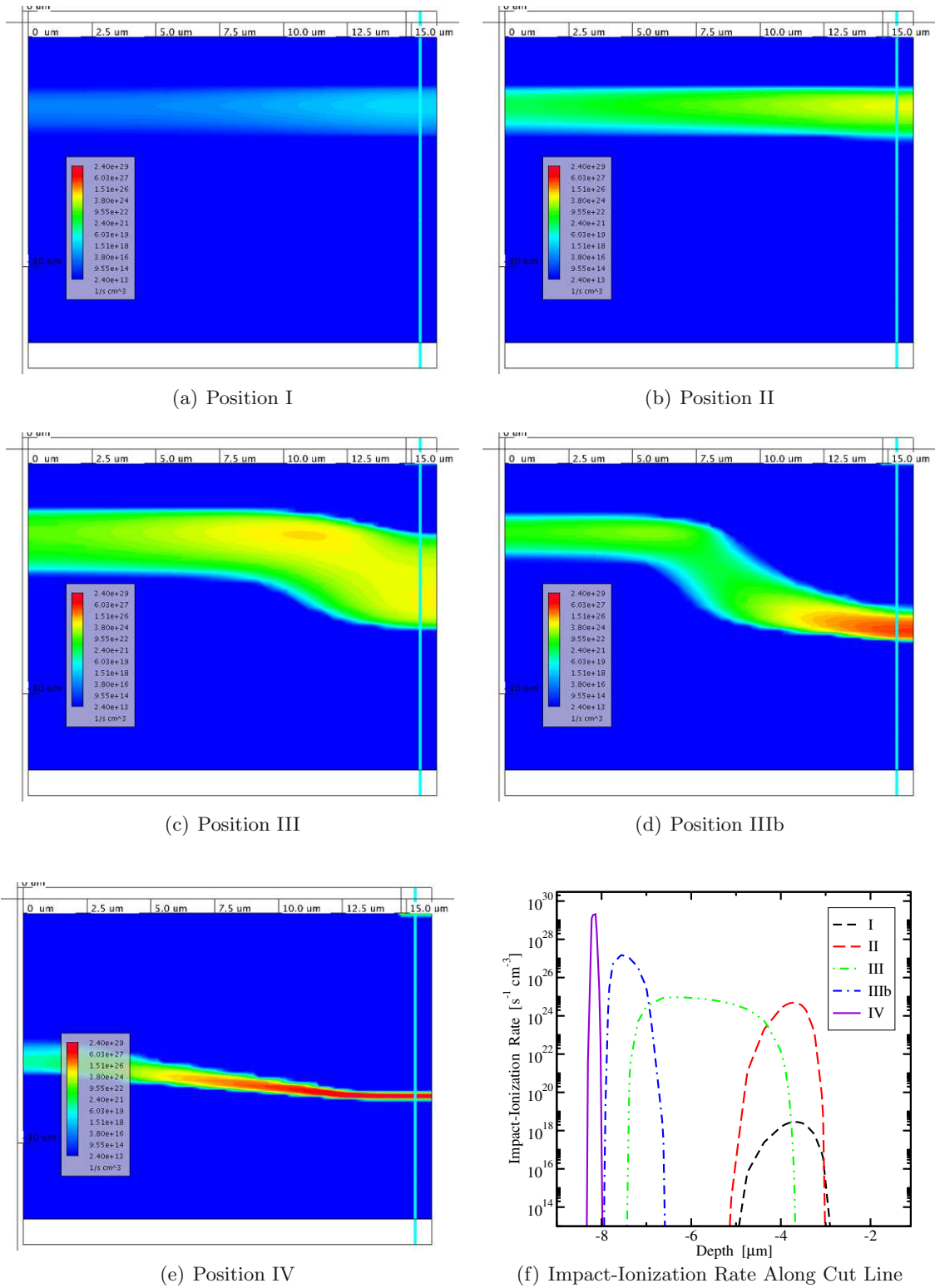


**Figure 5.9:** Impact-ionization generation rate at different positions in the snap-back curve (a)-(e); for the position marks I–IV see Fig. 5.8(b). The electron concentration along the cutline is shown in (f).

### 5.3. CASE STUDY: SIMULATION OF BREAKDOWN AND SNAP-BACK

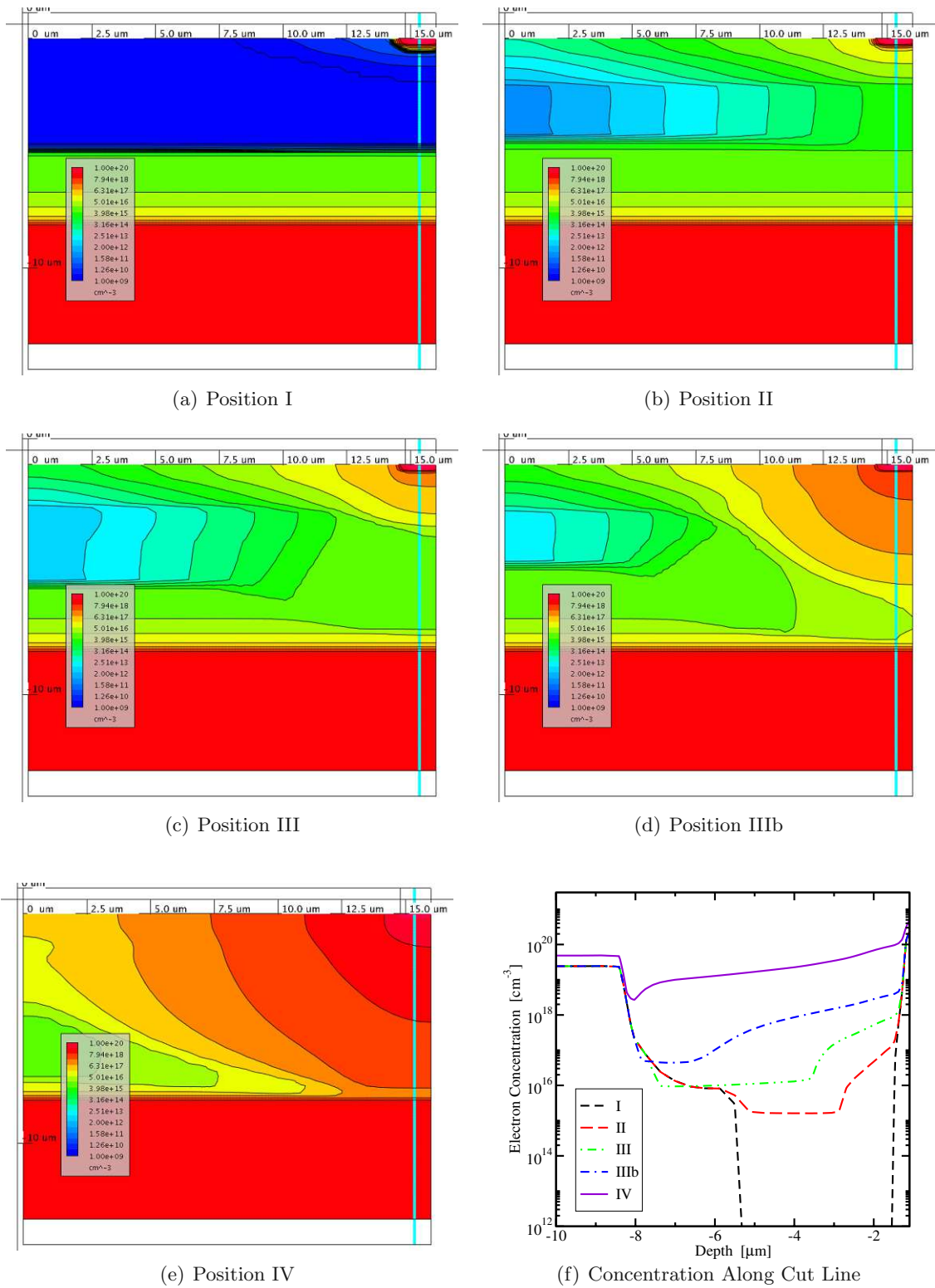


**Figure 5.10:** Electron concentration at different positions in the snap-back curve (a)-(e); for the position marks I-IV see Fig. 5.8(b). The electron concentration along the cutline is shown in (f).



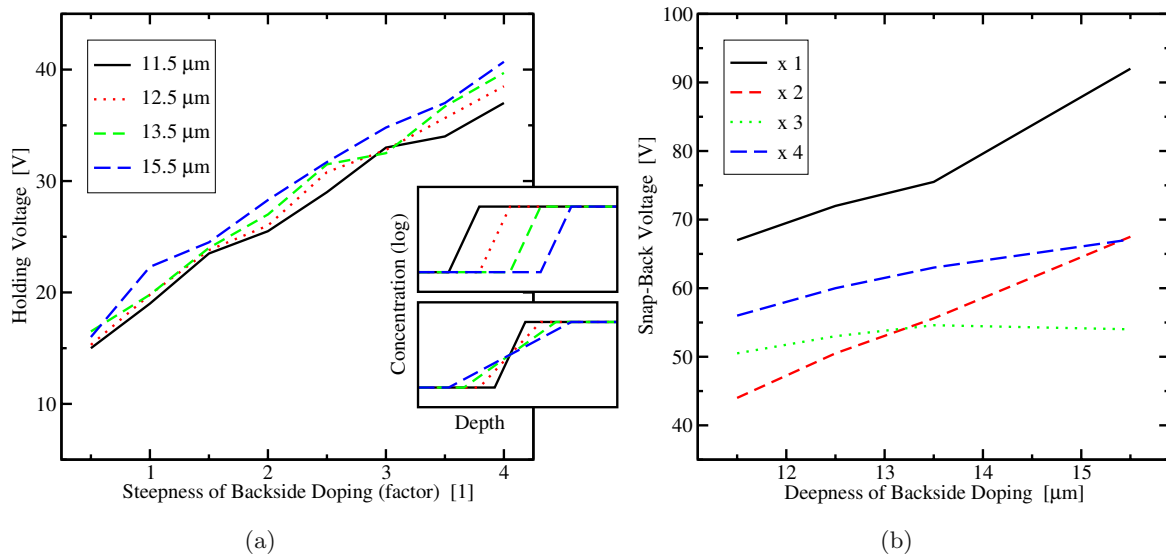


**Figure 5.11:** Holding (a) and snap-back voltage (b) in dependence on the backside doping. The upper inset symbolizes the variation of the backside doping in depth. The onset of the backside doping lies in the range of 11.5 to 15.5  $\mu\text{m}$ . The lower inset symbolizes the variation of the steepness. It is denoted by a “stretching” factor in the range of 1 to 4. The holding voltage in (a) strongly depends on the variation of the steepness, whereas a change of the depth has only minor impact. The snap-back voltage (b) especially depends on the depth of the backside doping. It also seems to be influenced by the steepness. However, this comes from the fact that a change of the steepness also changes the depth (compare lower inset).

### 5.3.3 Structure Variations

To investigate the influence of the doping profile on the snap-back curve further simulations have been performed. For this purpose, the structure is modified using doping profiles achieved from process simulations. The structure is extended further into the depth of the device, i.e., the direction towards the backside of the device. These modifications of the structure already show a higher holding voltage of approximately 20 V. For the further optimization of the holding voltage, the general requirements to the device architecture have to be considered. Therefore, only a few properties of the doping profile are allowed to be changed. To avoid any influence on the devices embedded in the process, the upper layers, i.e., the emitter and the base area, should remain unchanged. Also the doping concentrations of the EPI layer and the backside must be kept at the same level. This gave rise to the two possible variations, both concerning the n-n<sup>+</sup> junction. First, the depth of the junction can be varied, i.e. changing the thickness of the EPI layer. Also a variation of the junction steepness can be employed (see insets in Fig. 5.11).



### 5.3. CASE STUDY: SIMULATION OF BREAKDOWN AND SNAP-BACK

The increase of the EPI thickness leads, as shown in Fig. 5.11(b), to a change of the snap-back voltage. Here (point III), the evolving base push-out effect dominates the device behavior. A thicker EPI layer can withstand a higher voltage at approximately the same electric field. Therefore, the shift of the effective base-collector junction towards the backside doping occurs at higher voltages. This correlates to observations in [109]. Once the base push-out saturates, no differences in the device behavior can be observed. The holding voltage therefore remains unchanged.

The second variation which was investigated concerns the steepness of the backside doping. For the simulation study the profile was changed artificially (see inset in Fig. 5.11). The results are shown in Fig. 5.11(a). At the holding voltage the device is dominated by the high impact-ionization rate at the  $n-n^+$  junction. By flattening the junction, lower maximum fields and therefore lower impact-ionization rates can be expected. This tendency correlates with simulation the results, which show an increase of the holding voltage for a flattened profile. Note that the steepness variations also changed the EPI thickness in this setup. This explains the influence of the steepness on the snap-back voltage.

#### 5.3.4 Simulation Difficulties

Snap-back simulations often cannot be performed straight-forwardly with TCAD tools. The initial part, the voltage stepping up to the breakdown voltage, is a standard use-case of device simulations. Until this point, commonly no problems are faced. However, going beyond the breakdown gives rise to one or more of the following difficulties:

- The exponential dependence of the impact-ionization generation rate on the electric field yields quite severe local variations of the carrier concentrations.
- The avalanche generation and the base push-out effect change the device behavior. Additionally, the active zones are shifted within the device.
- Further, the current in the snap-back curve has a non-bijective dependence on the collector-emitter voltage. This requires a special treatment of boundary conditions for the simulation setup [218]. In the case presented, current stepping is sufficient. However, devices demonstrating such a non-bijective dependence of the current vs. the collector voltage also exist. For these cases, special curve tracing algorithms are required [219, 220].

The snap-back simulations often lead to bad convergency of the Newton iteration scheme [218]. To overcome this, small voltage and/or current stepping is required. In addition, a good mesh optimized for the snap-back simulation improves the overall convergence. This is especially true, due high local variations in the carrier concentrations, for example. Also effects like the base push-out mechanism have to be considered for the mesh generation. Additional discussions on numerical issues related to the simulation of impact-ionization phenomena and especially on problems encountered for high-voltage devices are found in Section 7.4.

## CHAPTER 5. IMPACT-IONIZATION GENERATION

### 5.3.5 Discussion

The reference simulation shows qualitatively good agreement as compared to the measurement data. Note that these results are obtained without performing extra calibrations. This means that even better results can be expected by performing a proper model calibration. This suggests that for this structure, the static iso-thermal simulations are sufficient for a proper description of the problem. However, other investigators claim that estimations without self-heating are not valid for snap-back modeling, which was especially observed in lateral devices [221]. Reconciling of this contradiction is the subject of the further research. For this purpose, three-dimensional device simulations have to be performed in order to capture the self-heating effects. However, such simulations should not be related to conceptual difficulties because MINIMOS-NT is capable for three-dimensional device modeling and incorporates the self-heating.

## Chapter 6

# Hot-Carrier Reliability Modeling

The term hot-carrier degradation used in this work describes the damage found in MOS devices leading to distortion of device parameters. In the beginnings of hot-carrier investigations, several groups of degradation modes have been differentiated based on the carrier generation mechanisms [222]. The first mode identified in this classification is caused by carriers accelerated by high electric fields along the channel and is called channel hot-carriers. The next type, the substrate hot-carrier generation, is based on carriers injected from the substrate. These carriers are accelerated towards the gate and are considered to be most important in the context of interface and oxide damage. The drain avalanche hot-carriers, especially active at low gate voltages, are generated by single carriers which trigger avalanche carrier generation. The last mode in this classification, is the secondarily generated hot-carrier degradation activated by minority carriers resulting from impact-ionization due to the substrate current. Following this classification, the channel hot-carriers including the avalanche induced secondary carriers are most important in the considerations of this work.

In the first section of this chapter, the most important characteristics of hot-carrier degradation observed in MOS transistors are discussed. The remaining part is devoted to modeling approaches. Section 6.2 gives a selection of common modeling approaches and Section 6.3 finally presents the hot-carrier degradation model recently developed by our group.

### 6.1 Characteristics of Hot-Carrier Degradation

During hot-carrier degradation interface states are created along the channel of MOS transistors. This effect is accelerated with the drain voltage and depends on the highly energetic carriers, which are called “hot”. The carriers bombarding the interface trigger the dissociation of Si–H bonds followed by a release of hydrogen and resulting in de-passivated dangling bonds. This interface state creation is highly localized, which distinguishes the degradation process from another degradation mechanism, from the negative bias temperature instability. While the latter one is considered as a one-dimensional process, hot-carrier degradation is a two-dimensional

## CHAPTER 6. HOT-CARRIER RELIABILITY MODELING

phenomenon. Carriers gain the highest energy near the drain end of the channel, where also the highest creation rate of interface states can be observed. The interface states created by this process can trap carriers forming interface charges which change the electrostatics of the device. This influences the threshold voltage of the transistor. Additionally these charges act as scattering centers leading to a reduction of the carrier mobility, the transconductance, and finally the drain current.

Over decades, the most severe degradation of n-MOSFET devices over stress-time, meaning the worst-case condition, was usually found at maximum substrate current [214, 223]. This maximum current originates from impact-ionization and therefore is related to the existence of high-energetic carriers. Thus, this worst-case scenario is found when the following interrelation between voltages is satisfied:  $V_{GS} \approx V_{DS}/2$ . In p-MOSFET devices, the worst-case condition is typically found at the maximum gate current [214, 224].

One of the first modeling approaches proposed was the so-called lucky electron model developed in the 80s by Hu *et al.* [203]. This model, which is explained in Section 6.2.1, also assumes that electrons reach energies high enough to surmount the potential barrier at the Si-SiO<sub>2</sub> interface. The degradation of  $g_m$  and  $V_T$  is described using the phenomenological power-law relation  $t^n$  and a physics-based reaction-diffusion relation is proposed. The application of the lucky electron model with carefully tuned parameters delivered reasonable results in long channel devices. During this time the devices were aggressively down-scaled without a proper reduction in the supply voltages. As a result, the electric field in transistors was substantially increased. This tendency led among other things to the reinforcement of hot-carrier degradation as well as related reliability issues. To avoid that, a special strategy was based on a careful field shaping design, especially regarding LDD structures [225–227].

Starting from the sub micrometer nodes the problems seemed to be overcome by the reduction of the drain voltages of scaled transistors. It was assumed that due to the low voltages the carriers cannot overcome the energy barriers required to trigger bond dissociation processes [223]. However, hot-carrier degradation was also observed at lower voltages [222, 228] and is still relevant even in highly down-scaled devices. However, the worst-case condition of hot-carrier degradation has shifted to higher gate voltages ( $V_{GS} \approx V_{DS}$ ). This suggests that the worst-case condition changed from the maximum carrier energy to the maximum number of carriers, i.e. the highest current [213, 229].

### 6.1.1 Multiple-Particle Process

The shift of the worst-case condition and the existence of HCD at low voltages suggested that there is not a single mechanism responsible for the interface state generation. Another argument supporting this idea was that the carrier flux rather than energy becomes important in scaled devices. All these considerations were explained in a series of papers published by the group of Hess [230, 231]. In long-channel devices carriers can become rather hot and can thereby activate a bond breakage process in a single collision. In contrast, in scaled devices the multiple-particle process plays the dominant role. Si–H bonds are broken by multiple excitations of

## 6.1. CHARACTERISTICS OF HOT-CARRIER DEGRADATION

phonon modes (due to bombardment by several colder particles) which eventually lead to bond breaking [230, 231]. This also agrees with the shift of the worst-case condition to maximum currents, i.e. the conditions with the highest number of carriers impinging on the interface, resulting in a high number of collisions.

In the simulation of hot-carrier degradation the single- (SP) and multiple-particle (MP) process, have to be considered. In larger devices where carriers can gain high energies the SP process will dominate. Therefore the worst-case condition will be found in the mid gate-voltage range in conjunction with the highest bulk-current. In highly down-scaled devices the MP process will prevail and the worst-case condition corresponds to the maximum drain-voltage. The highest currents give the maximum number of carriers, thereby enabling the multiple vibrational excitation of the bonds. Depending on geometry and operating conditions one of the two processes can be dominant. However, under real stress/operating conditions commonly both processes are active simultaneously.

### 6.1.2 Giant Isotope Effect

An experiment supporting the MP theory was performed on hydrogen and deuterium passivated surfaces using a tip of an STM (scanning tunneling microscopy) as a source of carriers tunneling through the vacuum [232]. The surfaces were bombarded by carriers below the threshold energy and the experiment showed that the deuterium passivated surface was much more robust against the electron bombardment than the hydrogen passivated one. In the former case, as shown in Fig. 6.1(a), a much higher current is required to gain the same desorption yield [233]. Two mechanisms have been identified to cause this behavior which were summarized by Hess *et al.* [230]: The first effect is the higher bonding energy between deuterium and silicon, also known as the large isotope effect. But the differences found in the desorption rate are much higher than the difference of the bonding energy would suggest. That's why this effect is also called the giant isotope effect of hydrogen. The reason for this huge impact was found to be the multiple vibrational excitation of the Si-H and Si-D. Bonds are excited by collisions with many carriers and lifted to higher energy levels until the bonds eventually dissociate. This is true for both, hydrogen and deuterium passivated surfaces. However, since the localized deuterium vibration is more closely matched to the silicon bulk, a more efficient cooling of excited bonds takes place. This leads to reduced bond heating and in consequence to a lower probability of deuterium desorption via the multiple collision mechanism. The behavior of hydrogen bonds at surfaces is comparable to the behavior of them at interfaces. Therefore, one may use the same conclusion to explain why MOS devices passivated with deuterium instead of hydrogen appear to have a higher resistivity against HCD [235]. The difference in the degradation process can be observed in Fig. 6.1(b). As a side effect, this experiment also confirms that interface bond breaking plays an crucial role in device degradation [234].

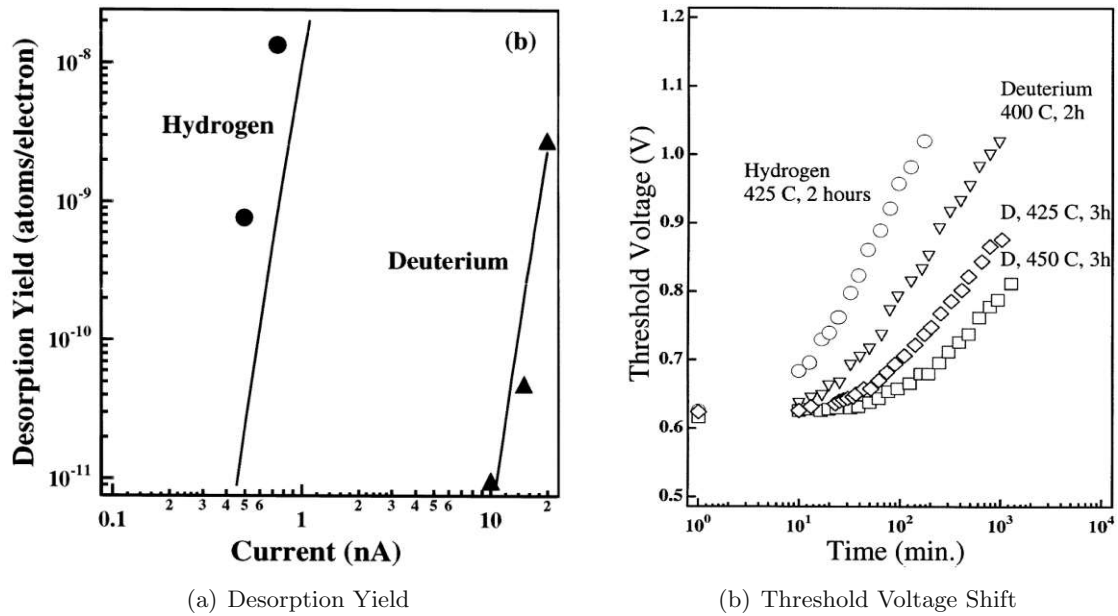


**Figure 6.1:** STM measurements from [233] showing the giant isotope effect of deuterium (a) and the threshold voltage degradation of a  $0.36\ \mu\text{m}$  n-MOS transistor taken from [234] (b).

## 6.2 Review of Modeling Approaches

During decades of hot-carrier degradation investigations, different modeling approaches have been proposed. Most models concentrate on the degradation of the Si-SiO<sub>2</sub> interface where the creation of interface states due to bond breaking has to be captured. Many of these approaches are phenomenological and use empirical expressions to describe the degradation. Therefore, they commonly only work for a special group of devices and have limited validity. Their predictive character is commonly low, and scaling of devices often requires parameter re-calibration. As a result, the need for models reproducing the physical phenomena responsible for hot-carrier degradation has grown. Therefore, it is of great importance to reveal and capture the physical picture behind HCD and be able to predict the degradation of arbitrary devices.

The electric field has long been used as the main driving force for the degradation process. But it soon became clear that the electric field alone is often not enough for proper modeling and the carrier energy distribution needs to be considered. One of the most important physical modeling approaches considering the carrier energies can be found in the work of Hess [236], Rauch and La Rosa [212], and Bravaix [223].

## 6.2. REVIEW OF MODELING APPROACHES

### 6.2.1 Lucky Electron Approach

Hu *et al.* [203] proposed a model for interface trap generation, assuming that bond dissociation is triggered by hot-carriers having energies above a certain threshold energy level  $\phi_{it}$  (assumed to be 3.7 eV in [203]). Deduced from the lucky electron concept [192], a relation for the interface trap generation can be written similarly to the lucky electron model used for impact-ionization in (5.17) as

$$\Delta N_{it} = C_2 \left[ t \frac{I_D}{W} \exp\left(-\frac{\mathcal{E}_{IT}}{qE_{\max}\lambda}\right) \right]^n. \quad (6.1)$$

In this model the trap generation rate depends on the maximum lateral electric field  $E_{\max}$  and the drain current  $I_D$ .  $W$  is the device width, while  $I_D/W$  is interpreted as the supply of cold carriers. The exponential expression depicts the probability that a carrier is accelerated without collisions over a distance  $\lambda$  to gain the energy  $\mathcal{E}_{IT}$ . The exponent  $n$  describes how  $\Delta N_{it}$  increases over time. For this empirically derived model, Hu presented in the same work a physical explanation based on the reaction-diffusion model leading to the same expression. For an estimation of the relation between substrate current and interface trap generation, one can combine the lucky electron model for impact-ionization (5.17) and for hot-carrier degradation (6.1) which results in

$$\Delta N_{it} = C \left[ t \frac{I_D}{W} \left( \frac{I_{\text{Sub}}}{I_D} \right)^{\mathcal{E}_{IT}/\mathcal{E}_{II}} \right]^n. \quad (6.2)$$

In this approach, the device life-time  $\tau$  is simply defined as the time until a certain critical value of  $\Delta N_{it}$  has been reached. Applying this, the lifetime can be estimated using

$$\tau \propto \frac{W}{I_D} \left( \frac{I_{\text{Sub}}}{I_D} \right)^{-\mathcal{E}_{IT}/\mathcal{E}_{II}}. \quad (6.3)$$

The equations lead to the conclusion that the worst-case condition for hot-carrier degradation coincides with the maximum substrate current.

This simple and often used model from the year 1985 cannot reproduce the degradation in modern devices. In extremely down-scaled devices the limitations of the model become clear: due to the small extensions the non-locality of the electric field leads to overestimated degradations. On the other hand, in low-voltage operation the energies stay below the threshold energy leading to vanishing degradation. Although the model shows to deliver wrong results for advanced and especially for highly down-scaled devices, it is still used for extrapolations of the device life-time and might still be the most widely used model. There are also extensions of the lucky electron model presented by different authors. Among them are Takeda and Suzuki [237], Goo [238], and Dreesen [239].

### 6.2.2 Hess Model

The work of Hess *et al.* [230, 234, 236] incorporates the two degradation mechanisms, the SP and MP processes, within the same framework. Breaking a bond means the release of bound hydrogen and the related desorption rate is derived considering the two degradation mechanisms:



## CHAPTER 6. HOT-CARRIER RELIABILITY MODELING

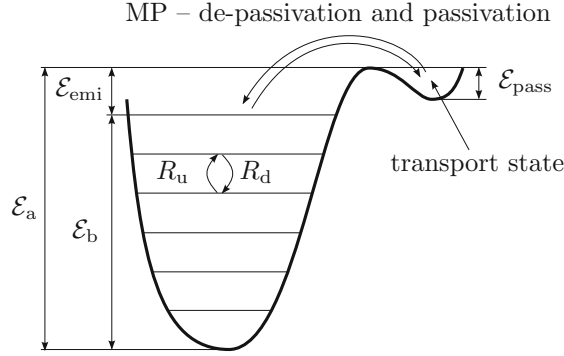


**Figure 6.2:** The Si-H as the truncated harmonic oscillator. The multiple vibrational bond is schematically shown. Phonon absorption shifts the energy state up, emission a step down. From the topmost bonding state the hydrogen release, i.e. bond de-passivation, is possible.

$R \approx R_{SP} + R_{MP}$ . Since these processes are not fully independent, this separation is only assumed to be an approximation.

The SP process describes the excitation of one of the bonding electrons to an anti-bonding state by a solitary hot carrier. Such an excitation leads to dissociation of the bond followed by release of the hydrogen atom. The dissociation rate can be estimated using

$$R_{SP} \propto \int_{\mathcal{E}_{th}}^{\infty} I(\mathcal{E}) P(\mathcal{E}) \sigma(\mathcal{E}) d\mathcal{E}, \quad (6.4)$$

where  $I(\mathcal{E})$  is the flux of carriers, i.e. the current of the carriers in the energy range  $[\mathcal{E}; \mathcal{E} + d\mathcal{E}]$ ,  $P(\mathcal{E})$  the desorption probability, and  $\sigma(\mathcal{E})$  the Keldysh-like reaction cross section (compare (5.21)). The lower boundary of the integration,  $\mathcal{E}_{th}$ , represents the minimum threshold energy required to break an interface bond with a single carrier.

The MP desorption rate is described in this model using the truncated harmonic oscillator (see Fig. 6.2) which can also be used to explain the giant isotope effect [235]. The bond energetics is described by a ladder of  $N$  bonded levels. The MP process initiates an excitation of the bond and an increase of the energy climbing the ladder of the energetic states. The vibrational mode excitation ends when the hydrogen is situated on the last bonded state. If the next portion of energy deposited by channel carriers exceeds the emission energy  $\mathcal{E}_{emi}$ , the hydrogen is released to the transport state. In the reverse direction the passivation rate is determined by the barrier energy  $\mathcal{E}_{pass}$ . Finally the desorption rate for de-passivation due to the MP process is written as [230]

$$R_{MP} \propto \left\{ \left( \frac{\mathcal{E}_b}{\hbar\omega} + 1 \right) \left[ P_d + \frac{1}{\tau} \exp \left( -\frac{\hbar\omega}{k_B T_L} \right) \right] \right\} \left[ \frac{P_u + \frac{1}{\tau}}{P_d + \frac{1}{\tau} \exp \left( -\frac{\hbar\omega}{k_B T_L} \right)} \right]^{-\frac{\mathcal{E}_b}{\hbar\omega}}, \quad (6.5)$$

where  $\mathcal{E}_b$  is the energy from the bottom of the energy well to the highest step of the energy ladder (see Fig. 6.2, [240]),  $\hbar\omega$  is the phonon-energy of the Si-H (Si-D) bond, and  $\tau$  is the



## 6.2. REVIEW OF MODELING APPROACHES

phonon life-time. The rates for vibrational mode excitation and decay between are described using the phonon absorption and emission rates  $P_u$  and  $P_d$ :

$$P_u \propto \int_0^{\infty} I(\mathcal{E}) \sigma_{ab}(\mathcal{E}) [1 - f_{PH}(\mathcal{E} + \hbar\omega)] d\mathcal{E}, \quad (6.6)$$

$$P_d \propto \int_{\hbar\omega}^{\infty} I(\mathcal{E}) \sigma_{em}(\mathcal{E}) [1 - f_{PH}(\mathcal{E} - \hbar\omega)] d\mathcal{E}. \quad (6.7)$$

$\sigma_{em}$  and  $\sigma_{ab}$  are the scattering cross-sections for bond-phonon emission and absorption, respectively, and  $f_{PH}(\mathcal{E})$  is the phonon occupation number.

In the model of Hess there are two important findings. First, the incorporation of the MP process for degradation modeling using the truncated harmonic oscillator model which agrees with the findings of the giant isotope effect. Second, the importance of the knowledge of the carrier energy distribution which is contained implicitly in  $I(\mathcal{E})$ . These peculiarities become important ingredients of other models presented later in this chapter.

Later, Hess highlights in [234] that threshold and activation energies are statistically scattered. It is shown that such a dispersion is an explanation for degradation time slopes lower than 1/2 [241], which cannot be explained using first-order kinetic equations for the interface bond-breakage. Additionally, the existence of two dominant activation energies widened due to the interface disorder has been suggested [236,242] explaining the different power-law slopes observed in degradation measurements as

$$N_{it} \approx \frac{p_1}{1 + (t/\tau_1)^{-\alpha_1}} + \frac{p_2}{1 + (t/\tau_2)^{-\alpha_2}}, \quad (6.8)$$

where  $p_1$  and  $p_2$  represent the probabilities of the realization of one of the dominant energies,  $\tau_1$  and  $\tau_2$  are characteristic times, and  $\alpha_1$  and  $\alpha_2$  describe the two different time slopes. The activation energies  $\mathcal{E}_{a,1}$  and  $\mathcal{E}_{a,2}$  can be modeled by the derivative of the Fermi-Dirac function [236,242] using

$$f(\mathcal{E}_{a,i}) = \frac{1}{\sigma_{a,i}} \frac{\exp\left(\frac{\overline{\mathcal{E}_{a,i}} - \mathcal{E}_{a,i}}{\sigma_{a,i}}\right)}{\left[1 + \exp\left(\frac{\mathcal{E}_{a,i} - \overline{\mathcal{E}_{a,i}}}{\sigma_{a,i}}\right)\right]^2}, \quad (6.9)$$

where the index  $i$  is either 1 or 2 for  $\mathcal{E}_{a,1}$  and  $\mathcal{E}_{a,2}$ , respectively. The corresponding mean values and the standard deviations are  $\overline{\mathcal{E}_{a,i}}$  and  $\sigma_{a,i}$ , respectively.

The microscopic modeling approach proposed by Hess incorporates many vital ingredients. The main breakthrough of the model is the consideration of competing SP and MP processes for interface trap creation and the employment of the formalism where the bond is modeled as a truncated harmonic oscillator. The missing features in this models are as follows: In the way the models were used, no solution for incorporating the real carrier energy distribution function was presented or applied. Another drawback is the missing link to the device level, the degradation is only described by the concentration of generated traps.

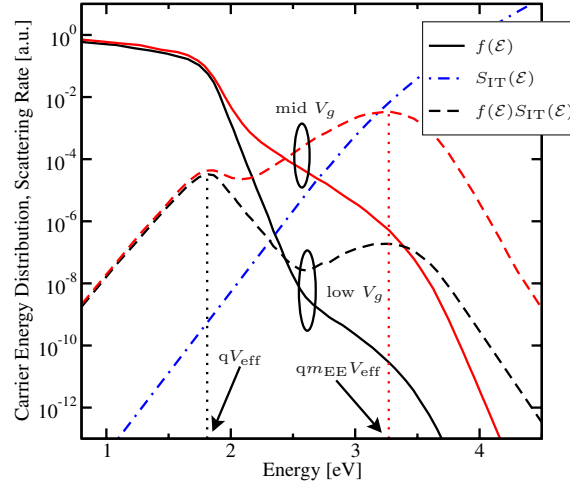


**Figure 6.3:** Carrier energy distribution function  $f(\mathcal{E})$ , desorption cross section  $S(\mathcal{E})$ , and resulting integrand with data taken from [243]. The two maxima of the rate are found at  $qV_{\text{eff}}$  and  $qm_{EE}V_{\text{eff}}$  and are used for modeling the HCD rate.

### 6.2.3 Energy Driven Approach by Rauch and La Rosa

Based on the lucky electron approach, La Rosa *et al.* [211] have assumed that the interface state generation is due to breaking of the Si-H interface bonds followed by the diffusion of hydrogen. This reaction is assumed to be reversible. The calculation of the degradation follows the approach used for impact-ionization already shown in Section 5.2.6, reading

$$\frac{dN_{\text{it}}}{dt} \propto F(I_S) \int S_{\text{IT}}(\mathcal{E}) f_c(\mathcal{E}) d\mathcal{E}. \quad (6.10)$$

Here  $f_c(\mathcal{E})$  is the carrier energy distribution function,  $S_{\text{IT}}(\mathcal{E})$  is the desorption cross section and  $F(I_S)$  is a function of the source current which appears to be either linear as  $F(I_S) = I_S$  or quadratic as  $F(I_S) = I_S^2$ . Also, for the interface state generation, the approximation (5.24) is applied, reducing (6.10) to a sum of products. In the following cases, a single dominant energy will be extracted reducing the equation to a single term.

Rauch *et al.* have shown in [212] that especially in the range of low operating voltages in short channel n-MOS devices the degradation can be explained by considering electron-electron scattering. This scattering mechanism increases the number of high energetic carriers leading to a significant hump in the carrier energy distribution function (see Fig. 6.3). The integrand in (6.10) therefore gives two maxima, one at the energy  $qV_{\text{eff}}$  and one at  $qm_{EE}V_{\text{eff}}$ . The first one is dominated by the knee near the maximum energy available from the steep potential drop at the drain [211] and can be approximated like shown for impact-ionization modeling (compare (5.28) on page 66). The second maximum comes from the hot-energy tail caused by the electron-electron scattering. This maximum is located at an energy approximately twice as

## 6.2. REVIEW OF MODELING APPROACHES

high as the first one. Electron-electron scattering increases quadratically with  $I_S$  [213] explaining the quadratic regime of (6.10).

Similar to the approach for the impact-ionization rate in (5.24), Rauch *et al.* used dominant energies in the model. Here this leads to two discrete maximum energies giving

$$\frac{dN_{it}}{dt} \propto I_S S_{IT}(qV_{eff}) \quad (6.11)$$

for the linear regime and

$$\frac{dN_{it}}{dt} \propto I_S^2 S_{IT}(qm_{EE}V_{eff}) \quad (6.12)$$

for the quadratic regime.

The emphasis of this modeling approach is again based on the importance of the carrier energy instead of the electric field. To receive an applicable model, the concept of estimating a single peak energy using the effective field instead of calculating the whole distribution function is used to make the calculations more simple.

### 6.2.4 Bravaix Model

In the hot-carrier degradation modeling approach by Bravaix *et al.* [223,244], three different modes depending on the carrier energy can be separated. The first mode is the high carrier energy regime, which usually coincides with lower currents. In this situation the lucky electron model appears valid. This SP degradation is used together with the dominant energy approach at knee points as proposed by Rauch *et al.* in (6.11). The device life-time in this regime is taken from (6.3) and is estimated with

$$\frac{1}{\tau_{SP}} \sim \frac{I_D}{W} \left( \frac{I_{Sub}}{I_D} \right)^{\mathcal{E}_{IT}/\mathcal{E}_{II}}, \quad (6.13)$$

based on substrate- ( $I_{Sub}$ ) and drain-current ( $I_D$ ), device width  $W$ , and the threshold energy levels  $\mathcal{E}_{II}$  and  $\mathcal{E}_{IT}$  for the impact-ionization and the SP bond dissociation process, respectively. The device-lifetime  $\tau_{SP}$  in this model is defined as the time until a certain number of interface traps have been generated.

The second mode corresponds to the electron-electron scattering induced degradation, also proposed by Rauch *et al.* using the formulation shown in (6.12). This leads to the device life-time

$$\frac{1}{\tau_{EES}} \sim \left( \frac{I_D}{W} \right)^2 \left( \frac{I_{Sub}}{I_D} \right)^{\mathcal{E}_{IT}/\mathcal{E}_{II}}. \quad (6.14)$$

The quadratic dependence on the current is due to impact-ionization and thereby created additional electron-hole pairs which are further accelerated up to energies required for triggering the bond dissociation.

## CHAPTER 6. HOT-CARRIER RELIABILITY MODELING

Finally the third mode is relevant at high electron fluxes but with carrier energies below the threshold energy for the SP process. Similar to the modeling approach by Hess, the MP mechanism is considered in this model. Furthermore, to describe the energetics of bond dissociation by this process the concept of the truncated harmonic oscillator shown in Fig. 6.2 is employed. The occupancies  $n_i$  of level  $i$  in the oscillator are described using rate equations. For the first and the following levels the rate equations are defined as [223]

$$\frac{dn_0}{dt} = P_d n_1 - P_u n_0 \quad (6.15)$$

$$\frac{dn_i}{dt} = P_d (n_{i+1} - n_i) - P_u (n_i - n_{i-1}), \quad (6.16)$$

with the rates  $P_d$  and  $P_u$  for bond excitation and decay. The great difference between the phonon life-time and the characteristic time of the hydrogen release suggests that the bonds reach the steady-state with  $dn_i/dt = 0$  practically immediately [223, 231]. Therefore the occupancy of each level can be determined recurrently using the ground state

$$n_i = \left( \frac{P_u}{P_d} \right)^i n_0. \quad (6.17)$$

When the steady-state of the oscillator is assumed to be established the transition over the last barrier can be considered. Thus, the equation for the last bonded level  $N$  can be rewritten as

$$\frac{dn_N}{dt} = P_u n_{N-1} - P_d \Delta N_{it} [H^*], \quad (6.18)$$

with the interface trap density  $\Delta N_{it}$  created during degradation and the concentration of the mobile hydrogen in the transport mode  $[H^*]$ . The density of traps generated during the stress is linked to the hydrogen concentration via  $\Delta N_{it} = [H^*] \lambda t$ . Combining this together with equations (6.17) and (6.18) leads to

$$\Delta N_{it} = \sqrt{n_0 \lambda \left( \frac{P_u}{P_d} \right)^N t^{0.5}}. \quad (6.19)$$

The rate  $\lambda$  corresponds to the thermally activated emission of the hydrogen atom over the barrier  $\mathcal{E}_{emi}$  (see Fig. 6.2) and is expressed as  $\lambda = \nu \exp(-\mathcal{E}_{emi}/k_B T)$ , where  $\nu$  is the attempt frequency. The derivation for (6.19) assumes a weak bond breakage intensity ( $\lambda t \ll 1$ ) and is therefore only valid as long as  $\Delta N_{it}$  is negligible compared to the whole population of Si-H bonds. The rates  $P_d$  and  $P_u$  consist of two components: the excitation and decay induced by the lattice and by a stimulation term (due to the carrier flux) for the vibrational modes  $S_{MP}$  [223]

$$P_u = S_{MP} (I_D/q) + w_e \exp(-\hbar\omega/k_B T) \quad (6.20)$$

$$P_d = S_{MP} (I_D/q) + w_e. \quad (6.21)$$

The breaking rate caused by the MP process,  $R_{MP}$ , can be used to describe the creation of interface traps in the form  $\Delta N_{it} = (R_{MP} t)^{0.5}$ . This rate evaluates to [223]

$$R_{MP} = n_0 \nu \left[ \frac{S_{MP} \left( \frac{I_D}{q} \right) + w_e \exp \left( -\frac{\hbar\omega}{k_B T} \right)}{S_{MP} \left( \frac{I_D}{q} \right) + w_e} \right]^{\frac{\mathcal{E}_b}{\hbar\omega}} \exp \left( -\frac{\mathcal{E}_{emi}}{k_B T} \right). \quad (6.22)$$

### 6.3. DISTRIBUTION FUNCTION BASED MODELING

Similar to the dominant energy approaches given by Rauch, Bravaix *et al.* suggest the approximation  $S_{MP} \sim (qV_{DS} - \hbar\omega)^{0.5}$ . With this approach, the life-time at a given temperature is estimated using

$$\frac{1}{\tau_{MP}} \propto \left[ V_{DS}^{0.5} \left( \frac{I_D}{W} \right) \right]^{\mathcal{E}_b/\hbar\omega}. \quad (6.23)$$

Under real stress/operating conditions all three modes presented contribute to the entire degradation process. Therefore all three regimes are taken into consideration in the Bravaix model. This finally leads to the device life-time

$$\frac{1}{\tau_d} = \frac{P_{SP}}{\tau_{SP}} + \frac{P_{EES}}{\tau_{EES}} + \frac{P_{MP}}{\tau_{MP}}, \quad (6.24)$$

with the fitting parameters  $P_{SP}$ ,  $P_{EES}$ , and  $P_{MP}$ .

To summarize, the Bravaix modeling approach combines and enhances the lucky electron model, the electron-electron scattering, and the truncated harmonic oscillator used to model the MP process. This approach has been shown to fit a large range of different devices.

### 6.3 Distribution Function Based Modeling

In our group a new physics-based modeling approach was developed and verified. This approach is based on TCAD device simulators, thereby providing good degradation results on the device level which can be used for reliable device lifetime prediction. The model spans from the microscopic level of interface defect generation up to the device level. The microscopic level considers SP and MP processes relying on the carrier energy distribution functions for electrons and holes. As for the device level, the drift-diffusion device simulation technique allows to extract the device parameter degradation. This gives the unique possibility to define the life-time using the design relevant attributes instead of simply dealing with trap concentrations. This is especially important, since the trap creation is highly localized and the effective device degradation depends on the position of the traps in the channel. The full device simulation step used in this approach gives a more accurate physical link between generated traps and device parameter degradation.

Like in the models by Hess and Bravaix, it is distinguished between single-particle and a multiple-particle components. In the first realizations of this model, only electrons were considered, giving good results for n-channel MOS devices with a channel length of  $0.5 \mu\text{m}$  [17, 245]. Later, also secondary generated holes were considered and consolidated by the model [18], as already proposed by other authors, e.g. Moens *et al.* [246, 247]. The degradation mechanism is driven by

## CHAPTER 6. HOT-CARRIER RELIABILITY MODELING

the acceleration integrals ( $I_{\text{SP}}$  and  $I_{\text{MP}}$ ) which are similarly defined as in the approaches by Hess and Bravaix, compare (6.4). These carrier acceleration integrals for the SP and MP process are

$$I_{\text{SP}} = \int_{\mathcal{E}_{\text{th,SP}}}^{\infty} f(\mathcal{E})g(\mathcal{E})\sigma_{\text{SP}}(\mathcal{E})v(\mathcal{E})d\mathcal{E}, \quad (6.25)$$

$$I_{\text{MP}} = \int_{\mathcal{E}_{\text{th,MP}}}^{\infty} f(\mathcal{E})g(\mathcal{E})\sigma_{\text{MP}}(\mathcal{E})v(\mathcal{E})d\mathcal{E}. \quad (6.26)$$

In contrast to the other presented modes, here the carrier energy distribution function is explicitly formulated as  $f(\mathcal{E})$ . Together with the density of states  $g(\mathcal{E})$  and the carrier velocity  $v(\mathcal{E})$  the quantity  $I(\mathcal{E})$  as used in (6.4) can be explicitly calculated. A Keldysh-like reaction cross section

$$\sigma_{\text{SP/MP}}(\mathcal{E}) = \sigma_{0,\text{SP/MP}}(\mathcal{E} - \mathcal{E}_{\text{th,SP/MP}})^{p_{\text{it}}} \quad (6.27)$$

with the values  $p_{\text{it}} = 11$  for SP and MP [223]. All equations exist for electrons and holes with corresponding  $f_{n/p}(\mathcal{E})$ ,  $g_{n/p}(\mathcal{E})$ ,  $v_{n/p}(\mathcal{E})$ ,  $\sigma_{n/p}(\mathcal{E})$ , and  $\mathcal{E}_{\text{th},n/p}$ , respectively. However, to increase the readability of the equations the subscripts are omitted here.

The interface state generation rate for the SP process in this model is assumed to be described by a first-order chemical reaction with the activation rate  $P_{\text{SP,act}}$ , giving

$$\frac{dn_0}{dt} = -P_{\text{SP,act}}n_0. \quad (6.28)$$

$n_0$  is the number of non-broken interface Si–H bonds. The activation rate  $P_{\text{SP,act}}$  is modeled using the attempt frequencies  $\nu_{\text{SP},n/p}$  and the acceleration integral as

$$P_{\text{SP,act}} = \nu_{\text{SP},n}I_{\text{SP},n} + \nu_{\text{SP},p}I_{\text{SP},p}. \quad (6.29)$$

The concentration  $n_0$  is related to the total number of interface bonds  $N_0$  and the number of broken interface bonds  $N_{\text{SP}}$ , i.e. the number of interface traps activated due to the SP process, as

$$N_{\text{SP}} = N_0 - n_0, \quad (6.30)$$

Together with the boundary condition of  $n_0(t = 0s) = N_0$ , the solution of (6.28) using (6.30) gives the number of interface traps created due to the SP process over time as

$$N_{\text{SP}} = N_0 \left(1 - \exp(-P_{\text{SP,act}}t)\right). \quad (6.31)$$

Like in the Bravaix approach, a truncated harmonic oscillator is employed to describe the bond energetics. However, we write the rate equations for the last bonded state in a different fashion: defined as

$$\frac{dn_0}{dt} = P_d n_1 - P_u n_0 \quad (6.32)$$

$$\frac{dn_i}{dt} = P_d(n_{i+1} - n_i) - P_u(n_i - n_{i-1}) \quad (6.33)$$

$$\frac{dn_{N_l}}{dt} = P_u n_{N_l-1} - P_d n_{N_l} - P_{\text{MP,act}} n_{N_l} + \tilde{P}_{\text{MP,pass}} N_{\text{MP}}^2. \quad (6.34)$$

### 6.3. DISTRIBUTION FUNCTION BASED MODELING

The rate equation for the topmost energy level (6.34) consists of four processes: the transition to the topmost level from the level below, the transition from the topmost level down to the level below, the desorption rate  $P_{\text{MP,act}}$  for the actual bond breaking, and the passivation rate  $P_{\text{MP,pass}}$ . The rates are defined following the Arrhenius relation,

$$P_{\text{MP,pass}} = \nu_{\text{MP,pass}} \exp\left(-\frac{\mathcal{E}_{\text{pass}}}{k_{\text{B}}T_{\text{L}}}\right) \quad (6.35)$$

$$P_{\text{MP,act}} = \nu_{\text{MP,act}} \exp\left(-\frac{\mathcal{E}_{\text{emi}}}{k_{\text{B}}T_{\text{L}}}\right), \quad (6.36)$$

using the energy barriers as shown in Fig. 6.2 and the attempt frequencies  $\nu_{\text{MP,pass}}$  and  $\nu_{\text{MP,act}}$ . The passivation reaction depends on the existence of a dangling bond and the existence of a hydrogen atom which can be passivated, making this a second-order reaction. The density of dangling bonds is equal to the density of generated traps. No initial free hydrogen is assumed, so the available number of hydrogen atoms corresponds to the number of generated traps. This leads to the quadratic dependence  $N_{\text{MP}}^2$  in (6.34). To satisfy the dimensionality, the passivation rate is written as  $\tilde{P}_{\text{MP,pass}} = P_{\text{MP,pass}}/N_0$ .

The great disparity between the times between bond excitation and decay on one side and hydrogen bond dissociation dictates that these two processes can be treated quasi-separately [223, 245]. The steady-state within the oscillator is assumed, which is established momentarily compared to the hydrogen release/absorption. By neglecting the last two terms in (6.34) the truncated harmonic oscillator is decoupled from the bond breaking process and the occupation dynamics give

$$n_i = \left(\frac{P_u}{P_d}\right)^i n_0. \quad (6.37)$$

In a second step, as the harmonic oscillator is considered in steady-state, for the bond dissociation the first two terms in (6.34) can be omitted. While solving this differential equation two assumptions were used. The first is similar to that in [223] and claims that the concentration of virgin bonds does not change drastically. The second is the boundary condition that initially all bonds are virgin. The trap concentration due to the MP process over time becomes

$$N_{\text{MP}} = N_0 \left[ \frac{P_{\text{MP,act}}}{P_{\text{MP,pass}}} \left(\frac{P_u}{P_d}\right)^{N_l} \left(1 - \exp(-P_{\text{MP,act}}t)\right) \right]^{1/2}. \quad (6.38)$$

For weak stresses and/or short stress times, meaning  $P_{\text{MP,act}}t \ll 1$ , a Taylor expansion gives the approximation  $1 - \exp(-P_{\text{MP,act}}t) \approx P_{\text{MP,act}}t$  and one receives the square root time dependence like in the Bravaix model, see (6.19).

The probabilities  $P_u$  and  $P_d$  for the excitation and decay of the Si-H bond are defined similarly to equations (6.20) and (6.21) in the Bravaix model, using the acceleration integrals, the phonon frequency  $w_e$  and the distance between the oscillator levels  $\hbar\omega$ :

$$P_u = \nu_{\text{MP},n} I_{\text{MP},n} + \nu_{\text{MP},p} I_{\text{MP},p} + w_e \exp\left(-\frac{\hbar\omega}{k_{\text{B}}T_{\text{L}}}\right) \quad (6.39)$$

$$P_d = \nu_{\text{MP},n} I_{\text{MP},n} + \nu_{\text{MP},p} I_{\text{MP},p} + w_e. \quad (6.40)$$



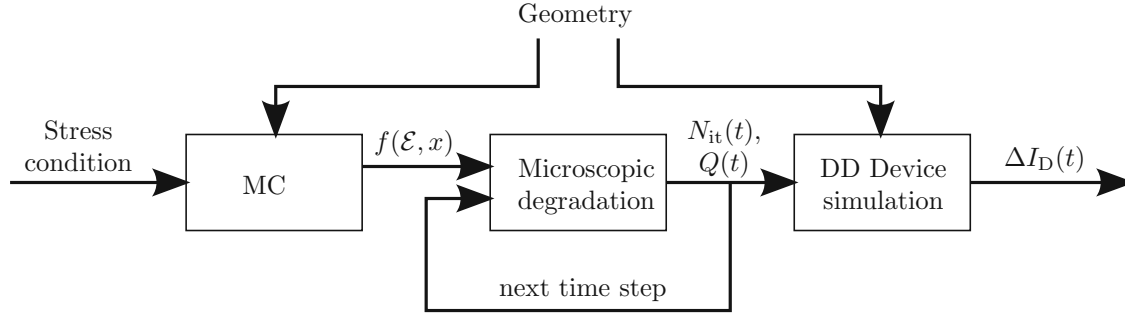


**Figure 6.4:** The flow chart of the distribution function based hot-carrier degradation model. The Monte Carlo (MC) simulator delivers the spatially varying carrier energy distribution function  $f(\mathcal{E}, x)$  for given stress conditions. This information is then used to calculate the density of generated traps for all time steps. For each time step the output characteristic of the device at operation condition is calculated using the macroscopic device simulation to evaluate the degradation, i.e.  $\Delta V_T(t)$ .

The excitation corresponds to a phonon absorption, meaning stimulation of the bond leading to a step up on the energy levels of the oscillator, and the decay corresponds to a phonon emission, meaning a step down one level.

The total trap concentration includes the two concurrent SP- and MP-processes and is combined using probabilities to balance the two processes as

$$N_{it} = p_{SP}N_{SP} + p_{MP}N_{MP}. \quad (6.41)$$

Due to the position dependence of the carrier energy distribution function, and therefore the acceleration integrals, the resulting concentration of generated traps also depends on the position.

The interface states created impact the device performance by trapping and de-trapping charges. This trapping process can be simulated using an interface Shockley-Read-Hall (SRH) modeling approach like shown in Section 4.2.2. Only the trapped charges influence the output characteristics of the degraded device. In this model the interface trap is characterized by its charge state evaluated for the given coordinate along the interface and particular stress/operating conditions. The charge influences the electrostatic potential and degrades the carrier mobilities due to Coulombic scattering mechanisms. A simple interface charge induced mobility reduction model has been presented in Section 4.2.1.

### 6.3.1 Model Implementation

The current implementation of the model spans from the microscopic trap generation level to the device operation level. The degradation is modeled using partly existing tools and partly newly implemented modules which are used to calculate the microscopic spatially distributed damage. The implementation consists of three components shown in Fig. 6.4. A Monte Carlo simulator is used to calculate the distribution functions, the degradation is calculated using the equations



### 6.3. DISTRIBUTION FUNCTION BASED MODELING

presented in the previous section, and the impact on the device performance is analyzed using a drift-diffusion simulator.

To calculate the carrier energy distribution function the Monte Carlo method is applied using the full-band device simulator MONJU [16]. To capture the hole contribution, impact-ionization needs to be considered. Simulations are performed on the device under test for a certain stress condition, i.e. drain- and gate-voltage. The output of this model is the electron and hole energy distribution functions along the Si-SiO<sub>2</sub> interface. Due to the stochastic nature of the Monte Carlo method, the convergency behavior is poor and long simulation times are required. This concerns especially high-energy tails of the distribution function, where the number of carriers is low. Therefore the computational process would take disproportionally long simulation times to obtain smooth, i.e. noiseless, results and therefore commonly noisy data has to be used.

In the next step, the distribution functions  $f(\mathcal{E})$  for electrons and holes are transferred to the degradation module (see Fig. 6.4) which calculates the trap density as a function of the lateral coordinate for each stress time step. The microscopic process of the generation for MP and the SP processes is described using the acceleration integrals in equations (6.25) and (6.26) and the trap generation in equations (6.31) and (6.38). As a result, the interface trap density at each position over time is available. In the current model implementation, the initially calculated distribution function is used for all time steps, because a self-consistent re-calculation using the Monte Carlo method would be extremely time-consuming. However, the change of the distribution function during the degradation has only a small impact on the results [248]. For the calculation of the charge trapped by interface states, the SRH equations have to be solved. The operation conditions in the reference measurements used for model validation ( $V_G = 2\text{ V}$ ) suggest that the traps are charged throughout the simulation. Hence, all interface traps are assumed as fixed interface charges.

Finally, the position dependent interface charge is then introduced into our multi-purpose device simulation tool MINIMOS-NT [120]. To gain reasonable simulation times, the drift-diffusion transport model as described in Section 4.1.2 is used.

#### 6.3.2 Model Evaluation

The presented model is evaluated by comparing simulation results employing a set of 5 V n-MOS transistors fabricated using the same architecture but with different channel lengths. The devices are part of a 0.35  $\mu\text{m}$  high-voltage mixed signal process by *ams*. The channel lengths are 0.5, 1.2, and 2.0  $\mu\text{m}$ . The 0.5  $\mu\text{m}$  device is depicted in Fig. 6.5. The devices are stressed at a gate voltage of  $V_{GS} = 2.0\text{ V}$  and a drain voltage of  $V_{DS} = 6.25\text{ V}$  at 25 °C. The stress was measured for a period of 10,000 s.

The simulation setup was used as described previously and the model was calibrated to fit the drain current degradation operating with a single parameter set. For the fitting process it was considered, that both acceleration integrals have the same functional structure. They differ only in the prefactors  $\nu$  (see (6.29), (6.39), and (6.40)). This leads to  $I_{SP} = I_{MP}$  for

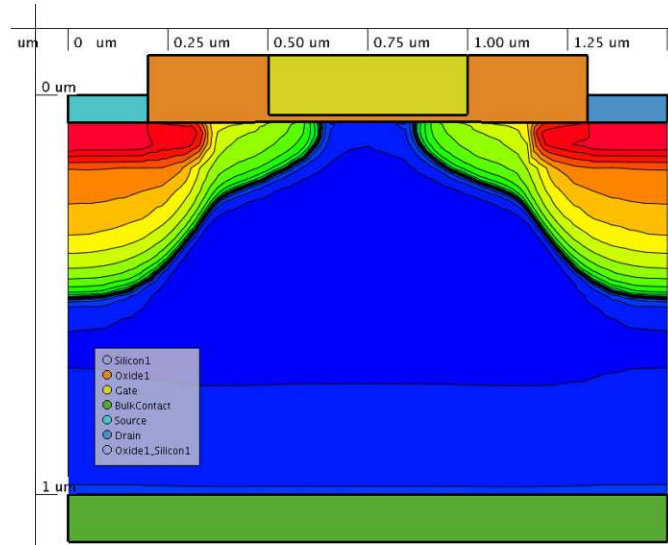


**Figure 6.5:** Geometry and net doping concentration of the 0.5  $\mu\text{m}$  n-MOSFET used for simulations. The device structure was generated using process simulation. Legend omitted due to non-disclosure agreement.

each carrier type. Hence, the resulting degradation in Fig. 6.6 shows a good agreement between simulations and measurements. For a proper model evaluation, the contributions from electron and hole components are plotted separately. As can be seen, the 0.5  $\mu\text{m}$  device is the only one in which the full degradation can be represented using only the electron induced degradation component. This tendency was also observed in [18] and is already mentioned on page 85. This can be investigated in more detail looking at the acceleration integral and the interface state density  $N_{it}$  along the channel, both are shown in Fig. 6.7. First, one can see that the worst degradation happens at the drain (right) end of the device, where the electrons accelerated along the channel have reached the highest energy. This part of the degradation is caused by the electron SP process. Note that the damage is partly located outside the channel. The hole contribution is caused by secondary holes generated by impact-ionization. Consequently, they are accelerated towards the source side (left), gain energy, and reach the maximum energy within the channel area. One can clearly see that the hole component of the acceleration integral is always shifted towards the source and is situated within the channel area. This explains why the hole contribution, which is characterized by a much lower portion of  $N_{it}$ , still plays a relevant role for the entire  $I_{D,lin}$  degradation.

An important analysis using this model has been done by Starkov *et al.* [249] comparing measurements and simulation results for the worst-case hot-carrier degradation. In the n-MOS transistor, the substrate current  $I_{Sub}$  is utilized as a criterion for the worst-case condition, reflecting the impact-ionization generation [223]. For the p-MOS transistor the gate current has been used as an indicator for maximum hot-carrier degradation [224]. In the simulations, the maxima of the acceleration integrals have been used to compare the severity of the ongoing degradation process. The impact has been compared with measurement data from the 0.5  $\mu\text{m}$

### 6.3. DISTRIBUTION FUNCTION BASED MODELING

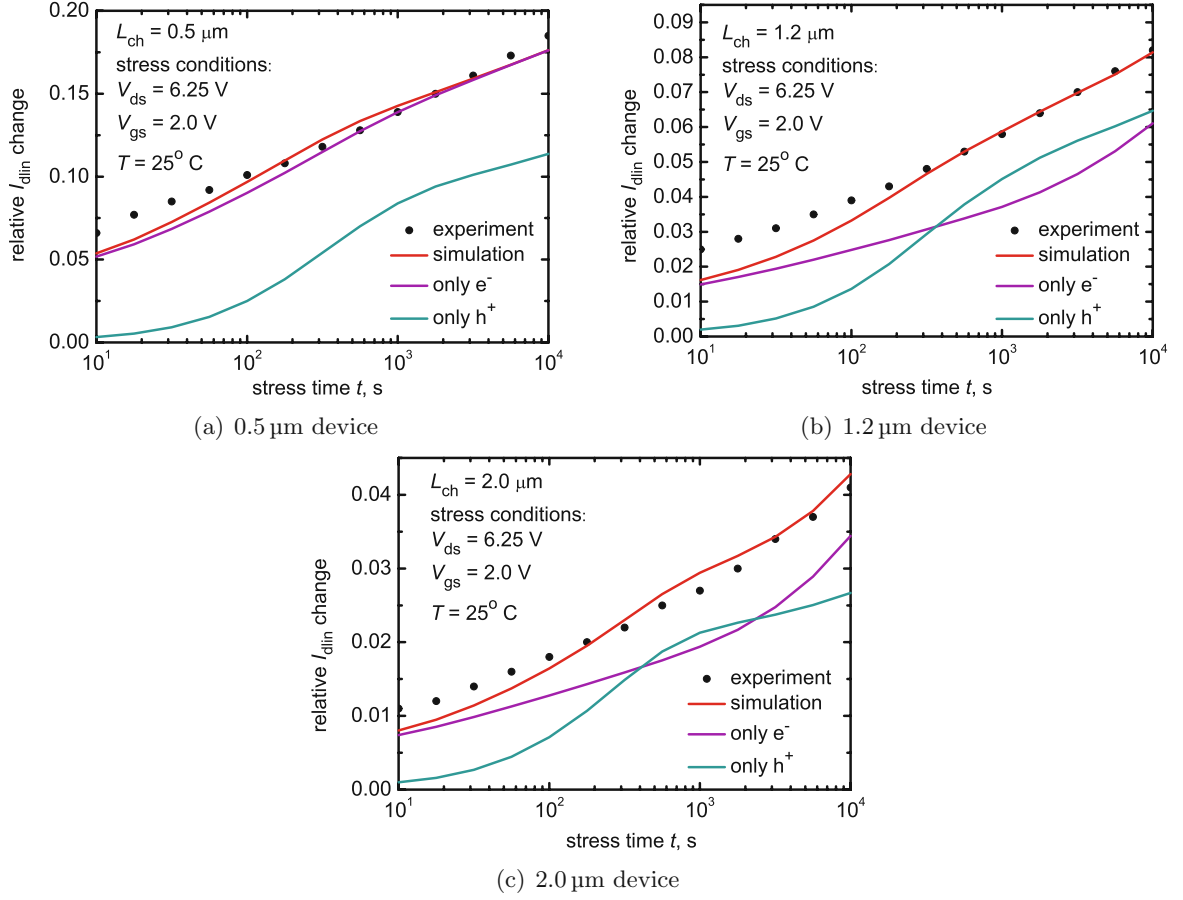


**Figure 6.6:**  $I_{D,lin}$  degradation in devices with different channel lengths. The simulation result using only electrons, only holes, and using both components are compared to the measurement results [18].

devices over a wide range of varying  $V_{DS}$  and  $V_{GS}$ . The results are depicted as a color map in Fig. 6.8. The figure reflects the correct tendency of the bias dependent hot-carrier stress.

#### 6.3.3 Model Discussion

This model tries to address the whole hierarchy of physical phenomena, taking information from the carrier energy distribution function to model the microscopic degradation processes, generating interface traps, and then simulating the influence of the traps on the device behavior. The evaluations performed on various levels show good agreement in comparison to the measurement data.

Unfortunately, the complexity of this approach, which considers the distribution function for electrons and holes, results in severe limitations regarding simulation time and flexibility of

## CHAPTER 6. HOT-CARRIER RELIABILITY MODELING

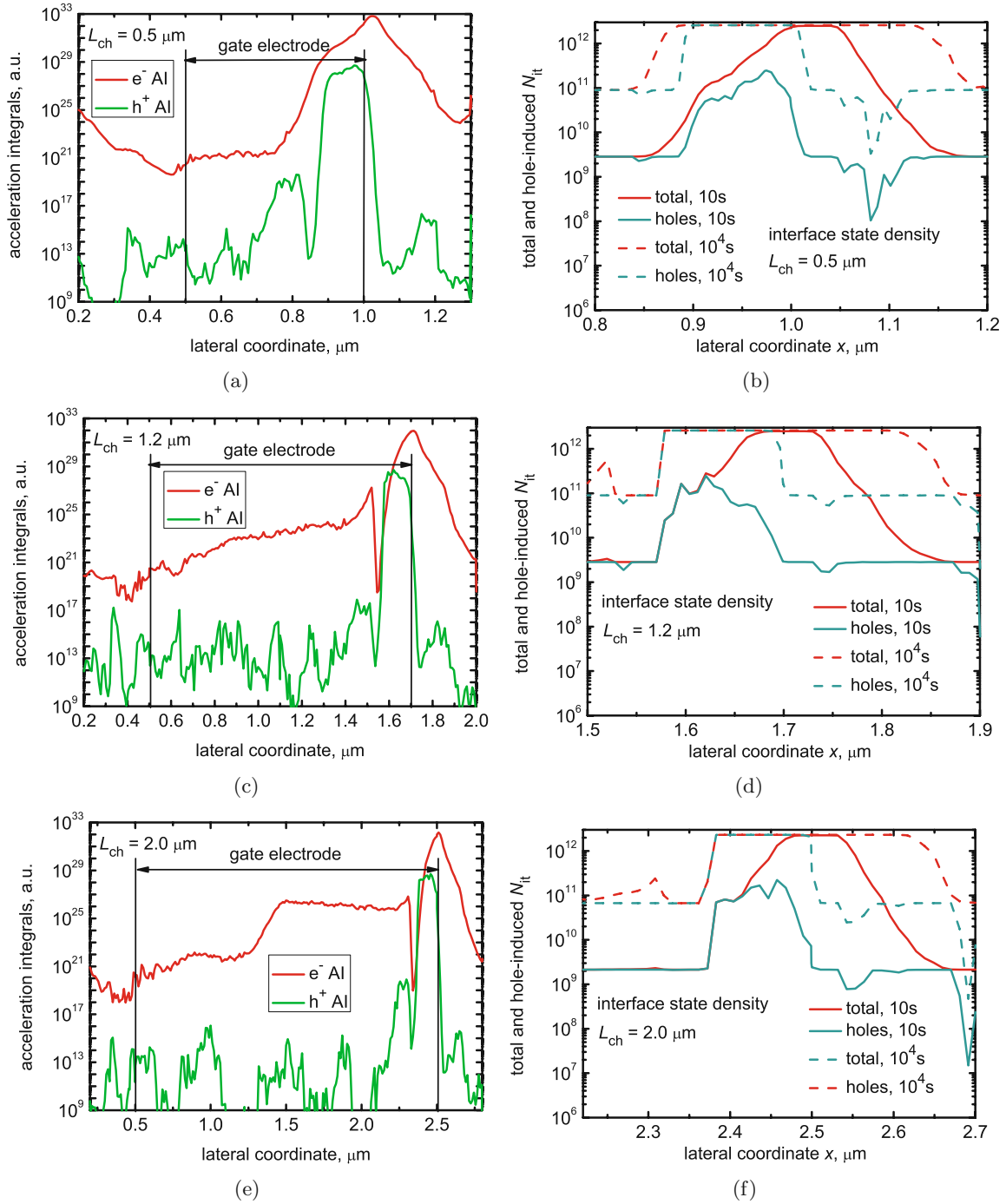


**Figure 6.7:** The figures show the acceleration integral for electrons and holes in the 0.5 (a), 1.2 (c), and 2.0  $\mu\text{m}$  (e) devices and the total  $N_{it}$  concentration as well as contributions to  $N_{it}$  produced only by holes also for 0.5 (b), 1.2 (d), and 2.0  $\mu\text{m}$  (f) channel MOSFETs [18]. All the quantities are plotted as functions of the lateral coordinate. The source corresponds to the abscissa origin. The  $N_{it}$  concentrations are shown after 10 and 10,000 s stress times.

### 6.3. DISTRIBUTION FUNCTION BASED MODELING

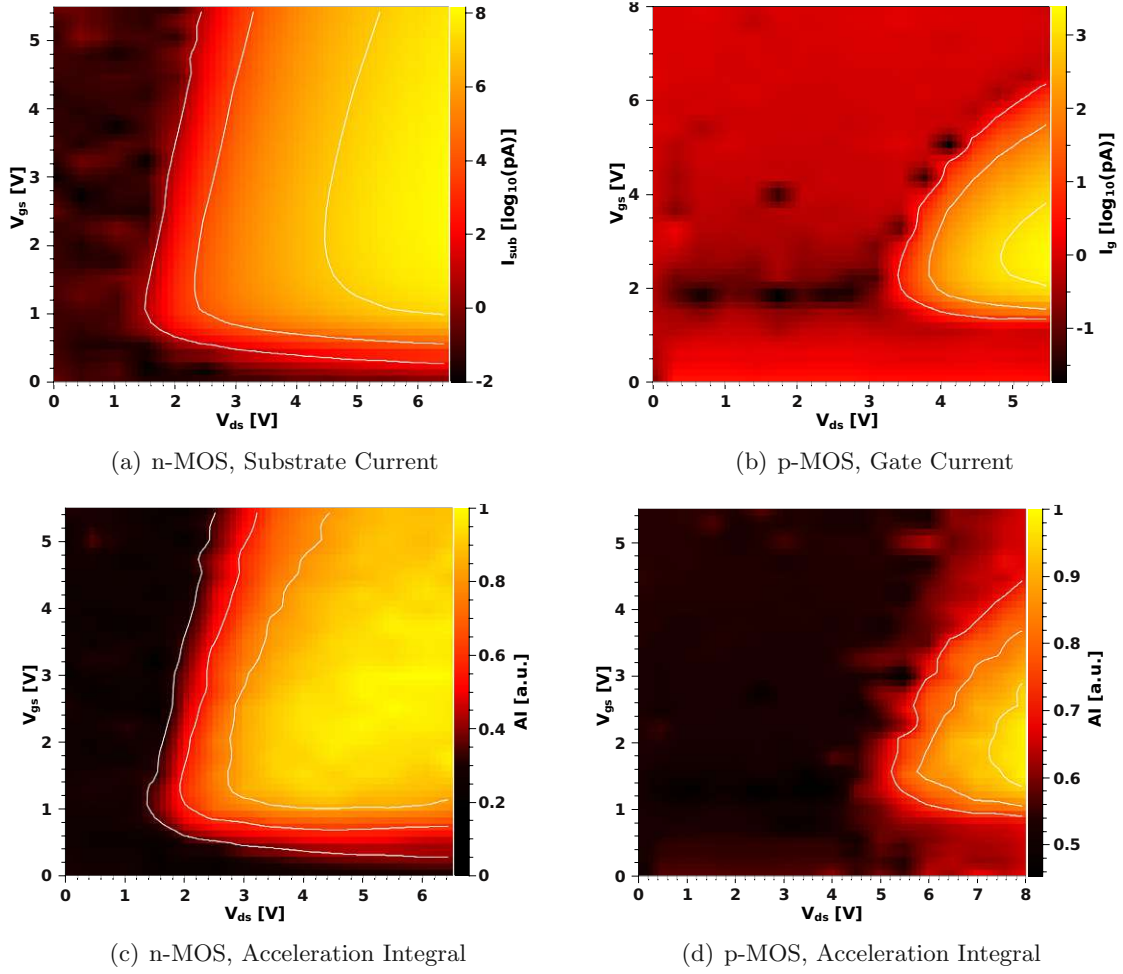


**Figure 6.8:** Color map plotted over the gate ( $V_{GS}$ ) and drain ( $V_{DS}$ ) voltages. The measured substrate current of the n-MOS (a) and of the gate current of the p-MOS (b) transistor are compared to the maximum value of the acceleration integral, shown in (c) and (d), respectively. (Figures taken from [249])

the simulation setup. The Monte Carlo simulations are very time consuming and it is only reasonable to calculate the set of distribution functions once, i.e. for the virgin device. Changes of the stress conditions during the stress cycle cannot be captured straightforward, and hence a new Monte Carlo simulation would be required for each step. Another method to calculate the carrier distribution functions is the spherical harmonics expansion [124,125]. A device simulator based on this approach is currently being developed at our institute and first results have been published [250]. However, while this approach is computationally much more efficient than Monte Carlo simulations, it still requires a huge amount of computers working memory, thereby posing some limitations in simulations of real devices. Therefore, other simplified approaches to overcome these problems are worthy to be discussed. A method which is solely based on drift-diffusion is the topic of the upcoming section Section 6.4.

## CHAPTER 6. HOT-CARRIER RELIABILITY MODELING

A weakness of the current model might be that so far only two limiting cases related to hydrogen desorption are considered, i.e. from the ground state (SP mechanism) and from the topmost energy level (MP mechanism) of the oscillator. An extension considering hydrogen desorption from all energy levels would represent the actual dissociation process more precisely. For this purpose, the rate equations must be extended and some new barriers need to be introduced for this. This approach has already been suggested by McMahon *et al.* [231].

Apart from the bond breakage at the interface, the model does not yet contribute to possible oxide bulk traps or charges [251]. However, up to this point the model seems to be able to represent the experimental data reasonably well and the matter whether bulk oxide traps contribute to hot-carrier degradation or not is unresolved. In fact, in the intimately related degradation mode, in bias temperature instability, just trapping/de-trapping in the oxide bulk is responsible for the recoverable component of the damage [252–254]. However, hot-carrier degradation demonstrates, if at all, rather weak recovery. This suggest that bulk oxide traps do not play a substantial role in hot-carrier degradation. At the same time, recent measurements have proven the existence of the threshold voltage turn-around effect that can be explained by oxide charges [248]. The next improvement steps can, therefore, be oriented towards the inclusion of oxide traps into the hot-carrier degradation model.

### 6.3.4 Modifications

There are some modification of our model that would make the formalism more complete. First, also the single particle process can be considered to undergo a passivation reaction, introducing the rate  $P_{\text{SP,pass}}$ , extending (6.28) to

$$\frac{dn_0}{dt} = -P_{\text{SP,act}}n_0 + \tilde{P}_{\text{SP,pass}}N_{\text{SP}}^2. \quad (6.42)$$

The formulation uses  $\tilde{P}_{\text{SP,pass}}$  instead of  $P_{\text{SP,pass}}$  to keep the units consistent.

The second modification suggested, concerns the fundamental splitting between the SP and the MP process introduced in (6.41). By using just a single trap density  $N_{\text{it}}$  instead of the two separate ones ( $N_{\text{SP}}$  and  $N_{\text{MP}}$ ), it is possible to combine the rate equations (6.32) – (6.34) and (6.42) leading to

$$\frac{dn_0}{dt} = P_d n_1 - P_u n_0 - P_{\text{SP,act}}n_0 + \tilde{P}_{\text{SP,pass}}N_{\text{it}}^2 \quad (6.43)$$

$$\frac{dn_i}{dt} = P_d(n_{i+1} - n_i) - P_u(n_i - n_{i-1}) \quad (6.44)$$

$$\frac{dn_{N_l}}{dt} = P_u n_{N_l-1} - P_d n_{N_l} - P_{\text{MP,act}}n_{N_l} + \tilde{P}_{\text{MP,pass}}N_{\text{it}}^2. \quad (6.45)$$

The model as presented evaluates the concentration of the broken bonds  $N_{\text{it}}$  in the range of  $[0 \dots N_0]$ . For a convenient handling, a fraction  $f = N_{\text{it}}/N_0$  can be used defining the relative

## 6.4. ACCELERATION INTEGRAL ESTIMATION IN DRIFT-DIFFUSION

bond breakage. For this, one can define the total number of passivated bonds (on all energy levels of the oscillator) as

$$N = \sum_{i=0}^{N_l} n_i = n_0 \sum_{i=0}^{N_l} \left( \frac{P_u}{P_d} \right)^i = n_0 k, \quad (6.46)$$

where the geometric series describing  $k$  can be evaluated as

$$k = \frac{\left( \frac{P_u}{P_d} \right)^{N_l+1} - 1}{\left( \frac{P_u}{P_d} \right) - 1}. \quad (6.47)$$

At time  $t = 0$  s no interface traps have been generated and the total number of bound traps is, therefore, equal to the maximal available number of bonds  $N_0$ . The relation between  $N$ ,  $N_0$ , and  $N_{it}$  is thus

$$N = N_0 - N_{it} \quad (6.48)$$

and inserting  $f = N_{it}/N_0$  gives

$$N = (1 - f) N_0. \quad (6.49)$$

Considering the oscillator in steady-state and by combining the SP and MP rates from equations (6.31) and (6.38), the resulting bond generation rate can then be written as

$$\frac{df}{dt} = [P_{SP,act} + P_{MP,act}] (1 - f) - \left[ P_{SP,pass} + k \left( \frac{P_d}{P_u} \right)^{N_l} P_{MP,pass} \right] f^2. \quad (6.50)$$

Note that the rates were substituted as  $P_{SP,pass} = \tilde{P}_{SP,pass} N_0$  and  $P_{MP,pass} = \tilde{P}_{MP,pass} N_0$ .

## 6.4 Acceleration Integral Estimation in Drift-Diffusion

The long simulation times required for the thorough calculation of the distribution function using the Monte Carlo method make the presented hot-carrier degradation model unsuitable for a wide spread industrial use. To overcome this problem, it is investigated in this work how to estimate the acceleration integral within the drift-diffusion framework. The absence of the distribution function makes only two basic approaches feasible. First, the distribution function can be approximated so that the integrals in equations (6.25) and (6.26) can be evaluated. Or second, a fitting formula for the acceleration integral has to be found. It is expected, that the disadvantages of such estimations, especially the reduced accuracy, can be partly compensated by the enormous performance gain which is achieved by omitting the Monte Carlo simulations. Another positive side effect of the short simulation time is the possibility to evaluate the acceleration integral at each time step. This means that the rate equations can be solved for every stress time step. Therefore self-consistent degradation simulations can be performed.



## CHAPTER 6. HOT-CARRIER RELIABILITY MODELING

The two concepts have been implemented and used in MINIMOS-NT. The implementation is based on the formulation in (6.50) and is solved self-consistently in the drift-diffusion framework. The occupation of created interface traps is modeled according to the Shockley-Read-Hall formalism, including the contributions to the Poisson and the continuity equation.

In the following, the simulations are based on the  $0.5\mu\text{m}$  device depicted in Fig. 6.5. This device was chosen because it is the only one of the devices analyzed in Section 6.3.2 where the electron contribution is sufficient for the degradation modeling (compare Fig. 6.6). Therefore, the effect of holes can be neglected. This limitation is important, because in the drift-diffusion scheme the carrier energy, and hence, the carrier distribution function can only be evaluated from the electric field. Therefore, in this paradigm it is impossible to distinguish between the individual carrier energies, and hence, to separate trap creation processes. To summarize, the hole contributions would introduce additional obstacles regarding the non-locality of the electric field, impact-ionization, and hole energy which could not be reproduced in the drift-diffusion model as required.

Where applicable, the parameters have been chosen equally to the results which were calibrated within the Monte Carlo approach. The mobility degradation model in (4.13) is used to contribute to the interface charge scattering.

### 6.4.1 Distribution Function Based Estimation

For the evaluation of the acceleration integral, first an approximation for the distribution function has to be defined. Possibilities for this have been shown in Section 4.3.2 on page 50. The formulation by Grassler in (4.28) gives the best results and is, therefore, used for the investigations in this work. The parameter  $\mathcal{E}_{\text{ref}}$  is always evaluated using (4.29). However, the parameter  $b$  was either evaluated using (4.31), or, as has been discussed on page 52, is set to  $b = 3.0$ . Both variants are used in the following. The acceleration integral for electrons is computed using (6.25) and (6.26). The calibrated reference curve based on the Monte Carlo results is calculated using  $\mathcal{E}_{\text{th}} = 0.1\text{ eV}$ . For the estimations in this section, however, different attempts with different threshold energies have been applied.

The results are summarized in the figures on the facing page. The reference data clearly show a peak of the acceleration integral at the drain edge of the gate at  $1\mu\text{m}$ . Both approximations, which use either a constant or non-constant value for  $b$ , result in a peak at the very same position. However, a second peak is also pronounced. In some constellations shown, this second peak is even more prominent. It is shifted towards the channel and is visible at the position of approximately  $0.9\mu\text{m}$ , which is near the pn-junction. This peculiarity can be explained by the interplay between the electric field and the electron concentration along the channel. In this model, both quantities influence the acceleration integral. The electric field explicitly defines the carrier distribution function, while the concentration enters via the normalization condition. Roughly speaking, the acceleration integral behavior can be explained by the product of the electric field and the concentration. Both quantities have extreme values at the end of the gate, whereas the electric field has a maximum and the carrier concentration a minimum. Here is



#### 6.4. ACCELERATION INTEGRAL ESTIMATION IN DRIFT-DIFFUSION

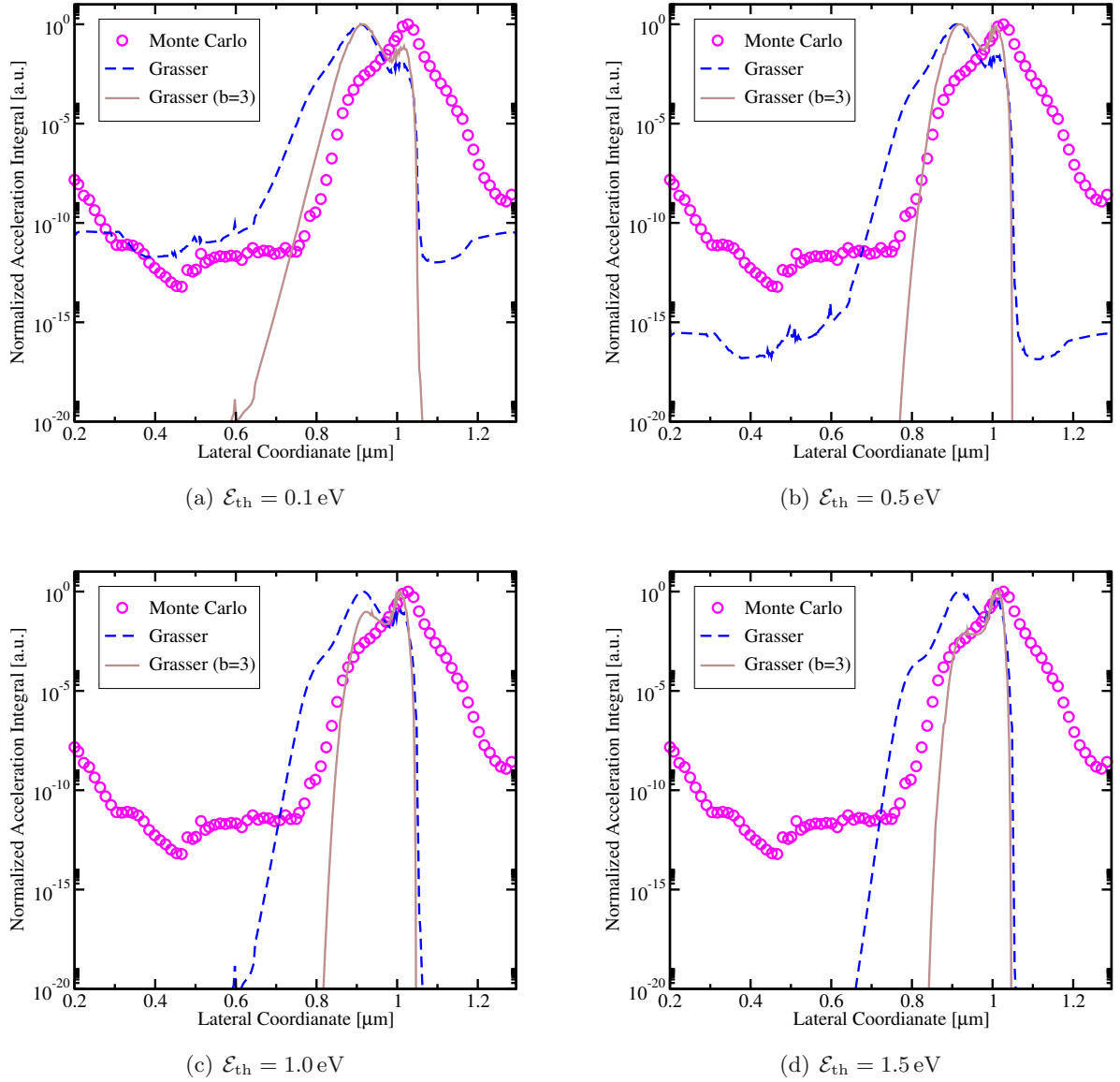


**Figure 6.9:** Evaluation of the acceleration integral for electrons in the  $0.5 \mu\text{m}$  test device using different representations of the distribution function and different threshold energies in comparison to reference Monte Carlo data ( $\mathcal{E}_{th} = 0.1 \text{ eV}$ ). The estimations show two peaks, one at the end of the gate, the other near the pn-junction. These two peaks come from an interplay between the electric field and carrier concentration along the channel.

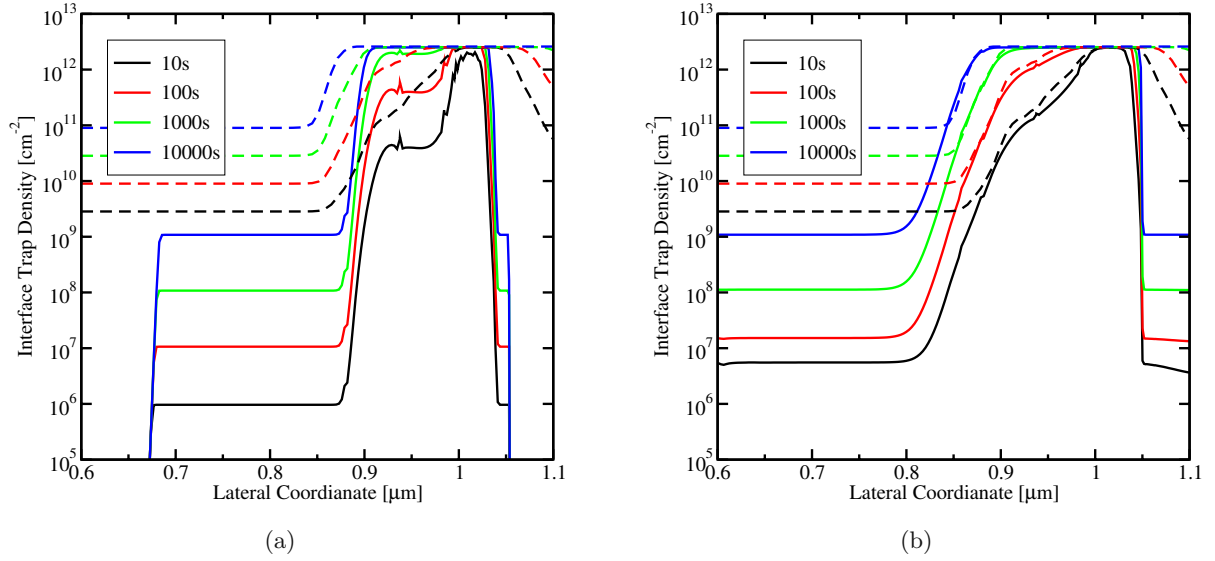


**Figure 6.10:** The evolution of the interface trap concentration with the stress time. The solid lines show the degradation using the distribution function estimation with the acceleration integral from Fig. 6.9(d) (a) and the carrier temperature based estimation with acceleration integral from Fig. 6.12 (b). The dashed lines are the references from the Monte Carlo based simulations.

the position of the first maximum. Towards the channel, the electric field decreases and the carrier concentration increase. This combination leads to the second maximum. By comparing the different approaches in Fig. 6.9, one can see that the curve in Fig. 6.9(d) is the only one that suppresses this second peak. This simulation uses the constant exponent  $b = 3.0$  and a threshold energy of 1.5 eV. Hence, this combination is selected to be used in the following.

The propagation of the interface trap creation over degradation time can be seen in Fig. 6.10(a). The flat area left to the main peak in the acceleration integral clearly maps to the flattened area in the  $N_{it}$  profile. The constantly increasing interface trap density in the range from approximately 0.7 to 0.9  $\mu\text{m}$  is caused by the MP process. The final degradation of the drain current using this approximation is shown in Fig. 6.11. It can be seen that the overall linear drain current change vs. time within the measurement window can be represented. However, the additional plateau in the peak area of the acceleration integral leads to an additional bending in the drain current degradation curve between 100 and 1000 s.

#### 6.4.2 Carrier Temperature Based Evaluation

As shown above, the attempt to evaluate the acceleration integral based on artificially created distribution functions does not give satisfying results. Therefore, an empirical approach is proposed, which employs the carrier temperature. The acceleration integral of the SP process

#### 6.4. ACCELERATION INTEGRAL ESTIMATION IN DRIFT-DIFFUSION

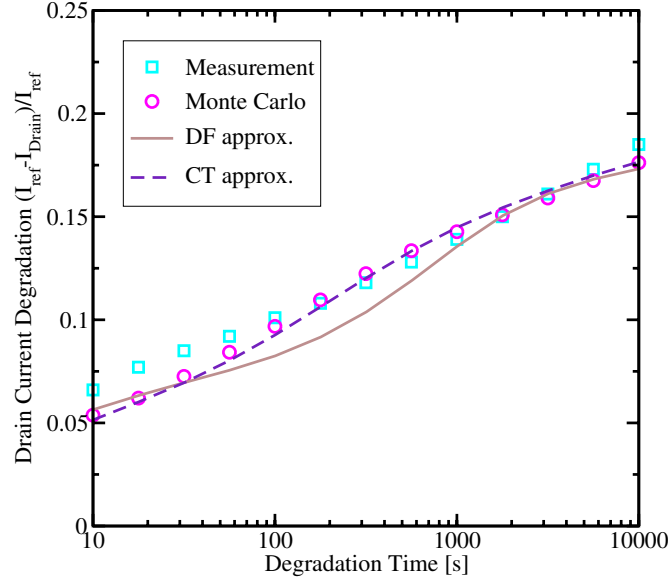


**Figure 6.11:** Measured and simulated relative drain current degradations. Simulations are performed using the Monte Carlo, the distribution function (DF) based, and the carrier temperature (CT) based estimation.

is driven by high-energy carriers. It is therefore linked to the electron temperature  $T_n$  and the empirical formula is used

$$I_{SP,n} \approx A_T \left( \frac{T_n}{T_{ref}} \right)^\beta, \quad (6.51)$$

where  $A_T$ ,  $T_{ref}$ , and  $\beta$  are fitting parameters. The carrier temperature is evaluated employing the energy balance equation in the stationary homogenous case according to Section 4.3.1. For the MP process the electron flux rather than energy is important. As a result, the electron current density  $J_n$  enters the expression for the acceleration integral of the MP process

$$I_{MP,n} \approx A_j \frac{J_n}{J_{ref}}, \quad (6.52)$$

where  $A_j$  and  $J_{ref}$  are used for model calibration. The two components are compared against the acceleration integral from the Monte Carlo simulations in Fig. 6.12. The SP process dominates in the drain area, where a good agreement between acceleration integrals can be found. Note that such peculiarities as the peak and slope are properly reproduced by the drift-diffusion based treatment. The right side, which reaches far into the drain area of the transistor, cannot be reproduced properly. This is due to the abrupt decrease of the electric field and therefore of the carrier temperature. In the channel area, the SP component is of minor interest and the MP component becomes dominant. It is mentioned in Section 6.3.2, that for the Monte Carlo simulations the same acceleration integral is used for the SP and MP process. Therefore, Fig. 6.12 also shows the sum of the two approximated components, which fits well in comparison to the Monte Carlo results.

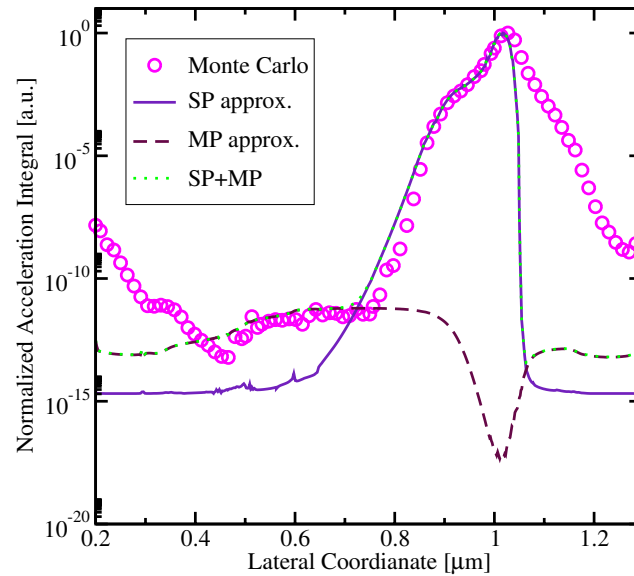


**Figure 6.12:** Comparing the SP and MP components of the empirical acceleration integral with the Monte Carlo reference. On the channel side, the slope of the SP component agrees well compared to the reference simulation. The extension into drain cannot be reproduced. The MP component shows a good agreement along the channel. The sum of the two components agrees well for the whole channel area.

The propagation of the interface trap creation over degradation time can be seen in Fig. 6.10(b). The comparison to the reference simulations shows a perfect agreement near the drain side on which the SP process dominates. However, in those channel areas in which the MP process dominates, the trap creation differs in the amplitude. This is caused by the assumptions that were made to obtain the closed solution in (6.38), which is used by the Monte Carlo model. The current carrier temperature based model solves equation (6.50) numerically. However, since the contributions of the MP process are relatively low, this difference does not influence the overall drain current degradation which is depicted in Fig. 6.11. In the range of available measurement data, the figure shows that this approximation of the acceleration integral gives a very good agreement in comparison to the measurement and Monte Carlo reference data. Unfortunately, no long term measurements are available for the device under test to observe the influence with an increasing MP contribution.

The main problem of this approach is that a fitting, as it is required for this model, is not universal. Despite the good agreement shown, the results are only of limited validity. This means that if the stress or operating conditions are changed, another fit based on the new conditions has to be done.

## 6.4. ACCELERATION INTEGRAL ESTIMATION IN DRIFT-DIFFUSION

### 6.4.3 Results and Discussion

Using the drift-diffusion approach, the acceleration integral can be estimated at least two orders of magnitude faster than using the Monte Carlo method. Therefore, the acceleration integral can be evaluated at every simulation step. Hence, it is possible to directly evaluate the rate equations (6.43) to (6.45) self-consistently. An arbitrarily shaped time dependent stress condition can, therefore, be simulated in short simulation times, as long as the model is used in a correctly fitted range.

The results obtained look very promising. Especially the carrier temperature based model in Section 6.4.2 shows a very good agreement in comparison with the time consuming Monte Carlo simulations. However, the model shows some limitations. These shortcomings can be summarized in the following points:

- The carrier temperature is based on the local electric field. Therefore, hot-energy tails in the distribution function cannot be captured and additional fitting parameters are introduced.
- Extra parameters are required in (6.51) and (6.52), for which no modeling approaches have been elaborated yet.
- The limitations of the drift-diffusion model are reached for smaller devices.
- The holes responsible for the interface degradation in larger devices cannot be modeled properly in the drift-diffusion model.

All those obstacles can be found either in the limitations of the drift-diffusion model or in the high number of fitting parameters required. The latter one is a consequence of the partly empirical assumptions made in this originally physics-based model. It is questionable if all those problems can either be solved or circumvented to become good predictive results using this model. However, if this can be accomplished, either generally or for specific applications, one can benefit from the enormous performance gain that can be achieved in comparison to the Monte Carlo approach.



## Chapter 7

# Numerical Considerations

In numerical device simulation environments, the physical properties of a semiconductor device are described using models based on differential equation systems as shown in Chapters 4–6. Generally, the problems cannot be solved analytically and numerical solution techniques are required. Discretization methods are used to transform the partial differential equation system to difference equations. Meshes are required to define the spatial discretization of the simulation domain. Section 7.1 will give a short introduction to this topic. The discretization of the semiconductor equations in the context of the box discretization method is introduced in Section 7.2. The difference equation system is then solved using nonlinear solving techniques, typically Newton’s iteration scheme is applied.

Special considerations are required to represent vector quantities in discretized systems. Section 7.3 will give an overview on that subject. Section 7.4 will discuss numerical consideration, which are especially important for simulations in high-voltage devices.

### 7.1 Meshing

The spatial discretization of the simulation domain is represented using a mesh consisting of vertices/nodes, edges, and elements. Quantities like the electrostatic potential or the electron and hole carrier concentrations are assigned to nodes, fluxes like the electron or hole current density are modeled along edges between the nodes. The structure of the real device obviously expands in three dimensions. However, to decrease the complexity of the problem, many applications can be reduced to a two-dimensional problem by assuming an infinite homogenous extension in the third dimension, which is considered as the width of the device. Fields and currents along the omitted dimension are neglected. This simplification obviously does not account for inhomogeneities along the width, effects near corners or changes in the doping profile at the border of the device. Further reduction of the problem complexity can be accomplished by utilizing symmetries in the device as much as possible without losing information.

## CHAPTER 7. NUMERICAL CONSIDERATIONS

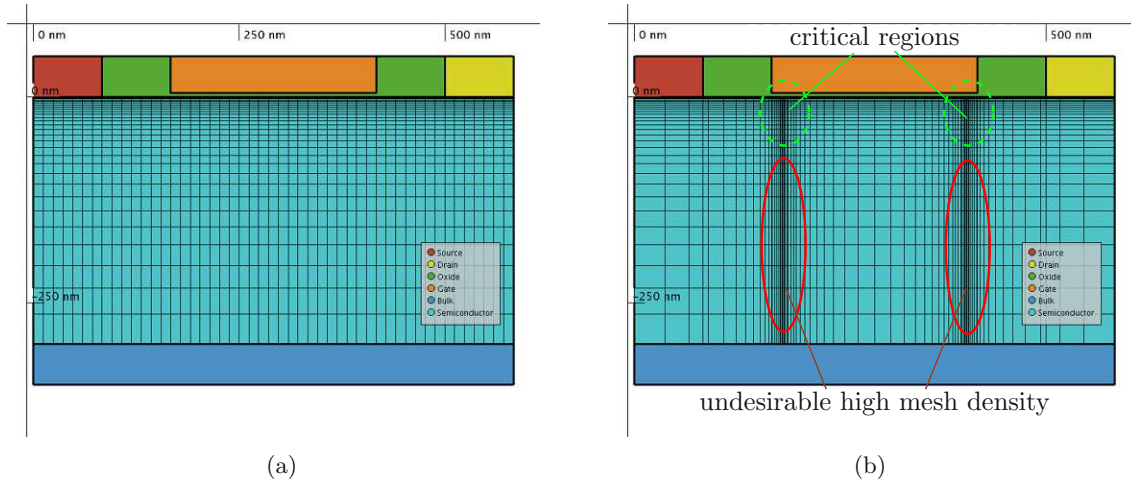


**Figure 7.1:** Simple orthogonal grid of a planar MOS field effect transistor using a finer mesh near the channel (a). Same transistor including a refinement near the drain side of the channel (b).

The simplest mesh type used in device simulation is represented by an orthogonal grid as shown in Fig. 7.1(a). This grid type consists of grid lines parallel to the rectangular simulation domain, which does not require much effort to generate and is easy to handle. In areas which need higher spatial resolutions, a higher density of grid lines can be inserted. Adding lines is straightforward but since grid lines are continued throughout the whole device, a high number of unnecessary mesh points are created also in areas of low interest (see Fig. 7.1(b)). This leads to long simulation times and poor convergence. An additional disadvantage of these structured grids becomes significant for devices with non-planar surfaces. The inflexibility of this mesh type does not permit a smooth representation of non-planar surfaces. An example of such a stepped geometry near a birds beak in an LDMOS transistor is shown in Fig. 7.2(a).

Utilizing unstructured meshes overcomes the disadvantages mentioned above. The mesh is based on triangular elements in two dimensions or tetrahedral elements in three dimensions. In Fig. 7.2(b) and 7.3 sample meshes are shown. These meshes are often based on structured meshes with refinements in areas of special interest. However, generation of unstructured meshes suitable for device simulation is a cumbersome task, especially in three-dimensional devices [255].

The box discretization introduced in the next section requires the mesh to fulfill the Delaunay criterion [257]. This criterion describes unstructured meshes constructed for a set of vertices such that no vertex lies inside the circumscribed circle of any triangle (see Fig. 7.4) or the circumscribed sphere of any tetrahedron. This is always valid for triangulated rectangular grids but can be difficult to guarantee in general.

Other obstacles during mesh generation are the proper representation of borders and surfaces and the definition of mesh refinement criteria for areas of special interest which require higher resolutions. The details of the mesh refinement procedure often have to be specified manually,



## 7.1. MESHING

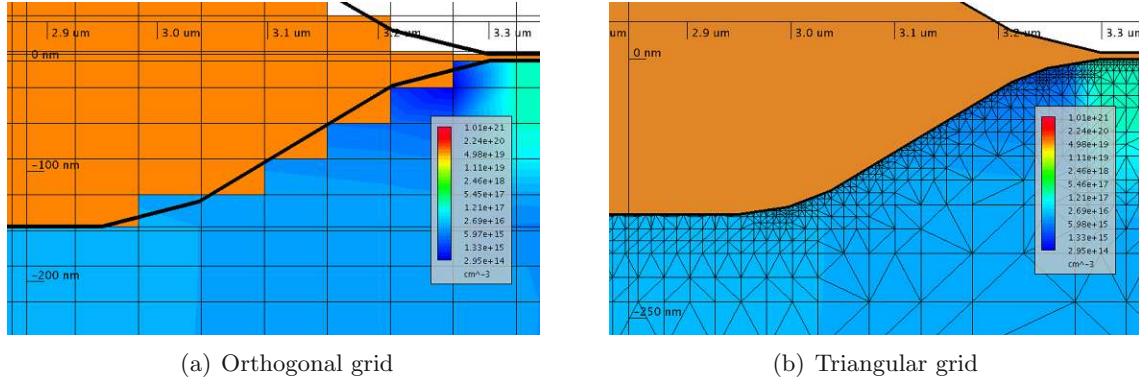


**Figure 7.2:** Representation of non-planar surfaces using orthogonal grids (a) and triangular grids (b).

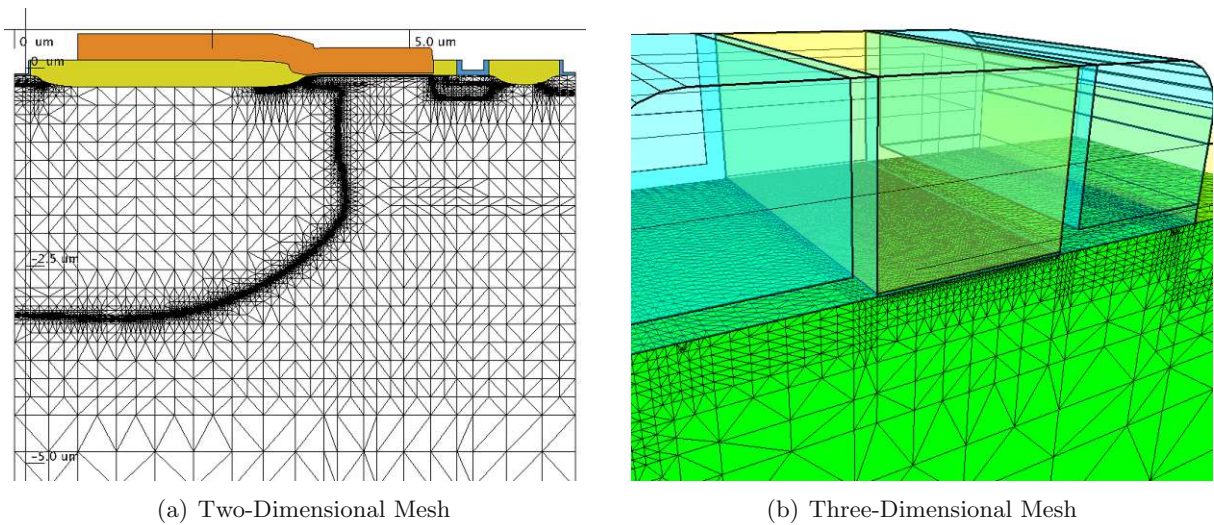


**Figure 7.3:** The mesh of the sample device is based on an orthogonal grid which is triangulated and refined. Areas of special interest are the channel and the junction regions which thus require a denser mesh (a). A three-dimensional sample mesh of the channel area of a MOS device (b).

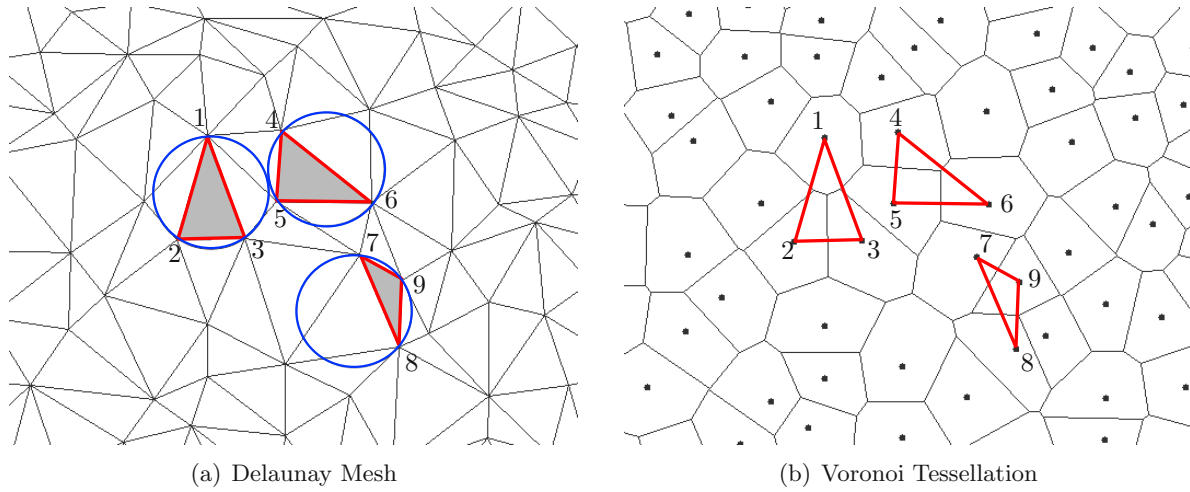


**Figure 7.4:** A Delaunay mesh (a) and its Voronoi tessellation (b), also called the dual mesh, is shown (created using [256]). The circumscribed circles of three randomly selected triangles are emphasized. Every mesh point has an associated volume — every point in the domain has exactly one associated box volume.

since mesh generation tools have no *a-priori* information of the device behavior. A typical refinement strategy is performed in the dependence of the gradient of the net dopant concentration which is equivalent to the built-in potential. This provides a fine mesh at the metallurgic pn-junctions. One has to consider that depending on the bias of the device in operation, the carrier concentrations can change so that the effective junctions and therefore the positions of the highest gradients of the electrostatic potential and carrier concentrations move. Also the current flow depends on the bias of the system and the direction of currents and fields can change. Special refinement in the channel areas in MOS transistors can be specified using rules which depend on the distance to the gate oxide segment. Depending on the simulations to be performed, a refinement in the gate oxide segments is required. Since fully automatic mesh generation would clearly simplify the work-flow, considerable efforts have been put into the development of methods for automatic mesh generation. A promising approach applies error estimation algorithms on simulation results [258]. This information is recursively used to optimize the simulation mesh.

## 7.2 Box Discretization

The discretization of the partial differential semiconductor equations in space and time is required to obtain difference equations which can be solved using numerical methods. A common approach for the discretization of the differential equations is the box discretization or box integration method [12, 259], also known as the finite volume method.

### 7.2.1 Derivation

To apply the box discretization method, the mesh has to fulfill the Delaunay criterion and can therefore be split into boxes using a Voronoi tessellation [257]. By applying the Voronoi tessellation a dual mesh is created so that every point in the domain is assigned to its closest vertex. All points which are closest to the same vertex form together an element of the dual mesh which is called box volume throughout this work (see Fig. 7.4). The transformation is bijective.

The box discretization method reformulates the equations based on this Voronoi tessellation and can be equally used in two- and three-dimensional simulation domains. Since the two-dimensional devices have a specified width which acts as a multiplier, all boxes are considered as volumes and the box boundary elements are considered as surfaces. The basic method of the box discretization concerns the divergence operator in the form

$$\nabla \cdot \mathbf{F} = g, \quad (7.1)$$

where  $\mathbf{F}$  and  $g$  are an arbitrary flux and generation term, respectively. The equation can be transformed by integration over a volume  $V$

$$\int_V \nabla \cdot \mathbf{F} dV = \int_V g dV, \quad (7.2)$$

and by applying Gauss's theorem,

$$\oint_{\partial V} \mathbf{F} d\mathbf{A} = \int_V g dV, \quad (7.3)$$

where  $\partial V$  is the surface of  $V$  and  $\mathbf{A}$  is the outwardly oriented surface area vector. In the next step equation (7.3) is applied to each Voronoi box in the mesh (see Fig. 7.5). With this spatial quantization in boxes the two-dimensional boundary  $\partial V$  is transferred to a polygon (in 2D) or polyhedron (in 3D) and can be split into planar surface elements perpendicular to the edges leading to the neighboring vertex. Every vertex  $i$  has an associated box volume  $V_i$  and a set of  $N_i$  neighboring boxes. Equation (7.3) can be approximated, i.e. discretized, for each vertex as

$$\sum_{j \in N_i} F_{ij} A_{ij} = \int_{V_i} g dV. \quad (7.4)$$

$F_{ij}$  is the flux through the boundary area  $A_{ij}$  between the boxes  $i$  and  $j$  (compare Fig. 7.5) and can be interpreted as the projection of  $\mathbf{F}$  on the edge between the vertices  $i$  and  $j$  as

$$F_{ij} = \xi_{ij} \cdot \mathbf{F}. \quad (7.5)$$

$\xi_{ij}$  is the unit vector pointing along edge  $ij$ . From the discretization point of view,  $F_{ij}$  must be the value of the quantity at the mid-point of the edge which is exactly the boundary between the boxes. As will be shown in the next section, the proper discretization of  $F_{ij}$  is relevant for numerically stable results and depends on the type of differential equation system used.

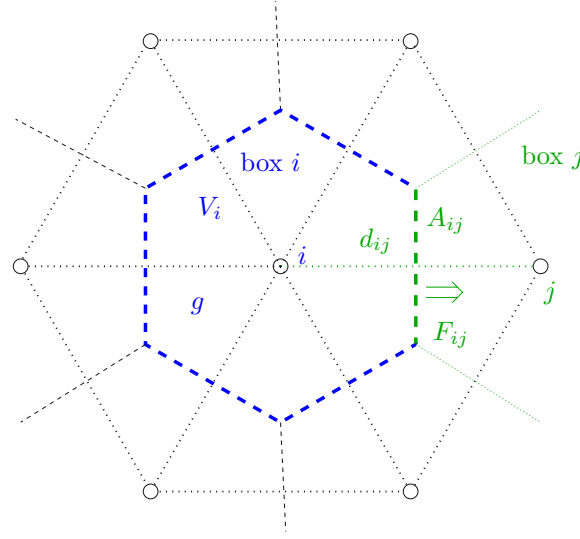


**Figure 7.5:** Voronoi box  $i$  (blue, dashed) of vertex  $i$  with connections to its neighboring vertices forming six adjacent triangular elements. The flux  $F_{ij}$  from box  $i$  to box  $j$  through the area  $A_{ij}$  is depicted. The edge length between  $i$  and  $j$  is  $d_{ij}$ .

The physical equations that describe semiconductor devices are laws of conservation. The derivation of the box discretization method is inherently conservative [260]. The box discretization scheme is, therefore, widely used in semiconductor device simulations [12]. In drift-diffusion simulations, the differential equations that have to be solved are Poisson's equation (4.1) and the current continuity equations (4.5) and (4.6). The flux quantities  $\mathbf{F}$  introduced in (7.1) are the dielectric flux density  $\mathbf{D} = \epsilon \mathbf{E}$  for Poisson's equation and the current densities  $\mathbf{J}_\nu$  for the continuity equation, respectively. The generation terms  $g$  in (7.1) are the charge density  $\rho$  and the carrier generation/recombination rates  $R/G$ , respectively.

A considerable advantage of the box discretization method is that the only information required is the unstructured neighborhood information. This neighborhood information consists basically of two lists. First, a list of all boxes in the simulation domain, together with their center points ( $i$ ), i.e. the vertices, and the box volumes ( $V_i$ ). Second, a list of all edges connecting the vertices, together with the edge length ( $d_{ij}$ ), i.e. the distance between the vertices, and the common surface between the neighboring boxes ( $A_{ij}$ ). It has to be noted that no more information about the elements is necessary for the evaluation of (7.4), which makes the box discretization independent of the box shape, including its dimensionality. This makes this scheme very straightforward to implement and a dimensional independent set-up of the simulator can be realized.

## 7.2.2 Discretization of Edges

The calculation of the one-dimensional projection of the flux on the edge depends on the type of the differential equation. For the dielectric flux density  $\mathbf{D}$  in Poisson's equation the flux from

## 7.2. BOX DISCRETIZATION

box  $i$  to box  $j$  along the connecting edge through the common boundary area  $A_{ij}$  is  $D_{ij}$ . This density is commonly approximated using the directional derivative of the electrostatic potential:

$$D_{ij} = \boldsymbol{\xi}_{ij} \cdot \mathbf{D} = -\epsilon \boldsymbol{\xi}_{ij} \cdot \nabla \psi = -\epsilon \frac{\partial \psi}{\partial \boldsymbol{\xi}_{ij}} \approx -\epsilon \frac{\psi_j - \psi_i}{d_{ij}}. \quad (7.6)$$

$d_{ij}$  is the distance between the two vertices and the permittivity  $\epsilon$  is considered as a constant in each element. In MINIMOS-NT, for example, the permittivity is taken as the average between the permittivities associated with the vertices  $i$  and  $j$  as  $\epsilon_{ij} = (\epsilon_i + \epsilon_j)/2$ .

For the current densities  $\mathbf{J}_\nu$  of the carrier type  $\nu$ , the discretization of  $J_{\nu,ij}$  is not as straightforward. Insertion of the drift-diffusion current relations from equations (4.7) and (4.8) in the continuity equations (4.5) and (4.6) results in a second order parabolic partial differential equation. Using a simple finite difference approach like in (7.6) leads to numerical oscillations if the drift term dominates over the diffusion term [261]. Very fine meshes would be necessary to stabilize the system. A stable discretization can be obtained using the Scharfetter-Gummel method [39] instead. Here, the drift-diffusion current equations (4.7) and (4.8) are used to solve the one-dimensional carrier concentrations,  $n$  and  $p$ , respectively, along the edge. The boundary conditions of the carrier concentrations are given using the values at the corresponding vertices  $i$  and  $j$ . The values of  $J_{n,ij}$  and  $J_{p,ij}$ ,  $E_{ij}$ , and  $\mu_n$  and  $\mu_p$  are considered constant along the edge. Solving this one-dimensional differential equation results in

$$J_{n,ij} = \frac{q\mu_n V_T}{d_{ij}} \left( n_j \mathcal{B}(\Delta_{ij}) - n_i \mathcal{B}(-\Delta_{ij}) \right) \quad (7.7)$$

for electrons and

$$J_{p,ij} = -\frac{q\mu_p V_T}{d_{ij}} \left( p_j \mathcal{B}(-\Delta_{ij}) - p_i \mathcal{B}(\Delta_{ij}) \right) \quad (7.8)$$

for holes, where the temperature voltage is defined as  $V_T = k_B T/q$ ,  $\Delta_{ij} = (\psi_j - \psi_i)/V_T$  and  $\mathcal{B}$  is the Bernoulli function defined as

$$\mathcal{B}(x) = \frac{x}{\exp(x) - 1}. \quad (7.9)$$

### 7.2.3 Discretization of the Right Hand Side

Up to now, the generation term  $g$  on the right hand side of (7.4), which is the charge density  $\rho$  in Poisson's equation and the carrier generation and recombination rate in the carrier equations, was only represented as an integral in continuum space. Most implementations calculate this integral by partitioning the box into pieces and adding the contributions to the integral of the box. Three different methods are considered in this work, each partitioning the Voronoi box differently. For the first assumption, the box is not split and the generation is considered constant over the whole box volume, as it is depicted in Fig. 7.6(a). This approach reduces the integral term of (7.4) to a simple product [12, 262] which reads

$$\int_{V_i} g \, dV \approx g_i V_i. \quad (7.10)$$

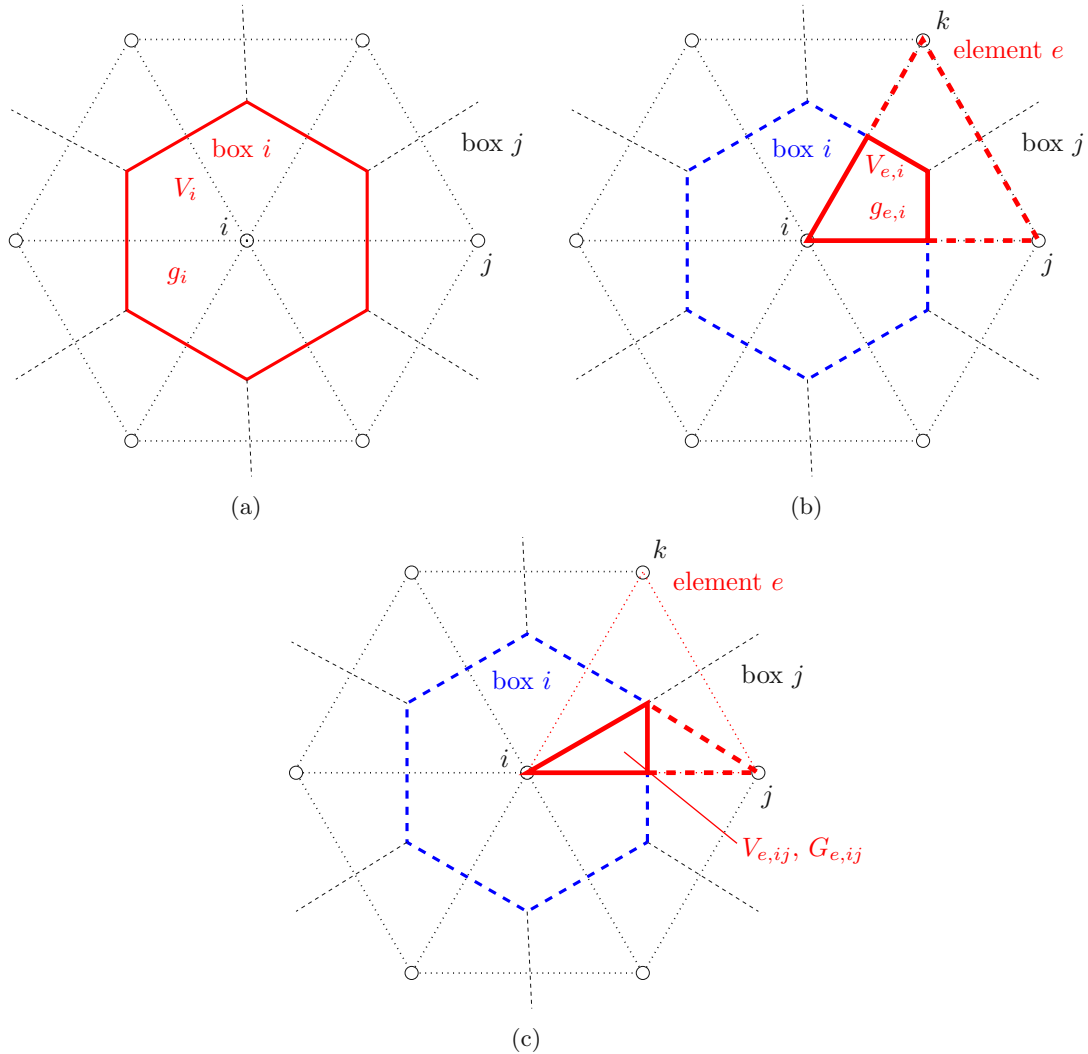


**Figure 7.6:** The Voronoi box  $i$  (blue) and the different approaches to decompose the generation for discretization. Areas of constant generation are surrounded in bold red (dashed plus solid), parts contributing to the box are shown in solid red, for (a) the box based methods, (b) the element based methods, and (c) the method proposed by Laux *et al.* [263].

This formulation perfectly fits to the box discretization method, because it only requires quantities which are stored on vertices and the only geometry information needed is the unstructured neighborhood information. This makes the assembling procedure of (7.10) very simple. MINIMOS-NT [120], for example, is one simulation tool using this technique. As will be discussed in Section 7.3, the calculation of vector quantities is somewhat more involved in this approach than for the other methods.



## 7.2. BOX DISCRETIZATION

Another approach for assembling the generation integral is to assume the generation rate to be constant within one mesh element. In this case, the integral for one box volume is assembled using contributions from all adjacent elements  $e$ . Using the naming conventions from Fig. 7.6(b), this reads

$$\int_{V_i} g \, dV \approx \sum_{e \in E_i} g_{e,i} V_{e,i}, \quad (7.11)$$

where  $E_i$  is the set of all elements that contribute to the volume  $V_i$ . In this scheme the generation term is estimated for each element (compare dashed red line in Fig. 7.6(b)), which might be a triangle, tetrahedra, box, or other mesh element. Its contributions can be used for all boxes the element is part of [264]. This element-wise assembly results in an implicitly increased resolution and a more accurate physical representation [265]. Some implementations associate different current densities for each edge pair (compare solid red line in Fig. 7.6(b)) and do not assume it to be constant within the whole element. In this case there are independent rates for each box the element is contained in. A method using this techniques is the edge-pair method [266].

The third approach in this classification is depicted in Fig. 7.6(c). This approach was presented for triangles only [263], but extensions to tetrahedra are possible. Here, each triangle is split into three different regions associated with the three edges. In each of them, a generation term is estimated, and two of them contribute to the sum of one box. Therefore, the summation for the generation integral of the box requires to consider two contributions per element:

$$\int_{V_i} g \, dV \approx \sum_{e \in E_i} (g_{e,ij} V_{e,ij} + g_{e,ik} V_{e,ik}) . \quad (7.12)$$

This approach was used by Laux *et al.* [263] in the context of calculating the impact-ionization rate. More on the calculations and the applied vector discretization in this approach will be given in Section 7.3.1. Note that this further splitting of the domain implicitly leads to a higher resolution and increased accuracy, which can be seen in the comparison in Section 7.3.3.

### 7.2.4 Limitations of the Box Discretization Method

The box method is used in most numerical device simulation environments as it is particle conservative and has proven to deliver good results, is numerically very stable, and is relatively simple to implement. Problems arise when the Delaunay criterion is violated. This leads to obtuse elements which degenerate the accuracy due to negative flux areas  $A_{ij}$  [264, 267]. Also, use of the one-dimensional Scharfetter-Gummel discretization to solve multiple dimensional problems leads to the crosswind diffusion effect resulting in artificial current components perpendicular to the actual current direction [268]. The accuracy of the discretization also degrades if triangles are aligned with the hypotenuse along the current flow. As depicted in Fig. 7.7, a vanishing boundary area  $A_{ki}$  leads according to (7.4) to a vanishing contribution of the current along this edge. A zig-zag characteristic of the discretized current is the result. There have been many proposals for more accurate discretizations (e.g. Patil in [267]). Some focus on the extension of the one-dimensional to a two-dimensional Scharfetter-Gummel current discretization [269, 270]. But

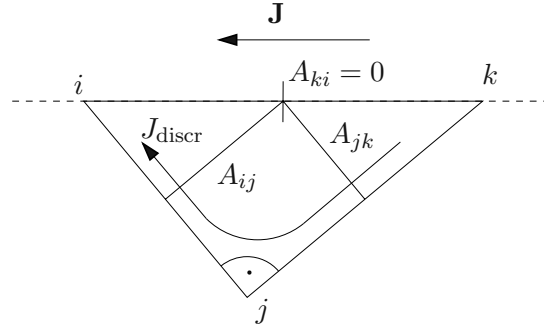


**Figure 7.7:** A triangle aligned with its hypotenuse along the current direction. Due to the vanishing Voronoi surface  $A_{ki}$  there is no contribution to the current from the hypotenuse.

none of these extensions is as universal to use as the box integration method which is dimension independent and can be used for structured and unstructured meshes alike.

### 7.3 Vectors in Discretized Systems

There are different methods of how directed quantities can be represented in box discretized systems. In the initial divergence equation (7.1) the vector quantities  $\mathbf{F}$  is transformed into one-dimensional edge discretized values  $F_{ij}$  which are subsequently used to assemble the box and flux equations. The single fluxes are estimated using quantities defined at the end nodes of the edges, like in relation (7.6) for the dielectric flux and (7.7) for the current density. No vector quantities are required to assemble the basic equations. However, vector attributes like the electric field and the current density are needed for the calculation of physical models. The electric field and the current density are required, for example, to model the high-field mobility or the impact-ionization rate in the drift-diffusion framework. For the representation of attributes as vector quantity, additional methods are required, some are represented in this section.

#### 7.3.1 Discretization Approach by Laux

In the work of Laux *et al.* [263] a discretization scheme is introduced for the accurate evaluation of the impact-ionization rate. The model assumes an unstructured triangular mesh. Since the potential and the electric field are based on linear functions, an electric field vector can be evaluated in a straightforward manner, consistent with the Poisson discretization. In a triangle  $ijk$ , each pairwise linear combination of  $\xi_{ij}E_{ij}$ ,  $\xi_{jk}E_{jk}$ , and  $\xi_{ki}E_{ki}$  gives the same constant value for the electric field  $\mathbf{E}_{ijk}$ .

Due to the non-linear dependence of the current density  $\mathbf{J}$  on the carrier concentrations in the Scharfetter-Gummel discretization, each linear combination of  $\xi_{ij}J_{ij}$ ,  $\xi_{jk}J_{jk}$ , and  $\xi_{ki}J_{ki}$  gives a different current density vector  $\mathbf{J}$ . The system in the triangle is overdetermined. Laux suggested



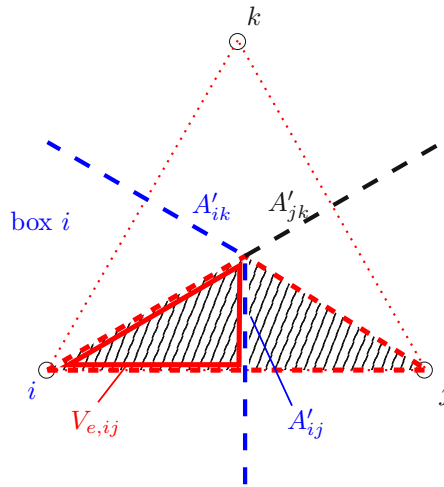


**Figure 7.8:** A triangular element showing the avalanche region defined by Laux *et al.* [263] (black hatched area) and the weighting surfaces  $A'_{ij}$ . The part contributing to the right hand side of box  $i$ ,  $V_{e,ij}$ , is bordered by the red solid line.

to partition each triangle into three avalanche regions associated with each edge as shown in Fig. 7.8. In this work, a current vector is defined for each avalanche region, i.e. for each edge. Note, that in the notations used here, the indices for the carrier type specification have been omitted. The current  $\mathbf{J}_{ij}$  associated to the edge between the vertices  $i$  and  $j$ , for example, is defined as

$$\mathbf{J}_{ij} = \frac{\mathbf{J}_j^* A'_{jk} + \mathbf{J}_i^* A'_{ik}}{A'_{jk} + A'_{ik}}, \quad (7.13)$$

weighted with the surface elements  $A'_{ij}$ . Note that  $A_{ij}$  is the whole surface between two boxes  $i$  and  $j$ , whereas  $A'_{ij}$  is only the part within the current element.  $\mathbf{J}_i^*$  is the current defined by the linear combination of the two to the vertex adjacent edges, given as

$$\begin{pmatrix} \xi_{ij}^T \\ \xi_{ik}^T \end{pmatrix} \mathbf{J}_i^* = \begin{pmatrix} J_{ij} \\ J_{ik} \end{pmatrix}. \quad (7.14)$$

The electric field  $\mathbf{E}$  and the current density  $\mathbf{J}_{ij}$  can now be used to calculate a field dependent model, in this context the impact-ionization rate, for the avalanche region. This region contributes as  $g_{e,ij}$  to the two boxes  $i$  and  $j$  which have to be assembled according to (7.12).

This approach for vector discretization gives good results as discussed in Section 7.3.3. The limitation to triangular grids (although an extension to tetrahedra is possible) and the higher complexity during equation assembly seem to be the main disadvantages of this method compared the box based vector discretization schemes presented in the next section.

### 7.3.2 Box Discretized Vector Quantities

Considering the calculation of the summand in the box approach (7.10), it seems to be most convenient to estimate the vectorial attribute for each box volume, i.e. for each vertex. The model evaluation within the box can then be performed straightforwardly, since all quantities, scalar and vectorial, are then available for the whole box. The results of model evaluation can be directly applied to the box integration equation. In the following, two schemes of vector discretization within boxes are presented. In addition to the simple coupling to the box discretization method, both approaches give accurate approximations for homogenous fields and are numerically stable.

#### Scheme A

The first scheme follows the derivation of the box discretization scheme itself [271]. Similar to the discussion regarding the right hand side of the box integral, the discretized vector quantities are assumed constant over the whole Voronoi box volume. The derivation of an according discretization scheme is shown for the electric field and can be generalized to auxiliary gradient fields. The electric field is defined as

$$\mathbf{E} = -\nabla\psi = -\nabla(\psi - \psi_{\text{ref}}), \quad (7.15)$$

where  $\psi_{\text{ref}}$  is an arbitrary reference potential. Similar to the method used to derive the box discretization method, an integration over a volume  $V$  is performed which leads to

$$\int_V \mathbf{E} dV = - \int_V \nabla(\psi - \psi_{\text{ref}}) dV. \quad (7.16)$$

Applying Gauss's theorem the equation can be written as

$$\int_V \mathbf{E} dV = - \oint_{\partial V} (\psi - \psi_{\text{ref}}) d\mathbf{A}, \quad (7.17)$$

where  $\mathbf{A}$  is the outwardly oriented surface vector of  $\partial V$ . Originally, Gauss's theorem is defined for divergence operation on vector fields, but it can be shown, that it is also applicable for gradients of potential fields. For the box  $i$  with  $N_i$  neighboring boxes  $j$ , the equation can be estimated to

$$V_i \mathbf{E}_i = - \sum_{j \in N_i} A_{ij} \xi_{ij} (\psi_{ij} - \psi_i). \quad (7.18)$$

In this derivation the electric field is constant over the box volume and the integral was split into the single box boundary surfaces.  $\psi_i$  was used as reference potential  $\psi_{\text{ref}}$ . The potential  $\psi_{ij}$  is the potential at the boundary between the boxes, which is the mid-point of the edge and can be estimated as

$$\psi_{ij} = \frac{\psi_j + \psi_i}{2}. \quad (7.19)$$

### 7.3. VECTORS IN DISCRETIZED SYSTEMS

Introducing  $E_{ij}$  as the projection on the electric field by following (7.6) one gets

$$E_{ij} = \boldsymbol{\xi}_{ij} \cdot \mathbf{E} \approx -\frac{\psi_j - \psi_i}{d_{ij}}. \quad (7.20)$$

Combining equations (7.18) to (7.20), the final relation for the electric field can be given as

$$\mathbf{E}_i = \frac{1}{2V_i} \sum_j A_{ij} d_{ij} \boldsymbol{\xi}_{ij} E_{ij}. \quad (7.21)$$

This scheme can be applied in Voronoi grids. The unstructured neighborhood information is sufficient to calculate the vectors. For the special case of homogenous fields  $\mathbf{E} = \mathbf{E}_H$  with the electrostatic potential  $\psi(\mathbf{x}) = -\mathbf{E}_H \cdot \mathbf{x}$ , the discretization step in (7.18), the estimation of the mid potential in (7.19), and the projected electric field in (7.20) are exact. This can be verified for orthogonal grids by entering  $E_{ij} = \boldsymbol{\xi}_{ij}^T \mathbf{E}_H$  into (7.21) and using the relation  $\boldsymbol{\xi}_{ij} (\boldsymbol{\xi}_{ij}^T \mathbf{E}_H) = (\boldsymbol{\xi} \otimes \boldsymbol{\xi}) \mathbf{E}_H$  which leads to

$$\mathbf{E}_i = \frac{1}{2V_i} \left[ \sum_j A_{ij} d_{ij} (\boldsymbol{\xi}_{ij} \otimes \boldsymbol{\xi}_{ij}) \right] \mathbf{E}_H = \mathbf{E}_H. \quad (7.22)$$

The discretization scheme is also analyzed in a one-dimensional formulation applying a linearly changing electric field  $E(x) = -2\alpha x$  and an corresponding quadratic electrostatic potential  $\psi(x) = \alpha x^2$ . Using only the x-axis and the naming convention from Fig. 7.9, (7.21) can be reduced for the linearly changing field to

$$E(x_0) = -\alpha(x_1 + x_2). \quad (7.23)$$

This fits exactly in the equidistant case, where  $x_0 = (x_1 + x_2)/2$ , but for non-equidistant cases, the result is not exact.

#### Scheme B

The second discretization scheme is an extension of the finite difference method and is based on a scheme suggested by Fischer [272]. The evaluation concentrates on the vector at the vertex itself. Considering the box 0 in a non-equidistant orthogonal mesh depicted in Fig. 7.9 and its neighboring box 1 (not shown explicitly), the electric field along the edge  $d_{01}$  can be expressed as  $E_{01} = -d\psi(x)/dx$ . At the boundary between the two boxes, i.e. the midpoint between 0 and 1, the finite difference method gives

$$E_{01} = -\frac{\psi_1 - \psi_0}{d_{01}}, \quad (7.24)$$

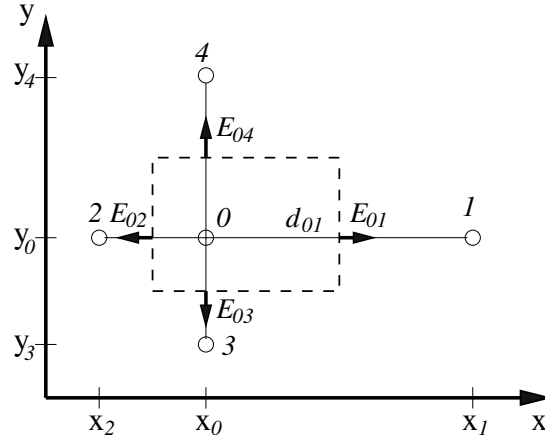


**Figure 7.9:** Rectangular Voronoi box of mesh point 0 with its neighboring points 1–4 in a non-equidistant orthogonal mesh. The contributing field components  $E_{ij}$  from the edges are depicted. (Idea of this picture taken from [272])

where  $\psi_i = \psi(x_i)$ . Note that this is the same result as in (7.20). The electric field  $E_0^x$  in direction  $\xi_x$  at mesh point 0 is expressed as a linear interpolation between  $E_{01}$  and  $E_{02}$ , the same is done for the component in direction  $\xi_y$  for  $E_0^y$ , which leads to

$$E_0^x = \frac{\frac{E_{01}}{x_1 - x_0} + \frac{E_{02}}{x_2 - x_0}}{\frac{1}{x_1 - x_0} + \frac{1}{x_2 - x_0}}, \quad (7.25)$$

$$E_0^y = \frac{\frac{E_{03}}{y_3 - y_0} + \frac{E_{04}}{y_4 - y_0}}{\frac{1}{y_3 - y_0} + \frac{1}{y_4 - y_0}}. \quad (7.26)$$

Following [272], equations (7.25) and (7.26) are extended to cover edges not aligned to the coordinate axis, reading

$$\frac{1}{x_j - x_i} \Rightarrow \frac{x_j - x_i}{(x_j - x_i)^2 + (y_j - y_i)^2} = \frac{x_j - x_i}{d_{ij}^2}. \quad (7.27)$$

The distance  $d_{ij}$  between the points  $i$  and  $j$  is defined as  $d_{ij} = |\mathbf{d}_{ij}|$  using

$$\mathbf{d}_{ij} = \mathbf{x}_j - \mathbf{x}_i = \begin{pmatrix} x_j - x_i \\ y_j - y_i \end{pmatrix}. \quad (7.28)$$

By using this generalized formulation (7.27) and assuming point 0 as a generalized point  $i$  of a box  $i$  with its neighboring boxes  $j$ , equations (7.25) and (7.26) can be reformulated to

$$\left( \sum_j \frac{x_j - x_i}{d_{ij}^2} \right) E_i^x = \sum_j \frac{x_j - x_i}{d_{ij}^2} E_{ij}, \quad (7.29)$$

$$\left( \sum_j \frac{y_j - y_i}{d_{ij}^2} \right) E_i^y = \sum_j \frac{y_j - y_i}{d_{ij}^2} E_{ij}. \quad (7.30)$$

### 7.3. VECTORS IN DISCRETIZED SYSTEMS

Introducing the electric field vector  $\mathbf{E}_i = (E_i^x \ E_i^y)^T$ , using  $\boldsymbol{\xi}_x^T \mathbf{E}_i = E_i^x$ , and adding the flux area  $A_{ij}$  as additional weight factor on both sides of the equations, the extended discretization scheme becomes

$$\sum_j \frac{x_j - x_i}{d_{ij}^2} A_{ij} \frac{1}{d_{ij}} \mathbf{d}_{ij}^T \mathbf{E}_i = \sum_j \frac{x_j - x_i}{d_{ij}^2} A_{ij} E_{ij}, \quad (7.31)$$

$$\sum_j \frac{y_j - y_i}{d_{ij}^2} A_{ij} \frac{1}{d_{ij}} \mathbf{d}_{ij}^T \mathbf{E}_i = \sum_j \frac{y_j - y_i}{d_{ij}^2} A_{ij} E_{ij}, \quad (7.32)$$

which can be combined to the single summation

$$\sum_j \frac{\mathbf{d}_{ij}}{d_{ij}^2} A_{ij} \frac{1}{d_{ij}} \mathbf{d}_{ij}^T \mathbf{E}_i = \sum_j \frac{\mathbf{d}_{ij}}{d_{ij}^2} A_{ij} E_{ij}. \quad (7.33)$$

Using  $\boldsymbol{\xi}_{ij} = \mathbf{d}_{ij}/d_{ij}$  and introducing the tensor product  $\boldsymbol{\xi}_{ij} \otimes \boldsymbol{\xi}_{ij} \equiv \boldsymbol{\xi}_{ij} \boldsymbol{\xi}_{ij}^T$  in the equation, the full formulation of the discretization scheme reads

$$\underbrace{\sum_j \frac{A_{ij}}{d_{ij}} (\boldsymbol{\xi}_{ij} \otimes \boldsymbol{\xi}_{ij})}_{\mathbf{M}_i} \mathbf{E}_i = \sum_j \frac{A_{ij}}{d_{ij}} \boldsymbol{\xi}_{ij} E_{ij}. \quad (7.34)$$

Note that (7.25) and (7.26) are still retained and can be extracted by using  $\boldsymbol{\xi}_{ij} = (1 \ 0)^T$  and  $\boldsymbol{\xi}_{ij} = (0 \ 1)^T$ , respectively.  $\mathbf{E}_i$  at the left side of (7.34) can be taken out of the sum and the remaining part of the sum results in a pure geometry dependent matrix, which is calculated once in the beginning of the simulation. This allows the convenient formulation of the final discretization rule for a vector  $\mathbf{E}_i$  in point  $i$  as

$$\mathbf{E}_i = \mathbf{M}_i^{-1} \sum_j g_{ij} \boldsymbol{\xi}_{ij} E_{ij}, \quad (7.35)$$

$$\mathbf{M}_i = \sum_j g_{ij} \boldsymbol{\xi}_{ij} \otimes \boldsymbol{\xi}_{ij}, \quad (7.36)$$

$$g_{ij} = \frac{A_{ij}}{d_{ij}}. \quad (7.37)$$

$\mathbf{M}_i$  is called the geometry matrix and  $g_{ij}$  the geometry factor, both of which depend only on the geometry and the mesh and do not change during the simulation.

Similar to Scheme A, the validation for homogenous fields using  $\mathbf{E} = \mathbf{E}_H$  and the electrostatic potential  $\psi(\mathbf{x}) = -\mathbf{E}_H \cdot \mathbf{x}$  is shown. Again, the relations  $E_{ij} = \boldsymbol{\xi}_{ij}^T \mathbf{E}_H$  and  $\boldsymbol{\xi}_{ij} (\boldsymbol{\xi}_{ij}^T \mathbf{E}_H) = (\boldsymbol{\xi} \otimes \boldsymbol{\xi}) \mathbf{E}_H$  are inserted into (7.35) which leads to

$$\mathbf{E}_i = \mathbf{M}_i^{-1} \sum_j g_{ij} (\boldsymbol{\xi}_{ij} \otimes \boldsymbol{\xi}_{ij}) \mathbf{E}_H = \mathbf{M}_i^{-1} \mathbf{M}_i \mathbf{E}_H = \mathbf{E}_H. \quad (7.38)$$

This box based discretization scheme therefore is always exact for homogenous fields. Also the one-dimensional verification of linearly changing fields  $E(x) = -2\alpha x$  and a corresponding

## CHAPTER 7. NUMERICAL CONSIDERATIONS

quadratic electrostatic potential  $\psi(x) = \alpha x^2$  has been done. Inserting these values in (7.35) and solving in one dimension using the labels as in Fig. 7.9 leads to the exact result

$$E(x_0) = -2\alpha x_0. \quad (7.39)$$

The geometry matrix  $\mathbf{M}_i$  introduced in this discretization scheme needs to be inverted for evaluation. The matrix results from a sum of symmetric matrices  $\boldsymbol{\xi}_{ij} \otimes \boldsymbol{\xi}_{ij}$  whose determinants equal to 0 and whose main diagonals are positive. The sum of matrices with these constraints and with non-negative determinants also result in a symmetric matrix with positive main diagonal and a non-negative determinant. If at least two of the participating matrices are linearly independent, the determinant of the geometry matrix is positive which is the case as long as the Delaunay criterion is fulfilled. The inverse of the geometry matrix can therefore always be calculated.

### Differentiability of the Discretized Vector Quantities

For the numerical solution process using Newton's method it must be possible to calculate all partial derivatives on quantities in all neighboring boxes. The derivatives need to be added to the Jacobian matrix. This makes it necessary that the discretization schemes are also differentiable on quantities  $\eta_k$  associated to a mesh point  $k$ . This is indeed possible and one obtains for Scheme A

$$\frac{\partial \mathbf{E}_i}{\partial \eta_k} = \frac{1}{2V_i} \sum_j A_{ij} \mathbf{d}_{ij} \frac{\partial E_{ij}}{\partial \eta_k} \quad (7.40)$$

and for Scheme B

$$\frac{\partial \mathbf{E}_i}{\partial \eta_k} = \mathbf{M}_i^{-1} \sum_j g_{ij} \boldsymbol{\xi}_{ij} \frac{\partial E_{ij}}{\partial \eta_k}. \quad (7.41)$$

In both discretization schemes, the existence of  $\frac{\partial E_{ij}}{\partial \eta_k}$  is sufficient to calculate  $\frac{\partial \mathbf{E}_i}{\partial \eta_k}$ .

### 7.3.3 Comparison of the Discretization Schemes

In this comparison, the vector discretization scheme proposed by Laux and the two box discretized schemes were implemented in MINIMOS-NT and used to calculate the impact-ionization rate. The generation integral on the right hand side of the continuity equation is assembled using (7.10) and (7.12), respectively. The implementation of the scheme by Laux is only limited to two-dimensional domains using triangular meshes, whereas the two other schemes are dimension and mesh independent and the same program code can be used for two- and three-dimensional simulations.

Simulation results from two devices are presented. The first device is a diode which was selected to investigate effects in a simple one-dimensional device. The second device used for the comparison is a parasitic  $n^+$ -p-n- $n^+$  structure of a smart power device which is significantly influenced by the two-dimensional extension. The diode uses an equidistant mesh and is investigated in reverse-biased operating condition for different mesh spacings. The parasitic bipolar

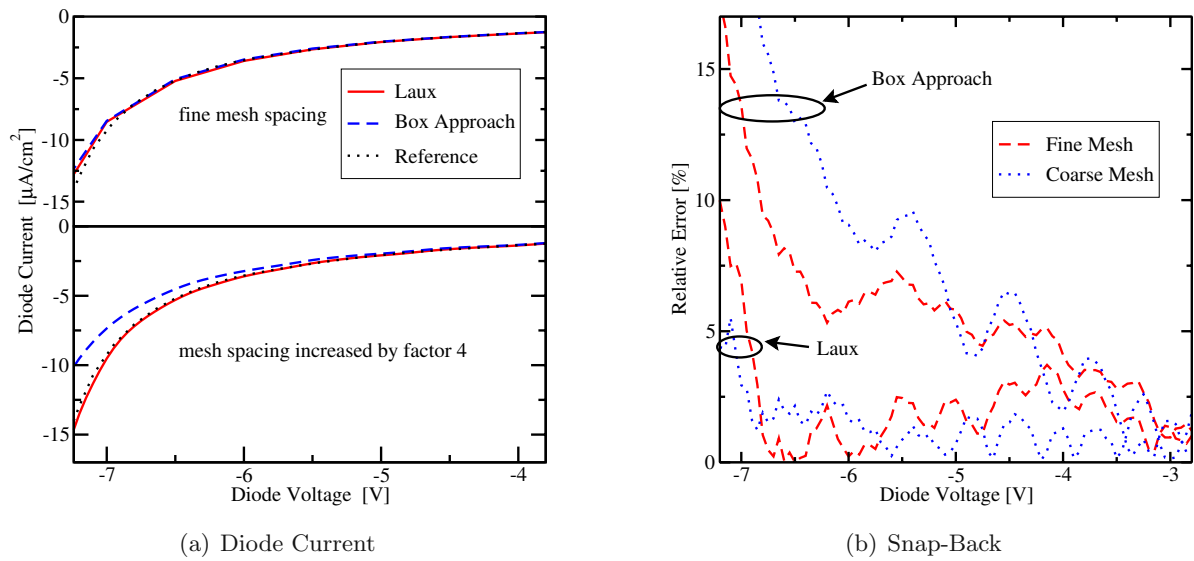


**Figure 7.10:** Comparison of the simulation results (a) and the error (b) for a reverse-biased diode near breakdown. Only Scheme B has been used in the comparison.

smart power structure is simulated in snap-back, a state the device can be driven in during voltage peaks on the power line.

Simulations on the diode structure clearly show that the mesh dependency is higher for the two box based discretization schemes. Using a high mesh density results, as expected, in a comparable output for all three discretization methods. Using a coarser mesh spacing, the results using Laux's scheme change very little, whereas the two box based schemes show larger deviations. In Fig. 7.10 an example using the diode clearly shows that an increased mesh spacing leads to a shift of the breakdown voltage using the box based schemes, whereas only a very small shift is observed using the scheme by Laux.

The results for the snap-back simulation in the smart power device are depicted in Fig. 7.11 and show only small deviations between the three schemes. The two box based schemes again show a voltage shift in comparison to the scheme by Laux. The latter one fits well to the reference solution which was generated using a high mesh density (not shown in the figure). The reason for the stronger mesh dependence of the box based schemes can be found in the implicitly finer discretization used in Laux's scheme.

The influence of the vector discretization scheme on the convergence behavior is also investigated on the reduced smart power structure as shown in Fig. 7.11(b). Only very little differences were noted and no trend favoring one or another scheme was observed. The convergence process is tracked using the norm of the right hand side. The investigated simulation step is a numerically critical current level step at the triggering phase of the snap-back. It can be clearly seen that the choice of discretization method has only very little influence, despite the critical simulation step.

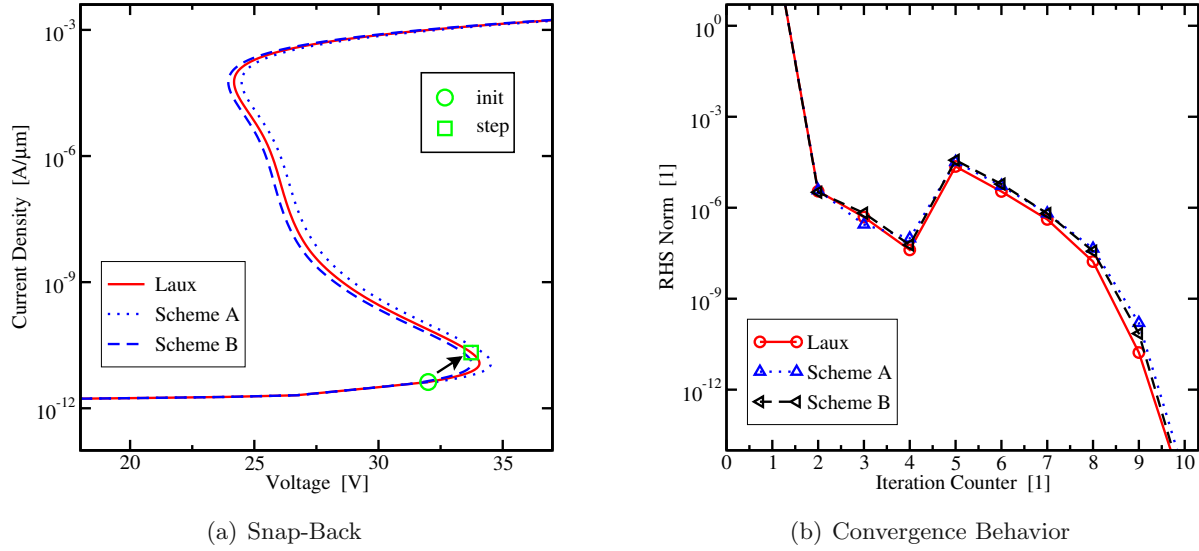


**Figure 7.11:** Snap-back simulations in a smart power structure using different vector discretization schemes (a). The influence of the discretization scheme on the Newton iteration process (b) during the transition marked in (a) is very small.

Although the Laux scheme gives results with a higher accuracy, the influence on the convergence behavior seems to be negligible. On the other hand, the box based schemes can be coupled straightforwardly to the box discretization scheme. Additionally, it is possible to reuse the same implemented code for arbitrary meshes in all dimensions. Throughout this work, the box based Scheme B has been used for all drift-diffusion simulations.

## 7.4 Numerical Challenges Related to High-Voltage Devices

It was already stated earlier in this chapter that the derivatives on quantities in other mesh points are needed for assembly of the Jacobian matrix. The electric field in box  $i$ , for example, depends on the potentials in box  $i$  and all neighboring boxes  $N_1 - N_i$ :

$$\mathbf{E} = f(\psi_i, \psi_{N_1}, \dots, \psi_{N_i}). \quad (7.42)$$

Solving Poisson's equation, for example, only the electrostatic potential enters the equation via (7.6) and not the electric field. In this context, the electric field is only a post-processing quantity, the numerical solution process is not influenced by those dependencies. However, field dependent mobility models (see (4.14), for example) or generation terms like the impact-ionization generation (5.3) bring additional dependencies on quantities on neighboring vertices in the current equation and the generation term, respectively. This dependence on vector quantities, especially on the current density, results in couplings to many neighboring mesh points which generate many entries in the Jacobian matrix. The high number of non-zero entries in



the system matrix often leads to poor performance or failure of iterative linear solvers [273]. Additionally, strong non-linear relations, for example the exponential dependence used to model the impact-ionization rate, might lead to poor convergence of the Newton iteration [218]. Many of the numerically problematic models are important in high-voltage and power devices and therefore have to be considered in the simulations.

An approach to overcome convergence issues is to calculate more intermediate solutions between the initial simulation step (equilibrium) and the desired operating point. This can be achieved by ramping the contact potentials step by step until the final value is achieved. Results from former steps are used as initial guesses for the Newton method in the next step. Decreasing the step size therefore improves the quality of the initial guess for the next step and finally for the desired operating point. Obviously a good balance between step size, robustness, and simulation time has to be found. Other approaches to overcome convergence issues are to tune the Newton procedure, for example, by changing parameters of the damping algorithm [274]. This changes the calculation of the Newton update vectors and is often required to achieve convergence.

Numerical problems are frequently caused by the simulation mesh used. For mesh design a trade-off between accuracy, simulation time, and numerical stability has to be found. High convergence rates can be achieved by having a moderate number of well shaped elements [275]. However, smaller elements usually lead to a higher resolution and therefore to a higher accuracy. On the other hand, the limited floating point precision in computer systems can result in numerical noise [276] which degrades the condition of the system matrix. For accurate results also a proper alignment of the elements regarding the direction of the current flow (see Fig. 7.7) is important. Near the channel area this often leads to poorly shaped thin elements having small internal angles. Creating a mesh for the simulation of high-voltage devices that has good numerical properties and delivers accurate results is very challenging.

Applications with special demands on the numerics of TCAD simulation tools are break-down, electro-static discharge (ESD), and snap-back simulations [221, 275]. A case study on snap-back simulations in a simplified smart power device structure is demonstrated in Section 5.3. Difficulties arise in such simulations from the strongly field dependent behavior and the physically unstable operating points. Physical quantities undergo strong variations near breakdown and snap-back. Effects, for example, the base pushout phenomenon, completely change the operation state of the device. This also impacts the convergence of the iterative solver, since the state transition leads to strong changes in the conductivity, of the current path, and of the carrier concentrations. The different states of the devices before and after snap-back additionally result in multivalued I/V curves. The boundary conditions therefore have to be selected appropriately to avoid unintentional transitions between the branches of the I/V curve. Special curve-tracing algorithms have been suggested to deal with these problems [219, 220].

## 7.5 Summary

It has been shown how the box discretization method can be applied to the drift-diffusion model and how the Scharfetter-Gummel method is used for current discretization. This is an

## CHAPTER 7. NUMERICAL CONSIDERATIONS

established method used in most TCAD simulation environments [120, 194, 265]. A major part of this chapter is focused on vector discretization and three different approaches have been presented and analyzed. Finally, the topic of possible numerical problems in device simulation has been shortly discussed.

## Chapter 8

# Conclusions and Outlook

This thesis covers the two important topics in the field of high-voltage and smart power devices, which are the simulation of devices of this class and the modeling of reliability issues. Based on this foundation, failure and degradation behavior related to the two phenomena, impact-ionization generation and hot-carrier degradation, were presented and integrated into a TCAD device simulator.

For the evaluation of impact-ionization, the snap-back behavior in a smart power structure was investigated. The obtained results demonstrated good agreements to measurement data. The relatively large devices permit to use the drift-diffusion model. Convergence problems during this simulation have been carefully analyzed in the context of vector discretization schemes. It was demonstrated that the different schemes have only little influence on the convergency behavior. However, differences in terms of accuracy could be shown.

For the hot-carrier degradation modeling, a physics-based model is presented, which relies on the thoroughly evaluated carrier energy distribution function obtained using the Monte Carlo method. Since the model is physics-based, it allows one to capture the main peculiarities of hot-carrier degradation as, e.g., an interplay between a single- and a multiple-particle process of the Si-H bond dissociation. However, more efficient approaches which are less computationally demanding than the Monte Carlo method are required to adapt the model for industrial needs. Therefore, a model based on the drift-diffusion framework was developed. It is demonstrated that the approach delivers a good agreement in comparison to the Monte Carlo results. However, the limitations of the drift-diffusion model have already been reached. First, a row of newly introduced fitting parameters requires a specific calibration for each particular device technology. Second, the interface damage caused by secondarily generated holes cannot be captured using the drift-diffusion model. Therefore, the degradation in devices with a channel length above  $0.5\text{ }\mu\text{m}$ , cannot be modeled.

Future work is therefore related to development of methods for an efficient calculation of the carrier energy distribution function. The most promising candidate for this is the deterministic solution of the Boltzmann transport equation based on the spherical harmonics expansion.

## CHAPTER 8. CONCLUSIONS AND OUTLOOK

First results obtained within this technique with the presented hot-carrier degradation model have already been accepted for publication. Additionally, the degradation model needs some extensions. The probably most important missing feature seems to be the consideration of oxide traps.

## Appendix A

# Derivation of the Impact-Ionization Integral

In the following the derivation of the impact-ionization integral from Section 5.1.2 on page 57 will be given. First, the differential equation

$$\frac{dI_p}{dx} - (\alpha_p - \alpha_n) I_p = \alpha_n I \quad (\text{A.1})$$

has to be solved. Using the simplified notation

$$y' + Py = Q, \quad (\text{A.2})$$

with  $P(x) = -(\alpha_p - \alpha_n)$  and  $Q(x) = \alpha_n I$ , one can derive the homogenous solution

$$y_h = C \exp \left( - \int_0^x P \, dx \right), \quad (\text{A.3})$$

where  $C$  is the constant of integration. Applying the method of variation of constants, the ansatz of the particular solution  $y_p$  is derived from the homogenous solution, using  $C \rightarrow C(x)$ . This ansatz function  $y_p$  can be differentiated to

$$y_p' = C' \exp \left( - \int_0^x P \, dx \right) - P y_p. \quad (\text{A.4})$$

Comparison of the coefficients between equations (A.2) and (A.4) gives

$$Q = C' \exp \left( - \int_0^x P \, dx \right) \quad (\text{A.5})$$

and  $C(x)$  evaluates to

$$C = \int_0^x Q \exp \left( \int_0^x P \, dx' \right) dx. \quad (\text{A.6})$$

## APPENDIX A. DERIVATION OF THE IMPACT-IONIZATION INTEGRAL

This leads to the particular solution

$$y_p = \exp \left( - \int_0^x P \, dx \right) \left[ \int_0^x Q \exp \left( \int_0^x P \, dx' \right) \, dx \right] \quad (\text{A.7})$$

and together with the homogenous solution  $y_h$  to the solution of (A.2)

$$y = \exp \left( - \int_0^x P \, dx \right) \left[ \int_0^x Q \exp \left( \int_0^x P \, dx' \right) \, dx + C \right]. \quad (\text{A.8})$$

Using (A.8) our initial problem (A.1) solves together with the boundary conditions  $I_p(0) = I_{p0}$  and  $I_p(W) = I = M_p I_{p0}$  to

$$I_p = I \exp \left( \int_0^x (\alpha_p - \alpha_n) \, dx \right) \left[ \int_0^x \alpha_n \exp \left( - \int_0^x (\alpha_p - \alpha_n) \, dx' \right) \, dx + \frac{1}{M_p} \right]. \quad (\text{A.9})$$

To simplify the solution (A.9) the following relationship can be used. Considering

$$U = \int_0^x y \, dx, \quad \frac{dU}{dx} = y, \quad \frac{d}{dU} \exp(U) = \exp(U), \quad (\text{A.10})$$

the following simplification can be performed:

$$\begin{aligned} \int y \exp \left( \int_0^x y \, dx' \right) \, dx &= \int y \exp(U) \, dx = \int \exp(U) \, dU = \exp(U) \\ &= \exp \left( \int_0^x y \, dx' \right). \end{aligned} \quad (\text{A.11})$$

Making the relation (A.11) applicable, (A.9) can be rewritten at the position  $x = W$  as

$$\begin{aligned} 1 = \exp \left( \int_0^W (\alpha_p - \alpha_n) \, dx \right) &\left[ \int_0^W \alpha_p \exp \left( - \int_0^x (\alpha_p - \alpha_n) \, dx' \right) \, dx \right. \\ &\quad \left. - \underbrace{\int_0^W (\alpha_p - \alpha_n) \exp \left( - \int_0^x (\alpha_p - \alpha_n) \, dx' \right) \, dx}_{- \exp \left( - \int_0^W (\alpha_p - \alpha_n) \, dx' \right) + 1} + \frac{1}{M_p} \right] \end{aligned} \quad (\text{A.12})$$

and simplified to

$$1 - \frac{1}{M_p} = \int_0^W \alpha_p \exp \left( - \int_0^x (\alpha_p - \alpha_n) \, dx' \right) \, dx. \quad (\text{A.13})$$

# Bibliography

- [1] A. Allan, D. Edenfeld, W. Joyner, A. B. Kahng, M. Rodgers, and Y. Zorian, “2001 technology roadmap for semiconductors,” *IEEE Computer*, vol. 35, no. 1, pp. 42–53, 2002.
- [2] C. A. Mack, “Fifty years of Moore’s law,” *IEEE Transactions on Semiconductor Manufacturing*, vol. 24, no. 2, pp. 202–207, 2011.
- [3] B. J. Baliga, “Smart power technology: An elephantine opportunity,” in *Technical Digest International Electron Devices Meeting (IEDM)*, pp. 3–6, 1990.
- [4] B. J. Baliga, “An overview of smart power technology,” *IEEE Transactions on Electron Devices*, vol. 38, no. 7, pp. 1568–1575, 1991.
- [5] M. Schrems, M. Knaipp, H. Enichlmair, V. Vescoli, R. Minixhofer, E. Seebacher, F. Leisenberger, E. Wachmann, G. Schatzberger, and H. Gensinger, “Scalable high voltage CMOS technology for smart power and sensor applications,” *Elektrotechnik und Informationstechnik*, vol. 125, pp. 109–117, April 2008.
- [6] A. Andreini, C. Contiero, and P. Galbiati, “BCD technology for smart power ICs,” in *Smart Power ICs* (B. Murari, F. Bertotti, and G. Vignola, eds.), ch. 1, pp. 1–52, Springer, 1996.
- [7] *The Authoritative Dictionary of IEEE Standards Terms – IEEE 100, 7<sup>th</sup> Edition*. IEEE Press, 2000.
- [8] S. Pendharkar, “Technology requirements for automotive electronics,” in *Proceedings IEEE Conference Vehicle Power and Propulsion*, pp. 834–839, 2005.
- [9] J.-M. Park, H. Enichlmair, and R. Minixhofer, “Hot-carrier behaviour of a 0.35  $\mu\text{m}$  high-voltage n-channel LDMOS transistor,” in *Proceedings Simulation of Semiconductor Processes and Devices (SISPAD)*, pp. 369–372, 2007.
- [10] H. Casier, P. Moens, and K. Appeltans, “Technology considerations for automotive,” in *Proceedings European Solid-State Device Research Conference (ESSDERC)*, pp. 37–41, 2004.
- [11] S. Selberherr, *Analysis and Simulation of Semiconductor Devices*. Springer-Verlag Wien New York, 1984.

## BIBLIOGRAPHY

- [12] K. Kramer, G. Nicholas, and W. Hitchon, *Semiconductor Devices, a Simulation Approach*. Prentice Hall Professional Technical Reference, 1997.
- [13] W. Fichtner, K. Esmark, and W. Stadler, “TCAD software for ESD on-chip protection design,” in *Technical Digest International Electron Devices Meeting (IEDM)*, pp. 14.1.1–14.1.4, 2001.
- [14] W. Fichtner, N. Braga, M. Ciappa, V. Mickevicius, and M. Schenkel, “Progress in technology CAD for power devices, circuits and systems,” in *Proceedings International Symposium on Power Semiconductor Devices and IC’s (ISPSD)*, pp. 1–9, 2005.
- [15] T. Grasser, T.-W. Tang, H. Kosina, and S. Selberherr, “A review of hydrodynamic and energy-transport models for semiconductor device simulation,” *Proceedings of the IEEE*, vol. 91, no. 2, pp. 251–274, 2003.
- [16] C. Jungemann and B. Meinerzhagen, *Hierarchical Device Simulation: The Monte-Carlo Perspective*. Springer, 2003.
- [17] S. Tyaginov, I. Starkov, O. Triebel, J. Cervenka, C. Jungemann, S. Carniello, J.-M. Park, H. Enichlmair, M. Karner, C. Kernstock, E. Seebacher, R. Minixhofer, H. Ceric, and T. Grasser, “Hot-carrier degradation modeling using full-band Monte-Carlo simulations,” in *Proceedings IEEE International Symposium on the Physical and Failure Analysis of Integrated Circuits (IPFA)*, pp. 1–5, 2010.
- [18] S. Tyaginov, I. Starkov, O. Triebel, H. Ceric, T. Grasser, H. Enichlmair, J.-M. Park, and C. Jungemann, “Secondary generated holes as a crucial component for modeling of HC degradation in high-voltage n-MOSFET,” in *Proceedings Simulation of Semiconductor Processes and Devices (SISPAD)*, pp. 123–126, 2011.
- [19] B. J. Baliga, “The future of power semiconductor device technology,” *Proceedings of the IEEE*, vol. 89, no. 6, pp. 822–832, 2001.
- [20] J. G. Bauer, T. Duetemeyer, E. Falck, C. Schaeffer, G. Schmidt, and H. Schulze, “Investigations on 6.5kV trench IGBT and adapted EmCon diode,” in *Proceedings International Symposium on Power Semiconductor Devices and IC’s (ISPSD)*, pp. 5–8, 2007.
- [21] M. Vellvehi, D. Flores, X. Jorda, S. Hidalgo, J. Rebollo, L. Coulbeck, and P. Waind, “Design considerations for 6.5 kV IGBT devices,” *Microelectronics Journal*, vol. 35, no. 3, pp. 269–275, 2004.
- [22] T. Fujii, K. Yoshikawa, T. Koga, A. Nishiura, Y. Takahashi, H. Kakiki, M. Ichijyou, and Y. Seki, “4.5 kV-2000 A power pack IGBT (ultra high power flat-packaged PT type RC-IGBT),” in *Proceedings International Symposium on Power Semiconductor Devices and IC’s (ISPSD)*, pp. 33–36, 2000.
- [23] C. Kleint, “Julius Edgar Lilienfeld: Life and profession,” *Progress in Surface Science*, vol. 57, pp. 253–327, April 1998.



- [24] E. J. Lilienfeld, "Method and apparatus for controlling electric currents," Jan 1930, U.S. Patent 1745175.
- [25] E. J. Lilienfeld, "Device for controlling electric current," March 1933, U.S. Patent 1900018.
- [26] M. M. Atalla, E. Tannenbaum, and E. J. Scheibner, "Stabilization of silicon surfaces by thermally grown oxides," *Bell System Technical Journal*, vol. 38, pp. 749–783, 1959.
- [27] R. G. Arns, "The other transistor: early history of the metal-oxide semiconductor field-effect transistor," *Engineering Science and Education Journal*, vol. 7, no. 5, pp. 233–240, 1998.
- [28] B. J. Baliga, "Trends in power semiconductor devices," *IEEE Transactions on Electron Devices*, vol. 43, no. 10, pp. 1717–1731, 1996.
- [29] B. J. Baliga, *Power Semiconductor Devices*. PWS Publishing Company, 1995.
- [30] B. J. Baliga, M. S. Adler, R. P. Love, P. V. Gray, and N. D. Zommer, "The insulated gate transistor: A new three-terminal MOS-controlled bipolar power device," *IEEE Transactions on Electron Devices*, vol. 31, no. 6, pp. 821–828, 1984.
- [31] T. R. Efland, C.-Y. Tsai, and S. Pendharkar, "Lateral thinking about power devices (LD-MOS)," in *Technical Digest International Electron Devices Meeting (IEDM)*, pp. 679–682, 1998.
- [32] S. Sze, *Physics of Semiconductor Devices*. New York: Wiley, second ed., 1981.
- [33] J. Appels and H. Vaes, "High voltage thin layer devices (RESURF devices)," in *Technical Digest International Electron Devices Meeting (IEDM)*, vol. 25, pp. 238 – 241, 1979.
- [34] P. Moens and G. Van den bosch, "Reliability assessment of integrated power transistors: Lateral DMOS versus vertical DMOS," *Microelectronics Reliability*, vol. 48, no. 8–9, pp. 1300–1305, 2008.
- [35] M. Amato and V. Rumennik, "Comparison of lateral and vertical DMOS specific on-resistance," in *Technical Digest International Electron Devices Meeting (IEDM)*, vol. 31, pp. 736–739, 1985.
- [36] M. Knaipp, G. Rohrer, R. Minixhofer, and E. Seebacher, "Investigations on the high current behavior of lateral diffused high-voltage transistors," *IEEE Transactions on Electron Devices*, vol. 51, no. 10, pp. 1711–1720, 2004.
- [37] P. Moens, S. Bychikhin, K. Reynders, D. Pogany, E. Gornik, and M. Tack, "Dynamics of integrated vertical DMOS transistors under 100-ns TLP stress," *IEEE Transactions on Electron Devices*, vol. 52, no. 5, pp. 1008–1013, 2005.
- [38] A. S. Grove, O. Leistiko, Jr., and W. W. Hooper, "Effect of surface fields on the breakdown voltage of planar silicon p-n junctions," *IEEE Transactions on Electron Devices*, vol. 14, no. 3, pp. 157–162, 1967.

## BIBLIOGRAPHY

- [39] D. Scharfetter and H. Gummel, "Large-signal analysis of a silicon read diode oscillator," *IEEE Transactions on Electron Devices*, vol. 16, no. 1, pp. 64–77, 1969.
- [40] A. W. Ludikhuizen, "A review of RESURF technology," in *Proceedings International Symposium on Power Semiconductor Devices and IC's (ISPSD)*, pp. 11–18, 2000.
- [41] Z. Hossain, T. Ishigwo, L. Tu, H. Corleto, F. Kuramae, and R. Nair, "Field-plate effects on the breakdown voltage of an integrated high-voltage LDMOS transistor," in *Proceedings International Symposium on Power Semiconductor Devices and IC's (ISPSD)*, pp. 237–240, 2004.
- [42] J. Roig, D. Flores, J. Urresti, S. Hidalgo, and J. Rebollo, "Modeling of non-uniform heat generation in LDMOS transistors," *Solid-State Electronics*, vol. 49, no. 1, pp. 77–84, 2005.
- [43] S. Gao, J. Chen, D. Ke, and L. Liu, "Analytical model for surface electrical field of double RESURF LDMOS with field plate," in *Proceedings Solid-State and Integrated Circuit Technology (ICSICT)*, pp. 1324–1326, 2006.
- [44] P. M. Shenoy, A. Bhalla, and G. M. Dolny, "Analysis of the effect of charge imbalance on the static and dynamic characteristics of the super junction MOSFET," in *Proceedings International Symposium on Power Semiconductor Devices and IC's (ISPSD)*, pp. 99–102, 1999.
- [45] L. Lorenz, G. Deboy, A. Knapp, and M. Marz, "COOLMOS<sup>TM</sup> – a new milestone in high voltage power MOS," in *Proceedings International Symposium on Power Semiconductor Devices and IC's (ISPSD)*, pp. 3–10, 1999.
- [46] A. Andreini, C. Contiero, and P. Galbiati, "A new integrated silicon gate technology combining bipolar linear, CMOS logic, and DMOS power parts," *IEEE Transactions on Electron Devices*, vol. 33, no. 12, pp. 2025–2030, 1986.
- [47] W. Horn and H. Zitta, "A robust smart power bandgap reference circuit for use in an automotive environment," *IEEE Journal of Solid-State Circuits*, vol. 37, no. 7, pp. 949–952, 2002.
- [48] T. Efland, J. Devore, A. Hastings, S. Pendharkar, and R. Teggatz, "Bipolar issues in advanced power BiCMOS technology," in *Proceedings Bipolar/BiCMOS Circuits and Technology Meeting*, pp. 20–27, 2000.
- [49] S. Mukherjee, "Technologies for high voltage ICs," in *Smart Power ICs* (K. Itoh, T. Lee, T. Sakurai, and D. Schmitt-Landsiedel, eds.), ch. 2, pp. 53–78, Springer, 1996.
- [50] S. L. Wong, S. Venkatasubrahmanian, M. J. Kim, and J. C. Young, "Design of a 60-V 10-A intelligent power switch using standard cells," *IEEE Journal of Solid-State Circuits*, vol. 27, no. 3, pp. 429–432, 1992.
- [51] A. Moscatelli, A. Merlini, G. Croce, P. Galbiati, and C. Contiero, "LDMOS implementation in a 0.35  $\mu\text{m}$  BCD technology (BCD6)," in *Proceedings International Symposium on Power Semiconductor Devices and IC's (ISPSD)*, pp. 323–326, 2000.

- [52] T. Trajkovic, N. Udugampola, V. Pathirana, A. Mihaila, F. Udrea, G. A. J. Amaratunga, B. Koutny, K. Ramkumar, and S. Geha, "High frequency 700V PowerBrane LIGBTs in 0.35  $\mu\text{m}$  bulk CMOS technology," in *Proceedings International Symposium on Power Semiconductor Devices and IC's (ISPSD)*, pp. 307–310, 2009.
- [53] F. Kawai, T. Onishi, T. Kamiya, H. Ishimabushi, H. Eguchi, K. Nakaharna, H. Aoki, and K. Hamada, "Multi-voltage SOI-BiCDMOS for 14V&42V automotive applications," in *Proceedings International Symposium on Power Semiconductor Devices and IC's (ISPSD)*, pp. 165–168, 2004.
- [54] Y.-K. Leung, Y. Suzuki, K. E. Goodson, and S. S. Wong, "Self-heating effect in lateral DMOS on SOI," in *Proceedings International Symposium on Power Semiconductor Devices and IC's (ISPSD)*, pp. 136–140, 1995.
- [55] H. Lim, F. Udrea, D. Garner, and W. Milne, "Modelling of self-heating effect in thin SOI and partial SOI LDMOS power devices," *Solid-State Electronics*, vol. 43, no. 7, pp. 1267–1280, 1999.
- [56] W. Denson, "The history of reliability prediction," *IEEE Transactions on Reliability*, vol. 47, no. 3, pp. SP321–SP328, 1998.
- [57] A. Goel and R. Graves, "Electronic systems reliability: Collating prediction models," *IEEE Transactions on Device and Materials Reliability*, vol. 6, no. 2, pp. 258–265, 2006.
- [58] I. Snook, J. Marshall, and R. Newman, "Physics of failure as an integrated part of design for reliability," in *Proceedings Annual Reliability and Maintainability Symposium*, pp. 46–54, 2003.
- [59] *Reliability Prediction of Electronic Equipment (MIL-HDBK-217F Notice 2)*. Military Handbook, U.S. Department of Defense, 1995.
- [60] M. Pecht and F. Nash, "Predicting the reliability of electronic equipment," *Proceedings of the IEEE*, vol. 82, no. 7, pp. 992–1004, 1994.
- [61] M. Cushing, D. Mortin, T. Stadterman, and A. Malhotra, "Comparison of electronics-reliability assessment approaches," *IEEE Transactions on Reliability*, vol. 42, no. 4, pp. 542–546, 1993.
- [62] S. Morris and J. Reilly, "MIL-HDBK-217 – A favorite target," in *Proceedings Annual Reliability and Maintainability Symposium*, pp. 503–509, 1993.
- [63] M. Ohring, *Reliability and Failure of Electronic Materials and Devices*. Academic Press, 1998.
- [64] H. H. Huston and C. P. Clarke, "Reliability defect detection and screening during processing-theory and implementation," in *Proceedings IEEE International Reliability Physics Symposium (IRPS)*, pp. 268–275, 1992.
- [65] K. L. Wong, "The bathtub does not hold water any more," *Quality and Reliability Engineering International*, vol. 4, no. 3, pp. 279–282, 1988.

## BIBLIOGRAPHY

- [66] K. L. Wong, "The roller-coaster curve is in," *Quality and Reliability Engineering International*, vol. 5, no. 1, pp. 29–36, 1989.
- [67] K. L. Wong, "The physical basis for the roller-coaster hazard rate curve for electronics," *Quality and Reliability Engineering International*, vol. 7, no. 6, pp. 189–495, 1991.
- [68] W. Kuo and M. J. Zuo, *Optimal Reliability Modeling – Principles and Applications*. Wiley, 2003.
- [69] M. Bebbington and C.-D. Lai, "Lifetime analysis of incandescent lamps: The Menon-Agrawal model revisited," *Reliability & Risk Analysis: Theory & Applications*, vol. 1, no. 1, pp. 97–108, 2008.
- [70] R. Degraeve, G. Groeseneken, R. Bellens, J. L. Ogier, M. Depas, P. J. Roussel, and H. E. Maes, "New insights in the relation between electron trap generation and the statistical properties of oxide breakdown," *IEEE Transactions on Electron Devices*, vol. 45, no. 4, pp. 904–911, 1998.
- [71] M. Pecht, "A model for moisture induced corrosion failures in microelectronic packages," *IEEE Transactions on Components, Hybrids, and Manufacturing Technology*, vol. 13, no. 2, pp. 383–389, 1990.
- [72] C. Chauvet and C. Laurent, "Weibull statistics in short-term dielectric breakdown of thin polyethylene films," *IEEE Transactions on Electrical Insulation*, vol. 28, no. 1, pp. 18–29, 1993.
- [73] R. Hill and E. Okoroafor, "Weibull statistics of fibre bundle failure using mechanical and acoustic emission testing: the influence of interfibre friction," *Composites*, vol. 26, no. 10, pp. 699–705, 1995.
- [74] W. Kuo, W.-T. K. Chien, and T. Kim, *Reliability, Yield, and Stress Burn-In*. Springer US, 1998.
- [75] K. O. Kim, W. Kuo, and W. Luo, "A relation model of gate oxide yield and reliability," *Microelectronics Reliability*, vol. 44, no. 3, pp. 425–434, 2004.
- [76] T. Kim and W. Kuo, "Modeling manufacturing yield and reliability," *IEEE Transactions on Semiconductor Manufacturing*, vol. 12, no. 4, pp. 485–492, 1999.
- [77] J. C. Lee, C. Ih-Chin, and H. Chenming, "Modeling and characterization of gate oxide reliability," *IEEE Transactions on Electron Devices*, vol. 35, no. 12, pp. 2268–2278, 1988.
- [78] F. Kuper, J. van der Pol, E. Ooms, T. Johnson, R. Wijburg, W. Koster, and D. Johnston, "Relation between yield and reliability of integrated circuits: experimental results and application to continuous early failure rate reduction programs," in *Proceedings IEEE International Reliability Physics Symposium (IRPS)*, pp. 17–21, 1996.
- [79] A. Buerke, H. Wendrock, and K. Wetzig, "Study of electromigration damage in Al interconnect lines inside a SEM," *Crystal Research and Technology*, vol. 35, no. 6-7, pp. 721–730, 2000.

- [80] J. R. Black, "Electromigration—a brief survey and some recent results," *IEEE Transactions on Electron Devices*, vol. 16, no. 4, pp. 338–347, 1969.
- [81] M. L. Green, E. P. Gusev, R. Degraeve, and E. L. Garfunkel, "Ultrathin ( $< 4$  nm) SiO<sub>2</sub> and Si–O–N gate dielectric layers for silicon microelectronics: Understanding the processing, structure, and physical and electrical limits," *Journal of Applied Physics*, vol. 90, no. 5, pp. 2057–2121, 2001.
- [82] E. Harari, "Conduction and trapping of electrons in highly stressed ultrathin films of thermal SiO<sub>2</sub>," *Applied Physics Letters*, vol. 30, no. 11, pp. 601–603, 1977.
- [83] S. Lombardo, J. H. Stathis, B. P. Linder, K. L. Pey, F. Palumbo, and C. H. Tung, "Dielectric breakdown mechanisms in gate oxides," *Journal of Applied Physics*, vol. 98, no. 12, pp. 121301–1–36, 2005.
- [84] J. S. Suehle, "Ultrathin gate oxide reliability: Physical models, statistics, and characterization," *IEEE Transactions on Electron Devices*, vol. 49, no. 6, pp. 958–971, 2002.
- [85] D. A. Buchanan, J. H. Stathis, E. Cartier, and D. J. DiMaria, "On the relationship between stress induced leakage currents and catastrophic breakdown in ultra-thin SiO<sub>2</sub> based dielectrics," *Microelectronic Engineering*, vol. 36, no. 1-4, pp. 329–332, 1997.
- [86] L. Pantisano and K. Cheung, "Stress-induced leakage current (SILC) and oxide breakdown: are they from the same oxide traps?," *IEEE Transactions on Device and Materials Reliability*, vol. 1, no. 2, pp. 109–112, 2001.
- [87] D. J. DiMaria, D. A. Buchanan, J. H. Stathis, and R. E. Stahlbush, "Interface states induced by the presence of trapped holes near the silicon–silicon-dioxide interface," *Journal of Applied Physics*, vol. 77, no. 5, pp. 2032–2040, 1995.
- [88] D. J. DiMaria, E. Cartier, and D. Arnold, "Impact ionization, trap creation, degradation, and breakdown in silicon dioxide films on silicon," *Journal of Applied Physics*, vol. 73, no. 7, pp. 3367–3348, 1993.
- [89] I. C. Chen, S. Holland, K. K. Young, C. Chang, and C. Hu, "Substrate hole current and oxide breakdown," *Applied Physics Letters*, vol. 49, no. 11, pp. 669–671, 1986.
- [90] K. F. Schuegraf and C. Hu, "Metal-oxide-semiconductor field-effect-transistor substrate current during Fowler–Nordheim tunneling stress and silicon dioxide reliability," *Journal of Applied Physics*, vol. 76, no. 6, pp. 3695–3700, 1994.
- [91] R. Degraeve, B. Kaczer, and G. Groeseneken, "Degradation and breakdown in thin oxide layers: mechanisms, models and reliability prediction," *Microelectronics Reliability*, vol. 39, no. 10, pp. 1445–1460, 1999.
- [92] J. W. McPherson and H. C. Mogul, "Underlying physics of the thermochemical E model in describing low-field time-dependent dielectric breakdown in SiO<sub>2</sub> thin films," *Journal of Applied Physics*, vol. 84, no. 3, pp. 1513–1523, 1998.

## BIBLIOGRAPHY

- [93] J. H. Stathis, “Percolation models for gate oxide breakdown,” *Journal of Applied Physics*, vol. 86, no. 10, pp. 5757–5766, 1999.
- [94] B. E. Weir, P. J. Silverman, D. Monroe, K. S. Krisch, M. A. Alam, G. B. Alers, T. W. Sorsch, G. L. Timp, F. Baumann, C. T. Liu, Y. Ma, and D. Hwang, “Ultra-thin gate dielectrics: they break down, but do they fail?,” in *Technical Digest International Electron Devices Meeting (IEDM)*, pp. 73–76, 1997.
- [95] R. Degraeve, B. Kaczer, and G. Groeseneken, “Reliability: a possible showstopper for oxide thickness scaling?,” *Semiconductor Science and Technology*, vol. 15, pp. 434–444, 2000.
- [96] T. Grasser and B. Kaczer, “Negative bias temperature instability: Recoverable versus permanent degradation,” in *Proceedings European Solid-State Device Research Conference (ESSDERC)*, pp. 127–130, 2007.
- [97] M. Alam and S. Mahapatra, “A comprehensive model of pMOS NBTI degradation,” *Microelectronics Reliability*, vol. 45, no. 1, pp. 71–81, 2005.
- [98] R. Entner, T. Grasser, O. Triebel, H. Enichlmair, and R. Minixhofer, “Negative bias temperature instability modeling for high-voltage oxides at different stress temperatures,” *Microelectronics Reliability*, vol. 47, no. 4–5, pp. 697–699, 2007.
- [99] T. Grasser, W. Göss, and B. Kaczer, “Dispersive transport and negative bias temperature instability: Boundary conditions, initial conditions, and transport models,” *IEEE Transactions on Device and Materials Reliability*, vol. 8, no. 1, pp. 79–97, 2008.
- [100] T. Grasser, P. Wagner, P. Hehenberger, W. Göss, and B. Kaczer, “A rigorous study of measurement techniques for negative bias temperature instability,” *IEEE Transactions on Device and Materials Reliability*, vol. 8, no. 3, pp. 526–535, 2008.
- [101] T. Grasser, B. Kaczer, W. Göss, T. Aichinger, P. Hehenberger, and M. Nelhiebel, “A two-stage model for negative bias temperature instability,” in *Proceedings IEEE International Reliability Physics Symposium (IRPS)*, 2009.
- [102] T. Grasser, B. Kaczer, W. Göss, T. Aichinger, P. Hehenberger, and M. Nelhiebel, “Understanding negative bias temperature instability in the context of hole trapping,” *Microelectronic Engineering*, vol. 86, no. 7–9, pp. 1876–1882, 2009.
- [103] K. Kawamoto and S. Takahashi, “An advanced no-snapback LDMOSFET with optimized breakdown characteristics of drain n-n<sup>+</sup> diodes,” *IEEE Transactions on Electron Devices*, vol. 51, no. 9, pp. 1432–1440, 2004.
- [104] D. Kontos, K. Domanski, R. Gauthier, K. Chatty, M. Muhammad, C. Seguin, R. Halbach, C. Russ, and D. Alvarez, “Investigation of external latchup robustness of dual and triple well designs in 65nm bulk CMOS technology,” in *Proceedings IEEE International Reliability Physics Symposium (IRPS)*, pp. 145–150, 2006.



- [105] D. Lin, “ESD sensitivity and VLSI technology trends: thermal breakdown and dielectric breakdown,” *Journal of Electrostatics*, vol. 33, no. 3, pp. 251–271, 1994.
- [106] S. Voldman, “A review of electrostatic discharge (ESD) in advanced semiconductor technology,” *Microelectronics Reliability*, vol. 44, pp. 33–46, 2004.
- [107] A. A. Salman, R. Gauthier, C. Putnam, P. Riess, M. Muhammad, M. Woo, and D. E. Ioannou, “ESD-induced oxide breakdown on self-protecting GG-nMOSFET in 0.1- $\mu\text{m}$  CMOS technology,” *IEEE Transactions on Device and Materials Reliability*, vol. 3, no. 3, pp. 79–84, 2003.
- [108] J. E. Vinson and J. J. Liou, “Electrostatic discharge in semiconductor devices: protection techniques,” *Proceedings of the IEEE*, vol. 88, no. 12, pp. 1878–1902, 2000.
- [109] V. De Heyn, G. Groeseneken, B. Keppens, M. Natarajan, L. Vacaressse, and G. Gallopyn, “Design and analysis of new protection structures for smart power technology with controlled trigger and holding voltage,” in *Proceedings IEEE International Reliability Physics Symposium (IRPS)*, pp. 253–258, 2001.
- [110] X. Gao, J. J. Liou, J. Bernier, G. Crof, W. Wong, and S. Vishwanathan, “Optimization of on-chip ESD protection structures for minimal parasitic capacitance,” *Microelectronics Reliability*, vol. 43, no. 5, pp. 725–733, 2003.
- [111] J. A. Salcedo, J. J. Liou, Z. Liu, and J. E. Vinson, “TCAD methodology for design of SCR devices for electrostatic discharge (ESD) applications,” *IEEE Transactions on Electron Devices*, vol. 54, no. 4, pp. 822–832, 2007.
- [112] D. Flandre, “Silicon-on-insulator technology for high temperature metal oxide semiconductor devices and circuits,” *Materials Science and Engineering: B*, vol. 29, no. 1–3, pp. 7–12, 1995.
- [113] R. W. Johnson, J. L. Evans, P. Jacobsen, J. R. Thompson, and M. Christopher, “The changing automotive environment: high-temperature electronics,” *IEEE Transactions on Electronics Packaging Manufacturing*, vol. 27, no. 3, pp. 164–176, 2004.
- [114] W. Wondrak, “Physical limits and lifetime limitations of semiconductor devices at high temperatures,” *Microelectronics Reliability*, vol. 39, no. 6–7, pp. 1113–1120, 1999.
- [115] S. Reggiani, M. Valdinoci, L. Colalongo, M. Rudan, G. Baccarani, A. Stricker, F. Illien, N. Felber, W. Fichtner, and L. Zullino, “Electron and hole mobility in silicon at large operating temperatures. Part I: Bulk mobility,” *IEEE Transactions on Electron Devices*, vol. 49, no. 3, pp. 490–499, 2002.
- [116] S. Reggiani, E. Gnani, M. Rudan, G. Baccarani, C. Corvasce, D. Barlini, M. Ciappa, W. Fichtner, M. Denison, N. Jensen, G. Groos, and M. Stecher, “Experimental extraction of the electron impact-ionization coefficient at large operating temperatures,” in *Technical Digest International Electron Devices Meeting (IEDM)*, pp. 407–410, 2004.

## BIBLIOGRAPHY

- [117] D. J. Frank, “Power-constrained CMOS scaling limits,” *IBM Journal of Research and Development*, vol. 46, no. 2, pp. 235–244, 2002.
- [118] A. Bar-Cohen and M. Iyengar, “Design and optimization of air-cooled heat sinks for sustainable development,” *IEEE Transactions on Components and Packaging Technologies*, vol. 25, no. 4, pp. 584–591, 2002.
- [119] Y. Li and C. Wong, “Recent advances of conductive adhesives as a lead-free alternative in electronic packaging: Materials, processing, reliability and applications,” *Materials Science and Engineering: R: Reports*, vol. 51, no. 1–3, pp. 1–35, 2006.
- [120] I $\mu$ E, *MINIMOS-NT 2.1 User’s Guide*. Institut für Mikroelektronik, Technische Universität Wien, Austria, 2004.
- [121] Global TCAD Solutions, *GTS Framework*. <http://www.globaltcad.com>.
- [122] C. Jacoboni and L. Reggiani, “The Monte Carlo method for the solution of charge transport in semiconductors with application to covalent materials,” *Reviews of Modern Physics*, vol. 55, no. 3, pp. 645–705, 1983.
- [123] M. Lundstrom, *Fundamentals of Carrier Transport*. Cambridge University Press, 2000.
- [124] G. A. Baraff, “Maximum anisotropy approximation for calculating electron distributions; application to high field transport in semiconductors,” *Physical Review*, vol. 133, no. 1A, pp. A26–A33, 1964.
- [125] C. Jungemann, A. T. Pham, B. Meinerzhagen, C. Ringhofer, and M. Bollhofer, “Stable discretization of the Boltzmann equation based on spherical harmonics, box integration, and a maximum entropy dissipation principle,” *Journal of Applied Physics*, vol. 100, no. 2, pp. 024502–1–13, 2006.
- [126] M. Vecchi and M. Rudan, “Modeling electron and hole transport with full-band structure effects by means of the spherical-harmonics expansion of the BTE,” *IEEE Transactions on Electron Devices*, vol. 45, no. 1, pp. 230–238, 1998.
- [127] G. Wachutka, “Rigorous thermodynamic treatment of heat generation and conduction in semiconductor device modeling,” *IEEE Transactions on Computer-Aided Design of Integrated Circuits and Systems*, vol. 9, no. 11, pp. 1141–1149, 1990.
- [128] R. Stratton, “Semiconductor current-flow equations (diffusion and degeneracy),” *IEEE Transactions on Electron Devices*, vol. 19, no. 12, pp. 1288–1292, 1972.
- [129] W. VanRoosbroeck, “Theory of flow of electrons and holes in germanium and other semiconductors,” *Bell System Technical Journal*, vol. 29, pp. 560–607, 1950.
- [130] T. Grasser, H. Kosina, M. Gritsch, and S. Selberherr, “Using six moments of Boltzmann’s transport equation for device simulation,” *Journal of Applied Physics*, vol. 90, no. 5, pp. 2389–2396, 2001.



- [131] R. Stratton, “Diffusion of hot and cold electrons in semiconductor barriers,” *Physical Review*, vol. 126, no. 6, pp. 2002–2014, 1962.
- [132] K. Bløtekjær, “Transport equations for electrons in two-valley semiconductors,” *IEEE Transactions on Electron Devices*, vol. 17, no. 1, pp. 38–47, 1970.
- [133] T. Grasser and S. Selberherr, “Limitations of hydrodynamic and energy-transport models,” in *Proceedings International Workshop on the Physics of Semiconductor Devices (IWPSD)*, pp. 584–591, 2001.
- [134] T. Grasser, H. Kosina, C. Heitzinger, and S. Selberherr, “Characterization of the hot electron distribution function using six moments,” *Journal of Applied Physics*, vol. 91, no. 6, pp. 3869–3879, 2002.
- [135] T. Grasser, C. Jungemann, H. Kosina, B. Meinerzhagen, and S. Selberherr, “Advanced transport models for sub-micrometer devices,” in *Proceedings Simulation of Semiconductor Processes and Devices (SISPAD)*, pp. 1–8, 2004.
- [136] V. Sverdlov, E. Ungersboeck, H. Kosina., and S. Selberherr, “Current transport models for nanoscale semiconductor devices,” *Materials Science and Engineering: R: Reports*, vol. 58, no. 6, pp. 228–270, 2008.
- [137] S. Vitinov, V. Palankovski, R. Quay, and E. Langer, “Two-dimensional numerical simulation of AlGaIn/GaN HEMTs,” in *Book of Proceedings TARGET Days*, pp. 81–84, 2006.
- [138] S. Selberherr, W. Hänsch, M. Seavey, and J. Slotboom, “The evolution of the MINIMOS mobility model,” *Solid-State Electronics*, vol. 33, no. 11, pp. 1425–1436, 1990.
- [139] C. Lombardi, S. Manzini, A. Saporito, and M. Vanzi, “A physically based mobility model for numerical simulation of nonplanar devices,” *IEEE Transactions on Computer-Aided Design of Integrated Circuits and Systems*, vol. 7, no. 11, pp. 1164–1171, 1988.
- [140] V. M. J. Agostinelli, H. Shin, and A. F. J. Tasch, “A comprehensive model for inversion layer hole mobility for simulation of submicrometer MOSFET’s,” *IEEE Transactions on Electron Devices*, vol. 38, no. 1, pp. 151–159, 1991.
- [141] M. Darwish, J. Lentz, M. Pinto, P. Zeitoff, T. Krutsick, and H. H. Vuong, “An improved electron and hole mobility model for general purpose device simulation,” *IEEE Transactions on Electron Devices*, vol. 44, no. 9, pp. 1529–1538, 1997.
- [142] B. Neinhüs, C. Nguyen, C. Jungemann, and B. Meinerzhagen, “A CPU efficient electron mobility model for MOSFET simulation with quantum corrected charge densities,” in *Proceedings European Solid-State Device Research Conference (ESSDERC)*, pp. 332–335, 2000.
- [143] T. Grasser, R. Entner, O. Triebel, H. Enichlmair, and R. Minixhofer, “TCAD modeling of negative bias temperature instability,” in *Proceedings Simulation of Semiconductor Processes and Devices (SISPAD)*, pp. 330–333, 2006.

## BIBLIOGRAPHY

- [144] V.-H. Chan and J. Chung, “Two-stage hot-carrier degradation and its impact on submicrometer LDD NMOSFET lifetime prediction,” *IEEE Transactions on Electron Devices*, vol. 42, no. 5, pp. 957–962, 1995.
- [145] S. Sun and J. Plummer, “Electron mobility in inversion and accumulation layers on thermally oxidized silicon surfaces,” *IEEE Transactions on Electron Devices*, vol. 27, no. 8, pp. 1497–1508, 1980.
- [146] H.-S. Wong, M. White, J. Krutsick, and R. Booth, “Modeling of transconductance degradation and extraction of threshold voltage in thin oxide MOSFET’s,” *Solid-State Electronics*, vol. 30, no. 9, pp. 953–968, 1987.
- [147] D. Caughey and R. Thomas, “Carrier mobilities in silicon empirically related to doping and field,” *Proceedings of the IEEE*, vol. 55, no. 12, pp. 2192–2193, 1967.
- [148] R. Jaggi and H. Weibel, “High-field electron drift velocities and current densities in silicon,” *Helvetica Physica Acta*, vol. 42, pp. 631–632, 1969.
- [149] R. Jaggi, “High-field drift velocities in silicon and germanium,” *Helvetica Physica Acta*, vol. 42, pp. 941–943, 1969.
- [150] S. Dhar, H. Kosina, G. Karlowatz, S. E. Ungersboeck, T. Grasser, and S. Selberherr, “High-field electron mobility model for strained-silicon devices,” *IEEE Transactions on Electron Devices*, vol. 53, no. 12, pp. 3054–3062, 2006.
- [151] T. Grasser and M. Karner, *Modellierung elektronischer Bauelemente*. Institute for Microelectronics, TU Vienna, 2006. Lecture Notes.
- [152] W. Shockley and W. Read, “Statistics of the recombinations of holes and electrons,” *Physical Review*, vol. 87, no. 5, pp. 835–842, 1952.
- [153] R. Hall, “Electron-hole recombination in germanium,” *Physical Review*, vol. 87, no. 2, p. 387, 1952.
- [154] D. Fleetwood, H. Xiong, Z.-Y. Lu, C. Nicklaw, J. Felix, R. Schrimpf, and S. Pantelides, “Unified model of hole trapping, 1/f noise, and thermally stimulated current in MOS devices,” *IEEE Transactions on Nuclear Science*, vol. 49, no. 6, pp. 2674–2683, 2002.
- [155] J. Brugler and P. Jespers, “Charge pumping in MOS devices,” *IEEE Transactions on Electron Devices*, vol. 16, no. 3, pp. 297–302, 1969.
- [156] P. Habas and S. Selberherr, “A closed-loop extraction of the spatial distribution of interface traps based on numerical model of the charge-pumping experiment,” in *Proceedings Solid State Devices and Materials (SSDM)*, pp. 170–172, 1992.
- [157] J. Dziewior and W. Schmid, “Auger coefficients for highly doped and highly excited silicon,” *Applied Physics Letters*, vol. 31, no. 5, pp. 346–348, 1977.

- [158] L. Hultdt, N. G. Nilsson, and K. G. Svantesson, "The temperature dependence of band-to-band Auger recombination in silicon," *Applied Physics Letters*, vol. 35, no. 10, pp. 776–777, 1979.
- [159] G. Hurkx, D. Klaassen, and M. Knuvers, "A new recombination model for device simulation including tunneling," *IEEE Transactions on Electron Devices*, vol. 39, no. 2, pp. 331–338, 1992.
- [160] H.-M. Lee, C.-J. Liu, C.-W. Hsu, M.-S. Liang, Y.-C. King, and C.-H. Hsu, "New trap-assisted band-to-band tunneling induced gate current model for p-channel metal-oxide-semiconductor field effect transistors with sub-3 nm oxides," *Japanese Journal of Applied Physics*, vol. 40, pp. 1218–1221, 2001.
- [161] J. Whitfield, C. Gill, J. Yang, H. Xu, C. Zhan, B. Baumert, and M. Zunino, "ESD MM failures resulting from transient reverse currents," in *Proceedings IEEE International Reliability Physics Symposium (IRPS)*, pp. 136–139, 2006.
- [162] V. d'Alessandro and N. Rinaldi, "A critical review of thermal models for electro-thermal simulation," *Solid-State Electronics*, vol. 46, no. 4, pp. 487–496, 2002.
- [163] P. Galy, V. Berland, B. Foucher, A. Guilhaume, J. Chante, S. Bardy, and F. Blanc, "Experimental and 3D simulation correlation of a gg-nMOS transistor under high current pulse," *Microelectronics Reliability*, vol. 42, no. 9–11, pp. 1299–1302, 2002.
- [164] H. Xie, R. Zhan, A. Wang, and R. Gafiteanu, "Real 3D electro-thermal simulation and analysis for ESD protection structures," in *Proceedings IEEE Devices, Circuits and Systems*, vol. 1, pp. 61–64, 2004.
- [165] S. Gaur and D. Navon, "Two-dimensional carrier flow in a transistor structure under nonisothermal conditions," *IEEE Transactions on Electron Devices*, vol. 23, no. 1, pp. 50–57, 1976.
- [166] M. Adler, "Accurate calculations of the forward drop and power dissipation in thyristors," *IEEE Transactions on Electron Devices*, vol. 25, no. 1, pp. 16–22, 1978.
- [167] J. Slotboom and H. de Graaff, "Bandgap narrowing in silicon bipolar transistors," *IEEE Transactions on Electron Devices*, vol. 24, no. 8, pp. 1123–1125, 1977.
- [168] S. Selberherr and E. Langer, "Low temperature MOS device modeling," in *Proceedings Workshop On Low Temperature Semiconductor Electronics*, pp. 68–72, 1989.
- [169] R. Tsu and L. Esaki, "Tunneling in a finite superlattice," *Applied Physics Letters*, vol. 22, no. 11, pp. 562–564, 1973.
- [170] R. H. Fowler and L. Nordheim, "Electron emission in intense electric fields," *Proceedings Royal Society A*, vol. 119, no. 781, pp. 173–181, 1928.
- [171] M. Herrmann and A. Schenk, "Field and high-temperature dependence of the long term charge loss in erasable programmable read only memories: Measurements and modeling," *Journal of Applied Physics*, vol. 77, no. 9, pp. 4522–4540, 1995.

## BIBLIOGRAPHY

- [172] R. Entner, T. Grasser, S. Selberherr, A. Gehring, and H. Kosina, “Modeling of tunneling currents for highly degraded CMOS devices,” in *Proceedings Simulation of Semiconductor Processes and Devices (SISPAD)*, pp. 219–222, 2005.
- [173] M. Wagner, M. Karner, and T. Grasser, “Quantum correction models for modern semiconductor devices,” in *Proceedings International Workshop on the Physics of Semiconductor Devices (IWPSD)*, vol. 1, pp. 458–461, 2005.
- [174] G. Paasch and H. Übensee, “A modified local density approximation,” *Physica status solidi (b)*, vol. 113, no. 1, pp. 165–178, 1982.
- [175] W. Hänsch, T. Vogelsang, R. Kircher, and M. Orlowski, “Carrier transport near the Si/SiO<sub>2</sub> interface of a MOSFET,” *Solid-State Electronics*, vol. 32, no. 10, pp. 839–849, 1989.
- [176] M. van Dort, P. Woerlee, and A. Walker, “A simple model for quantisation effects in heavily-doped silicon MOSFETs at inversion conditions,” *Solid-State Electronics*, vol. 37, no. 3, pp. 411–414, 1994.
- [177] M. Vasicek, *Advanced Macroscopic Transport Models*. Dissertation, Technische Universität Wien, Oktober 2009. <http://www.iue.tuwien.ac.at/phd/vasicek/>.
- [178] V. Palankovski, *Simulation of Heterojunction Bipolar Transistors*. Dissertation, Technische Universität Wien, 2000. <http://www.iue.tuwien.ac.at/phd/palankovski/>.
- [179] J. Slotboom, G. Streutker, M. van Dort, P. Woerlee, A. Pruijmboom, and D. Gravesteijn, “Non-local impact ionization in silicon devices,” in *Technical Digest International Electron Devices Meeting (IEDM)*, pp. 127–130, 8–11 Dec. 1991.
- [180] D. Cassi and B. Riccò, “An analytical model of the energy distribution of hot electrons,” *IEEE Transactions on Electron Devices*, vol. 37, no. 6, pp. 1514–1521, 1990.
- [181] A. Concannon, F. Piccinini, A. Mathewson, and C. Lombardi, “The numerical simulation of substrate and gate currents in MOS and EPROMs,” in *Technical Digest International Electron Devices Meeting (IEDM)*, pp. 289–292, 1995.
- [182] T. Grasser, H. Kosina, and S. Selberherr, “Influence of the distribution function shape and the band structure on impact ionization modeling,” *Journal of Applied Physics*, vol. 90, no. 12, pp. 6165–6171, 2001.
- [183] A. Gehring, *Simulation of Tunneling in Semiconductor Devices*. Dissertation, Technische Universität Wien, November 2003. <http://www.iue.tuwien.ac.at/phd/gehring/>.
- [184] P. G. Scrobohaci and T.-B. Tang, “Modeling of the hot electron subpopulation and its application to impact ionization in submicron silicon devices-Part I: transport equations,” *IEEE Transactions on Electron Devices*, vol. 41, no. 7, pp. 1197–1205, 1994.
- [185] K. Sonoda, S. Dunham, M. Yamaji, K. Taniguchi, and C. Hamaguchi, “Impact ionization model using average energy and average square energy of distribution function,” *Japanese Journal of Applied Physics*, vol. 35, no. 2B, pp. 818–825, 1996.

- [186] T. Grasser, H. Kosina, and S. Selberherr, “Hot carrier effects within macroscopic transport models,” *International Journal of High Speed Electronics and Systems*, vol. 13, no. 3, pp. 873–901, 2003.
- [187] T. Grasser, H. Kosina, C. Heitzinger, and S. Selberherr, “Accurate impact ionization model which accounts for hot and cold carrier populations,” *Applied Physics Letters*, vol. 80, no. 4, pp. 613–615, 2002.
- [188] G. Karlowatz, E. Ungersboeck, W. Wessner, and H. Kosina, “Full-band Monte Carlo analysis of electron transport in arbitrarily strained silicon,” in *Proceedings Simulation of Semiconductor Processes and Devices (SISPAD)*, pp. 63–66, 6–8 Sept. 2006.
- [189] R. van Overstraeten and H. de Man, “Measurement of the ionization rates in diffused silicon p-n junctions,” *Solid-State Electronics*, vol. 13, no. 5, pp. 583–608, 1970.
- [190] Y. Taur and T. Ning, *Fundamentals of Modern VLSI Devices*. Cambridge University Press, 1998.
- [191] A. G. Chynoweth, “Ionization rates for electrons and holes in silicon,” *Physical Review*, vol. 109, pp. 1537–1540, Mar 1958.
- [192] W. Shockley, “Problems related to p-n junctions in silicon,” *Solid-State Electronics*, vol. 2, no. 1, pp. 35–67, 1961.
- [193] P. A. Wolff, “Theory of electron multiplication in silicon and germanium,” *Physical Review*, vol. 95, no. 6, pp. 1415–1420, 1954.
- [194] Synopsys, Inc., originally published by ISE, *ISE TCAD Release 9.5 - ATLAS*, 2003.
- [195] G. A. Baraff, “Distribution functions and ionization rates for hot electrons in semiconductors,” *Physical Review*, vol. 128, no. 6, pp. 2507–2517, 1962.
- [196] C. R. Crowell and S. M. Sze, “Temperature dependence of avalanche multiplication in semiconductors,” *Applied Physics Letters*, vol. 9, no. 6, pp. 242–244, 1966.
- [197] A. Sutherland, “An improved empirical fit to Baraff’s universal curves for the ionization coefficients of electron and hole multiplication in semiconductors,” *IEEE Transactions on Electron Devices*, vol. 27, no. 7, pp. 1299–1300, 1980.
- [198] T. Lackner, “Avalanche multiplication in semiconductors: A modification of Chynoweth’s law,” *Solid-State Electronics*, vol. 34, no. 1, pp. 33–42, 1991.
- [199] J. Slotboom, G. Streutker, G. Davids, and P. Hartog, “Surface impact ionization in silicon devices,” in *Technical Digest International Electron Devices Meeting (IEDM)*, vol. 33, pp. 494–497, 1987.
- [200] M. van Dort, J. Slotboom, G. Streutker, and P. Woerlee, “Lifetime calculations of MOSFETs using depth-dependent non-local impact ionization,” *Microelectronics Journal*, vol. 26, pp. 301–305, 1995.

## BIBLIOGRAPHY

- [201] C. Jungemann, S. Yamaguchi, and H. Goto, "Is there experimental evidence for a difference between surface and bulk impact ionization in silicon?," in *Technical Digest International Electron Devices Meeting (IEDM)*, pp. 383–386, 1996.
- [202] Y. Okuto and C. R. Crowell, "Ionization coefficients in semiconductors: A nonlocalized property," *Physical Review B*, vol. 10, no. 10, pp. 4284–4296, 1974.
- [203] C. Hu, S. C. Tam, F.-C. Hsu, P.-K. Ko, T.-Y. Chan, and K. W. Terrill, "Hot-electron-induced MOSFET degradation – model, monitor, and improvement," *IEEE Transactions on Electron Devices*, vol. 32, no. 2, pp. 375–385, 1985.
- [204] Y. A. El-Mansy and D. M. Caughey, "Modelling weak avalanche multiplication currents in IGFETs and SOS transistors for CAD," in *Technical Digest International Electron Devices Meeting (IEDM)*, vol. 21, pp. 31–34, 1975.
- [205] B. Meinerzhagen, "Consistent gate and substrate current modeling based on energy transport and the lucky electron concept," in *Technical Digest International Electron Devices Meeting (IEDM)*, pp. 504–507, 1988.
- [206] K. Katayama and T. Toyabe, "A new hot carrier simulation method based on full 3d hydrodynamic equations," in *Technical Digest International Electron Devices Meeting (IEDM)*, pp. 135–138, 1989.
- [207] Y. Apanovich, E. Lyumkis, B. Polsky, A. Shur, and P. Blakey, "Steady-state and transient analysis of submicron devices using energy balance and simplified hydrodynamic models," *IEEE Transactions on Computer-Aided Design of Integrated Circuits and Systems*, vol. 13, no. 6, pp. 702–711, 1994.
- [208] F. M. Bufler, Y. Asahi, H. Yoshimura, C. Zechner, A. Schenk, and W. Fichtner, "Monte Carlo simulation and measurement of nanoscale n-MOSFETs," *IEEE Transactions on Electron Devices*, vol. 50, no. 2, pp. 418–424, 2003.
- [209] L. Keldysh, "Concerning the theory of impact ionization in semiconductors," *Soviet Physics JETP*, vol. 21, pp. 1135–1144, 1965.
- [210] Y. Kamakura, H. Mizuno, M. Yamaji, M. Morifuji, K. Taniguchi, C. Hamaguchi, T. Kuniyoshi, and M. Takenaka, "Impact ionization model for full band Monte Carlo simulation," *Journal of Applied Physics*, vol. 75, no. 7, pp. 3500–3506, 1994.
- [211] G. La Rosa and S. E. Rauch, III, "Channel hot carrier effects in n-MOSFET devices of advanced submicron CMOS technologies," *Microelectronics Reliability*, vol. 47, no. 4–5, pp. 552–558, 2007.
- [212] S. E. Rauch, III, F. J. Guarin, and G. La Rosa, "Impact of e-e scattering to the hot carrier degradation of deep submicron NMOSFETs," *IEEE Electron Device Letters*, vol. 19, no. 12, pp. 463–465, 1998.



- [213] S. E. Rauch, III, G. La Rosa, and F. J. Guarin, “Role of e-e scattering in the enhancement of channel hot carrier degradation of deep sub-micron NMOSFETs at high  $V_{GS}$  conditions,” in *Proceedings IEEE International Reliability Physics Symposium (IRPS)*, pp. 399–405, 2001.
- [214] I. Starkov, S. Tyaginov, O. Triebel, J. Cervenka, C. Jungemann, S. Carniello, J.-M. Park, H. Enichlmair, M. Karner, C. Kernstock, E. Seebacher, R. Minixhofer, H. Ceric, and T. Grasser, “Analysis of worst-case hot-carrier conditions for high voltage transistors based on full-band Monte-Carlo simulations,” in *Proceedings IEEE International Symposium on the Physical and Failure Analysis of Integrated Circuits (IPFA)*, pp. 1–6, 2010.
- [215] S. E. Rauch, III and G. La Rosa, “The energy driven paradigm of NMOSFET hot carrier effects,” in *Proceedings IEEE International Reliability Physics Symposium (IRPS)*, pp. 708–709, 2005.
- [216] J. G. Kassakian and D. J. Perreault, “The future of electronics in automobiles,” in *Proceedings International Symposium on Power Semiconductor Devices and IC’s (ISPSD)*, pp. 15–19, 2001.
- [217] T. Maloney and N. Khurana, “Transmission line pulsing techniques for circuit modeling,” in *Electrical Overstress/Electrostatic Discharge Symposium Proceedings*, pp. 49–54, 1985.
- [218] Z. Yu, D. Chen, R. J. G. Goossens, R. W. Dutton, P. Vande Voorde, and S.-Y. Oh, “Accurate modeling and numerical techniques in simulation of impact-ionization effects on BJT characteristics,” in *Technical Digest International Electron Devices Meeting (IEDM)*, pp. 901–904, 1991.
- [219] R. J. G. Goossens, S. Beebe, Z. Yu, and R. Dutton, “An automatic biasing scheme for tracing arbitrarily shaped I-V curves,” *IEEE Transactions on Computer-Aided Design of Integrated Circuits and Systems*, vol. 13, no. 3, pp. 310–317, 1994.
- [220] M. Bartels, S. Decker, B. Neinhuis, and B. Meinerzhagen, “A robust curve tracing scheme for the simulation of bipolar breakdown characteristics with nonlocal impact ionization models,” in *Proceedings European Solid-State Device Research Conference (ESSDERC)*, vol. 1, pp. 492–495, 1999.
- [221] C. Salaméro, N. Nolhier, A. Gendron, M. Bafleur, P. Besse, and M. Zécari, “TCAD methodology for ESD robustness prediction of smart power ESD devices,” *IEEE Transactions on Device and Materials Reliability*, vol. 6, no. 3, pp. 399–407, 2006.
- [222] E. Takeda, N. Suzuki, and T. Hagiwara, “Device performance degradation due to hot-carrier injection at energies below the Si-SiO<sub>2</sub> energy barrier,” in *Technical Digest International Electron Devices Meeting (IEDM)*, vol. 29, pp. 396–399, 1983.
- [223] A. Bravaix, C. Guerin, V. Huard, D. Roy, J. M. Roux, and E. Vincent, “Hot-carrier acceleration factors for low power management in DC-AC stressed 40nm NMOS node at high temperature,” in *Proceedings IEEE International Reliability Physics Symposium (IRPS)*, pp. 531–548, 2009.

## BIBLIOGRAPHY

- [224] W. Qin, W. Chim, D. Chan, and C. Lou, "Modelling the degradation in the subthreshold characteristics of submicrometre LDD PMOSFETs under hot-carrier stressing," *Semiconductor Science and Technology*, vol. 13, p. 453, 1998.
- [225] S. Ogura, P. J. Tsang, W. W. Walker, D. L. Critchlow, and J. F. Shepard, "Design and characteristics of the lightly doped drain-source (LDD) insulated gate field-effect transistor," *IEEE Transactions on Electron Devices*, vol. 27, no. 8, pp. 1359–1367, 1980.
- [226] T.-Y. Huang, "Effects of channel shapes on MOSFET hot-electron resistance," *Electronics Letters*, vol. 21, no. 5, pp. 211–212, 1985.
- [227] F.-C. Hsu and H. R. Grinolds, "Structure-enhanced MOSFET degradation due to hot-electron injection," *IEEE Electron Device Letters*, vol. 5, no. 3, pp. 71–74, 1984.
- [228] T. Mizuno, A. Toriumi, M. Iwase, M. Takahashi, H. Niiyama, M. Fukumoto, and M. Yoshimi, "Hot-carrier effects in 0.1  $\mu\text{m}$  gate length CMOS devices," in *Technical Digest International Electron Devices Meeting (IEDM)*, pp. 695–698, 1992.
- [229] E. Li, E. Rosenbaum, J. Tao, G. C.-F. Yeap, M.-R. Lin, and P. Fang, "Hot carrier effects in nMOSFETs in 0.1  $\mu\text{m}$  CMOS technology," in *Proceedings IEEE International Reliability Physics Symposium (IRPS)*, pp. 253–258, 1999.
- [230] K. Hess, L. F. Register, B. Tuttle, J. Lyding, and I. C. Kizilyalli, "Impact of nanostructure research on conventional solid-state electronics: The giant isotope effect in hydrogen desorption and CMOS lifetime," *Physica E*, vol. 3, no. 1–3, pp. 1–7, 1998.
- [231] W. McMahon, K. Matsuda, J. Lee, K. Hess, and J. Lyding, "The effects of a multiple carrier model of interface trap generation on lifetime extraction for MOSFETs," in *Proceedings NSTI-Nanotech*, vol. 1, pp. 576–579, 2002.
- [232] P. Avouris, R. E. Walkup, A. R. Rossi, T.-C. Shen, G. C. Abeln, J. R. Tucker, and J. W. Lyding, "STM-induced H atom desorption from Si(100): isotope effects and site selectivity," *Chemical Physics Letters*, vol. 257, no. 1–2, pp. 148–154, 1996.
- [233] J. W. Lyding, K. Hess, G. C. Abeln, D. S. Thompson, J. S. Moore, M. C. Hersam, E. T. Foley, J. Lee, Z. Chen, S. T. Hwang, H. Choi, P. Avouris, and I. C. Kizilyalli, "Ultrahigh vacuum-scanning tunneling microscopy nanofabrication and hydrogen/deuterium desorption from silicon surfaces: implications for complementary metal oxide semiconductor technology," *Applied Surface Science*, vol. 130–132, pp. 221–230, 1998.
- [234] K. Hess, L. Register, W. McMahon, B. Tuttle, O. Aktas, U. Ravaioli, J. Lyding, and I. Kizilyalli, "Theory of channel hot-carrier degradation in MOSFETs," *Physica B*, vol. 272, no. 1–4, pp. 527–531, 1999.
- [235] R. Biswas, Y.-P. Li, and B. C. Pan, "Enhanced stability of deuterium in silicon," *Applied Physics Letters*, vol. 72, no. 26, pp. 3500–3502, 1998.



- [236] K. Hess, A. Haggag, W. McMahon, B. Fischer, K. Cheng, J. Lee, and J. Lyding, "Simulation of Si-SiO<sub>2</sub> defect generation in CMOS chips: from atomistic structure to chip failure rates," in *Technical Digest International Electron Devices Meeting (IEDM)*, pp. 93–96, 2000.
- [237] E. Takeda and N. Suzuki, "An empirical model for device degradation due to hot-carrier injection," *IEEE Electron Device Letters*, vol. 4, no. 4, pp. 111–113, 1983.
- [238] J.-S. Goo, Y.-G. Kim, H. L'Yee, H.-Y. Kwon, and H. Shin, "An analytical model for hot-carrier-induced degradation of deep-submicron n-channel LDD MOSFETs," *Solid-State Electronics*, vol. 38, no. 6, pp. 1191–1169, 1995.
- [239] R. Dreesen, K. Croes, J. Manca, W. De Ceuninck, L. De Schepper, A. Pergoot, and G. Groeseneken, "Modelling hot-carrier degradation of LDD NMOSFETs by using a high-resolution measurement technique," *Microelectronics Reliability*, vol. 39, no. 6–7, pp. 785–790, 1999.
- [240] S. Tyaginov, I. Starkov, H. Enichlmair, J.-M. Park, C. Jungemann, and T. Grasser, "Physics-based hot-carrier degradation models," *ECS Transactions*, vol. 35, no. 4, pp. 321–352, 2011.
- [241] W. McMahon, L. F. Register, and K. Hess, "Effect of disorder-induced variations among the bond energies of passivated silicon dangling bonds on the time-dependence of nMOS-FET degradation," in *Annual March Meeting American Physical Society*, 2000.
- [242] A. Haggag, K. Hess, W. McMahon, and L. F. Register, "Impact of scaling on CMOS IC failure rate and design rules for reliability," in *Proceedings International Workshop of Computational Electronics (IWCE)*, pp. 49–50, 2000.
- [243] S. E. Rauch, III and G. La Rosa, "CMOS hot carrier: From physics to end of life projections, and qualification," in *Proceedings IEEE International Reliability Physics Symposium (IRPS)*, 2010.
- [244] C. Guerin, V. Huard, and A. Bravaix, "The energy-driven hot carrier degradation modes," in *Proceedings IEEE International Reliability Physics Symposium (IRPS)*, pp. 692–693, 2007.
- [245] S. Tyaginov, I. Starkov, O. Triebel, J. Cervenka, C. Jungemann, S. Carniello, J.-M. Park, H. Enichlmair, M. Karner, C. Kernstock, E. Seebacher, R. Minixhofer, H. Ceric, and T. Grasser, "Interface traps density-of-states as a vital component for hot-carrier degradation modeling," *Microelectronics Reliability*, vol. 50, no. 9–11, pp. 1267–1272, 2010.
- [246] P. Moens, M. Tack, R. Degraeve, and G. Groeseneken, "A novel hot-hole injection degradation model for lateral nDMOS transistors," in *Technical Digest International Electron Devices Meeting (IEDM)*, pp. 39.6.1–39.6.4, 2001.
- [247] P. Moens, J. Mertens, F. Bauwens, P. Joris, W. De Ceuninck, and M. Tack, "A comprehensive model for hot carrier degradation in LDMOS transistors," in *Proceedings IEEE International Reliability Physics Symposium (IRPS)*, pp. 492–497, 2007.

## BIBLIOGRAPHY

- [248] I. Starkov, H. Enichlmair, S. Tyaginov, and T. Grasser, “Analysis of the threshold voltage turn-around effect in high-voltage n-MOSFETs due to hot-carrier stress,” in *Proceedings IEEE International Reliability Physics Symposium (IRPS)*, pp. XT.7.1–XT.7.6, 2012.
- [249] I. Starkov, H. Ceric, H. Enichlmair, J.-M. Park, S. Tyaginov, T. Grasser, and C. Jungemann, “Analysis of worst-case hot-carrier degradation conditions in the case of n- and p-channel high-voltage MOSFETs,” in *Proceedings Simulation of Semiconductor Processes and Devices (SISPAD)*, pp. 127–130, 2011.
- [250] M. Bina, K. Rupp, S. Tyaginov, O. Triebel, and T. Grasser, “Modeling of hot carrier degradation using a spherical harmonics expansion of the bipolar Boltzmann transport equation,” in *Technical Digest International Electron Devices Meeting (IEDM)*, 2012. (in print).
- [251] D. DiMaria and J. Stasiak, “Trap creation in silicon dioxide produced by hot electrons,” *Journal of Applied Physics*, vol. 65, no. 6, pp. 2342–2356, 1989.
- [252] P. Hehenberger, T. Aichinger, T. Grasser, W. Göss, O. Triebel, B. Kaczer, and M. Nelhiebel, “Do NBTI-induced interface states show fast recovery? A study using a corrected on-the-fly charge-pumping measurement technique,” in *Proceedings IEEE International Reliability Physics Symposium (IRPS)*, pp. 1033–1038, 2009.
- [253] T. Grasser, H. Reisinger, P. Wagner, F. Schanovsky, W. Göss, and B. Kaczer, “The time dependent defect spectroscopy (TDDS) for the characterization of the bias temperature instability,” in *Proceedings IEEE International Reliability Physics Symposium (IRPS)*, pp. 16–25, 2010.
- [254] T. Grasser, B. Kaczer, W. Göss, H. Reisinger, T. Aichinger, P. Hehenberger, P. Wagner, F. Schanovsky, J. Franco, P. Roussel, and M. Nelhiebel, “Recent advances in understanding the bias temperature instability,” in *Technical Digest International Electron Devices Meeting (IEDM)*, pp. 4.4.1–4.4.4, 2010.
- [255] P. Fleischmann, *Mesh Generation for Technology CAD in Three Dimensions*. Dissertation, Technische Universität Wien, 1999. <http://www.iue.tuwien.ac.at/phd/fleischmann/>.
- [256] L. P. Chew, “Create a Voronoi diagram or Delaunay triangulation by clicking points,” 2007. <http://www.cs.cornell.edu/home/chew/Delaunay.html>.
- [257] A. Okabe, B. Boots, and K. Sugihara, *Spatial Tessellations*. John Wiley and Sons Ltd, 1992.
- [258] M. Spevak, R. Heinzl, P. Schwaha, and T. Grasser, “Simulation of microelectronic structures using a posteriori error estimation and mesh optimization,” in *5th Mathmod Vienna Proceedings*, pp. 5.1–5.8, 2006.
- [259] R. Bank, D. Rose, and W. Fichtner, “Numerical methods for semiconductor device simulation,” *IEEE Transactions on Electron Devices*, vol. 30, no. 9, pp. 1031–1041, 1983.

- [260] Z. Stanojević, M. Karner, K. Schnass, C. Kernstock, O. Baumgartner, and H. Kosina, “A versatile finite volume simulator for the analysis of electronic properties of nanostructures,” in *Proceedings Simulation of Semiconductor Processes and Devices (SISPAD)*, pp. 143–146, 2011.
- [261] S. J. Polak, C. den Heijer, and W. Schilders, “Semiconductor device modelling from the numerical point of view,” *International Journal for Numerical Methods in Engineering*, vol. 24, pp. 763–838, 1987.
- [262] O. Triebel and T. Grasser, “Investigation of vector discretization schemes for box volume methods,” in *Proceedings NSTI-Nanotech*, vol. 3, pp. 61–64, 2007.
- [263] S. Laux and B. Grossman, “A general control-volume formulation for modeling impact ionization in semiconductor transport,” *IEEE Transactions on Electron Devices*, vol. 32, no. 10, pp. 2076–2082, 1985.
- [264] J. Bürgler, R. Bank, W. Fichtner, and R. Smith, “A new discretization scheme for the semiconductor current continuity equations,” *IEEE Transactions on Computer-Aided Design of Integrated Circuits and Systems*, vol. 8, no. 5, pp. 479–489, 1989.
- [265] Synopsys, Inc., originally published by ISE, *ISE TCAD Release 9.5 - DESSIS*, 2003.
- [266] H. Shao, *Numerical Analysis of Meshing and Discretization for Anisotropic Convection-Diffusion Equations with Applications*. Dissertation, Duke University, Aug. 1999.
- [267] M. Patil, “New discretization scheme for two-dimensional semiconductor device simulation on triangular grid,” *IEEE Transactions on Computer-Aided Design of Integrated Circuits and Systems*, vol. 17, no. 11, pp. 1160–1165, 1998.
- [268] Y. He and G. Cao, “A generalized Scharfetter-Gummel method to eliminate crosswind effects,” *IEEE Transactions on Computer-Aided Design of Integrated Circuits and Systems*, vol. 10, no. 12, pp. 1579–1582, 1991.
- [269] W. Allegretto, A. Nathan, and H. Baltes, “Numerical analysis of magnetic-field-sensitive bipolar devices,” *IEEE Transactions on Computer-Aided Design of Integrated Circuits and Systems*, vol. 10, no. 4, pp. 501–511, 1991.
- [270] H. Kosina, O. Triebel, and T. Grasser, “Box method for the convection-diffusion equation based on exponential shape functions,” in *Proceedings Simulation of Semiconductor Processes and Devices (SISPAD)*, vol. 12, pp. 317–320, 2007.
- [271] O. Triebel and T. Grasser, “Vector discretization schemes in technology CAD environments,” *Romanian Journal of Information Science and Technology*, vol. 10, no. 2, pp. 167–176, 2007.
- [272] C. Fischer, *Bauelementsimulation in einer computergestützten Entwurfsumgebung*. Dissertation, Technische Universität Wien, May 1994. <http://www.iue.tuwien.ac.at/phd/fischer/>.

## BIBLIOGRAPHY

- [273] O. Schenk, M. Hagemann, and S. Rollin, “Recent advances in sparse linear solver technology for semiconductor device simulation matrices,” in *Proceedings Simulation of Semiconductor Processes and Devices (SISPAD)*, pp. 103–108, 2003.
- [274] P. Deuffhard, “A modified Newton method for the solution of ill-conditioned systems of nonlinear equations with application to multiple shooting,” *Numerische Mathematik*, vol. 22, pp. 289–315, 1974.
- [275] V. Axelrad, “Grid quality and its influence on accuracy and convergence in device simulation,” *IEEE Transactions on Computer-Aided Design of Integrated Circuits and Systems*, vol. 17, no. 2, pp. 149–157, 1998.
- [276] N. Shigyo, H. Tanimoto, and T. Enda, “Mesh related problems in device simulation: Treatments of meshing noise and leakage current,” *Solid-State Electronics*, vol. 44, pp. 11–16, 2000.

## Own Publications

- [1] M. Bina, K. Rupp, S. Tyaginov, O. Triebel, and T. Grasser, “Modeling of hot carrier degradation using a spherical harmonics expansion of the bipolar Boltzmann transport equation,” in *Technical Digest International Electron Devices Meeting (IEDM)*, 2012. (in print).
- [2] M. Bina, O. Triebel, B. Schwarz, M. Karner, B. Kaczer, and T. Grasser, “Simulation of reliability on nanoscale devices,” in *Proceedings Simulation of Semiconductor Processes and Devices (SISPAD)*, pp. 109–112, 2012.
- [3] S. Tyaginov, I. Starkov, O. Triebel, H. Ceric, T. Grasser, H. Enichlmair, J.-M. Park, and C. Jungemann, “Secondary generated holes as a crucial component for modeling of HC degradation in high-voltage n-MOSFET,” in *Proceedings Simulation of Semiconductor Processes and Devices (SISPAD)*, pp. 123–126, 2011.
- [4] O. Triebel and T. Grasser, “Numerical Power/HV device modeling,” in *Power/HVMOS Devices Compact Modeling* (W. Grabinski and T. Gneiting, eds.), ch. 1, pp. 1–32, Springer, 2010. ISBN: 978-90-481-3045-0.
- [5] S. Tyaginov, I. Starkov, O. Triebel, J. Cervenka, C. Jungemann, S. Carniello, J.-M. Park, H. Enichlmair, M. Karner, C. Kernstock, E. Seebacher, R. Minixhofer, H. Ceric, and T. Grasser, “Interface traps density-of-states as a vital component for hot-carrier degradation modeling,” *Microelectronics Reliability*, vol. 50, no. 9–11, pp. 1267–1272, 2010.
- [6] S. Tyaginov, I. Starkov, O. Triebel, J. Cervenka, C. Jungemann, S. Carniello, J.-M. Park, H. Enichlmair, M. Karner, C. Kernstock, E. Seebacher, R. Minixhofer, H. Ceric, and T. Grasser, “Interface traps density-of-states as a vital component for hot-carrier degradation modeling,” in *Proceedings European Symposium on Reliability Electron Devices, Failure Physics and Analysis (ESREF)*, 2010.
- [7] I. Starkov, S. Tyaginov, O. Triebel, J. Cervenka, C. Jungemann, S. Carniello, J.-M. Park, H. Enichlmair, M. Karner, C. Kernstock, E. Seebacher, R. Minixhofer, H. Ceric, and T. Grasser, “Analysis of worst-case hot-carrier conditions for high voltage transistors based on full-band Monte-Carlo simulations,” in *Proceedings IEEE International Symposium on the Physical and Failure Analysis of Integrated Circuits (IPFA)*, pp. 1–6, 2010.
- [8] S. Tyaginov, I. Starkov, O. Triebel, J. Cervenka, C. Jungemann, S. Carniello, J.-M. Park, H. Enichlmair, M. Karner, C. Kernstock, E. Seebacher, R. Minixhofer, H. Ceric, and

## OWN PUBLICATIONS

- T. Grasser, “Hot-carrier degradation modeling using full-band Monte-Carlo simulations,” in *Proceedings IEEE International Symposium on the Physical and Failure Analysis of Integrated Circuits (IPFA)*, pp. 1–5, 2010.
- [9] I. Starkov, S. Tyaginov, H. Enichlmair, O. Triebel, J. Cervenka, C. Jungemann, S. Carniello, J.-M. Park, H. Ceric, and T. Grasser, “HC degradation model: interface state profile – simulations vs. experiment,” in *Book of Abstracts Workshop on Dielectrics in Microelectronics (WODIM)*, p. 128, 2010.
- [10] P. Hehenberger, T. Aichinger, T. Grasser, W. Gös, O. Triebel, B. Kaczer, and M. Nelhiebel, “Do NBTI-induced interface states show fast recovery? A study using a corrected on-the-fly charge-pumping measurement technique,” in *Proceedings IEEE International Reliability Physics Symposium (IRPS)*, pp. 1033–1038, 2009.
- [11] H. Kosina, O. Triebel, and T. Grasser, “Box method for the convection-diffusion equation based on exponential shape functions,” in *Proceedings Simulation of Semiconductor Processes and Devices (SISPAD)*, vol. 12, pp. 317–320, 2007.
- [12] O. Triebel and T. Grasser, “Vector discretization schemes in technology CAD environments,” *Romanian Journal of Information Science and Technology*, vol. 10, no. 2, pp. 167–176, 2007.
- [13] O. Triebel and T. Grasser, “Investigation of vector discretization schemes for box volume methods,” in *Proceedings NSTI-Nanotech*, vol. 3, pp. 61–64, 2007.
- [14] R. Entner, T. Grasser, O. Triebel, H. Enichlmair, and R. Minixhofer, “Negative bias temperature instability modeling for high-voltage oxides at different stress temperatures,” *Microelectronics Reliability*, vol. 47, no. 4–5, pp. 697–699, 2007.
- [15] O. Triebel and T. Grasser, “Vector discretization schemes based on unstructured neighborhood information,” in *Proceedings International Semiconductor Conference (CAS)*, vol. 2, pp. 337–340, 2006.
- [16] T. Grasser, R. Entner, O. Triebel, H. Enichlmair, and R. Minixhofer, “TCAD modeling of negative bias temperature instability,” in *Proceedings Simulation of Semiconductor Processes and Devices (SISPAD)*, pp. 330–333, 2006.
- [17] M. Wagner, G. Span, S. Holzer, V. Palankovski, O. Triebel, and T. Grasser, “Power output improvement of silicon-germanium thermoelectric generators,” in *SiGe and Ge: Materials, Processing, and Devices*, vol. 3, pp. 1151–1162, ECS Transactions, 2006.
- [18] M. Wagner, G. Span, S. Holzer, O. Triebel, and T. Grasser, “Power output improvement of SiGe thermoelectric generators,” in *Abstracts Joint International Meeting of the Electrochemical Society (ECS)*, p. 1516, 2006.
- [19] O. Triebel, “Verfolgen von teilweise verdeckten Kanten mit Hilfe von Suchlinien,” Master’s thesis, Technische Universität Wien, 2005.



# Curriculum Vitae

## **Dipl.-Ing. Oliver Triebel**

2352 Gumpoldskirchen, Friedrich-Schiller-Straße 21

### **since January 2011**

Restarted working on various projects for the *Institute for Microelectronics, Vienna University of Technology*.

### **since October 2010**

Working for Global TCAD Solutions GmbH.

### **April – September 2010**

Traveled through Latin America, studying Spanish.

### **May 2005**

Entered doctoral program at the *Institute for Microelectronics, Vienna University of Technology*, under the supervision of Prof. Tibor Grasser.

### **March 2005**

Received degree of Diplom-Ingenieur (comparable to M.Sc.) in Electrical Engineering, specialization in Computer Engineering from the *Vienna University of Technology* (with honors).

### **June 2003 – May 2004**

Compulsory year of civil service: Served as ambulance officer.

### **February – June 2000**

Exchange semester at the *University of Aalborg, Denmark*: Attended the course *Intelligent Multimedia*.

### **since October 1996**

Working part time as IT administrator for *Activa Wirtschaftstreuhand GmbH*.

### **October 1996 – March 2005**

Enrolled in Electrical Engineering at *Vienna University of Technology*.

### **June 1996**

High school graduation (Matura) at the *Höhere Technische Bundeslehr- und Versuchsanstalt Mödling* (with honors).

### **August 5, 1977**

Born in Vienna, Austria.